7-23-2018 10:40 AM

Transformerless High-Power Medium-Voltage Multi-Module PV Converters

Hasan Bayat
The University of Western Ontario

Supervisor
Yazdani, Amirnaser
The University of Western Ontario

Graduate Program in Electrical and Computer Engineering
A thesis submitted in partial fulfillment of the requirements for the degree in Doctor of Philosophy
© Hasan Bayat 2018

Abstract

This thesis is focused on the modular multilevel converter (MMC) for Photovoltaic (PV) applications. It is an attempt to address the issues associated with the modeling, control, and power mismatch elimination of the MMC-based PV systems. Firstly, a new real power reference generation scheme is proposed that creates a linear relationship between the real power reference of the system and the dc link voltage of the submodules. The proposed real power reference generation scheme ensures accurate control of dc link voltages of the submodules using a simple Proportional-Integral (PI) controller.

Further, a new power mismatch elimination strategy is proposed for the MMC-based PV system which ensures balanced currents are delivered to the host grid regardless of leg and arm power mismatches. The proposed strategy transfers power between the legs of the converter to equalize the powers injected to the grid from the phases of the converter.

The thesis also proposes a new configuration for embedding battery energy storage (BES) systems into the arms of the converter. Then, an enabling control scheme is proposed for the MMC-based PV-BES system which employs the embedded BES systems to eliminate power mismatches and smoothen the output power of the PV generators. The proposed power mismatch elimination strategy for the MMC-based PV-BES system uses the power exchange with the embedded BES systems to eliminate small power mismatches. To mitigate large power mismatches which are outside the power rating of the BES systems, the proposed strategy uses a combination of power exchange with BES systems and power transfer between the legs of the converter.

Finally, a modified power mismatch elimination strategy is proposed to ensure balanced grid currents even if the grid voltage is unbalanced. To achieve this goal, unequal powers are delivered to the grid from the phases of the system according to the voltage magnitude of each phase.

Keywords: Modular multilevel converter, MMC-based PV system, power mismatch, unbalanced grid, differential current, battery energy storage, photovoltaic, grid integration.

Dedication

To my parents,

and my wife,

for their endless love and generous support.

Acknowledgments

I would like to express my sincere gratitude to Dr. Amirnaser Yazdani for his excellent supervision, immense knowledge, and continuous encouragement throughout the course of this research. It has been a great privilege and honor to pursue my higher education under his supervision.

Furthermore, I thank my Ph.D. examination committee, Dr. Mehrdad Kazerani from University of Waterloo, Dr. Rajiv K. Varma, Dr. George K. Knopf, and Dr. Quazi Rahman from University of Western Ontario, for their review of this thesis, discussions, and comments.

I also would like to thank my friends in London, Ontario, who were extremely supportive throughout my Ph.D. program.

Contents

List of Figures

List of Tables

List of Appendices

List of Acronyms

AVM   Average value model

BES   Battery energy storage

CAES   Compressed air energy storage

CCSC   Circulating current suppressing compensator

CHB   Cascaded h-bridge

DAB   Dual active bridge

DCC   Differential current controller

DSP   Digital signal processor

EDLC   Electrochemical double-layer capacitor

EPIA   European photovoltaic industry association

ESS   Energy storage system

FC   Flying capacitor

HVDC   High-voltage direct current

IEA   International energy agency

IGBT   Insulated-gate bipolar transistor

KVL   Kirchoff's voltage law

LS-PWM   Level-shifted pulse-width modulation

MMC   Modular multilevel converter

MPPT   Maximum power point tracking

MVD   Medium-voltage drive

NLM   Nearest level modulation

NPC   Neutral point clamped

PCC   Point of common coupling

PHS	Pumped hydro storage
PI	Proportional integral
PID	Potential-induced degradation
PLL	Phase-locked loop
PR	Proportional resonant
PS-PWM	Phase-shifted pulse-width modulation
PV	Photovoltaic
PVPS	Photovoltaic power systems programme
PWM	Pulse-width modulation
RSF	Reduced switching frequency
SM	Submodule
SMA	Simple moving average
SMES	Superconductive magnetic energy storage
SOC	State of charge
STC	Standard testing condition
SVM	Space vector modulation
TEES	Thermoelectric energy storage
THD	Total harmonic distortion
VSC	Voltage-sourced converter

Convention for Notations

For clarity and consistency, the following conventions for notations are used in this thesis.

- Circuit parameters are denoted by uppercase letters, for example, R, L.

- Instantaneous variables are denoted by lowercase letters, for example, i_s, v_s.

- Real and reactive powers are denoted by lowercase letters, for example, p_s, q_s.

- Subscript s denotes a PCC variable.

- Subscript g denotes a grid variable.

- Subscript D and Q denote a DQ-frame variable.

- Subscript d denotes a differential variable.

- Subscript e denotes an internal variable of the converter.

- Subscript sm denotes a submodule variable.

- Superscript B denotes a battery energy storage variable.

- Superscript $*$ denotes the reference value of a variable.

- Overline $\overline{(.)}$ denotes the average of the variable over a fundamental frequency period.

Nomenclature

N Number of PV submodules per MMC arm

n Number of DAB converters per PV submodule

R Arm equivalent series resistance

L Arm series inductance

R_g Grid's Thevenin resistance

L_g Grid's Thevenin inductance

$v_{s,k}$ Grid (PCC) voltage for phase k

$i_{s,k}$ Grid current for phase k

$v_{e,k}$ Internal voltage of the MMC for phase k

$i_{u,k}$ Upper arm current in leg k

$v_{u,k}$ Upper arm voltage in leg k

$i_{\ell,k}$ Lower arm current in leg k

$v_{\ell,k}$ lower arm voltage in leg k

C Submodule capacitance

C_{pv} PV-side capacitance of DAB converter

$v_{sm,jk}$ Ac voltage of the j$^{\text{th}}$ submodule in leg k

$v_{sm,jk}^{dc}$ Dc voltage of the j$^{\text{th}}$ submodule in leg k

$p_{sm,jk}^{ac}$ Average ac power leaving the ac-side terminals of the j$^{\text{th}}$ submodule in leg k

$p_{sm,jk}^{dc}$ Dc power delivered by the PV generators to the dc-side terminals of the j$^{\text{th}}$ submodule in leg k

$p_{d,k}$ Differential dc power of leg k

q_d Sum of the reactive powers exchanged with the MMC arms

p_k^{ex} Power mismatch of leg k

p_k^{dc} Aggregate power delivered by the PV generators of leg k

$p_{u,k}^{dc}$ Aggregate power delivered by the PV generators of the upper arm in leg k

$p_{\ell,k}^{dc}$ Aggregate power delivered by the PV generators of the lower arm in leg k

$p_{u,k}^{B}$ Power of the BES of the upper arm in leg k

$p_{u,k}^{BM}$ Power of the BES of the upper arm in leg k due to power mismatch elimination function

$p_{u,k}^{BS}$ Power of the BES of the upper arm in leg k due to power smoothing function

$p_{\ell,k}^{B}$ Power of the BES of the lower arm in leg k

$p_{\ell,k}^{BM}$ Power of the BES of the lower arm in leg k due to power mismatch elimination function

$p_{\ell,k}^{BS}$ Power of the BES of the lower arm in leg k due to power smoothing function

P_{PV} Aggregate power generated by the PV generators

P_B Aggregate power of the BES systems

p_s Real power output of the PV system

q_s Reactive power output of the PV system

f Power system frequency

$i_{d,k}$ Differential component of the arm currents in leg k

$i_{d,k}^{ac}$ Ac differential current (ac component of $i_{d,k}$)

$i_{d,k}^{dc}$ Dc differential current (dc component of $i_{d,k}$)

$v_{d,k}$ Differential component of the arm voltages

v_p Positive dc link voltage of the MMC

v_n Negative dc link voltage of the MMC

$\hat{v}_e$ Peak value of $v_{e,k}$

$\hat{i}_d^1$ Peak value of the positive-sequence component of $i_{d,k}^{ac}$

$\hat{i}_d^2$ Peak value of the negative-sequence component of $i_{d,k}^{ac}$

v_{dcf} Voltage of the virtual dc link

$SM_{j,k}$ Submodule j in leg k

$SM_{k,u}^B$ BES submodule of the upper arm of leg k

$SM_{k,\ell}^B$ Submodule of the lower arm of leg k

Chapter 1

Introduction

1.1   Background and Motivation

Year 2014 marked the 60th anniversary of the first public demonstration of photovoltaic (PV) cell developed by Bell Labs [1]. After almost three decades of research and improvement in efficiency and technology, the first grid-connected PV system commissioned in 1983 by Atlantic Richfield company (ARCO Solar) in central California [2]. Since then, many high power PV systems have been constructed and connected to power systems, many exceeding 100 MW in power rating. According to the photovoltaic power systems programme (PVPS) annual report of international energy agency (IEA) and European photovoltaic industry association (EPIA) data, the year 2017 has seen more than 98 GW of additional grid-connected PV solar systems installed worldwide, approximately %48 more than the total installed capacity in the year of 2015 and raising the cumulative installed capacity close to 402 GW [3], [4]. This large amount of PV solar power generation installed in span of one year shows the great pace of penetration of PV solar power into power systems. Figure 1.1 presents the grid-connected capacities which best describes the role of PV solar power in the energy system. Figure 1.2 shows the growth scenarios of the global installed PV power capacity which predicts close to 1 TW total installed PV solar power by the year 2021.
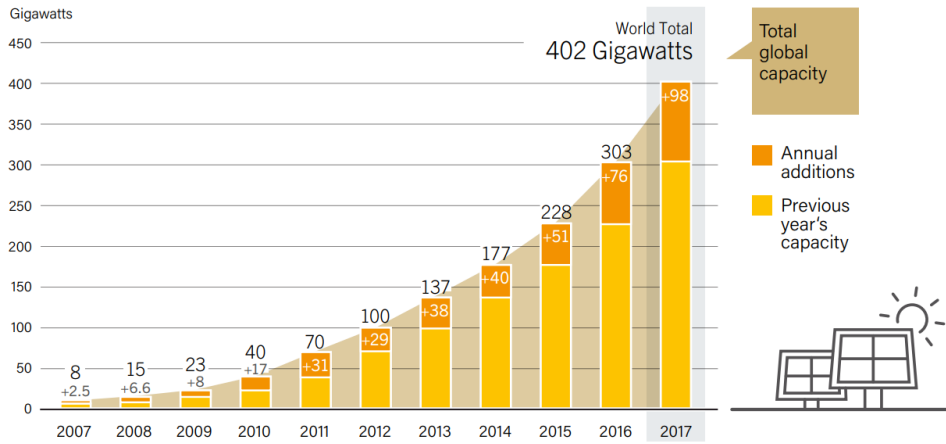
Figure 1.1: Cumulative global PV solar power installed capacity [5]

Canada is one of the top 10 countries in the world with respect to the total installed PV solar power capacity. Since 2001, Canada's PV solar power sector has been witnessing a significant growth in investments year after year. According to the national survey report of PV solar power applications in Canada, as shown in Figure 1.3, the cumulative installed PV solar power capacity had grown to about 2661 MW in 2016 [6].
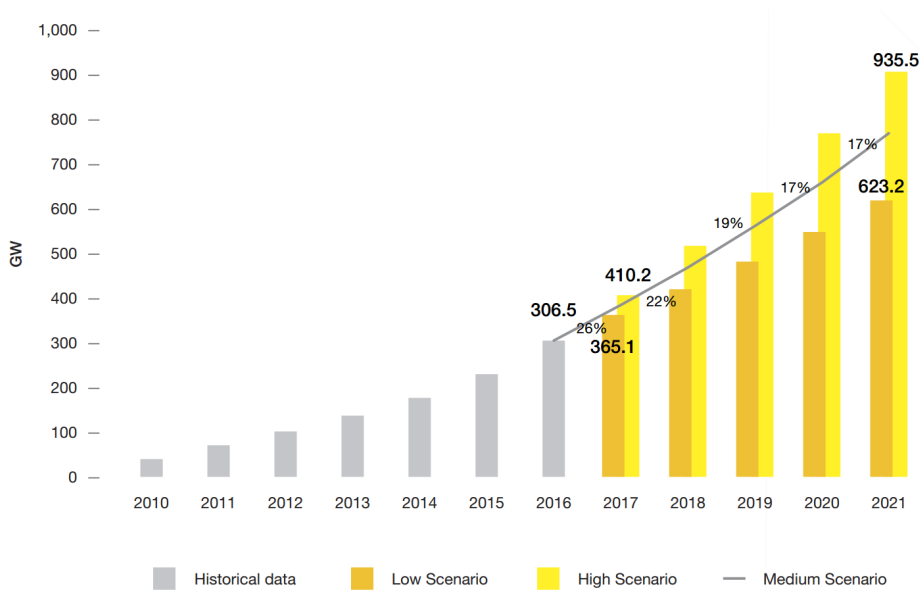
Figure 1.2: Growth scenarios of global installed PV solar power capacity [4]
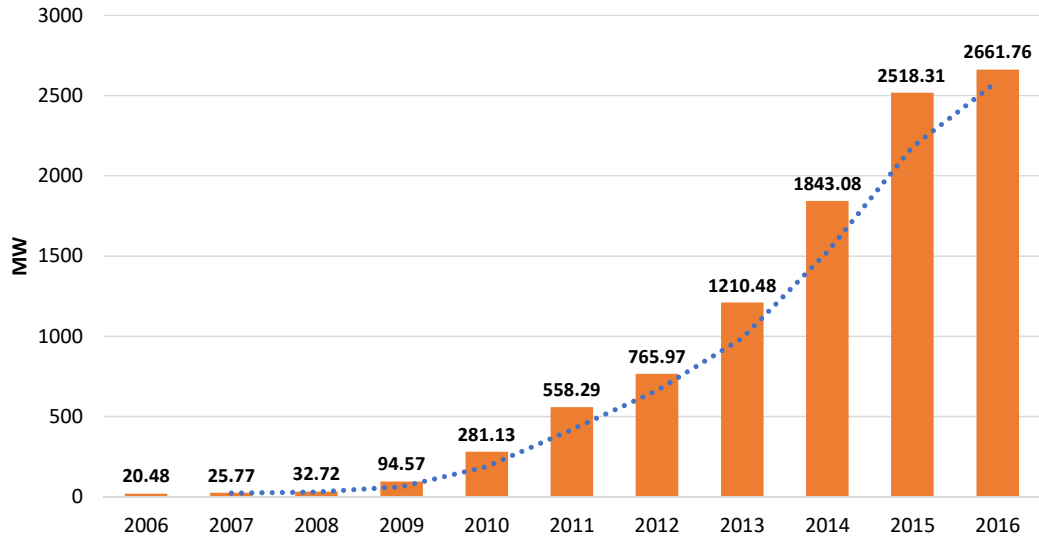
Figure 1.3: Cumulative PV solar power capacity installed in Canada [6]

As presented earlier, the installed PV solar power capacity in the world is growing rapidly and the majority of the growth is related to grid-connected utility-scale installations. These types of PV farms require high-power converters to enable interconnecting into power system. Since the advent of grid-connected PV systems, the related technologies have undergone major changes and improvements. The thyristor, for instance, which was the main switching devices choice for power converters in PV applications, have been replaced by new semiconductor devices such as insulated-gate bipolar transistor (IGBT) [7]. Thus far, the two- and three-level three-phase voltage-sourced converters (VSCs) have served as the building blocks of the PV systems. However, these converters have problems that have motivated researchers to seek new topologies which are more suitable for PV integration. The main challenges facing the application of conventional two- and three-level converters are as follows.

- A large capacitor is required at the dc side of conventional VSCs [8].

- The power quality of the conventional converters is low since they generate two- and three-level output voltage that contains high harmonic contents [9].

- Conventional VSCs use series and parallel combination of switching devices to reach

the voltage and current ratings of the converter, respectively. Unequal voltage sharing across semiconductor switches is one of the problems of such combinations [10].

- High switching frequency is needed in conventional VSCs that leads to high switching losses [9, 11].

Another challenge of the two- and three-level conventional VSCs is their power rating. The power rating of the largest commercially available VSCs is in the range of 1.5 MW that is limited by the insulation of PV generators. In order to integrate a utility-scale PV farm, a large number of conventional VSCs are needed which accumulates the problems associated with individual VSCs including power conversion efficiency and power quality degradation.

The problems associated with conventional two- and three-level VSCs have motivated researchers to seek innovative means for integration of PV farms. Multilevel VSCs are a new topology of power converters which have been proposed in the literature to overcome the shortcomings of the conventional two- and three-level converters. Multilevel converters can synthesize the output voltage in multiple levels which mimics the sinusoidal waveform in a better manner. Although multilevel converters are fairly new technologies, the concept is rather old [12]. The idea is to create higher number of output levels that resembles sinusoidal waveform. There are multiple advantages associated with multilevel topologies that makes them suitable for high-power and high-voltage applications such as integration of utility-scale PV farms into power system. The main advantages of multilevel converters are outlined here.

- Multilevel topologies eliminate the need for bulky line transformer since they can reach medium- and high-voltage levels owing to their multilevel output voltage. This feature saves space and material while being advantageous economically [13], [14].

- They have less ac filtering requirements because of the multilevel output voltage

waveform that has less harmonic content concentrated at higher frequencies compared to their two- and three-level counterparts [15].

- They provide higher power quality towards meeting mandates of tighter grid codes [16]. Providing an output voltage with limited amount of harmonics is one of the main requirements for high-power converters.

Multilevel converters offer multiple advantages over their predecessors as mentioned here. The only disadvantage outlined in the literature for multilevel converters is the complexity of their control which stems from multiple energy storage elements and high number of switching devices [17]. However, this challenge is solved nowadays with advancements in computer hardware and software industry.

Different topologies of multilevel converters have their own pros and cons which justifies their concurrent existence in the market. The most popular multilevel converter topologies are neutral point clamped (NPC) [18], flying capacitor (FC) [19], and cascaded h-bridge (CHB) [20]. These topologies have been studied extensively in the literature and used for different applications including motor drives and PV integration.

Modular multilevel converter (MMC), first presented in [21], is a new and emerging breed of multilevel converter topologies which has the potential to be used for integration of PV systems. The main application of this topology is in high voltage direct current (HVDC) systems where it offers advantages which are outside the scope of this thesis and are not discussed herein. Siemens and ABB are two manufacturers of the MMC-based HVDC systems namely HVDC plus and HVDC light, respectively. These two converters are identical in technology but have two distinct commercial names since they are manufactured by two different companies. These two companies have close to 40 installed MMC-based HVDC systems worldwide [22], [23].

As mentioned earlier, multilevel converters offer some appealing advantages over their conventional counterparts. Retaining all the advantages of multilevel converters outlined earlier, MMC possesses other features that makes it a unique multilevel converter. The features of the MMC are as follows.

- Switching frequency of the switching devices in MMC topology is much lower than the ones in conventional converters. This characteristic translates to lower switching losses in the MMC [24, 25].

- Scaling the voltage and power ratings of MMC topology is simple and is achieved by cascading submodules [26, 27].

- Redundant switching states are realized simply [26]. Redundancy feature is the ability to generate each output voltage level with different combination of on and off switches.

- It features longer maintenance intervals and improved reliability [28].

- MMC is independent of technology of the fast developing switching devices [29]. In other words, each submodule in the converter can be realized using different type of switching technologies without affecting the operation of the converter.

- It features a modular design based on identical converter cells that reduces the production cost due to bulk production [26, 27].

Since new installations of PV systems are growing in power and number, the need for new converter topologies with higher power rating and more flexible features become more evident. Consequently, this thesis is dedicated to study the application of MMC, which is capable of meeting the required power rating and flexibility levels, for integration of PV systems.

1.2 Statement of Problem and Thesis Objectives

PV farms are categorized into different configurations based on the way they are connected to power system. These configurations include centralized, string, multi-string, and ac-module topologies. MMC introduces a new and unique PV farm configuration combining features of the aforementioned PV farm topologies. In this topology, dc power

form PV generators is delivered directly to the arms of the MMC, rather than being injected into a common dc link. As illustrated in Figure 1.4, PV generators are connected to the submodules of the MMC; hence, the real power is directly injected into the arms of the MMC-based PV system. This topology suffers from power mismatch problem, meaning that if the aggregate powers injected into the arms of each phase are not equal, or the aggregate powers injected into the legs of the converter are not equal, the system will fail to inject balance currents into power grid. The different types of power mismatches are as follows

- Arm power mismatch is characterized as unequal aggregate PV power injection into the upper and lower arms of a phase in the MMC.

$$p_{u,a}^{dc} \neq p_{\ell,a}^{dc} \quad or \quad p_{u,b}^{dc} \neq p_{\ell,b}^{dc} \quad or \quad p_{u,c}^{dc} \neq p_{\ell,c}^{dc} \tag{1.1}$$

  where $p_{u,k}^{dc}$ and $p_{\ell,k}^{dc}$ are the aggregate powers delivered to the upper and lower arms of leg k, respectively.

- Leg power mismatch is characterized as unequal aggregate PV power injection into legs of the MMC.

$$p_a^{dc} \neq p_b^{dc} \neq p_c^{dc} \tag{1.2}$$

  where p_k^{dc} is the aggregate power delivered to leg k of the converter and is defined as

$$p_k^{dc} = p_{u,k}^{dc} + p_{\ell,k}^{dc} \tag{1.3}$$

- Submodule power mismatch is characterized as unequal aggregate PV power injection into submodules of one arm.

If any of the aforementioned power mismatches happens in the MMC-based PV system, the converter will fail to inject balanced currents into power system [30]. According to the IEEE Std 1547.2-2008, inverter-based distributed generation (DG) units are not
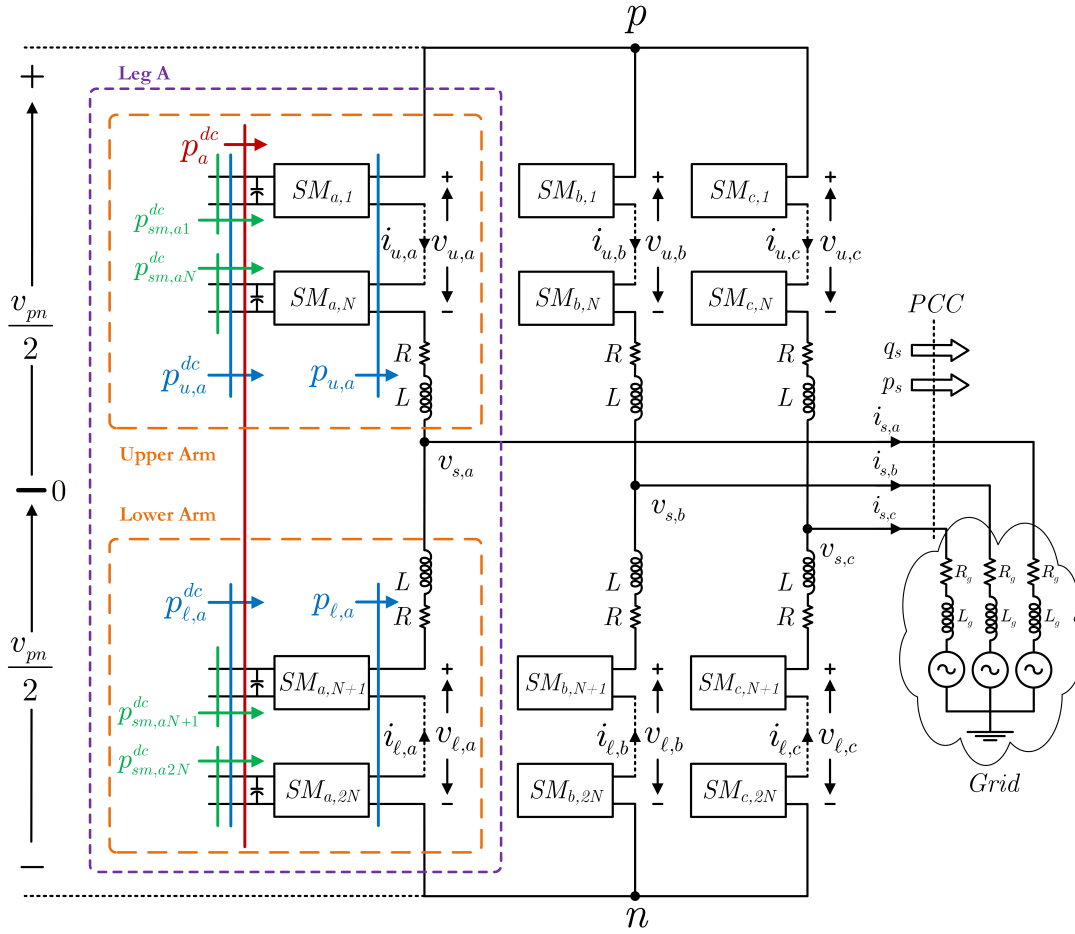
Figure 1.4: Schematic of the MMC-based PV system

allowed to inject unbalanced currents into power system [31]. However, according to the IEEE Std 1547-2018, distributed generation units are required to provide voltage regulation through reactive power exchange with the grid [32]. The same requirements are mandated by grid codes in different countries. Injection of unbalanced currents into the host grid results in unequal voltage drops across the phases of the power system that deteriorates the quality of the power supplied to neighboring loads. The operation of three phase motors, large chiller compressors, and three-phase loads are gravely affected by the unbalanced voltage of the system. If the voltage unbalance is significant (i.e., 2.5% to 3% or more), the motor or device may overheat or become inoperative. Figure 1.5 shows illustrative three-phase output currents of the MMC-based PV system while
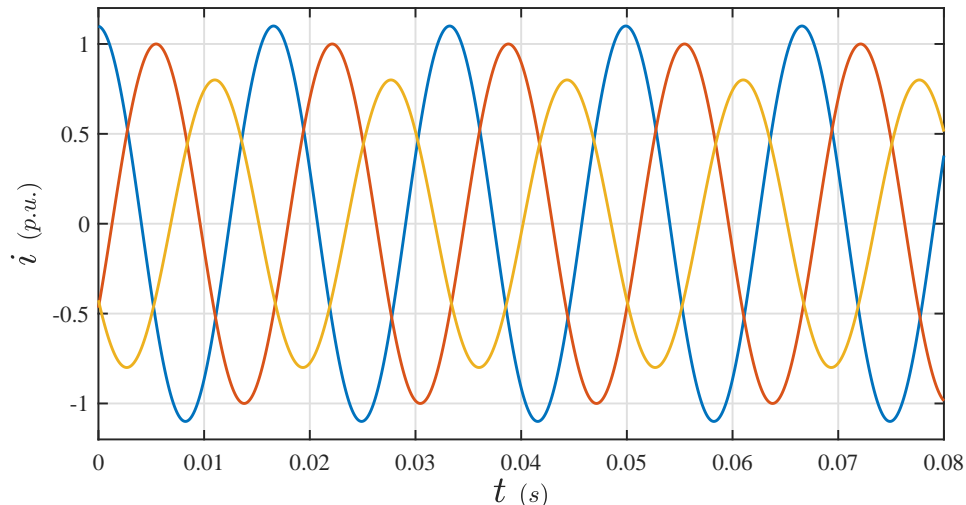
Figure 1.5: Illustrative output currents of the MMC-based PV system while power mismatch exists in the system

power mismatches exist in the structure of the converter. The shown output currents are not balanced and the magnitude of each phase current is different depending on the power injected into the grid from the corresponding phase. The illustrative unbalanced three-phase currents shown in Figure 1.5 contain 0.97 p.u. positive, 0.09 p.u. negative, and 0.09 p.u. zero sequence current components.

The objectives of this thesis are outlined as

- The main objective is to design a control strategy for MMC-based PV system which extracts the maximum possible power from the PV generators, maintains balanced voltages at the terminals of the converter, and injects balanced currents into the power grid in spite of the presence of power mismatches in the structure of the converter.

- The secondary objective of this thesis is to introduce new hardware modifications to embed battery energy storage (BES) systems into the structure of the MMC-based PV system and develop its associated control strategies.

- Development of a new power mismatch elimination strategy which takes into account the grid voltage imbalances is the final objective of the thesis.

1.3 Literature Survey Pertinent to the Thesis Objectives

This section includes the literature survey related to the application of the MMC for PV integration and its challenges. The literature survey is divided into five categories including application of the MMC for PV integration, existing power mismatch elimination methods, modeling, control, and simulation of the MMC.

1.3.1 Application of the MMC for PV Integration

MMC benefits from all the features of multilevel converters plus some unique features as stated in Section 1.1 that make it suitable to be used in PV integration. Majority of the research conducted in the literature are focused on HVDC application of the MMC [33–37]. Application of the MMC for HVDC transmission systems is a mature and well-established topic and as stated earlier, many installations of the MMC-based HVDC systems exist nowadays. MMC also has been used for medium voltage drives (MVD) in the literature providing some interesting features [38–40]. One interesting feature of the MMC for MVD applications is its redundant switching states which enables the converter to eliminate common mode voltage in MVD applications [41]. However, the application of the MMC in MVDs is not a mature topic and still is in progress.

Reference [11] has used the MMC for integration of large-scale PV power plants into power system. Terminal behavioral model developed in [42] is used in this paper to design the controllers of the MMC. As shown in Figure 1.6, the only difference between this configuration and HVDC application is the source of the dc power. In HVDC applications, the dc power is supplied by the converter located at the other end of the dc link; however, in the topology proposed in [11], the dc power source is replaced by a PV generator. This configuration suffers from most of the problems of the centralized topology. The only problem that has been partially addressed in [11] is the modularity problem of the central converter. Although MMC is inherently a modular converter,
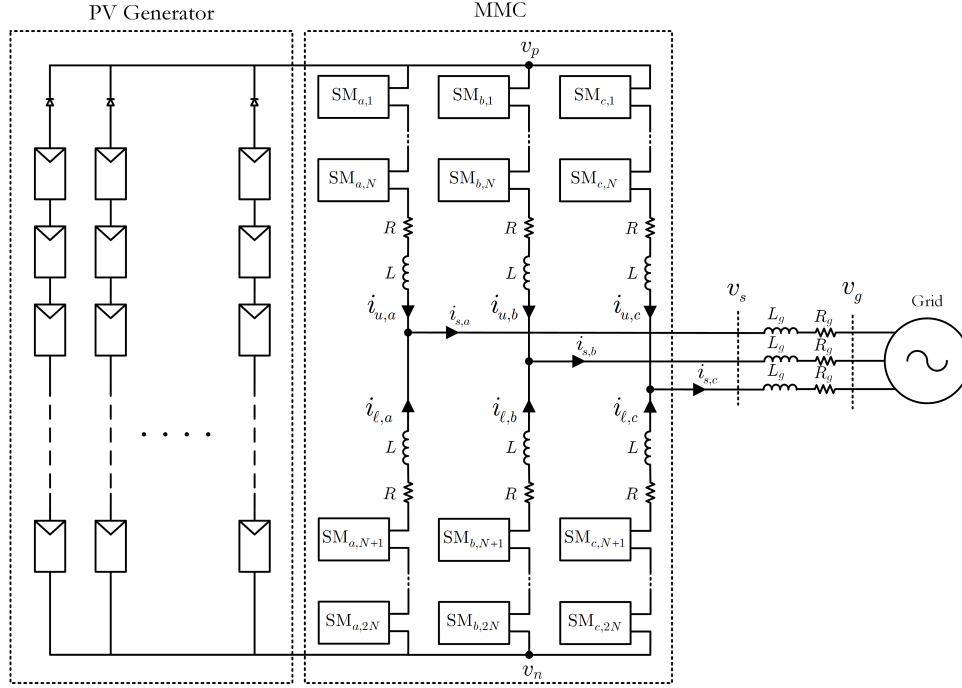
Figure 1.6: MMC as central converter used for PV integration in reference [11]

this feature of the MMC has not been fully exploited in [11]. If any failure happens in the PV generator, the whole system will loose its functionality, meaning that the single point failure is still a challenge for this configuration. Authors of [11] have overlooked the differential current problem in this converter and no discussion is presented in the paper to address this crucial challenge of the MMC.

Reference [43] has used MMC to integrate PV generators into a dc grid. The submodules of the MMC are used as the power conversion stage to inject the dc power exerted form the PV generators into a dc grid with different voltage level. A dc-dc flyback converter is used to implement maximum power point tracking (MPPT) on PV generators and the output voltage of the submodule's converter is also a dc voltage. Hence, the output of this configuration is not an ac voltage, the converter is comprised of one leg, and the differential current will not be a problem in this configuration. Figure 1.7 shows the topology used in [43] to integrate PV generators into a dc grid.

Multi-string PV farm configuration is combined with MMC topology to exploit the
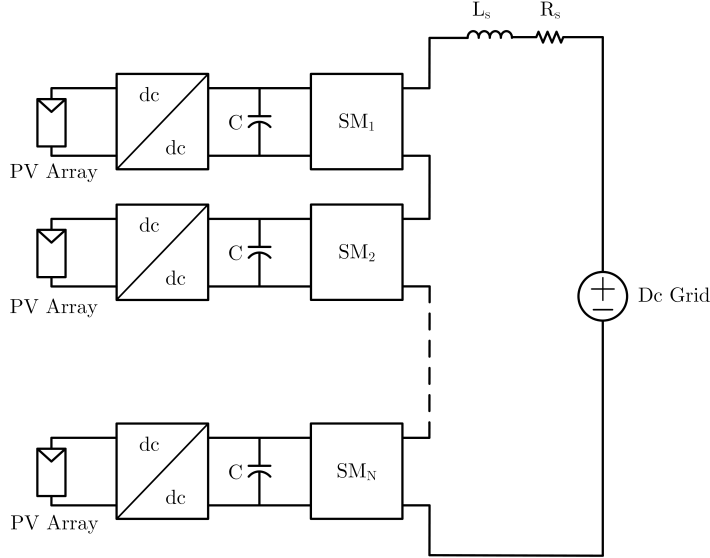
Figure 1.7: MMC as a dc-dc converter to integrate PV generators into a dc grid used in reference [43]

features of both topologies in reference [30]. Several PV strings are connected to the submodules of the MMC using dc-dc converters. The dc-dc converters are employed to implement MPPT on PV generators and step up the dc voltage of the PV strings. Flyback converter, though it does not suit high power applications due to its low power rating of up to 1 kW, is used as the dc-dc converter to connect the PV generators to the submodules of the MMC. The resultant dc power delivered to each submodule is processed through a full-bridge converter and is injected into the arms of the MMC. The authors have addressed the power mismatch problem in this paper using a min-max zero sequence voltage injection method which has numerous problems that are identified in Section 1.3.2. The authors of [30] also have failed to address the differential currents problem in the MMC-based PV system. Figure 1.8 shows the configuration of the MMC-based PV system proposed in [30].

The literature surrounding the application of the MMC for PV integration is very limited and only few works have been conducted in this field. In this thesis, a configuration similar to the one proposed in [43] is employed to integrate the PV generators with an ac power system.
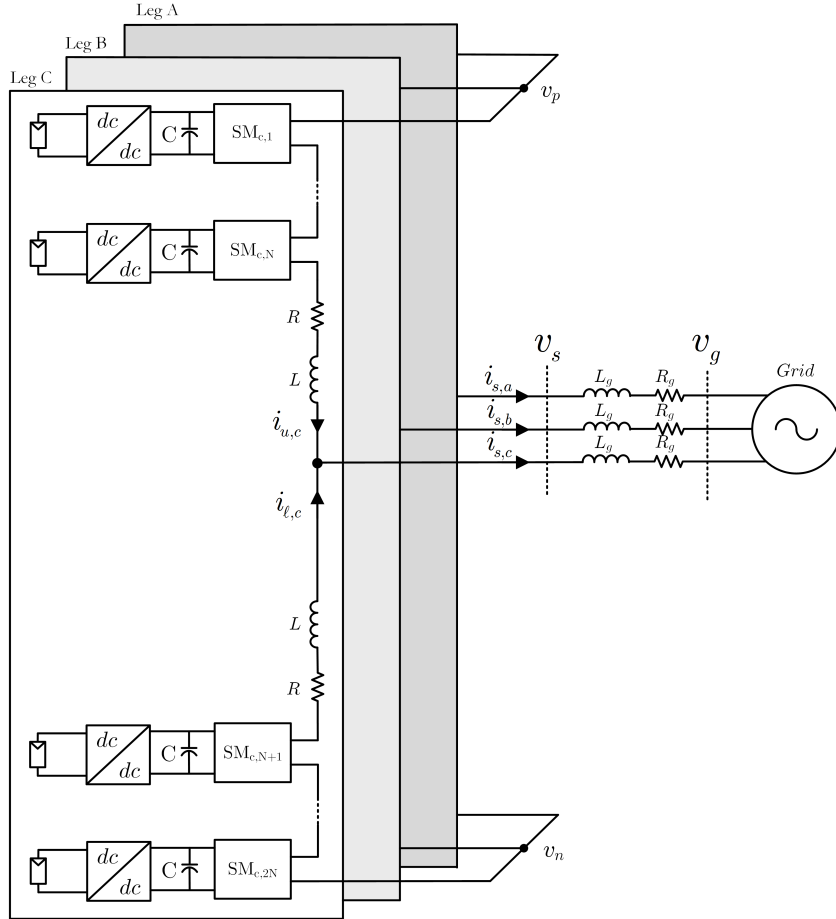
Figure 1.8: MMC used to integrate PV strings into power system in reference [30]

1.3.2   Existing Power Mismatch Elimination Methods

Power mismatch problem in the MMC-based PV system is addressed in the literature using voltage injection methods. The idea of voltage injection methods is to unbalance the terminal voltages of the converter proportional to the amount of the power being delivered to their associated legs. As a result, the converter leg with higher power will have a higher terminal voltage to pass higher power to the host grid with a current equal to the other two phases [44]. There exist multiple methods namely double 1/6 third harmonic injection [45], fundamental frequency zero sequence voltage injection [46], optimal zero sequence voltage injection [47], and weighted min-max voltage injection [48] which all are proposed for cascaded h-bridge converter for PV applications. The weighted

min-max voltage injection is extended for MMC-based PV systems in the literature. The wighted min-max voltage injection method presented in [48] moves the neutral point of the converter in a way that the currents injected into the host grid become balanced while the terminal voltages are unbalanced. Since all these methods rely on unbalancing the terminal voltage of the converter, they all lead to deterioration of the power quality for the neighboring loads. The amount of power mismatch that can be eliminated before driving the converter into over-modulation region is also limited with voltage injection methods. In other words, large amounts of power mismatch can not be eliminated by this method.

In the MMC-based PV system, the PV power is directly injected into the arms of the MMC. As a result, if the powers injected into the arms of a leg are not equal, an arm power mismatch will develop in the structure of the MMC that results in unbalanced current injection into the power system. Likewise, if the powers delivered to the legs of the MMC are not equal, the leg power mismatch problem will develop which will cause the converter to inject unbalanced currents into the grid. Power mismatches also can lead to instability of the dc link voltages of the submodules.

Reference [30] applies min-max voltage injection on an MMC-based PV system to eliminate power mismatches. However, this method results in very high oscillations in the dc link voltage of the MMC. It also creates uncontrolled differential currents in the structure of the converter. The other limitations of this method is the fact that it does not consider the power mismatches between the arms of one leg and if this type of power mismatch happens, the method proposed in [30] injects unbalanced currents into the grid. Moreover, the amount of power mismatch that can be eliminated with this method before driving the converter into over-modulation region is limited. In other words, large amounts of power mismatches can not be eliminated by this method. The other challenge of the min-max voltage injection method presented in [30] is an scaling factor in the equations used to calculate magnitude of the min-max voltage. The authors have not provided a method to calculate the scaling factor and have not given any explanation

about it. The scaling factor also is different for each amount of power mismatch.

The power mismatch ratios in reference [30] are calculated as

$$r_{u,k} = 1 + K\left(1 - \frac{p_{u,k}}{p_{av,k}}\right)$$

$$r_{\ell,k} = 1 + K\left(1 - \frac{p_{\ell,k}}{p_{av,k}}\right) \quad (1.4)$$

where $k = a, b, c$ denotes the legs of the MMC. The term K is scaling factor which has been used in the paper without being defined or presenting a method to define its value. The term $p_{av,k}$ is the average power of the arms of leg k defined as

$$p_{av,k} = \frac{p_{u,k} + p_{\ell,k}}{2} \quad (1.5)$$

The min-max zero sequence is calculated using

$$v_{u,0} = \frac{max\left[r_{u,a}v^*_{u,a} + r_{u,b}v^*_{u,b} + r_{u,c}v^*_{u,c}\right] + min\left[r_{u,a}v^*_{u,a} + r_{u,b}v^*_{u,b} + r_{u,c}v^*_{u,c}\right]}{2}$$

$$v_{\ell,0} = \frac{max\left[r_{\ell,a}v^*_{\ell,a} + r_{\ell,b}v^*_{\ell,b} + r_{\ell,c}v^*_{\ell,c}\right] + min\left[r_{\ell,a}v^*_{\ell,a} + r_{\ell,b}v^*_{\ell,b} + r_{\ell,c}v^*_{\ell,c}\right]}{2} \quad (1.6)$$

where $v^*_{u,k}$ and $v^*_{\ell,k}$ are the reference voltage of the upper and lower arm of leg k, respectively. The terms $v_{u,0}$ and $v_{\ell,0}$ are the weighted min-max voltages of the upper and lower arms, respectively. Having calculated the imbalance ratios using (1.4) and the min-max voltages for the upper and lower arms of the MMC using (1.6), the adjusted reference voltages for the arm of the MMC are calculated as

$$\tilde{v}^*_{u,k} = v^*_{u,k} - v_{u,0} \qquad \tilde{v}^*_{\ell,k} = v^*_{\ell,k} - v_{\ell,0} \quad (1.7)$$

where $\tilde{v}^*_{u,k}$ and $\tilde{v}^*_{\ell,k}$ are the adjusted reference voltages of the upper and lower arms of leg k.

1.3.3 Modeling of the MMC and Component Sizing

The modeling of the MMC is very important step towards controlling the converter. There are two main objectives while modeling an MMC-based PV system. The two objectives are formulating dynamics of the current injected into the host grid and the differential currents of the converter. The first objective is crucial to the operation of the converter since it controls the amount of power that the MMC injects into the grid and keeps its dc link voltages at their reference values. The second objective becomes crucial in an MMC-based PV system where the amount of power injected into each arm of the converter can be different. Consequently, understanding the internal power flow dynamics is very important in MMC-based PV systems.

The models of the MMC presented in the literature are mainly developed for HVDC applications [21, 24, 25, 28, 49]. Although one study has proposed an average dc link voltage control for MMC-based PV system to generate the real power reference to be exchanged with the grid [30], a thorough model which considers the MMC application for PV integration does not exist.

One of the features of the MMC-based PV system is that a dc current is not needed in the legs of the converter since the real power is directly injected into the arms of the converter and is not supplied from the common dc link. This feature affects the component rating of the converter and they do not need to be sized for dc currents. However, zero dc current in the legs of the converter is an ideal case and in a real installation which power mismatches happen between the legs of the MMC-based PV system, a dc current flowing through the legs of the converter is inevitable. This dc current is still much smaller than the dc current in an MMC for HVDC applications.

Since the literature is not very rich for application of the MMC for PV integration, the existing models and component rating selection methods for HVDC applications are used for the MMC-based PV system [49, 50].

1.3.4 Control of the MMC

Controller of the MMC has two main objectives including ac-side terminal current control and differential current control. The ac-side terminal currents can be controlled based on the classical methods applied in the conventional two- and three-level VSCs [51]. However, for the differential current controller, several strategies are proposed in the literature [33, 52–54].

Circulating current suppressing compensator (CCSC) proposed in [33] is one of the first controllers designed for suppression of the differential currents in the MMC for HVDC applications. This method is based on DQ-frame controller designed for negative sequence of second harmonic current. Second harmonic differential current is the main contributor to the differential current in the MMC structure. Consequently, suppressing the second harmonic, as proposed in [33], is an effective way to eliminate differential currents. However, this method is prone to failure in case of having an unbalanced grid voltages. To solve the unbalanced grid voltage problem, the differential current controller strategy proposed in [52], divides differential current into zero-, positive-, and negative-sequence and a dedicated controller is assigned to control each sequence component. Another differential suppressing controller is proposed in [53] which utilizes a resonant compensator (RC) tuned at specific harmonic to suppress the differential current of each leg of the MMC. Another method which uses an RC alongside a proportional integrator (PI) to suppress the differential currents of each leg is proposed in [55].

The model derived in [49] for the grid-side and differential currents of the MMC alongside the differential current controller method proposed in [52] are used to design a controller which controls the internal power flow of the converter in [56]. The internal power flow controller proposed in [56] is suitable for applications which the grid is unbalanced since it uses dedicated sequence current controllers and is capable of controlling the internal power flow of the MMC. As a result, the internal power flow controller proposed in [56] is adapted in this thesis to control the differential currents of the MMC-based PV system.

1.3.5   Simulation of the MMC

Simulation of the MMC-based PV system with hundreds of submodules, hundreds of energy storage elements, and switched model for SM converters is very computation-heavy process. Thus, the researchers have proposed models to facilitate the simulation of the MMC [15, 42, 57–59].

The method proposed in [15] is based on partitioning the admittance matrix of the simulated system and deriving a time-varying Thevenin's equivalent for the MMC. Its objective is to model the behavior of the MMC at its dc and ac terminals without considering the internal power flow or differential currents inside the converter [42, 58]. Using average model for SM converters and condensing the average models of the SMs in each arm of the converter into one equivalent average model is the approach taken to simulate the MMC in electromagnetic transient softwares in [57]. The main assumption of this model is that all the submodules in each leg are the same and can be lumped into one average model.

The simulation models for MMC are thoroughly studied and classified into six distinct categories in [60]. Type 1 is full physics-based model which considers the exact behavior of the switching devices and can model every aspect of the switching process including losses [61]; however, this method requires extremely small time steps to capture the details of the switching. Type 2 is a detailed nonlinear IGBT-based model which uses an ideal controlled switch instead of the IGBT and non-ideal diodes and snubber circuit [62]. Type 3 is simplified IGBT-based model which considers the switching device as a two-state resistance namely conductive and open-circuit resistances. Type 4 is detailed equivalent-circuit-based model which creates a Thevenin's equivalent for each arm of the converter by using the assumptions of type 3 model [15]. Type 5 is average value model (AVM) based on switching functions that model the behavior of the MMC using controlled voltage and current sources [62]. The existing AVM-based models assume that all the variables inside the MMC are perfectly controlled including SM capacitor voltages and differential currents. Type 6 is AVM based on fundamental frequency that uses the same approach

in type 5 except the modulation block which exists in type 5 and is suppressed in type 6. Consequently, the model does not consider the effects of switching and represents the MMC as a fundamental frequency voltage source.

In this thesis the MMC-based PV system is simulated using type 5 and type 3 simulation models. Model type 5 is used to model the system and design its controllers while model type 3 is used to simulate the system in a transient simulation software. The combination of two simulation methods gives detailed insight into the differential current controller schemes and the proposed power mismatch elimination methods.

1.3.6   Pros and Cons of MMC-based PV systems

The existing topologies for PV farms featuring MMC are discussed in Section 1.3.1. The application of the MMC as central converter is proposed in the literature [11]. This topology rectifies the modularity problem of the central converter. However, the other challenges of the central configuration including low power conversion efficiency due to single MPPT voltage, single failure point, and partial shading problems are not addressed.

The application of the MMC to integrate PV generators into a dc grid is proposed in [43]. This paper has used the MMC as a dc-dc converter which comprises of only one leg. The authors have failed to address the isolation challenges in case that the voltage of the dc grid is higher than the insulation rating of the PV panels. Connecting the PV generators to the dc side of the SMs of the MMC is proposed in [30]. This approach injects real power directly into the arms of the MMC and has the potential to rectify all the shortcomings of central, string, multi-string, and ac-module configurations. The challenges of this configuration is to manage the power mismatches between the arms of the MMC when the power injected into the arms of the converter are not equal. Tackling this challenge and injecting balanced currents into the host grid while holding the balanced converter terminal voltages in spite of power mismatches between the arms and legs of the MMC-based PV system is the main objective of this thesis.

1.4   Thesis Outline

The remainder of this thesis is organized as follows:

In chapter 2, first, grid-connected PV farm configurations are described and their advantages and disadvantages are outlined. Then, the structure of the MMC-based PV system for integration of PV generators is described which includes the topologies used in the submodules of the converter. Next, the mathematical model of the system is developed including the equations describing the dynamics of the converter seen from its grid side, differential current dynamics, and common dc link model. In the modeling section, a new reference power generation scheme is derived which defines a virtual dc link voltage to generate the real power reference for the system.

Furthermore, design procedures for grid current controller, differential current controller, and virtual dc link voltage controller are elaborated. The algorithm for regulation of the dc link voltage of the submodules of each arm is presented next. The existing voltage modulations for the MMC are thoroughly presented as the final section of Chapter 2.

Chapter 3 presents the proposed power mismatch elimination strategy for the MMC-based PV system. Possible power mismatches which can happen in the structure of the MMC-based PV system are elaborately studied first. The mathematical model of the submodule dc link voltage with and without differential currents is derived to study the effect of differential currents on the dc link voltage of the submodules.

Moreover, the logics and mathematics behind the proposed power mismatch elimination strategy is presented which includes leg and arm power mismatch elimination functions. Finally, the performance of the proposed strategy is evaluated in four different cases using simulations on a representative model of the system in PSCAD/EMTDC environment.

Chapter 4 presents the proposed structure of the MMC-based PV-BES system which embeds one storage system in each arm of the converter. An overview of the energy

storage systems including the characteristics of storage systems and their technologies is given. Then reference generation for energy storage system including proposed power mismatch elimination and power smoothing functions are presented. Next, the proposed hybrid power mismatch elimination strategy that uses power exchange with embedded BES systems and power transfer between the legs of the converter to eliminate power mismatches is elaborated. At the end of Chapter 4, the performance of the proposed hybrid power mismatch elimination strategy for the MMC-based PV-BES system is evaluated in three cases using simulations on a representative model of the system in PSCAD/EMTDC environment.

Chapter 5 is dedicated to study the performance of the proposed power mismatch elimination strategies in an unbalanced grid. A modification for the proposed power mismatch elimination strategies is proposed that takes into account the impacts of grid voltage imbalance. The proposed strategy manipulates the amount of power that is delivered from each phase of the system to ensure that grid current remains balanced in spite of power mismatches and unbalanced grid voltage. The mathematics are presented to derive the modifications based on the magnitude of the voltage of each phase. Finally, the performance of the proposed modifications to the power mismatch elimination strategies are evaluated using simulations in PSAD/EMTDC environment.

Chapter 6 presents summary, conclusions, contributions, and suggestions for the future research work.

Parameters of the PV generator and its mathematical model are presented in Appendix A. The model used for the BES systems is presented in Appendix B. Average model of the dual active bridge converter which is used to interface the PV generators and battery banks with the dc side of their respective submodules is presented in Appendix C. It should be noted that since the power transfer from the PV generators is unidirectional, other variations of the DAB could be used as presented in Section 2.4.

Chapter 2

Modeling of the MMC

This chapter is dedicated to derive the mathematical model of the MMC-based PV system. The derived model is based on the existing models presented in the literature for HVDC applications. The modeling process has three distinct objectives including grid-side current dynamics model, differential currents dynamics model, and real power reference generation model. However, there are prerequisites to the modeling of the MMC-based PV system which are presented before deriving the equations of the system. Firstly, the configurations of PV farms are presented which clarifies the difference between the MMC-based PV system and the conventional VSC applications. Secondly, the assumptions regarding the modeling of the MMC-based PV system are reviewed. Next, the structure of the MMC-based PV system and its submodules are presented. Then, the equations governing the behavior of the MMC-based PV system with respect to the host grid and internal power flow of the converter are derived.

Modeling of the MMC-based PV system enables one to design proper controllers in order to control all aspects of the converter. The controller design for MMC-based PV system is the next topic covered in this chapter. Having generated the reference voltages for the MMC, modulation stage is used to synthesize the reference voltage using switching sequences. Finally, different modulation techniques and their pros and cons are studied at the end of this chapter.

2.1 Grid-connected PV Farm Configurations

A survey on grid-connected PV farm configurations is presented in this Section that shows the differences between the MMC-based PV system and the existing PV farm configurations. The presented PV farm configurations employ the conventional two- or three-level VSCs for power conversion. The application of the conventional VSCs for grid integration of large-scale PV farms leads to the challenges that are outlined in the Chapter 1.

Various configurations for large-scale PV farms are presented in the literature [63,64]. These configurations are categorized into four groups as follows:

1. **Centralized configuration:** as shown in Figure 2.1, a large amount of PV power is concentrated on the dc link and is processed through one central dc-ac converter [65,66]. The shortcomings of this configuration are

   - Low power quality since the output voltage is a two- or three-level voltage which has high harmonic content.

   - High switching frequency and consequently high switching losses.

   - Single failure point since a large amount of power is processed through one converter. If the converter fails for any reason, the whole generation will be lost.

   - Poor MPPT implementation since many PV modules are connected in series and parallel while only one MPPT voltage is possible.

   - Bulky transformer due to limited dc link voltage magnitude which stems from safety concerns and insulation limitations of the PV panels.

   - Lack of modularity in the power generation and conversion stages.

   - Low power conversion efficiency due to partial shading and power mismatch between the PV strings.
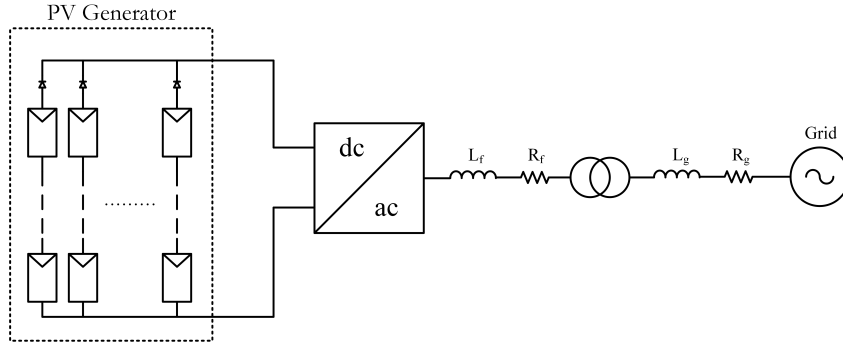
Figure 2.1: Centralized PV farm configuration

2. **String configuration:** each PV string is connected to power grid using a dedicated inverter as depicted in Figure 2.2. This configuration rectifies some of challenges of the centralized configuration [65]. The persisting problems in this configuration are as follows: rid

   • Low power quality due to two- and three-level output voltage.

   • High switching frequency and consequently high switching losses.

   • Bulky grid-side transformer since the dc link voltages of the converters are limited.
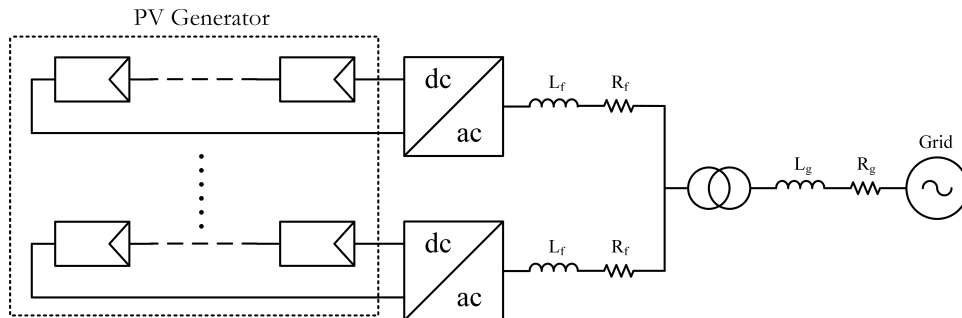
Figure 2.2: String PV farm configuration

3. **Multi-string configuration:** as shown in Figure 2.3, each PV string is connected to a common dc link using a dedicated dc-dc converter. The dc-dc converters implement MPPT on their associated PV strings. The aggregate generated power is injected into the host grid using a central inverter. This configuration alleviates

some of the problems outlined in centralized configuration. The persistent problems are:

- Low power quality since the output voltage is a two- or three-level voltage that has high harmonic content.

- High switching frequency and consequently high switching losses.

- Single failure point as the whole power is processed through one converter.

- Bulky transformer since the dc link voltage is limited due to safety and insulation concerns.

- Lack of modularity
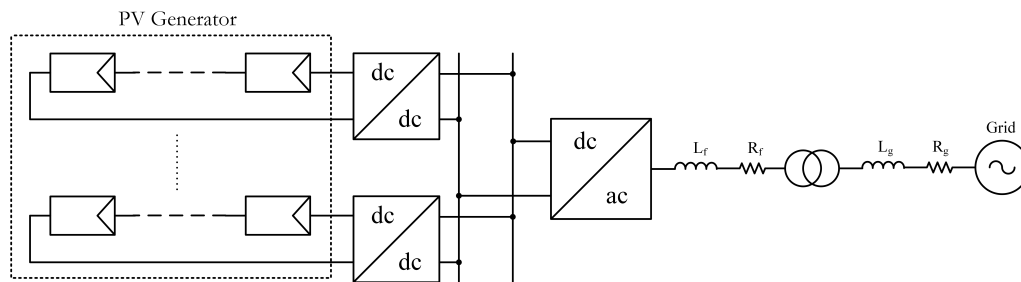
Figure 2.3: Multi-string PV farm configuration

4. **Ac-module configuration:** in this configuration, each PV module is connected to the host grid using a dedicated dc-ac converter [67], as shown in Figure 2.4. This configuration is suitable for low power applications which are within the power rating of a single PV module. The limitations of this configuration are:

- Low power quality since the output voltage is a two- or three-level voltage that has high harmonic content.

- High switching frequency and consequently high switching losses.

- Bulky transformer since the dc link voltage is limited due to existence of only one module in each PV generator.

- Not suitable for high-power applications.
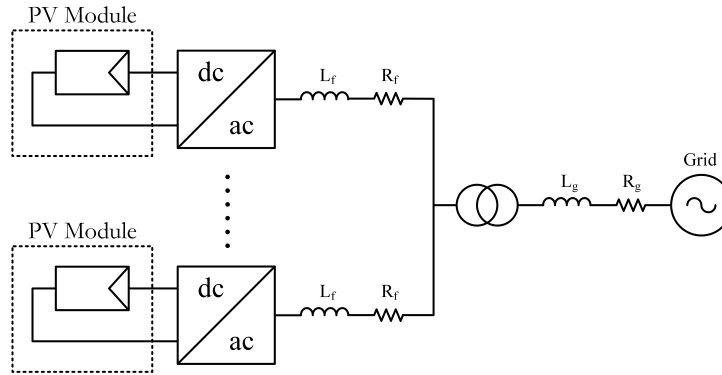
Figure 2.4: Ac-module PV farm configuration

Having reviewed the conventional the PV farm configurations for grid-connected PV farms, the new PV farm configuration which is a unique characteristic of the MMC is presented in the following Sections.

2.2   Conventional Structure of the MMC

In the literature, MMC is mainly used for HVDC applications since it provides characteristics which are suitable for HVDC systems. It can reach high dc and ac voltages without the need for series connection of the switching devices. MMC also offers dc-side fault current blocking in HVDC systems which is a unique feature of this topology. In HVDC applications, each submodule of the MMC consists of a half-bridge converter interfaced from its dc side with a capacitor as an energy storage device. There is no active power exchange at the submodules and the real power is supplied from the common dc link of the MMC.

As shown in Figure 2.5, the MMC for HVDC applications consists of three legs where each leg is associated with one phase of the system. Each leg of the converter is comprised of two arms called upper and lower arms. Each arm of the converter, in turn, has N submodules that are responsible for insertion or bypassing of their associated energy storage device. The common dc link voltage is regulated by the converter at the other end of the HVDC link and is used to transfer power from the rectifier to the inverter.
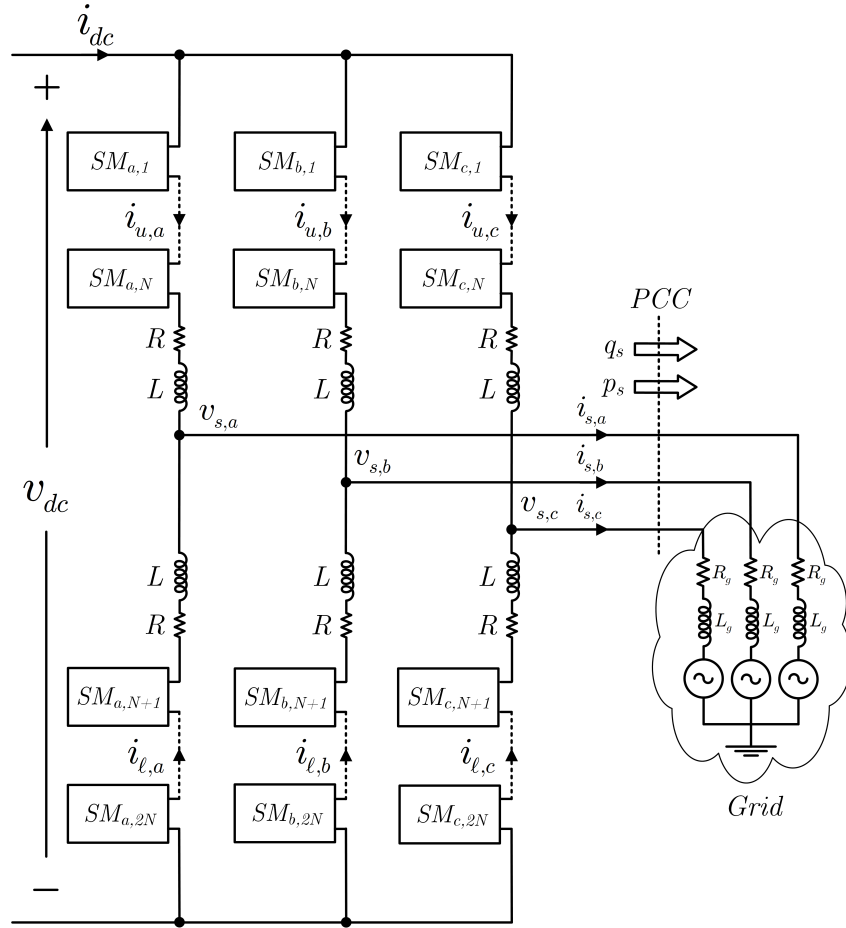
Figure 2.5: MMC for HVDC systems

Half-bridge dc-ac converter is the converter of choice for the submodules of the conventional MMC [21, 62]. However, in some publications, full-bridge converter is utilized that is due to the fact that the MMC is used as an ac-ac converter which requires submodules that are able to generate bipolar voltage at their ac-side terminals [13]. MMC-based HVDC system with dc-side fault current blocking is another reason for using full-bridge converter in the submodules of the MMC. Moreover, some papers have used multilevel converters for the dc-ac converter of the submodules in MMC [68, 69]. The use of multilevel converters for the dc-ac converter of the submodules adds to complexity of the converter and does not contribute much to the output voltage quality of the MMC. Figure 2.6 shows different configurations of the submodules of the MMC. Figure 2.6(c) shows the concept of multilevel converters in general. Multilevel converters synthesize

(a) Half-bridge submodule   (b) Full-bridge submodule

(c) Multilevel submodule
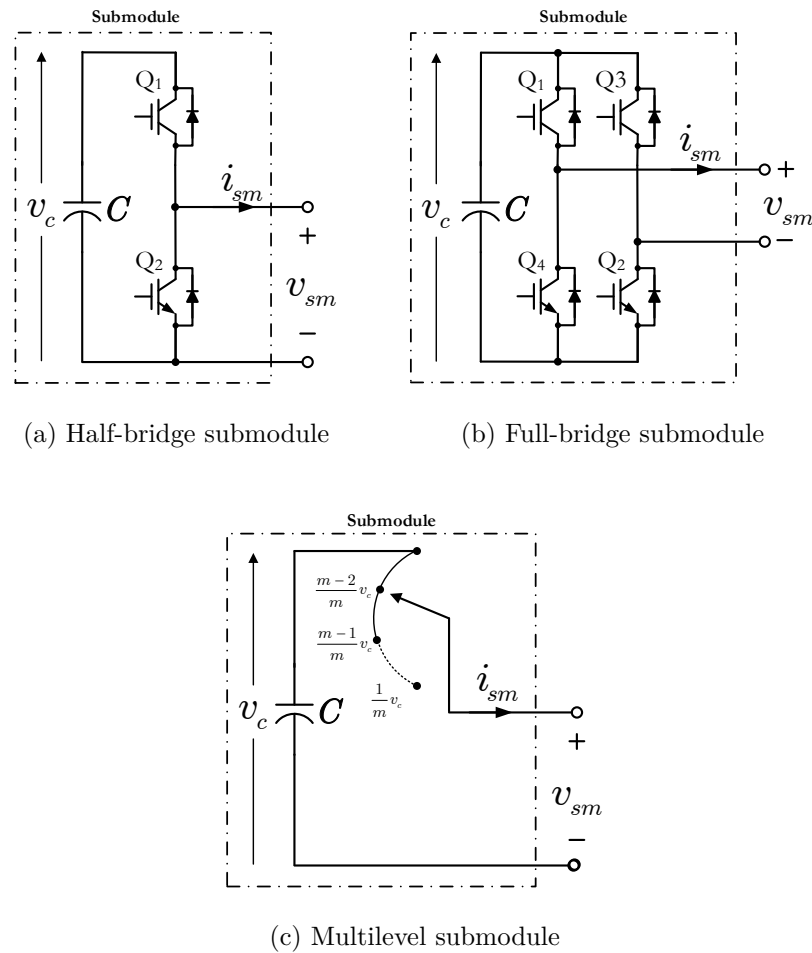
Figure 2.6: Different topologies for the submodules of the MMC

their reference voltage in multiple levels, providing lower harmonic content and higher power quality. Some multilevel topologies, including MMC, feature interleaved switching frequency effect. In other words, the switches are switched at lower frequency, however the effective switching frequency of the resultant output voltage is much higher than that of the individual switches.

2.3   MMC-based PV System Configuration

MMC-based PV system is comprised of three legs where each leg is associated with one phase of the system. Each leg of the system is comprised of two arms, called upper

and lower arms throughout this thesis. The arms of the converter are formed by series connection of N submodules. As discussed in Section 2.2, the topology of the dc-ac converter of the submodules can be different. However, the half-bridge topology is used in this thesis which is due to its lower number of switching devices, its popularity in the literature, and its sufficiency to fulfill its purpose. Each arm of the converter is connected to the point of common coupling (PCC) using a RL low-pass filter. Arm resistor, R, represents the equivalent resistance of the arm including the conduction resistance of the switching devices and the cables in between. The arm inductance, L, is inserted to enable current control scheme implementation, suppress the transient voltages caused by switchings, and limit the magnitude of differential current in the structure of the MMC [52, 70]. Differential current is a current that circulates inside the structure of the MMC-based PV system without entering the grid. Common dc link of the MMC-based PV system, which is identified by nodes p and n in Figure 2.7, is not interfaced with another converter and no dc power is injected to this link. Figure 2.7 shows the configuration of the MMC-based PV system while identifying the currents of the system.

2.4 Structure of the Submodules of the MMC-based PV System

In the MMC-based PV system shown in Figure 2.7, real power is directly injected into the arms of the converter by PV generators. PV generators are interfaced with the dc side of the submodule converter using a dc-dc converter. The dc-dc converter is responsible for implementation of MPPT on the PV generators. Since the MMC-based PV system is connected to the grid without a unit transformer, the galvanic isolation has to be provided by the dc-dc converters. Any dc-dc converter providing galvanic isolation and required power rating could potentially be utilized. As a result, dual active bridge (DAB) is a suitable topology for this application and is used to interface the PV generators with
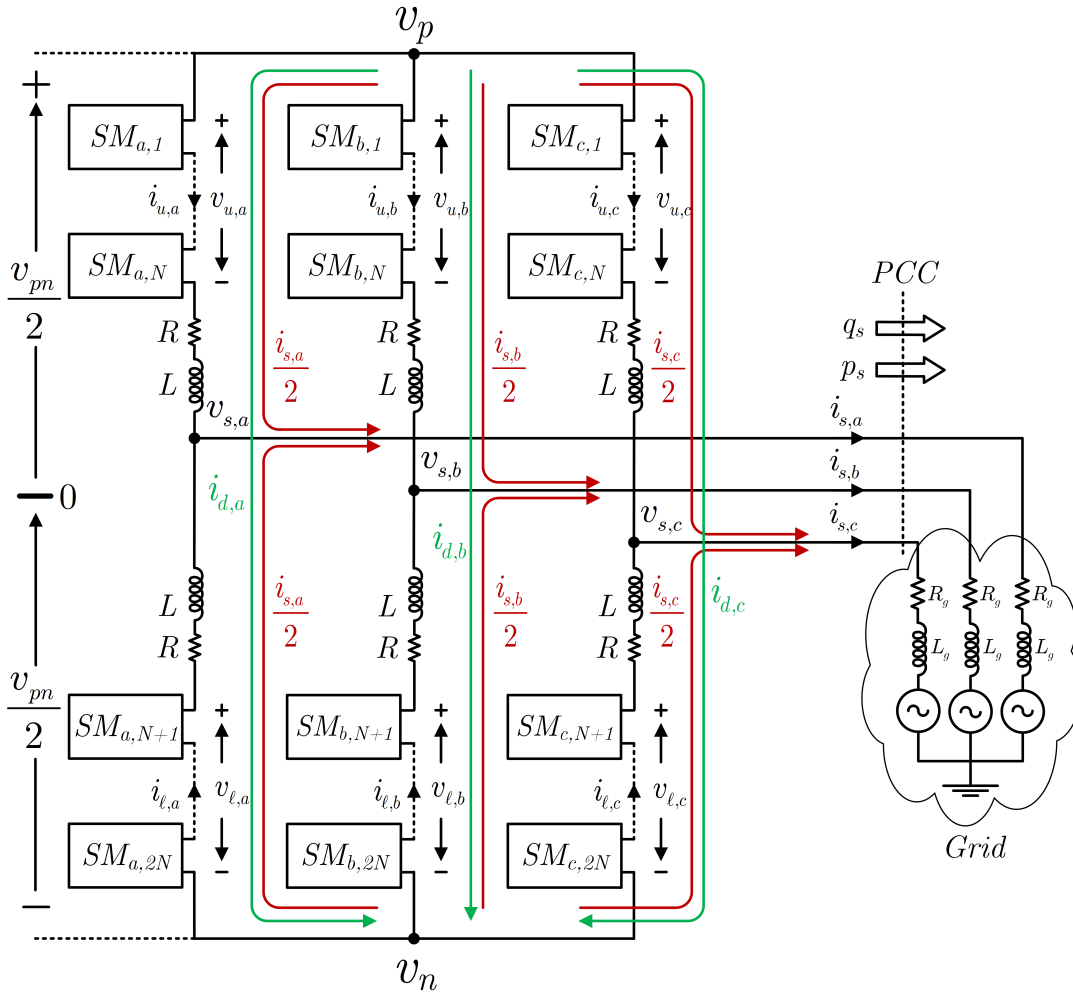
Figure 2.7: MMC-based PV system

the submodules of the system. The rating of the PV generators connected to each submodule is chosen in such a way that the current rating of the switches of the dc-ac half-bridge converter is limited to 600-700 A. As a result, there is no need to connect the switching devices in parallel since IGBTs with the aforementioned current rating are available. The output voltage of the submodule does not need to synthesize negative voltages which justifies the output connection of the half-bridge converter. Figure 2.8 shows the configuration of the submodules of the MMC-based PV system shown in Figure 2.7.

The PV generators are connected to the submodule converter using n isolated DAB
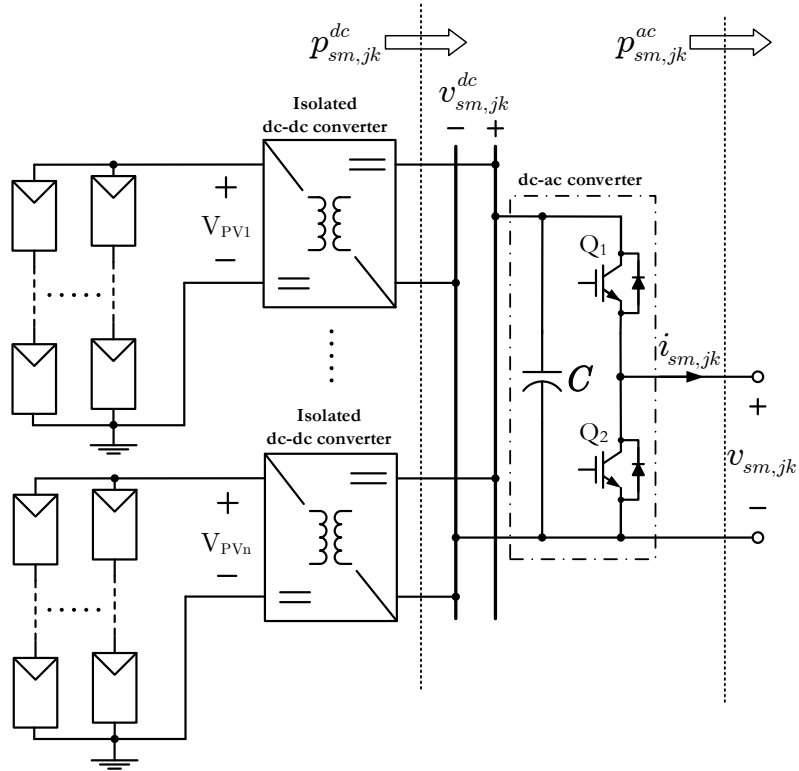
Figure 2.8: Configuration of the submodules in MMC-based PV system

dc-dc converters. Multiple DAB converters are shown in Figure 2.8 to generalize the configuration. In other words, the submodules could have high power rating in different converters and the depicted configuration in Figure 2.8 is the most general form that can accommodate any power rating.

The topology of DAB converter is shown in Figure 2.9. The converter offers galvanic isolation owing to its high-frequency isolation transformer. DAB consists of two independent full-bridge converters, called PV-side and SM-side active bridges in this thesis, interfaced from their ac-sides using a high-frequency transformer (Tr). The high-frequency transformer of the DAB converter boosts the voltage to match the input and output voltages. The full-bridge converters generate a high frequency ac voltage at their ac terminals and the power transfer is controlled by the phase angle between two ac voltages. The galvanic isolation has three distinct roles in this configuration. First, since
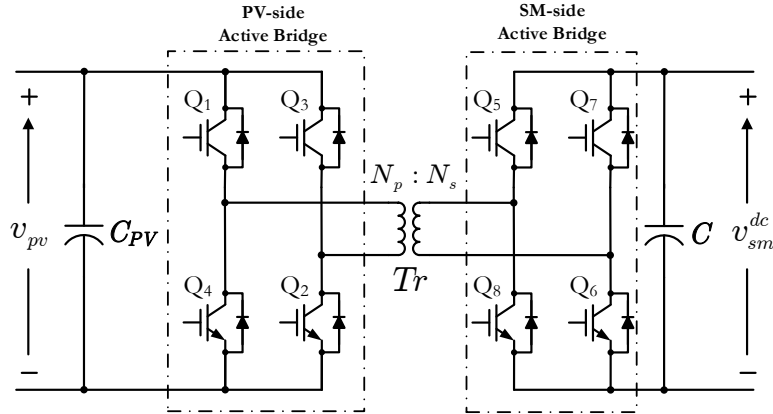
Figure 2.9: Dual active bridge (DAB) converter

the MMC-based PV system is a transformerless topology, the galvanic isolation of the DAB converters acts as the isolation stage for the PV system. Second, it prevents the PV generators from being exposed to high voltages which are outside the insulation rating of the PV panels. Third, it enables grounding of the negative pole of the PV strings to alleviate the potential-induced degradation (PID) [71].

The DAB topology illustrated in Figure 2.9 features bi-directional power transfer capability. However, in PV applications the power only flows from the PV-side to SM-side of the converter. Consequently, a variant of this topology which uses an active full-bridge at its PV-side and a diode bridge at its SM-side can be used for MMC-based PV system. Figure 2.10 shows the described variant of the DAB converter.
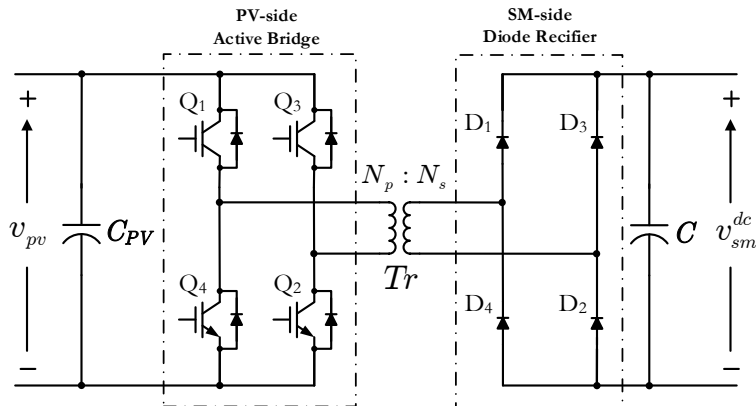
Figure 2.10: A variant of DAB converter

2.5   Model of the MMC-based PV System

This section presents mathematical modeling of the MMC-based PV system. Equations governing dynamics of the current injected into the host grid are derived that are the basis for designing the grid current controller for the converter. The equations governing the differential current of the MMC are also derived that are used to design internal power flow controller for the MMC. Moreover, the proposed reference power generation scheme for the MMC-based PV system is presented.

2.5.1   Grid Current Model

Grid current is the current that is injected into the host grid by the MMC-based PV system. The grid current defines the amount of real and reactive power exchanged between the grid and the converter. This current has to be controlled precisely at its reference to ensure that the amount of real and reactive power exchanged are according to their references.

The function of the current-control scheme is to regulate $i_{s,abc}$, which is the ac-side current of the voltage-sourced converter (VSC), by means of a modulation switching strategy. However, before controlling the converter, a mathematical model for the grid current has to be derived. Figure 2.7 shows the structure of the MMC-based PV system alongside the notations used for parameters of the system. The current of the arms of the converter consists of two components: grid and differential current components. The grid current component enters the grid and the differential current component circulates inside the structure of the converter. The positive direction of differential current is defined from node p towards n. The reference directions of arm currents are defined as shown in Figure 2.7. Consequently, in the upper arms the two current components are added and in the lower arms the differential current is subtracted from the grid current. Owing to the symmetry of the converter in terms of the number of submodules in the upper and lower arms, half of the grid current is supplied from each arm. Consequently,

the relationship between the arm currents, grid currents, and differential currents are

$$i_{u,k} = \frac{i_{s,k}}{2} + i_{d,k} \qquad k = a, b, c \tag{2.1}$$

$$i_{\ell,k} = \frac{i_{s,k}}{2} - i_{d,k} \qquad k = a, b, c \tag{2.2}$$

Equations (2.1) and (2.2) can be rewritten as

$$i_{s,k} = i_{u,k} + i_{\ell,k} \qquad k = a, b, c \tag{2.3}$$

$$i_{d,k} = \frac{i_{u,k} - i_{\ell,k}}{2} \qquad k = a, b, c \tag{2.4}$$

where $i_{u,k}$ and $i_{\ell,k}$ are the upper and lower arm currents of phase k, respectively. Currents $i_{s,k}$ and $i_{d,k}$ are the grid and differential currents of phase k, respectively. Differential and grid currents are shown using green and red traces in Figure 2.7, respectively.

Considering the positive and negative nodes of the common dc link, node p and n, and applying KCL, one finds

$$node \quad p: \quad i_{u,a} + i_{u,b} + i_{u,c} = 0 \tag{2.5}$$

$$node \quad n: \quad i_{\ell,a} + i_{\ell,b} + i_{\ell,c} = 0 \tag{2.6}$$

Substituting the variables in (2.5) or (2.6) with the expressions given in (2.1) through (2.4), the following equation is derived.

$$\frac{1}{2} \Big(\underbrace{i_{s,a} + i_{s,b} + i_{s,c}}_{A} \Big) + \Big(\underbrace{i_{d,a} + i_{d,b} + i_{d,c}}_{B} \Big) = 0 \tag{2.7}$$

The term A in (2.7) is zero due to the balanced operation of the converter. Consequently, the term B has to be zero at all times. In other words, the sum of the differential currents at nodes p and n has to be zero.

Regarding node "0", that is the fictitious dc-side midpoint of the MMC, as the po-

tential reference node and applying KVL from nodes p and n towards node s, one finds

$$\frac{v_p - v_n}{2} - L\frac{di_{u,k}}{dt} - Ri_{u,k} - v_{u,k} = v_{s,k} \qquad k = a, b, c \tag{2.8}$$

$$-\frac{v_p - v_n}{2} - L\frac{di_{\ell,k}}{dt} - Ri_{\ell,k} + v_{\ell,k} = v_{s,k} \qquad k = a, b, c \tag{2.9}$$

Adding (2.8) and (2.9), one finds

$$-L\left(\frac{di_{u,k}}{dt} + \frac{di_{\ell,k}}{dt}\right) - R\left(i_{u,k} + i_{\ell,k}\right) - v_{u,k} + v_{\ell,k} = 2v_{s,k} \tag{2.10}$$

Substituting $i_{u,k}$ and $i_{\ell,k}$ with (2.1) and (2.2), (2.10) can be rewritten as

$$-L\frac{di_{s,k}}{dt} - Ri_{s,k} - v_{u,k} + v_{\ell,k} = 2v_{s,k} \tag{2.11}$$

Then follows

$$\frac{L}{2}\frac{di_{s,k}}{dt} + \frac{R}{2}i_{s,k} - \frac{-v_{u,k} + v_{\ell,k}}{2} = -v_{s,k} \tag{2.12}$$

Defining

$$v_{e,k} = \frac{-v_{u,k} + v_{\ell,k}}{2} \tag{2.13}$$

Equation (2.12) can be rewritten as

$$\frac{L}{2}\frac{di_{s,k}}{dt} + \frac{R}{2}i_{s,k} = v_{e,k} - v_{s,k} \qquad k = a, b, c \tag{2.14}$$

where $v_{e,k}$ and $v_{s,k}$ are the internal voltage of the MMC and the grid voltage at PCC, respectively.

Equation (2.14) describes the currents dynamics between two voltage sources called $v_{e,k}$ and $v_{s,k}$ that are interfaced with a low-pass RL. Figure 2.11 shows the representation of the system described by (2.14). Figure 2.11 also signifies that the dq-frame current controller used in conventional VSCs [51] can be applied to control the fundamental component of the grid-side current of the MMC-based PV system.
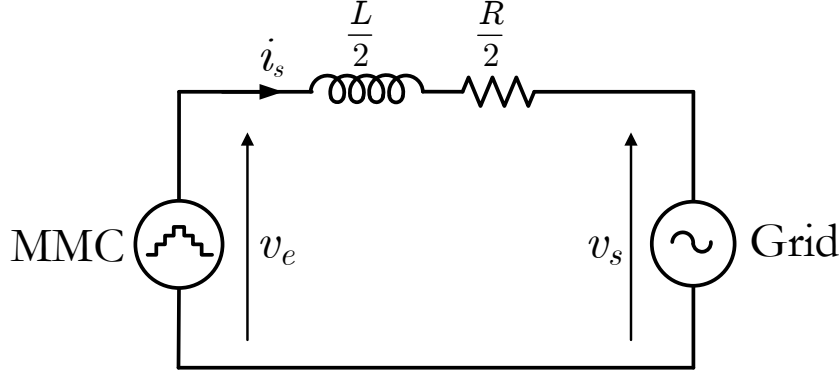
Figure 2.11: Equivalent circuit of MMC-based PV system and the host grid at PCC

2.5.2   Differential Current Model

Differential current is a current that circulates inside the structure of the MMC without entering the grid. One of the objectives of MMC controllers is to nullify this current since it contributes to losses in the system and threatens the stability of the converter. As a result, the dynamics of the differential currents have to be expressed using the controllable variables of the converter. This section derives the equations governing dynamics of the differential currents.

Subtracting (2.9) from (2.8), one finds

$$v_p - v_n - L\left(\frac{di_{u,k}}{dt} - \frac{di_{\ell,k}}{dt}\right) - R\left(i_{u,k} - i_{\ell,k}\right) - v_{u,k} - v_{\ell,k} = 0 \qquad k = a, b, c \quad (2.15)$$

Replacing the upper and lower arm currents in (2.15) with (2.1) and (2.2), one finds

$$v_p - v_n - 2L\frac{di_{d,k}}{dt} - 2Ri_{d,k} - v_{u,k} - v_{\ell,k} = 0 \qquad k = a, b, c \qquad (2.16)$$

Then

$$L\frac{di_{d,k}}{dt} + Ri_{d,k} = \underbrace{\frac{v_p - v_n}{2} - \frac{v_{u,k} + v_{\ell,k}}{2}}_{A} \qquad k = a, b, c \qquad (2.17)$$

The right side of (2.17), which is labeled as A, is called differential voltage of phase k.

$$v_{d,k} = \frac{v_p - v_n}{2} - \frac{v_{u,k} + v_{\ell,k}}{2} \qquad k = a, b, c \qquad (2.18)$$

As described by (2.17), the differential voltage is the voltage drop across the arm inductor and resistor due to the differential current. Consequently, the differential current of the legs of the converter can be controlled by controlling the differential voltage according to (2.17).

2.5.3   Common dc Link Model

The KVL starting from node p and ending at node n formulates dynamics of the common dc link voltage of the MMC-based PV system. This KVL can be written for each leg of the converter which means that there are three independent equations that affect the dc link voltage. The KVL from node p to n yields

$$v_p - v_n = 2L\frac{di_{d,k}}{dt} + 2Ri_{d,k} + v_{u,k} + v_{\ell,k} \qquad k = a, b, c \qquad (2.19)$$

Equation (2.19) is the same as (2.17), meaning that the dynamics of the common dc link of the MMC-based PV system is related to the differential currents in its structure. It is noteworthy to mention that the grid current has no impact on the common dc link voltage. The voltage of the common dc link has to be at least two time the magnitude of the grid phase voltage to enable real power exchange control.

2.5.4   Proposed Reference Power Generation Scheme

Stable operation of the MMC-based PV system requires that right amount of real power is delivered to the host grid such that the power balance is maintained in both steady-state and transient regimes. This objective is achieved by a proposed virtual dc-link voltage regulation scheme whose function is to produce the commands for real power of the

converter. The current controller used for controlling the MMC-based PV system requires a reference real and reactive power for generation of the dq-frame grid currents. The reactive power reference of the converter can be defined by terminal voltage regulation scheme or can be set to zero. However, a mechanism is needed to generate the reference for the active power exchange. This section presents the proposed active power reference generation scheme.

Ignoring the power losses of the DAB converters interfacing the PV generators with the dc link of the submodules, the dc voltage dynamics for each submodule of the MMC-based PV system is governed by

$$\frac{1}{2}C\frac{d}{dt}(v_{sm,jk}^{dc}(t))^2 = p_{sm,jk}^{dc}(t) - p_{sm,jk}^{ac}(t) \tag{2.20}$$

where $p_{sm,jk}^{dc}(t)$ and $p_{sm,jk}^{ac}(t)$ are the aggregate dc power injected into the dc link of submodule and the ac power leaving the ac terminal of the submodule j in phase k, respectively. Assuming equal capacitance for all submodule capacitors, (2.20) can be represented as

$$\frac{1}{2}C\frac{d}{dt}v_{dcf}^2(t) = \underbrace{\sum_{k=a,b,c}\sum_{j=1}^{2N}p_{sm,jk}^{dc}(t)}_{A} - \underbrace{\sum_{k=a,b,c}\sum_{j=1}^{2N}p_{sm,jk}^{ac}(t)}_{B} \tag{2.21}$$

where, the terms A and B are the aggregate dc power injected into the submodules of the converter from all PV generators and the aggregate ac power leaving the ac side of the submodules, respectively. It should be noted that the term A corresponds to the aggregate power delivered to the MMC-based PV system from the PV generators while term B corresponds to the real power delivered to the host grid by the MMC-based PV system. The voltage of the virtual dc link is defined as

$$v_{dcf}^2(t) = \sum_{k=a,b,c}\sum_{j=1}^{2N}(v_{sm,jk}^{dc}(t))^2 \tag{2.22}$$

Thus, the variable $v_{dcf}(t)$ can be regarded as a virtual dc-link voltage for the MMC. As a result, (2.21) describes dynamics of $v_{dcf}^2(t)$ in terms of the aggregate power generated by the PV panels, p_{PV}, and the real power that the PV system delivers to the grid, p_s. Equation (2.21) then forms a basis for the regulation of $v_{dcf}^2(t)$ at its reference value, v_{dcf}^{2*}, while p_{PV} (shown as A in (2.21)) acts as a disturbance signal. Thus the difference between $v_{dcf}^2(t)$ and v_{dcf}^{2*} is processed by a compensator whose output is the real power reference, p_s^*, and is delivered to the grid current control scheme. The parameters of the compensator can be determined using the techniques employed for the conventional VSC [51], which are discussed in Section 2.6.1.

Regulation of v_{dcf}^2 at a constant setpoint will, based on (2.21), result in $p_s \simeq p_{PV}$, which is the ultimate goal of the PV system. Considering that the MMC-based PV system consists of 6 arms and N submodule exist in each arm, the variable v_{dcf}^{2*} is assigned a value of $6N(v_{sm,jk}^{dc*})^2$. Figure 2.12 shows the schematic of the virtual dc link.

$$p_{PV}(t) = \sum_{k=a,b,c} \sum_{j=1}^{2N} p_{sm,jk}^{dc}(t) \qquad p_s(t) = \sum_{k=a,b,c} \sum_{j=1}^{2N} p_{sm,jk}^{ac}(t)$$
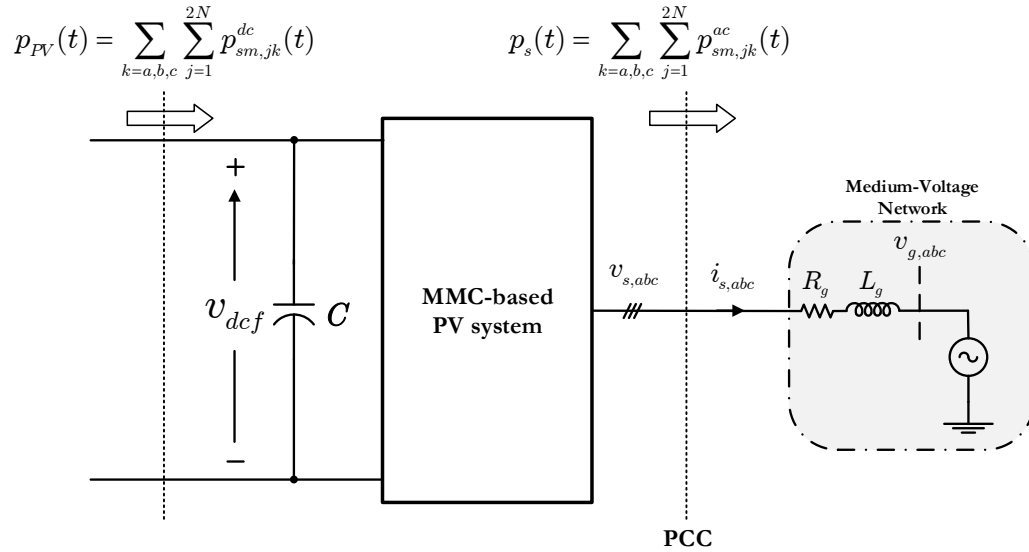
Figure 2.12: Block diagram of the virtual dc link

2.6   Controller of the MMC-based PV System

This section presents the controllers used to control the MMC-based PV system. Two different current controllers are required to control the MMC-based PV system. Firstly, the grid current is needed to be controlled which is achieved by conventional current controller implemented in DQ-frame. Secondly, the differential current in the structure of the converters needs to be nullified. Otherwise, it could threaten the stability of the converter.

2.6.1   Grid Current Controller

Grid current controller is the main controller of the system which regulates the active and reactive power exchanged with the host grid. The current controller can be implemented in different reference frames including three dimensional abc-frame, stationary two dimensional $\alpha\beta$-frame, and rotating two dimensional DQ-frame.

The MMC-based PV system employs a decoupled DQ-frame current control scheme to ensure that the ac current components, i_D and i_Q, are independently controlled and rapidly track their respective reference commands, i_D^* and i_Q^*. Figure 2.13 shows the block diagram of the current controller alongside the grid and converter representations.

The current control is performed in rotating DQ-frame whose D-axis is aligned with the phasor of the phase a of the terminal voltage, $v_{s,abc}$, and its Q-axis component is controlled to be zero using a phase-locked loop (PLL) [51]. The real- and reactive-power that the PV system delivers to the network are independently controlled by the D-axis current, i_D, and the Q-axis current, i_Q , respectively. The virtual dc link voltage controller generates the real power reference while the reactive power reference is issued by the reactive power control scheme represented in Figure 2.13.

The decoupled DQ-frame current control scheme, shown in Figure 2.13, receives the references for real and reactive powers and generates the D- and Q-axis components of the internal voltage of the converter. The ac-side voltage of the converter, $v_{s,abc}$, is
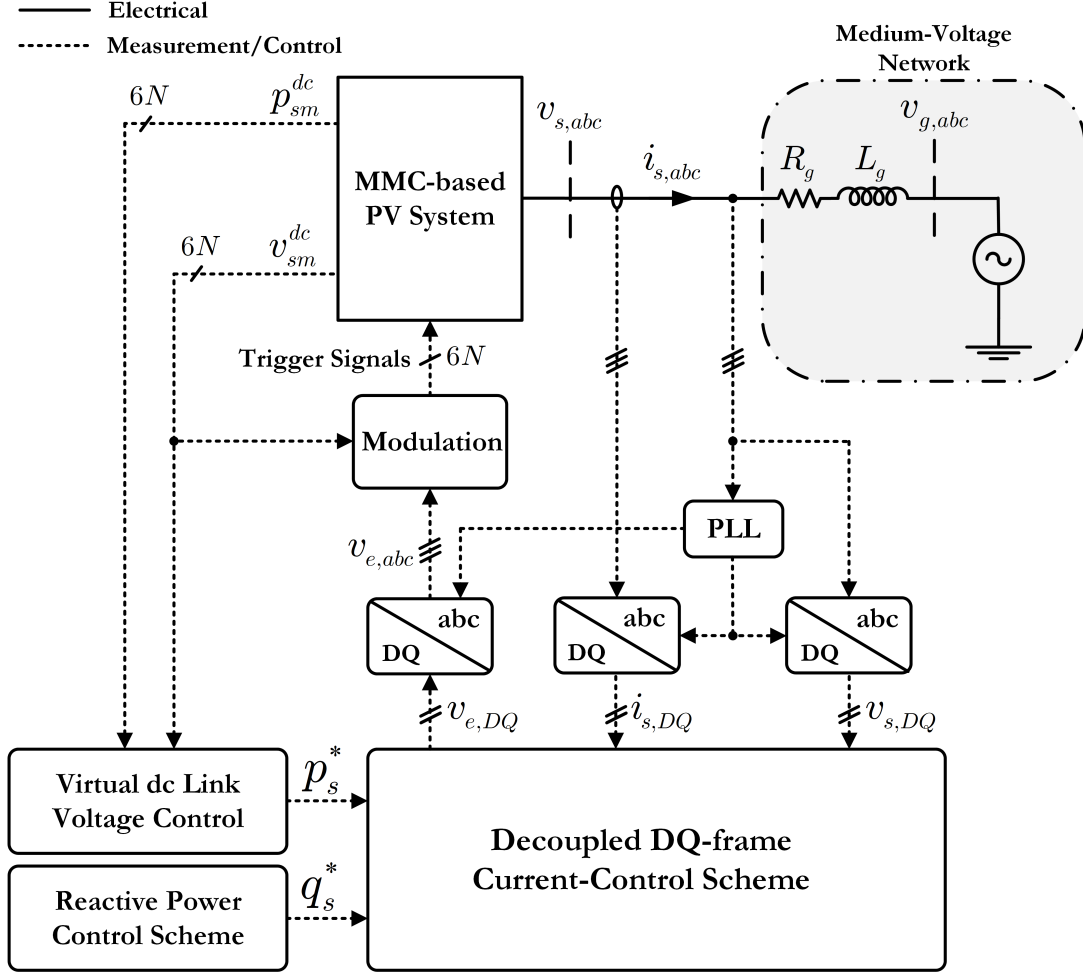
Figure 2.13: Block diagram of the current controller

transformed to $v_{s,D}$ and $v_{s,Q}$ by using the abc- to DQ-frame transformation block [51]. The D- and Q-axis components of the internal voltage of the converter are transferred to abc-frame and are fed to the modulation stage. Then, triggering signals are issued to the switching devices of the converter to generate the desired voltage at the terminals of the MMC-based PV system. Figure 2.14 shows detailed diagram of the current controller.

As shown in Figure 2.14, i_D and i_Q are the state variables, $v_{s,D}^*$ and $v_{s,Q}^*$ are the outputs, and the ac-side voltage components, $v_{s,D}$ and $v_{s,Q}$, are the disturbances which are used as feedforward signals and processed through a low-pass filter, H(s). To regulate the ac-side currents, two PI compensators process the error between the reference and the measured currents and generate new control inputs, $v_{s,D}^*$ and $v_{s,Q}^*$. Then, the reference
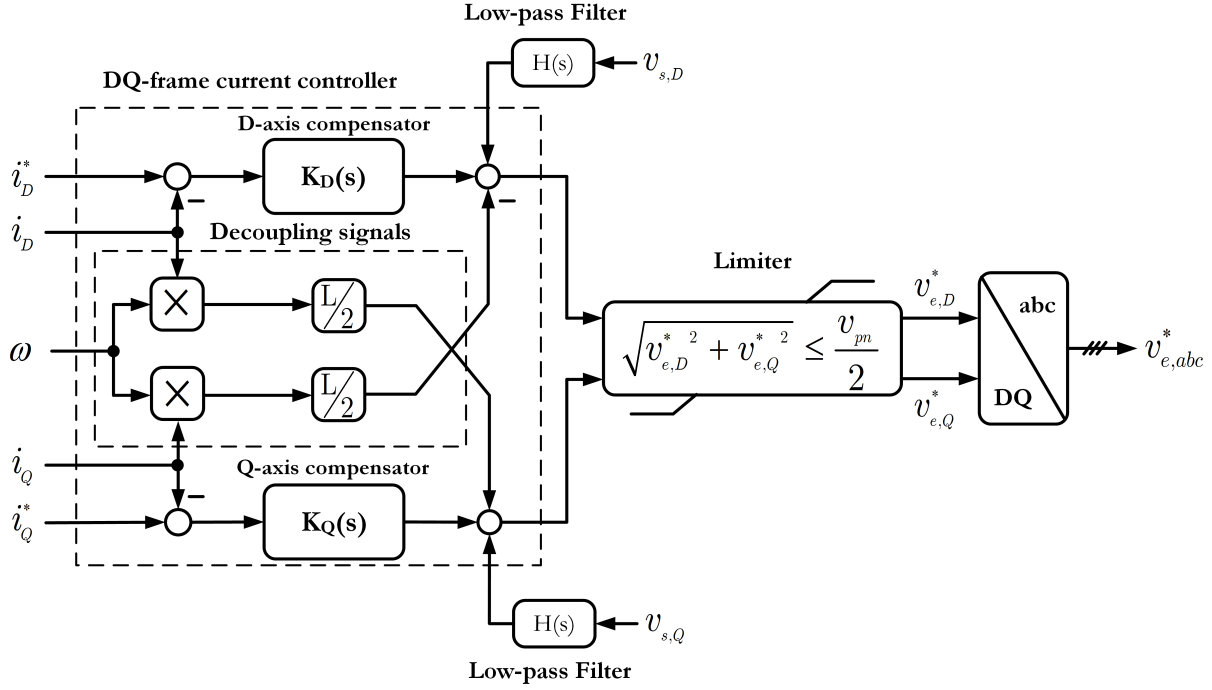
Figure 2.14: Detailed diagram of the current control scheme

D- and Q-axis terminal voltages are examined to satisfy the over-modulation criteria and then they are converted to abc-frame. Having generated the abc-frame reference terminal voltage, modulation stage is used to synthesize the reference voltages at the terminals of the converter.

Since D- and Q-axis current-control loops are identical, their compensators are also identical. Thus, based on [51], the compensators in Figure 2.14 are defined as

$$K_D(s) = K_Q(s) = \frac{k_1 s + k_2}{s} \tag{2.23}$$

where k_1 and k_2 are the proportional and integral gains, respectively. If k_1 and k_2 are set to

$$k_1 = \frac{L/2}{\tau_i} \tag{2.24}$$

$$k_2 = \frac{R/2}{\tau_i} \tag{2.25}$$

then i_D and i_Q independently track their respective setpoints, $i_{s,D}^*$ and $i_{s,Q}^*$, according to

the following transfer function

$$\frac{I_D(s)}{I_D^*(s)} = \frac{I_Q(s)}{I_D^*(s)} = \frac{1}{1 + \tau_i s} \tag{2.26}$$

where time constant, τ_i, is a design choice.

It should be noted that for fast current-control response, the time constant, τ_i, should be made small but adequately large so that $\frac{1}{\tau_i}$ is smaller than the switching frequency. As mentioned earlier, i_D and i_Q are used to control the real and reactive power of the converter, respectively. The real and reactive power components, p_s and q_s, in DQ-frame are formulated as

$$p_s = \frac{3}{2} v_{s,D} i_{s,D} \tag{2.27}$$

$$q_s = -\frac{3}{2} v_{s,D} i_{s,Q} \tag{2.28}$$

Figures 2.15(a) and 2.15(b) show the real and reactive power reference and the response of the current controller to step change in their references. As illustrated, the real and reactive powers are controlled at their reference values and the response time is according to the current controller's time constant (τ_i).

2.6.2   Differential Current Controller (DCC)

As presented in Section 2.5.2, the MMC-based PV system has a differential current in its structure. This current is considered a negative factor contributing to the lossless of the system and threatening the stability of the converter. Consequently, this current needs to be controlled and nullified. Equation (2.17), rewritten below for reference purposes, forms the basis for controlling the differential current of the converter.

$$L\frac{di_{d,k}}{dt} + Ri_{d,k} = v_{d,k} \qquad k = a, b, c \tag{2.29}$$

The control of the differential current can be implemented in any reference frame.

(a) Real power

(b) Reactive power
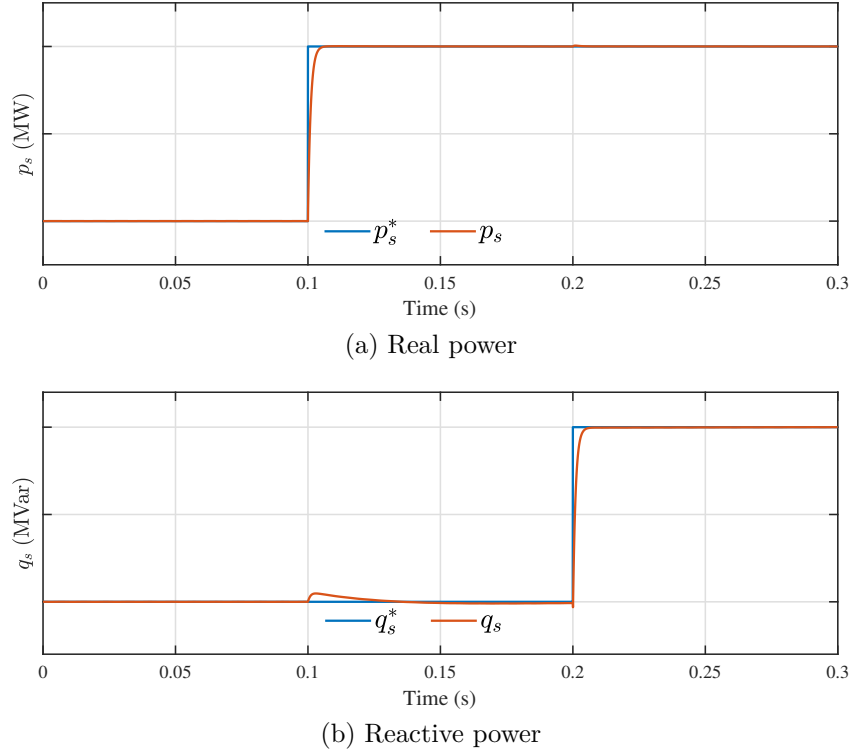
Figure 2.15: Response of the current controller

However, considering that PLL is required in rotating two-dimensional frame, the control is better carried out in stationary $\alpha\beta$-frame [56]. Figure 2.16 shows the general block diagram of the differential current controller. The differential current controller consists of a PI compensator for controlling the dc component of the differential current and multiple second order resonance compensators for controlling the fundamental frequency and its harmonics. The proportional resonant compensators have a phase of zero and magnitude of one at the resonance frequency and one PR controller is used for each harmonic of the differential current.

Depending on the application and the need for controlling second or third harmonics of the differential current, the differential current controller shown in Figure 2.16 can feature different number of resonance compensators.

Figure 2.17(a) through (c) show the reference currents for the differential currents of the legs of the system and the response of the DCC. The differential current in the legs

Dc differential current compenster

$$\frac{k_{P2}s + k_{I2}}{s}$$

Fundamental frequency differential current compensator

$$\frac{k_{P3}s + k_{I3}}{s^2 + 2\zeta\omega_n s + \omega_n^2}$$

Second harmonic differential current compensator

$$\frac{k_{P4}s + k_{P4}}{s^2 + 2\zeta(2\omega_n)s + (2\omega_n)^2}$$

Third harmonic differential current compensator

$$\frac{k_{P5}s + k_{I5}}{s^2 + 2\zeta(3\omega_n)s + (3\omega_n)^2}$$

$i_{d,k}^*$ $i_{d,k}$ $v_{d,k}^*$
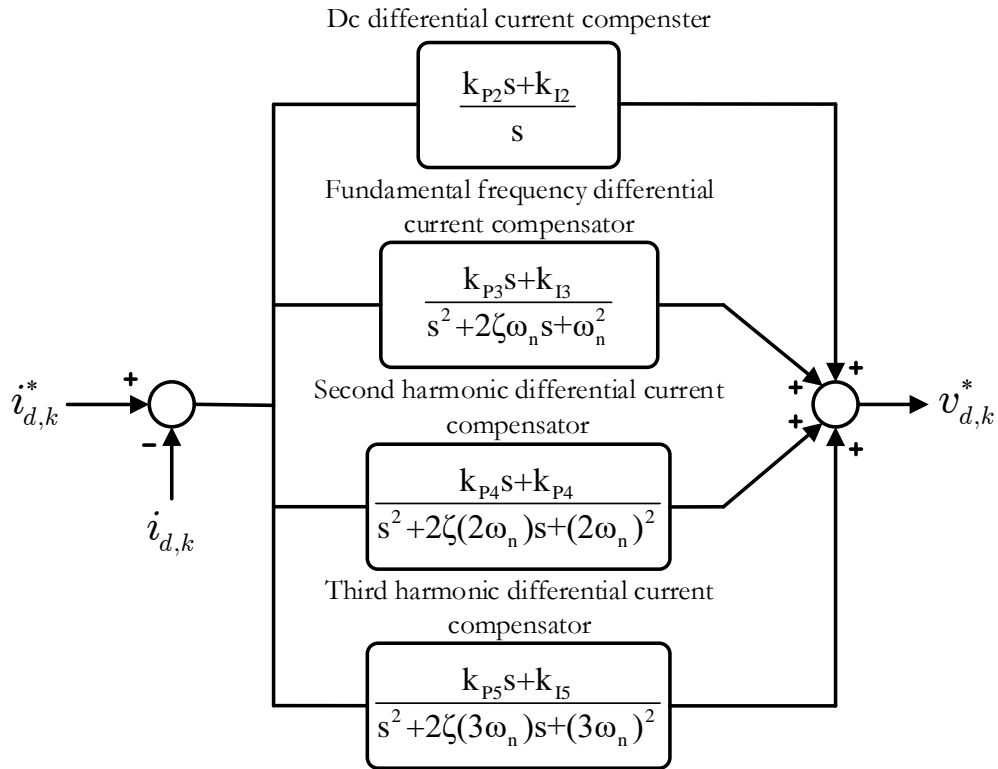
Figure 2.16: General form of the differential current controller

of the MMC-based PV system is controlled accurately at its reference.

2.6.3 Virtual dc Link Voltage Controller

The proposed virtual dc link concept is applied to generate the real power reference that needs to be delivered to the grid in order to maintain power balance. The methodology to generate the real power reference using the virtual dc link voltage is analogous to the one applied in the conventional VSCs. The virtual dc link voltage controller adjusts the amount of real power being delivered to the grid in such a way that the virtual dc link voltage is regulated at its setpoint. Mathematical model of the virtual dc-link voltage is adapted from [51]. According to Figure 2.12 and (2.27), a reduced-order model of the

(a) Leg a

(b) Leg b

(c) Leg c
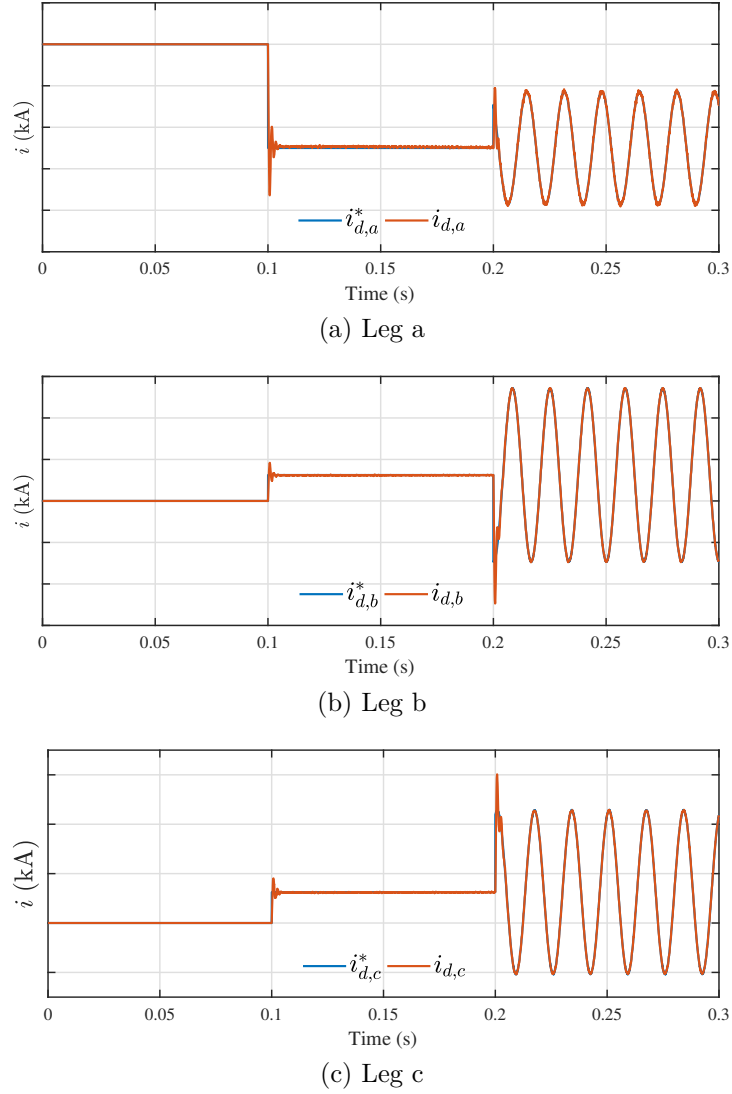
Figure 2.17: Differential current references and the response of the DCC

virtual dc-link voltage dynamics can be written as

$$
\begin{aligned}
\frac{1}{2}C\frac{dv_{dcf}^2}{dt} &\simeq p_{PV} - \frac{3}{2}v_{s,D}i_{s,D} \\
&\simeq p_{PV} - \frac{3}{2}v_{s,D}i_{s,D}^*
\end{aligned}
\tag{2.30}
$$

As (2.30) indicates, the virtual dc-link voltage can be controlled by i_D. Since τ_i is assumed to be a small value, $i_D \simeq i_D^*$ implies a fast operation of the current-control loop.

As depicted in Figure 2.18, a PI controller processes the error between the squared
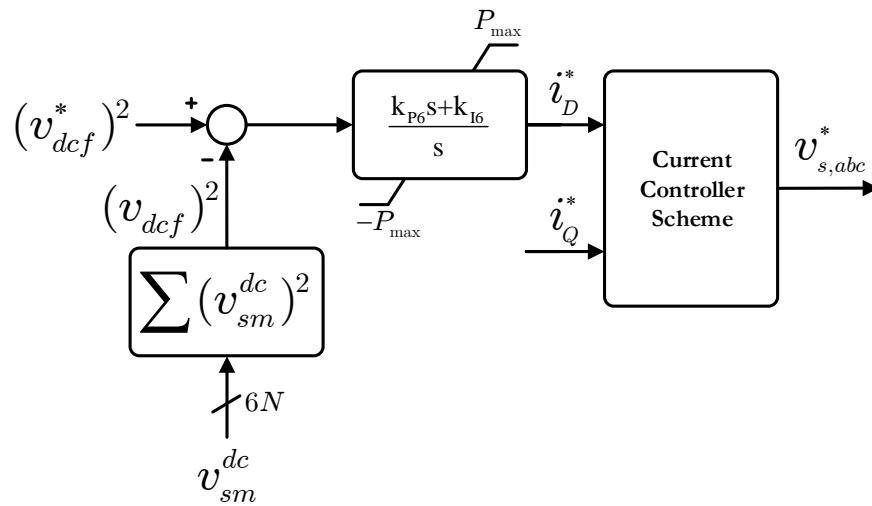
Figure 2.18: Schematic of the virtual dc link voltage controller

virtual dc link voltage, $(v_{dcf})^2$, and its setpoint, $(v_{dcf}^*)^2$, to issue the D-axis current command, i_D^*. Then, the reference for D-axis current is delivered to the current controller which regulates the D-axis current at its reference.

Figure 2.19 shows the response of the virtual dc link voltage controller to a step change.
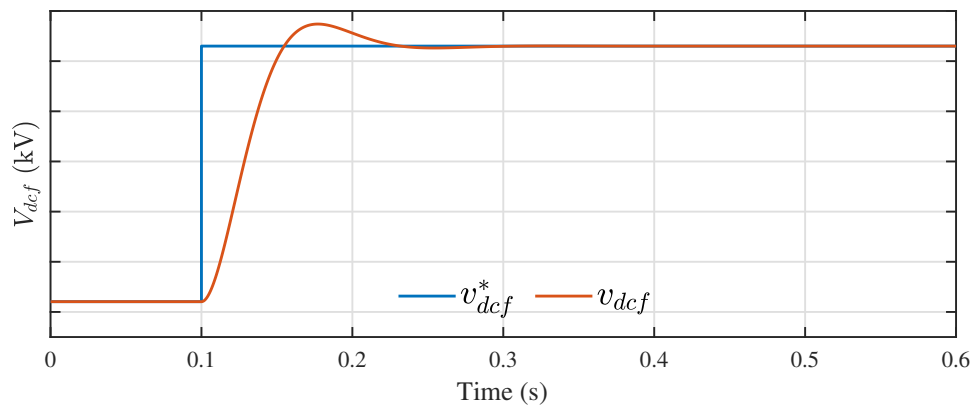
Figure 2.19: Step response of the virtual dc link voltage controller

2.6.4   Submodule dc link Voltage Regulation

The virtual dc link voltage controller ensures that the amount of real power exchanged with the grid is controlled in such a way that the power balance happens between the aggregated power generated by the PV generators and the real power delivered to the host grid. However, the virtual dc link voltage controller does not guarantee the regulation of the submodules' dc link voltage at its reference.

Voltage sorting algorithm is used in this thesis to regulate the dc link voltage of each submodule at its reference voltage. The sorting algorithm proposed in [21] is used for the submodules' dc link voltage balancing. There are other variations to this submodule voltage balancing algorithm which aim to minimize the number of switchings per fundamental frequency cycle by inserting a submodule only if the arm voltage level is required to change [33].

Conventional sorting algorithm for voltage balancing receives the number of the submodules that are needed to be inserted into the arm, n, from modulation stage. The voltages of the capacitors are periodically measured and sorted in ascending or descending order. According to Figure 2.8, in case of positive current (discharging capacitors), n submodule with highest voltages are inserted. In case of negative current (charging capacitors), n submodule with lowest voltage are inserted. By this method, continuous balancing of the capacitor voltages is guaranteed. Inherently, this concept supports an optimized utilization of the stored energy and evenly distributes power losses between the submodules. Table 2.1 shows the truth table of the voltage balancing algorithm. The notations used in Table 2.1 are based on Figure 2.8

Reduced switching frequency (RSF) voltage balancing algorithm, proposed in [33], decreases the average switching frequency of the submodules by ensuring that the submodules are inserted only if the number of inserted submodules need to change. The RSF voltage balancing proposed in [33] is shown in Figure 2.20. The switching principles of the RSF method are summarized as follows.
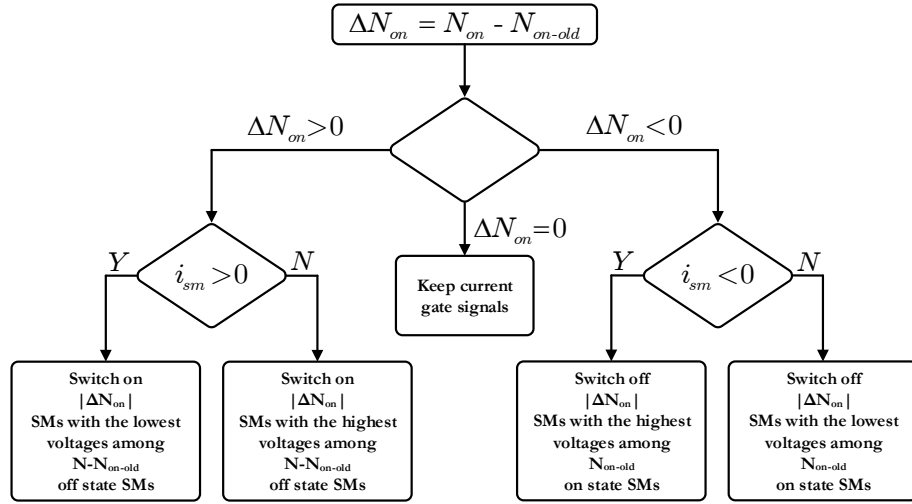
Figure 2.20: Switching principles of RSF voltage balancing algorithm

- If extra SMs are needed to be switched on during the following control cycle (i.e. ΔN_{on} is positive), no switching is applied to those SMs currently in the on state.

- If some SMs that are currently in the on state need to be switched off during the following control cycle (i.e. ΔN_{on} is negative), no additional SMs that are currently in the off state will be switched on.

where ΔN_{on} is the extra number of SMs that need to be switched on in the following control cycle and ΔN_{on-old} is the number of SMs that are already in on state in the current control cycle. The term N_{on} is newly calculated number of SMs that need to be on in the following control cycle.

Table 2.1: Voltage balancing states

Q_1	Q_2	i_{sm}	$\frac{dv_{sm}^{dc}}{dt}$	
ON	OFF	> 0	< 0	Discharging capacitor
ON	OFF	< 0	> 0	Charging capacitor
OFF	ON	> 0	0	Capacitor bypassed - No change
OFF	ON	< 0	0	Capacitor bypassed - No change

(a) Sumodule 1 in upper arm of leg a

(b) Sumodule 1 in lower arm of leg a

(c) Sumodule 1 in upper arm of leg b

(d) Sumodule 1 in lower arm of leg b

(e) Sumodule 1 in upper arm of leg c

(f) Sumodule 1 in lower arm of leg c
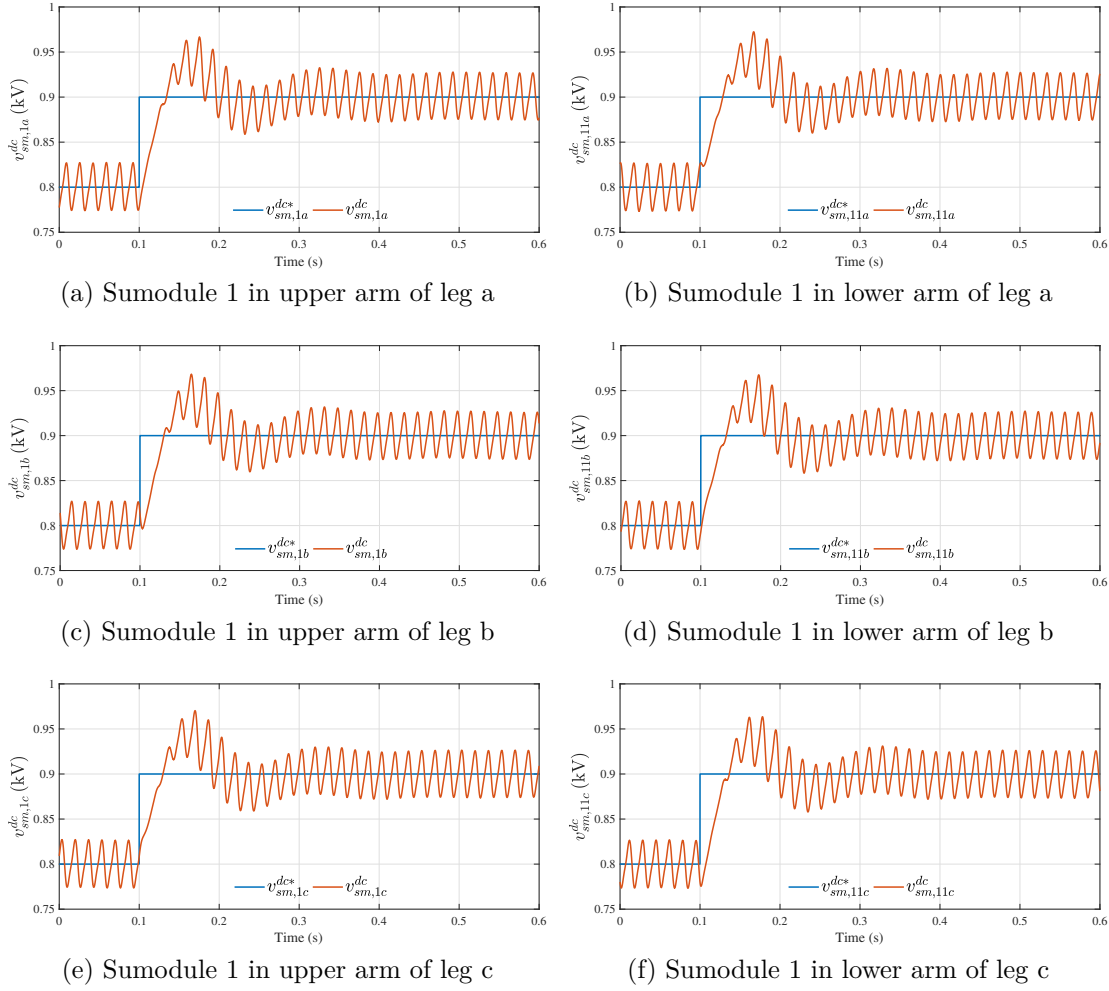
Figure 2.21: Dc link voltage of example submodules

Figure 2.21(a) through(f) show the dc link voltage of one submodule from each arm alongside their reference voltage. At $t = 0.1\,s$, the reference voltage for the dc link of the submodules is changed from $0.8\,kV$ to $0.9\,kV$. Consequent to the reference change, the voltage balancing algorithm regulates the voltages of the submodules at the new reference.

2.7   MMC's Voltage Modulation

Modulation algorithm ensures that the converter generates the reference voltage at its terminals. The moving average or first harmonic of the waveform generated at the termi-

nals of the MMC will be equal to the reference voltage. The modulation techniques of the MMC may be classified into pulse width modulation (PWM), space vector modulation (SVM), and nearest level modulation (NLM). The reference voltages for the arms of the converter are calculated using the internal voltage of the MMC.

The reference voltage of the arms have a dc component which ensures that the arm reference voltage does not become negative in any circumstance. As a result, the output voltage of the submodules do not require to generate negative voltages. Each level of the arm voltage is synthesized by inserting a number of submodules according to the number received from the modulation stage. This section elaborates on merits and limitations of each modulation technique for the MMC-based PV system.

2.7.1   Space Vector Modulation (SVM)

The basics of the SVM technique were first introduced in reference [72]. The SVM technique is based on space vector representation of the voltages in $\alpha\beta$-frame. SVM features good utilization of dc-link voltage, low current ripple, and relatively easy hardware implementation by a digital signal processor (DSP). As the number of levels increases, redundant switching states and the complexity of selecting switching states increase dramatically which is considered a limitation for the SVM technique. Figure 2.22 shows the space vector for a four-level converter. The depicted vector diagram is universal regardless of the topology of the multilevel converter. According to [73], the desired voltage vector can be synthesized by its adjacent three vectors by computing the duty cycles (T_1, T_2, and T_3,) for each vector as

$$V^* = \frac{T_1 V_1 + T_2 V_2 + T_3 V_3}{T}$$
$$T = T_1 + T_2 + T_3 \tag{2.31}$$

where T is the switching period.
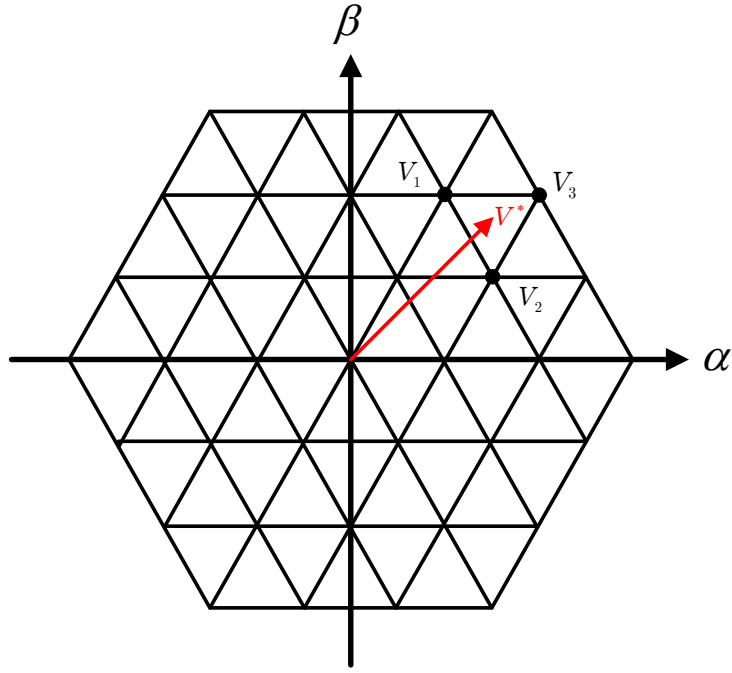
Figure 2.22: SVM diagram for a four level converter

2.7.2 Nearest Level Modulation (NLM)

For an MMC converter with N submodules per arm or equivalently (N+1) levels in the output voltage, average dc link voltage of the SMs in each arm can be represented as

$$v_{sm}^{dc} = \frac{V_{pn}}{N} \tag{2.32}$$

The number of submodules in the on-state in the upper and lower arms can be calculated as

$$N_{on,uk} = int(\frac{v_{u,k}^*}{v_{sm}^{dc}}) \tag{2.33}$$

$$N_{on,\ell k} = int(\frac{v_{\ell,k}^*}{v_{sm}^{dc}}) \tag{2.34}$$

where k=a,b,c and int(y) represents the nearest integer number of variable y. At any given time, the total number of submodules in on-sate in each leg of the MMC-based PV
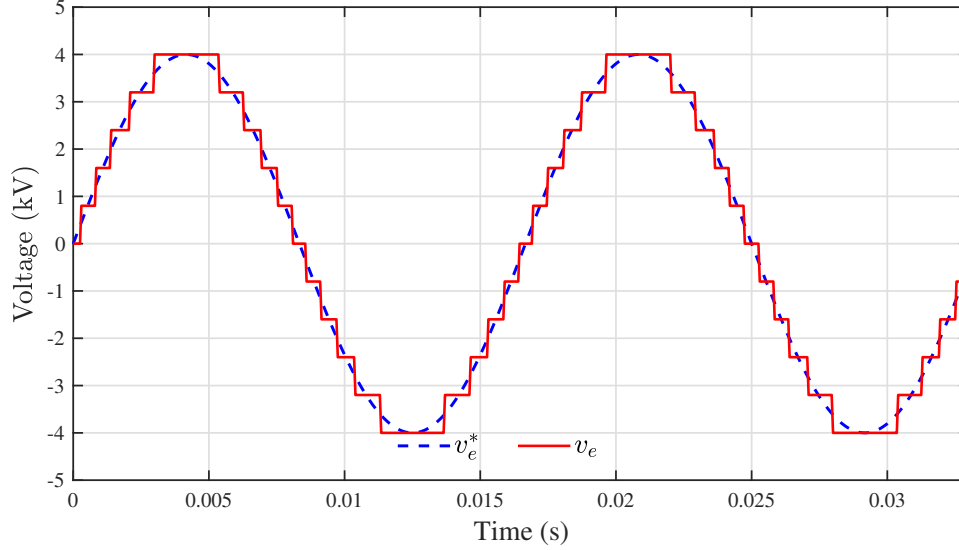
Figure 2.23: Exemplary output voltage using NLM technique

system is equal to the number of the submodules in each arm and is given by

$$N = N_{on,uk} + N_{on,\ell k} \tag{2.35}$$

The exemplary output voltage of the NLM technique is shown in Figure 2.23. Nearest level modulation technique is suitable for MMC with high number of submodules in each arm which can lead to high output voltage quality.

2.7.3   Pulse Width Modulation (PWM)

Pulse width modulation technique ensures that the moving average (first harmonic) of the output voltage of the converter follows the reference voltage while shifting the harmonics of the output voltage to higher frequencies. Since the harmonics of the output voltage are shifted to higher frequencies with PWM technique, less filtering is needed. The PWM for multilevel converters is divided into two main categories including phase-shifted (PS-PWM) and level-shifted (LS-PWM). As shown in Figure 2.24(a) and (b), the main difference between the two categories is the placement of the carrier signal.

In LS-PWM technique, all the carrier signals have the same phase angle while their
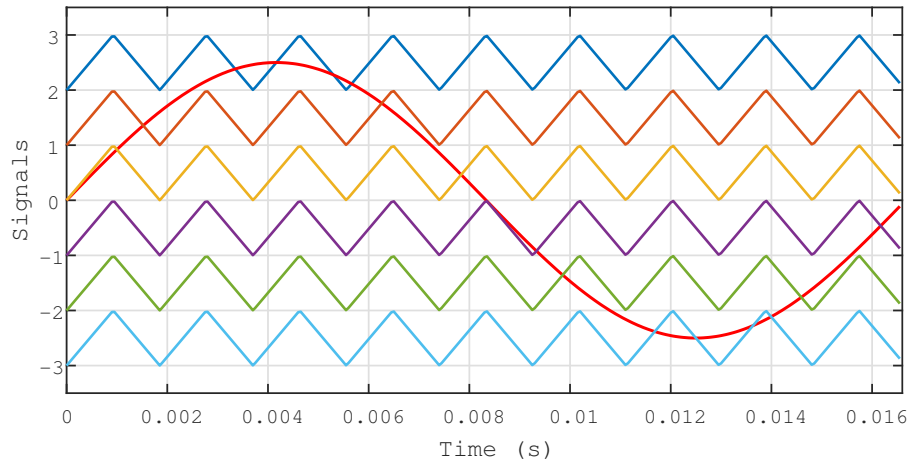
(a) Level-shifted PWM (LS-PWM)
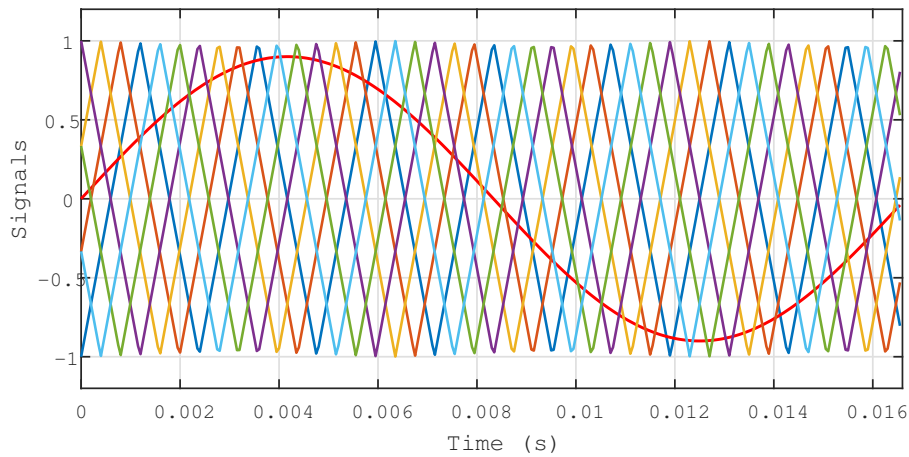
(b) Phase-shifted PWM (PS-PWM)

Figure 2.24: Reference and carrier signals of two PWM techniques

dc value is different. It must be pointed out that the LS-PWM is not preferred for MMC, as it causes uneven power distribution among the different SMs [64]. As a result, the PS-PWM technique is widely used in the literature for MMC converter. The PS-PWM technique has some distinctive features such as

- The semiconductor stress and the power handled by each SM are evenly distributed. Hence, the capacitor voltage balancing control can be easily achieved.

- The output voltage has higher resulting switching frequency and a low total harmonic distortion (THD) due to interleaved operation of the submodules.

- Consistent with the structure of MMC, each triangular carrier associated with a particular SM presents the nature of modularity and scalability.

Consequently, PS-PWM is the modulation technique used in this thesis.

In order to reach best harmonic cancellation features, the N triangular carriers of each arm are shifted by $2\pi/N$ incrementally [74]. Therefore, the phase angle of the ith carrier signal in the lower arm is given by

$$\theta_{\ell,i} = \frac{2\pi}{N}(i-1) \tag{2.36}$$

where $\theta_{\ell,i}$ is the phase angle of the carrier signal associated with the ith submodule in the lower arm. As for the ith carrier in the upper arm, that is

$$\theta_{u,i} = \theta + \frac{2\pi}{N}(i-1) \tag{2.37}$$

where $\theta_{u,i}$ and θ are the phase angles of the carrier signal associated with the ith submodule in the upper arm and the displacement angle between the carrier signals of the upper and lower arms, respectively. Displacement angle, θ, has a significant impact on the harmonic features of the MMC-based PV system. According to [75], in order to remove all the switching harmonics from the differential currents, the displacement angle needs to be

$$\theta = \begin{cases} \frac{\pi}{N} & N \ is \ odd \\ 0 & N \ is \ even \end{cases} \tag{2.38}$$

Under this condition, a pure differential current can be achieved without unwanted switching harmonics. The displacement angle also has a significant impact on the output voltage harmonics. According to [75], in order to achieve minimum harmonic distortion

for the internal voltage of the MMC, the displacement angle has to be set according to

$$
\theta = \begin{cases} 0 & N \ is \ odd \\[2ex] \frac{\pi}{N} & N \ is \ even \end{cases} \tag{2.39}
$$

Based on the objective of the modulation stage, the displacement angle can be chosen to minimize the switching harmonics of the synthesized terminal voltage or eliminate switching harmonics from the differential current.

2.8   Summary

In this chapter, the MMC-based PV system was introduced as an emerging configuration for large-scale PV systems. The model of the MMC-based PV system was derived which includes grid current, differential current, common dc link, and virtual dc link voltage models. Having modeled different aspects of the MMC-based PV system, a thorough controller was envisioned and introduced in this chapter.

The controller of the MMC-based PV system ensures that right amount of real power is injected into the host grid by receiving the active power reference from the virtual dc link controller. The differential current controller ensures that the differential currents in the legs of the converter are nullified.

Chapter 3

Power Mismatch Elimination in MMC-based PV system

3.1 Introduction

The amount of power delivered to the legs, arms, and submodules of the MMC-based PV system are not necessarily equal since the dc power is directly delivered to the submodules of the converter by their PV generators. Considering that the utility-scale PV farms stretch over a large area, the PV submodules could be subjected to different ambient conditions such as different temperature and solar irradiation. As a result, the amount of aggregate power delivered to the arms and legs of the converter are very likely to be unequal.

The MMC-based PV system featuring a conventional current controller delivers unbalanced currents to the host grid in presence of arm or leg power mismatches. The proposed power mismatch elimination strategy is thoroughly explored in this chapter. Moreover, the performance of the proposed power mismatch elimination strategy in presence of the different types of power mismatches is evaluated.

3.2   Possible Power Mismatches

Different types of power mismatches can happen in an MMC-based PV system that can compromise stable operation of the converter. Consequently, power mismatches have to be identified and the features of each power mismatch needs to be studied in order to eliminate them. This section presents the possible power mismatches within the structure of the MMC-based PV system. Then, according to the features of each power mismatch, a power mismatch elimination method is presented.

3.2.1   Leg Power Mismatch

The MMC-based PV system is comprised of three legs which are associated with three phases of the system. The nominal power rating of the PV generators of the legs are equal by design. Consequently, if all PV generators are identical and are exposed to the same ambient conditions, their generated powers are expected to be equal. In this condition, the conventional current-control scheme is adequate for controlling the MMC-based PV system. However, due to reasons including module mismatch and different ambient conditions such as unequal temperature and solar irradiation, the amount of power delivered to the legs and arms of the converter by their associated PV generators are not always equal. Consequently, power mismatches develop in the structure of the MMC-based PV system that results in injection of unbalanced and asymmetrical currents into the host grid and threatens stable operation of the converter in terms of having bounded submodule dc link voltages. Figure 3.1 shows an exemplary leg power mismatch where the dc powers delivered to the legs of the MMC-based PV system are not equal.

A power mismatch between the legs of the converter leads to injection of unbalanced currents into the host grid. As shown in Figure 3.1 the legs of the converter generate 0.8 p.u. power, then at $t = 1$ s the power delivered to leg a drops from 0.8 p.u. to 0.6 p.u. which causes leg power mismatch. The same change happens to phase b, as shown in Figure 3.1(b), that causes its power to decline from 0.8 p.u. to 0.7 p.u. at $t = 2$ s. Finally,
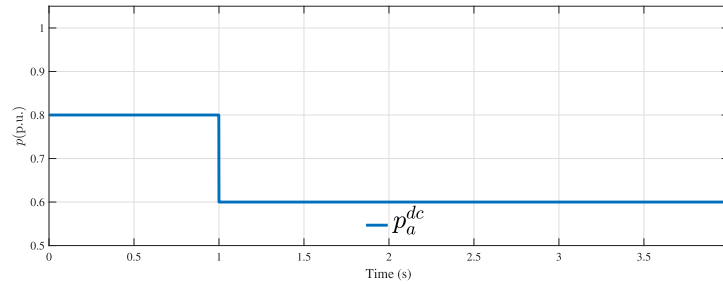
(a) Leg a
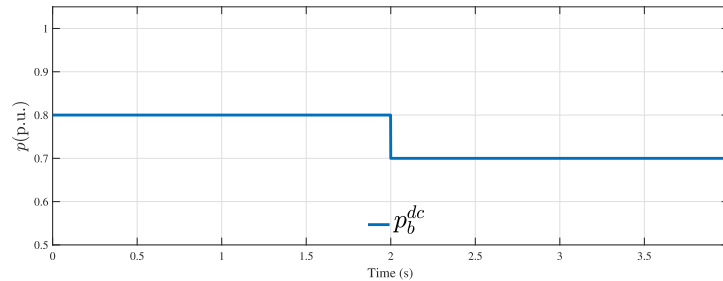
(b) Leg b
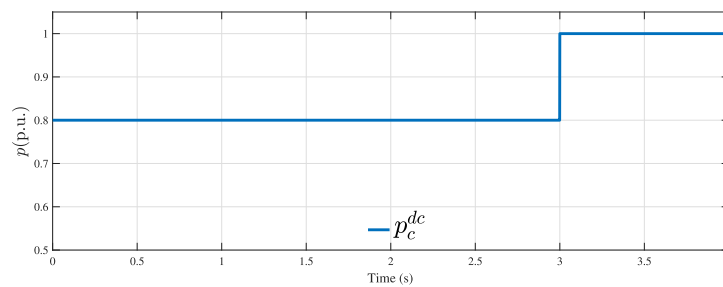
(c) Leg c

Figure 3.1: Dc powers delivered to the legs of the converter

as shown in Figure 3.1(c) at $t = 3\,\text{s}$, the power yield of leg c is increased to $1\,\text{p.u.}$ from $0.8\,\text{p.u.}$ which leads to initiation of another power mismatch.

3.2.2   Arm Power Mismatch

Arm power mismatch happens between the upper and lower arms of one phase. The same as a leg power mismatch, the arm power mismatch also leads to injection of unbalanced currents into the grid. The arm power mismatch happens when the amount of power delivered to one arm of a phase is different from that of the other arm in the same phase. The arm power mismatch also leads to a leg power mismatch if the amount of power

mismatches of the three phases are not equal. Figure 3.2 shows exemplary arm power mismatches.
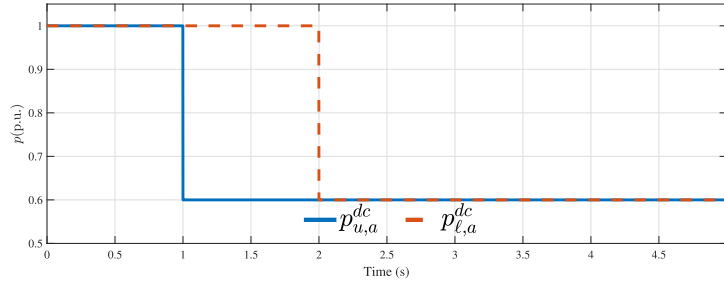
(a) Leg a
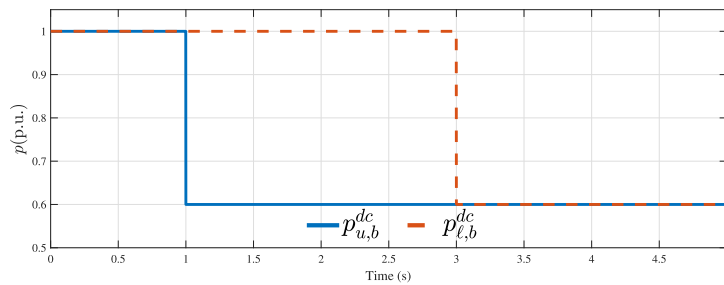
(b) Leg b
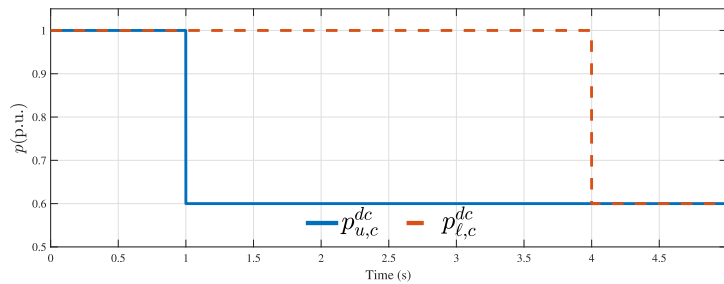
(c) Leg c

Figure 3.2: Dc powers delivered to the arms of the converter

At $t = 1\,$s, the power yield of the upper arms of the legs decrease to $0.6\,$p.u from $1\,$p.u. This condition means that an arm power mismatch exists in all three legs. At $t = 2\,$s, the power yield of the lower arm of phase a also declines to $0.6\,$p.u from $1\,$p.u. Consequently, the arm power mismatch does not exist in leg a anymore since both upper arm and lower arm PV generators produce the same amount of power. The same scenario happens to legs b and c at $t = 3\,$s and $t = 4\,$s, respectively, causing their arm power mismatch to be removed. The presence of arm power mismatch leads to development of leg power

mismatch, as well. Figure 3.3 shows the corresponding aggregate dc powers delivered to the legs of the converter.

As shown in Figure 3.3, the inception of equal arm power mismatches in all legs of the converter does not create a leg power mismatches since the aggregate power of the legs are still equal. At $t = 2\,s$, the power of the lower arm of phase a drops to 60% of its nominal power which causes a leg power mismatch since the aggregate power delivered to leg a becomes less than the aggregate power of the other two legs. The same scenario is repeated for legs b and c at at $t = 3\,s$ and $t = 4\,s$, respectively. After $t = 4\,s$, the aggregate power of all three legs become equal again, meaning that the leg power mismatch becomes zero. The arm power mismatch does not necessarily create a leg power mismatch. However, if the aggregate power delivered to the legs of the converter become different due to arm power mismatches, a leg power mismatch will develop as a result of the arm power mismatch.

3.2.3   Submodule Power Mismatch

Submodule power mismatch happens when the amount of the powers supplied to the submodules of one arm are not equal. This power mismatch is considered a minor power
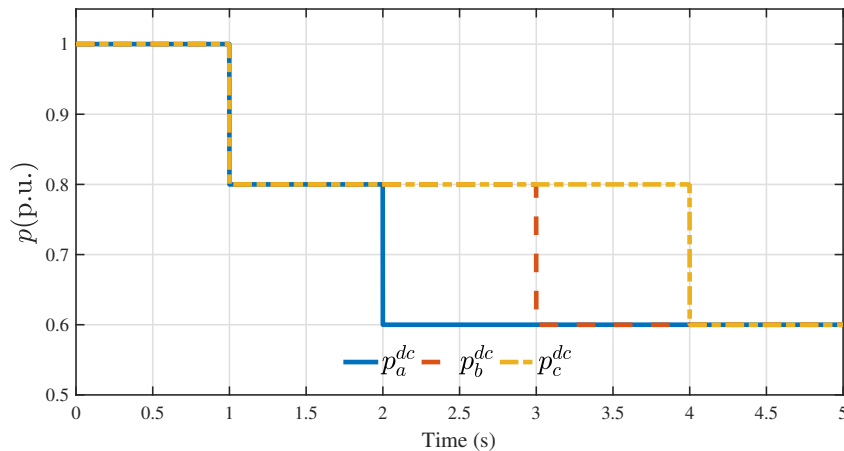
Figure 3.3: Aggregate dc powers of the MMC legs corresponding to arm power mismatches

mismatch in the MMC-based PV system firstly because their power rating is usually very small with respect to the power rating of the system. The second reason is that the submodules are physically located close to each other. Consequently, they are most probably subjected to the same ambient conditions and their power yield will not be very different. However, no matter how small the submodule power mismatch is, it needs to be eliminated effectively to ensue stable operation of the converter.

The submodule power mismatch potentially can cause arm and leg power mismatches since the aggregate power delivered to the legs and arms of the converter is the sum of the powers delivered to their submodules. The submodule power mismatch is automatically eliminated by the voltage balancing algorithm introduced in Section 2.6.4. The sorting algorithm inserts a submodule into the arm or bypasses it according to its dc link voltage. Consequently, the voltage balancing algorithm regulates the dc link voltage of the submodules at their reference value by ensuring that the amount of power delivered to the submodule, $p_{sm,jk}^{dc}$, is equal to the amount of power leaving the ac side of the submodule, $p_{sm,jk}^{ac}$. As a result, the power mismatches between the submodules is eliminated without any modifications to the structure or controller of the MMC-based PV system.

3.3   Submodule dc link voltage model

The dc link voltage of the submodules oscillates around its nominal value at second harmonic frequency. This stems from the fact that the instantaneous power leaving the ac side of the submodules is oscillatory since the submodules ac side is a single-phase system. This section derives the equations of the dc link voltage of the submodules of each arm as a whole. Then, the effect of the differential current on the dc link voltage of the submodule is formulated.

3.3.1   Lumped Model of the MMC-based PV System

In order to evaluate the effect of differential currents on the dc link voltage of the submodules, a model representing each arm as a single converter has to be developed. The

reason is that the voltage balancing algorithm regulates the dc link voltages of the sub-modules of the arm as a single entity and an explicit representation of the dc link voltage of a submodule does not exist. This section represents a lumped model for the arms of the converter which uses a single average model for each arm of the converter.

Ignoring the power losses of the conversion stages in the submodules including the losses of the dc-dc and dc-ac converters, the following relationship is deduced.

$$P_{sm,jk}^{dc} = P_{sm,jk}^{PV} \tag{3.1}$$

According to Figure 3.4, which shows the schematic of the submodules of the system, and (3.1), the dc link voltage dynamics can be represented as

$$\frac{1}{2}C\frac{d(v_{sm,jk}^{dc})^2}{dt} = p_{sm,jk}^{dc} - p_{sm,jk}^{ac} \tag{3.2}$$

Equation (3.2) applies to the submodules of the system regardless of their location in the arms and legs of the converter. The submodules of each arm can be represented as a single submodule using (3.2). The dynamics of the dc link voltages of the submodules
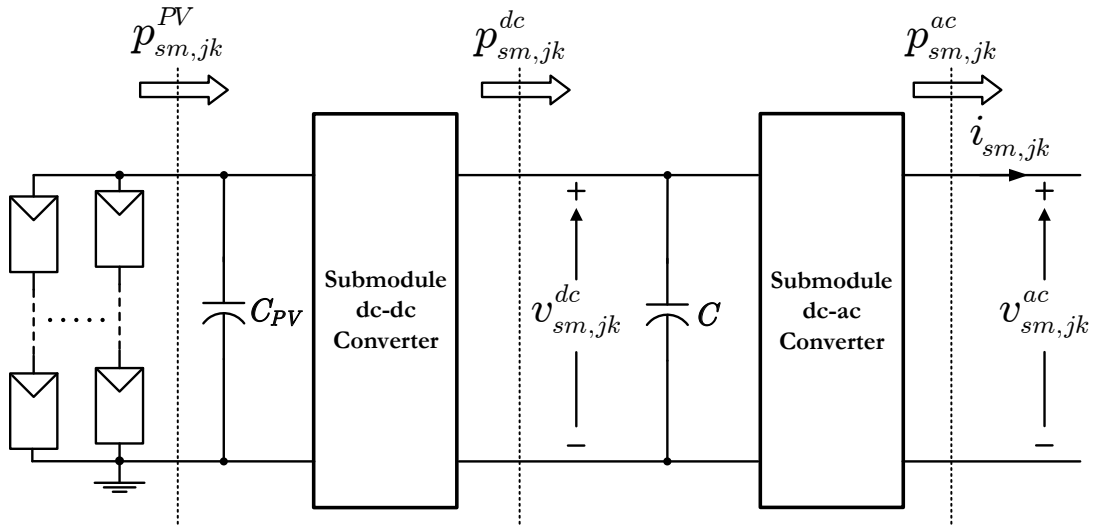
Figure 3.4: Schematic of the submodules in the MMC-based PV system

in the upper arm of phase a, as an example, are shown below.

$$\frac{1}{2}C\frac{d(v_{sm,1a}^{dc})^2}{dt} = p_{sm,1a}^{dc} - p_{sm,1a}^{ac}$$

$$\frac{1}{2}C\frac{d(v_{sm,2a}^{dc})^2}{dt} = p_{sm,2a}^{dc} - p_{sm,2a}^{ac}$$

$$.$$

$$.$$

$$.$$

$$\frac{1}{2}C\frac{d(v_{sm,Na}^{dc})^2}{dt} = p_{sm,Na}^{dc} - p_{sm,Na}^{ac} \tag{3.3}$$

Assuming the same dc link voltage dynamics for the submodules of the arm and adding the left and right side of (3.3), yields

$$\frac{1}{2}C\frac{d}{dt}\sum_{j=1}^{N}(v_{sm,ja}^{dc})^2 = \underbrace{\sum_{j=1}^{N}p_{sm,ja}^{dc}}_{A} - \underbrace{\sum_{j=1}^{N}p_{sm,ja}^{ac}}_{B} \tag{3.4}$$

where terms A and B represent the aggregate power delivered to the upper arm of leg a by its associated PV generators, $p_{u,a}^{dc}$, and the ac power leaving the arm, $P_{u,a}^{ac}$, respectively. Equation (3.4) represents the submodules of the upper arm of leg a as a single equivalent submodule. In order to study the dc link voltage of the submodules in each arm, the arms of the converter are substituted with their corresponding equivalent submodule according to (3.4).

Figure 3.5 shows the model of the MMC-based PV system featuring the equivalent submodule for each arm of the converter. The dc link voltage of the equivalent submodule of the upper arm of leg k is

$$(v_{u,k}^{dc})^2 = \sum_{j=1}^{N}(v_{sm,jk}^{dc})^2 \tag{3.5}$$

The dc link voltage of the equivalent submodule of the lower arm of leg k is
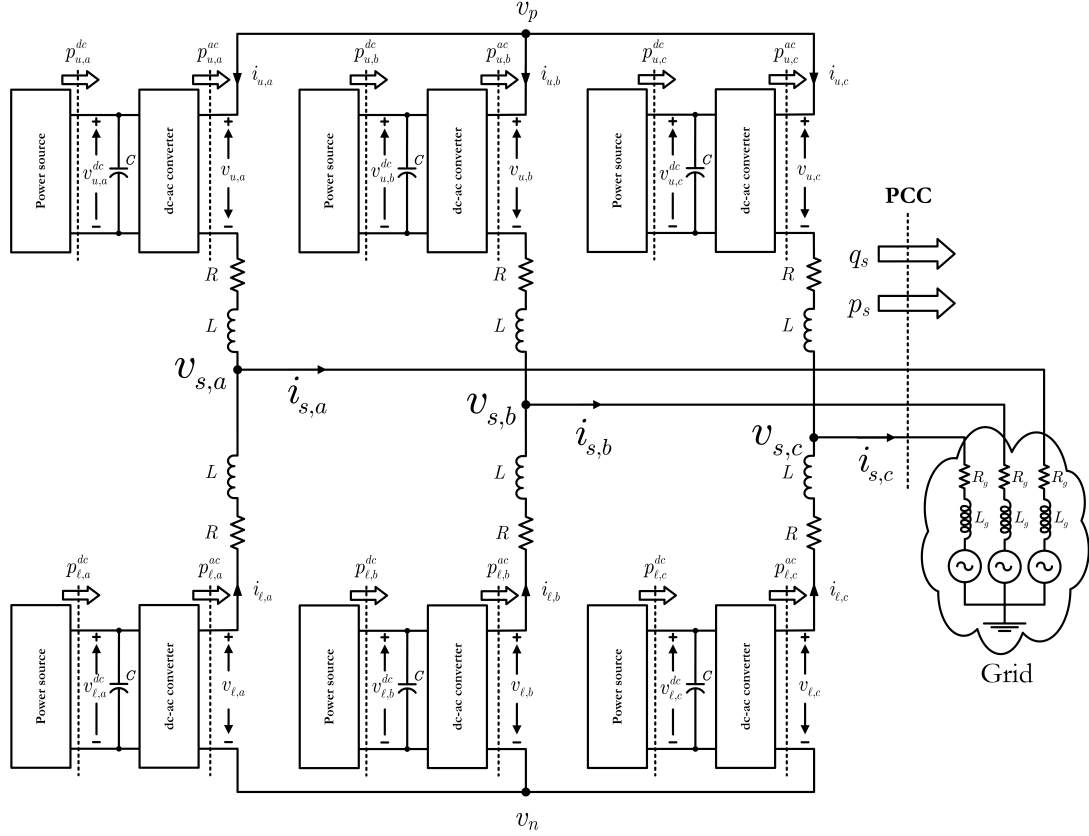
Figure 3.5: MMC-based PV system model using equivalent submodule for each arm

$$\left(v_{\ell,k}^{dc}\right)^2 = \sum_{j=N+1}^{2N} \left(v_{sm,jk}^{dc}\right)^2 \tag{3.6}$$

Having represented each arm of the converter with a single converter model, dc link voltage of the equivalent submodule can be derived using the power balance at the dc-ac converter. The assumption is that the dc-ac converter is lossless and the average power leaving the ac terminal of the equivalent submodule is equal to the power delivered to the equivalent submodule.

3.3.2 Without Differential Current

If the differential current is nullified in the structure of the MMC-based PV system, the power exchange at the ac terminals of the equivalent submodule will merely be product

of the ac arm voltage and currents. The arm voltage has two components including a dc component which maintains the common dc link voltage and the ac component which forms the internal voltage of the converter. The voltages of the upper and lower arms are represented as

$$v_{u,k} = \frac{1}{2}v_{pn} - v_{e,k}$$
$$v_{\ell,k} = \frac{1}{2}v_{pn} + v_{e,k} \tag{3.7}$$

The arm currents in this case are equal to half of their respective phase currents. Consequently,

$$i_{u,k} = \frac{1}{2}i_{s,k}$$
$$i_{l,k} = \frac{1}{2}i_{s,k} \tag{3.8}$$

multiplying (3.7) and (3.8) yields the ac power exchanged at the ac terminals of the equivalent upper arm submodule as

$$p_{u,k} = -v_{u,k}i_{u,k} = -(\frac{1}{2}v_{pn} - v_{e,k})(\frac{1}{2}i_{s,k}) \tag{3.9}$$

The negative sign in (3.9) is the result of the power flow direction shown in Figure 3.5. The ac power exchanged at the ac terminals of the equivalent lower arm submodule is

$$p_{\ell,k} = v_{\ell,k}i_{\ell,k} = (\frac{1}{2}v_{pn} + v_{e,k})(\frac{1}{2}i_{s,k}) \tag{3.10}$$

The general form of the terminal voltage of the converter at PCC is given as

$$v_{s,k} = \hat{v}_s sin(\omega t) \tag{3.11}$$

Assuming unity power factor operation for the converter (as is in normal operation

mode), the internal voltage of the converter leads the terminal voltage by ϕ_e which enables the power transfer. Consequently, the internal voltage of the converter can be represented using a sinusoidal waveform with angle of ϕ_e with respect to the terminal voltage of the converter (v_s). The internal voltage of the converter is represented as

$$v_{e,k} = \hat{v}_e sin(\omega t + \phi_e) \tag{3.12}$$

The terminal current of the converter is in phase with the terminal voltage as a result of unity power factor operation. As a result, the terminal current is represented as

$$i_{s,k} = \hat{i}_s sin(\omega t) \tag{3.13}$$

Substituting the internal voltage and terminal current in (3.9) and (3.10) with their sinusoidal representations from (3.12) and (3.13) yields

$$p_{u,k}^{ac} = -\left(\frac{1}{2}v_{pn} - \hat{v}_e sin(\omega t + \phi_e)\right)\left(\frac{1}{2}\hat{i}_s sin(\omega t)\right) \tag{3.14}$$

The power exchange at the terminal of the lower arm equivalent submodule will be

$$p_{\ell,k}^{ac} = \left(\frac{1}{2}v_{pn} + \hat{v}_e sin(\omega t + \phi_e)\right)\left(\frac{1}{2}\hat{i}_s sin(\omega t)\right) \tag{3.15}$$

The average of the ac power exchanged at the terminals of the upper and lower arm equivalent submodules are equal to the dc power delivered to the upper and lower arms by their PV generators. Consequently, the difference between the two quantities is the amount of the power that the dc link capacitor has to buffer. According to (3.4), the dc link voltage dynamics of the upper arm equivalent submodule is represented as

$$\begin{aligned}
\frac{1}{2}C\frac{d}{dt}(v_{u,k}^{dc})^2 &= p_{u,k}^{dc} - p_{u,k}^{ac} \\
&= p_{u,k}^{dc} - \left(\frac{1}{2}v_{pn} - \hat{v}_e sin(\omega t + \phi_e)\right)\left(\frac{1}{2}\hat{i}_s sin(\omega t)\right)
\end{aligned} \tag{3.16}$$

As described earlier, the dc power of the upper equivalent submodule and its ac power average are equal. Consequently,

$$
\begin{aligned}
p_{u,k}^{dc} &= -\overline{\left(\frac{1}{2}v_{pn} - \hat{v}_e sin(\omega t + \phi_e)\right)\left(\frac{1}{2}\hat{i}_s sin(\omega t)\right)} \\
&= \underline{-\frac{1}{4}v_{pn}\hat{i}_s sin(\omega t)} + \overline{\frac{1}{2}\hat{v}_e\hat{i}_s sin(\omega t + \phi_e)sin(\omega t)} \\
&= \underbrace{-\frac{1}{4}v_{pn}\hat{i}_s sin(\omega t)}_{=0} + \frac{1}{4}\hat{v}_e\hat{i}_s cos(\phi_e) - \underbrace{\overline{\frac{1}{4}\hat{v}_e\hat{i}_s cos(2\omega t + \phi_e)}}_{=0}
\end{aligned}
\tag{3.17}
$$

Substituting $p_{u,k}^{dc}$ in (3.16) with its equivalent representation from (3.17), the dc link voltage of the upper arm equivalent submodule is given as

$$
\frac{1}{2}C\frac{d}{dt}(v_{u,k}^{dc})^2 = -\frac{1}{4}v_{pn}\hat{i}_s sin(\omega t) - \frac{1}{4}\hat{v}_e\hat{i}_s cos(2\omega t + \phi_e)
\tag{3.18}
$$

Then, $v_{u,k}^{dc}$ in steady state is calculated as

$$
(v_{u,k}^{dc})^2 = (v_{u,k}^{dc*})^2 + \frac{1}{2\omega C}v_{pn}\hat{i}_s cos(\omega t) - \frac{1}{4\omega C}\hat{v}_e\hat{i}_s sin(2\omega t + \phi_e)
\tag{3.19}
$$

The same process can be applied to calculate the dc link voltage of the lower arm equivalent submodule. From (3.4) and (3.10), the dc link voltage dynamics of the lower arm equivalent submodule is given as

$$
\begin{aligned}
\frac{1}{2}C\frac{d}{dt}(v_{\ell,k}^{dc})^2 &= p_{\ell,k}^{dc} - p_{\ell,k}^{ac} \\
&= p_{\ell,k}^{dc} - \left(\frac{1}{2}v_{pn} + \hat{v}_e sin(\omega t + \phi_e)\right)\left(\frac{1}{2}\hat{i}_s sin(\omega t)\right)
\end{aligned}
\tag{3.20}
$$

The average power leaving the ac terminals of the equivalent submodule is equal to the aggregate dc power injected to the arm by its PV generators. As a result,

$$p_{\ell,k}^{dc} = \overline{\left(\frac{1}{2}v_{pn} + \hat{v}_e sin(\omega t + \phi_e)\right)\left(\frac{1}{2}\hat{i}_s sin(\omega t)\right)}$$

$$= \overline{\frac{1}{4}v_{pn}\hat{i}_s sin(\omega t)} + \overline{\frac{1}{2}\hat{v}_e\hat{i}_s sin(\omega t + \phi_e)sin(\omega t)}$$

$$= \underbrace{\overline{\frac{1}{4}v_{pn}\hat{i}_s sin(\omega t)}}_{=0} + \frac{1}{4}\hat{v}_e\hat{i}_s cos(\phi_e) - \underbrace{\overline{\frac{1}{4}\hat{v}_e\hat{i}_s cos(2\omega t + \phi_e)}}_{=0} \qquad (3.21)$$

Using (3.21) and (3.20), the dc link voltage of the lower arm equivalent voltage can be formulated as

$$\frac{1}{2}C\frac{d}{dt}(v_{\ell,k}^{dc})^2 = \frac{1}{4}v_{pn}\hat{i}_s sin(\omega t) - \frac{1}{4}\hat{v}_e\hat{i}_s cos(2\omega t + \phi_e) \qquad (3.22)$$

Then, $v_{\ell,k}^{dc}$ in steady state is calculated as

$$(v_{\ell,k}^{dc})^2 = (v_{\ell,k}^{dc*})^2 - \frac{1}{2\omega C}v_{pn}\hat{i}_s cos(\omega t) - \frac{1}{4\omega C}\hat{v}_e\hat{i}_s sin(2\omega t + \phi_e) \qquad (3.23)$$

The waveforms of the dc link voltage of the equivalent submodules for the upper and lower arm are expressed using (3.19) and (3.23).

3.3.3 With dc and ac Differential Currents

The existence of a differential current in the structure of the MMC-based PV system is a vital factor to maintain stable operation of the MMC-based PV system. An eigenvalue analysis can be beneficial in defining the stability limits of the converter with respect to the amount of uncontrolled differential current in the system. However, this analysis is not carried out in this thesis since it was not the objective of this work. The submodule capacitors have to be designed to withstand the voltage oscillations in presence of differential currents. There exist some oscillations on the dc link voltage of the submodules even when the arms carry only half of the terminal currents which stems from oscillatory nature of single phase power transfer. However, the presence of differential currents would change the magnitude and phase angle of the dc link voltage oscillations.

This section presents the mathematics to calculate the dc link voltage of the equivalent submodules in presence of differential currents.

The arms of the converter are represented with a single equivalent submodule for this study, as shown in Figure 3.5. The arm voltages are complemented with adding the differential voltage as

$$
\begin{aligned}
v_{u,k} &= \frac{1}{2}v_{pn} - v_{e,k} - v_{d,k} \\
v_{\ell,k} &= \frac{1}{2}v_{pn} + v_{e,k} - v_{d,k}
\end{aligned}
\tag{3.24}
$$

The currents of the arms are augmented with adding a dc and ac components. The arm currents are

$$
\begin{aligned}
i_{u,k} &= \frac{1}{2}i_{s,k} + i_{d,k} \\
i_{l,k} &= \frac{1}{2}i_{s,k} - i_{d,k}
\end{aligned}
\tag{3.25}
$$

The differential current is assumed to consist of a dc and an ac component. Consequently, it can be shown as

$$
\begin{aligned}
i_{d,k} &= i_{d,k}^{dc} + i_{d,k}^{ac} \\
&= i_{d,k}^{dc} + i_{d,k}^{\hat{ac}}sin(\omega t + \phi_{id})
\end{aligned}
\tag{3.26}
$$

where $i_{d,k}^{\hat{}}$ and ϕ_d are the magnitude of the differential current and its phase angle w.r.t the terminal voltage of the converter. The differential voltage can be shown as

$$
v_{d,k} = \hat{v}_{d,k}sin(\omega t + \phi_{vd})
\tag{3.27}
$$

Since the arm inductor and resistor are small, the voltage drop across arm impedance due to differential current, $v_{d,k}$, will be small and can be neglected. Multiplying the arm voltages and currents and following the procedure used in Section 3.3.2, yields the power

exchange at each arm as

$$
\begin{aligned}
p_{u,k}^{ac} = & -\overline{\left(\frac{1}{2}v_{pn} - \hat{v}_e sin(\omega t + \phi_e)\right)\left(\frac{1}{2}\hat{i}_s sin(\omega t) + i_{d,k}^{dc} + i_{d,k}^{\hat{ac}} sin(\omega t + \phi_{id})\right)} \\
= & -\underbrace{\overline{\frac{1}{4}v_{pn}\hat{i}_s sin(\omega t)}}_{=0} - \frac{1}{2}v_{pn}i_{d,k}^{dc} - \underbrace{\overline{\frac{1}{2}v_{pn}i_{d,k}^{\hat{ac}} sin(\omega t + \phi_{id})}}_{=0} + \frac{1}{4}\hat{v}_e\hat{i}_s cos(\phi_e) - \underbrace{\overline{\frac{1}{4}\hat{v}_e\hat{i}_s cos(2\omega t + \phi_e)}}_{=0} \\
& + \underbrace{\overline{\hat{v}_e i_{d,k}^{dc} sin(\omega t + \phi_e)}}_{=0} + \frac{1}{2}\hat{v}_e i_{d,k}^{\hat{ac}} cos(\phi_e - \phi_{id}) - \underbrace{\overline{\frac{1}{2}\hat{v}_e i_{d,k}^{\hat{ac}} cos(2\omega t + \phi_e + \phi_{id})}}_{=0} \qquad (3.28)
\end{aligned}
$$

According to (3.20), the dc link voltage dynamics of the upper arm equivalent submodule can be shown as

$$
\begin{aligned}
\frac{1}{2}C\frac{d}{dt}(v_{u,k}^{dc})^2 = & -\frac{1}{4}v_{pn}\hat{i}_s sin(\omega t) - \frac{1}{2}v_{pn}i_{d,k}^{\hat{ac}} sin(\omega t + \phi_{id}) - \frac{1}{4}\hat{v}_e\hat{i}_s cos(2\omega t + \phi_e) \\
& + \hat{v}_e i_{d,k}^{dc} sin(\omega t + \phi_e) - \frac{1}{2}\hat{v}_e i_{d,k}^{\hat{ac}} cos(2\omega t + \phi_e + \phi_{id}) \qquad (3.29)
\end{aligned}
$$

The dc link voltage of the upper arm equivalent submodule can be expressed as

$$
\begin{aligned}
(v_{u,k}^{dc})^2 = & (v_{u,k}^{dc*})^2 + \frac{1}{2\omega C}v_{pn}\hat{i}_s cos(\omega t) + \frac{1}{\omega C}v_{pn}i_{d,k}^{\hat{ac}} cos(\omega t + \phi_{id}) - \frac{1}{4\omega C}\hat{v}_e\hat{i}_s sin(2\omega t + \phi_e) \\
& - \frac{2}{\omega C}\hat{v}_e i_{d,k}^{dc} cos(\omega t + \phi_e) - \frac{1}{2\omega C}\hat{v}_e i_{d,k}^{\hat{ac}} sin(2\omega t + \phi_e + \phi_{id}) \qquad (3.30)
\end{aligned}
$$

The power exchange at the ac terminals of the lower arm equivalent submodule is given as

$$
\begin{aligned}
p_{\ell,k}^{ac} = & \left(\frac{1}{2}v_{pn} + \hat{v}_e sin(\omega t + \phi_e) - \hat{v}_{d,k} sin(\omega t + \phi_{vd})\right)\left(\frac{1}{2}\hat{i}_s sin(\omega t) - i_{d,k}^{dc} - i_{d,k}^{\hat{ac}} sin(\omega t + \phi_{id})\right) \\
= & \underbrace{\overline{\frac{1}{4}v_{pn}\hat{i}_s sin(\omega t)}}_{=0} - \frac{1}{2}v_{pn}i_{d,k}^{dc} - \underbrace{\overline{\frac{1}{2}v_{pn}i_{d,k}^{\hat{ac}} sin(\omega t + \phi_{id})}}_{=0} + \frac{1}{4}\hat{v}_e\hat{i}_s cos(\phi_e) - \underbrace{\overline{\frac{1}{4}\hat{v}_e\hat{i}_s cos(2\omega t + \phi_e)}}_{=0} \\
& - \underbrace{\overline{\hat{v}_e i_{d,k}^{dc} sin(\omega t + \phi_e)}}_{=0} - \frac{1}{2}\hat{v}_e i_{d,k}^{\hat{ac}} cos(\phi_e - \phi_{id}) + \underbrace{\overline{\frac{1}{2}\hat{v}_e i_{d,k}^{\hat{ac}} cos(2\omega t + \phi_e + \phi_{id})}}_{=0} \qquad (3.31)
\end{aligned}
$$

According to (3.20), the dc link voltage dynamics of the lower arm equivalent sub-

module can be expressed as

$$\frac{1}{2}C\frac{d}{dt}(v_{\ell,k}^{dc})^2 = \frac{1}{4}v_{pn}\hat{i}_s sin(\omega t) - \frac{1}{2}v_{pn}i_{d,k}^{\hat{ac}}sin(\omega t + \phi_{id}) - \frac{1}{4}\hat{v}_e\hat{i}_s cos(2\omega t + \phi_e)$$

$$- \hat{v}_e i_{d,k}^{dc}sin(\omega t + \phi_e) + \frac{1}{2}\hat{v}_e i_{d,k}^{\hat{ac}}cos(2\omega t + \phi_e + \phi_{id}) \qquad (3.32)$$

As a result, the dc link voltage of the lower arm equivalent submodule can be expressed as

$$(v_{\ell,k}^{dc})^2 = (v_{\ell,k}^{dc*})^2 - \frac{1}{2\omega C}v_{pn}\hat{i}_s cos(\omega t) + \frac{1}{\omega C}v_{pn}i_{d,k}^{\hat{ac}}cos(\omega t + \phi_{id}) - \frac{1}{4\omega C}\hat{v}_e\hat{i}_s sin(2\omega t + \phi_e)$$

$$+ \frac{2}{\omega C}\hat{v}_e i_{d,k}^{dc}cos(\omega t + \phi_e) + \frac{1}{2\omega C}\hat{v}_e i_{d,k}^{\hat{ac}}sin(2\omega t + \phi_e + \phi_{id}) \qquad (3.33)$$

The oscillations of the dc link voltage of the equivalent submodule with and without differential current is shown and compared in Figure 3.6. Introduction of differential currents does not increase the oscillations of the dc link voltages. Consequently, the dc link capacitors do not need to be augmented. Ac differential current is in phase with the terminal voltage of the converter in Figure 3.6 which is the reason that the oscillations of the upper arm and lower arm dc link voltages are different.

3.4   Proposed Power Mismatch Elimination Strategy

This section presents the proposed power mismatch elimination strategy which mitigates all the possible power mismatches presented in Section 3.2. As mentioned earlier, the submodule power mismatch is eliminated using the voltage balancing technique based on the sorting algorithm. However, the other two power mismatches need to be eliminated using the proposed power mismatch elimination strategy. Leg and arm power mismatch elimination method is thoroughly presented in the following sections.

The ultimate control objective for the MMC-based PV system is to deliver the aggregate power generated by the PV generators to the grid in such a way that symmetrical
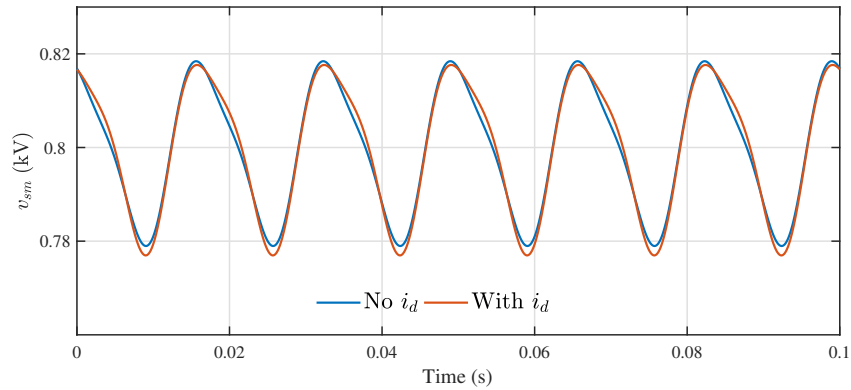
(a) Upper arm
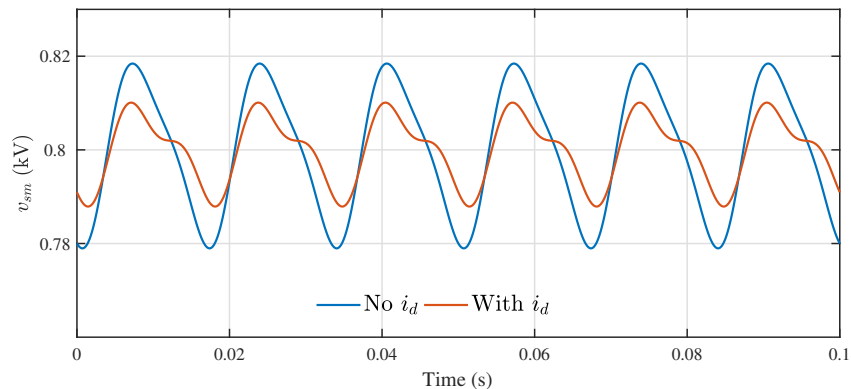
(b) Lower arm

Figure 3.6: Dc link voltage of the equivalent submodules

and balanced currents are injected into the grid. The fulfillment of this objective calls for the satisfaction of the following requirements:

1. Exactly one-third of the power produced by all the PV generators must flow through each phase of the PV system; and

2. The average power that leaves the ac-side terminals of each submodule must be equal to the aggregate power delivered by the PV generators of that submodule. This is fundamental in ensuring stabilization of the submodule dc voltages.

The control schemes presented in the following subsections satisfy the aforementioned requirements.

3.4.1   Leg Power Mismatch Elimination

For each phase of the PV system, requirement 1 of Section 3.4 can be translated mathematically to

$$
\underbrace{p_{u,k} + p_{\ell,k}}_{p_k} + p_k^{ex} =
$$

$$
\frac{1}{3}\left(\underbrace{p_{u,a} + p_{\ell,a}}_{p_a} + \underbrace{p_{u,b} + p_{\ell,b}}_{p_b} + \underbrace{p_{u,c} + p_{\ell,c}}_{p_c} \right) \qquad k = a, b, c
$$

(3.34)

where $p_k^{ex}(t)$ is a term that must be added to the aggregate power delivered by the submodules of arm k, in order to make the power flowing to the grid through phase k of the MMC equal to one-third of the power generated by all PV system submodules. The term is referred hereafter to as the *power mismatch* of leg k.

Defining

$$
p_{av}(t) = \frac{1}{3} \sum_{k=a,b,c} p_k^{dc}(t) \qquad k = a, b, c
$$

(3.35)

one can rewrite (3.34) in a more compact way as

$$
p_k^{ex}(t) = p_{av}(t) - p_k^{dc}(t) \qquad k = a, b, c
$$

(3.36)

Thus, based on (3.36), a positive $p_k^{ex}(t)$ means that the power delivered collectively by the PV generators (and hence by the two arms) of phase k is smaller than the average phase power and, therefore, power must be transferred from the other two phases to phase k. Similarly, a negative $p_k^{ex}(t)$ means that the arms of k deliver more power than the average phase power and, consequently, some power must be exported out of the leg. Since the only linkage (other than the grid) between the three legs of the MMC is through their common dc ports, the required inter-leg power transfers call for corresponding dc arm currents. In addition, since no dc current is permitted into the grid, the dc currents can

only be components of the differential currents (also known as the circulating currents) of the MMC. Thus, the dc differential current for each leg can be determined as

$$i_{d,k}^{dc*}(t) = \frac{p_k^{ex}(t)}{v_{pn}} \qquad k = a, b, c \tag{3.37}$$

As a requirement, the dc differential currents have to sum up to zero at nodes n and p. The sum of these currents at the common dc nodes is represented as

$$
\begin{aligned}
i_{d,a}^{dc*} + i_{d,b}^{dc*} + i_{d,c}^{dc*} &= \frac{p_a^{ex} + p_b^{ex} + p_c^{ex}}{v_{pn}} \\
&= \frac{3p_{av} - \overbrace{(p_a^{dc} + p_b^{dc} + p_c^{dc})}^{P_{PV}}}{v_{pn}} = 0
\end{aligned}
\tag{3.38}
$$

According to (3.35), the numerator of (3.38) is zero which means that the dc currents sum up to zero at both positive and negative nodes of the common dc link. Consequently, the dc differential current do not enter the grid.

3.4.2 Arm AC-DC Power Mismatch Elimination

This section addresses partial fulfillment of requirement 2 of Section 3.4. The scheme discussed in Section 3.5 complements that detailed in this section, for complete fulfillment of requirement 2.

With the dc link voltage of the submodules controlled at their nominal values, the submodules of each arm can be represented with a single equivalent submodule, as discussed in Section 3.3.1. The dc power injected into the dc side of the equivalent submodule is equal to the sum of the powers generated by the PV generators of each arm and the ac power leaving the equivalent submodule is equal to the sum of the ac powers leaving the ac sides of the submodules of each arm. With the dc differential current $i_{d,k}^{dc}$ introduced in Section 3.4.1, the ac power leaving the equivalent submodule can be formulated as

$$p_{u,k} \simeq -\overline{v_{u,k}i_{u,k}} = -\overline{(\frac{1}{2}v_{pn} - v_{e,k})(\frac{1}{2}i_{s,k} + i_{d,k}^{dc})}$$
$$= -\frac{1}{2}v_{pn}i_{d,k}^{dc} + \overline{\frac{1}{2}v_{e,k}i_{s,k}} \tag{3.39}$$

$$p_{\ell,k} \simeq \overline{v_{\ell,k}i_{\ell,k}} = \overline{(\frac{1}{2}v_{pn} + v_{e,k})(\frac{1}{2}i_{s,k} - i_{d,k}^{dc})}$$
$$= -\frac{1}{2}v_{pn}i_{d,k}^{dc} + \overline{\frac{1}{2}v_{e,k}i_{s,k}} \tag{3.40}$$

where overline denotes the average value, and $v_{e,k}$ is the so-called internal voltage of leg k:

$$v_{e,k} = \frac{-v_{u,k} + v_{\ell,k}}{2} \tag{3.41}$$

where $v_{u,k}$ and $v_{\ell,k}$ are the ac voltages of the upper and lower arm of phase k, respectively.

Comparing (3.39) and (3.40), one finds that the powers leaving the upper and lower arms are equal, however, a mechanism is needed to enable different power extraction from each arm of the converter. To fix the aforementioned issue, $i_{u,k}$ and $i_{\ell,k}$ can be supplemented by additional components in a process that is referred in this chapter to as the *arm ac-dc power mismatch elimination*. The supplementing current components, however, must be of the differential nature to not interfere with the grid current. Additionally, they cannot be dc, or they interfere with the leg power mismatch elimination process. Thus, let us denote this *ac differential current* by $i_{d,k}^{ac}$. Hence, (3.39) and (3.40) can be rewritten as

$$p_{u,k} \simeq -\overline{v_{u,k}i_{u,k}} = -\overline{(\frac{1}{2}v_{pn} - v_{e,k})(\frac{1}{2}i_{s,k} + i_{d,k}^{dc} + i_{d,k}^{ac})}$$
$$= -\frac{1}{2}v_{pn}i_{d,k}^{dc} + \overline{\frac{1}{2}v_{e,k}i_{s,k}} + \overline{v_{e,k}i_{d,k}^{ac}} \tag{3.42}$$

$$p_{\ell,k} \simeq \overline{v_{\ell,k}i_{\ell,k}} = \overline{(\frac{1}{2}v_{pn} + v_{e,k})(\frac{1}{2}i_{s,k} - i_{d,k}^{dc} - i_{d,k}^{ac})}$$
$$= -\frac{1}{2}v_{pn}i_{d,k}^{dc} + \overline{\frac{1}{2}v_{e,k}i_{s,k}} - \overline{v_{e,k}i_{d,k}^{ac}} \tag{3.43}$$

where the approximations indicated in (3.42) and (3.43) are due to the switching power losses of the submodules.

Subtracting (3.43) from (3.42), one finds

$$p_{d,k} = \frac{p_{u,k} - p_{\ell,k}}{2} \simeq \overline{v_{e,k} i_{d,k}^{ac}} \tag{3.44}$$

where $p_{d,k}(t)$ is called the *differential power* of leg k. Having lumped the submodules of each arm into one equivalent submodule, the power balance at the capacitor of the equivalent submodule can be written as

$$p_{u,k}^{C} = p_{u,k}^{dc} - p_{u,k} \tag{3.45}$$

$$p_{\ell,k}^{C} = p_{\ell,k}^{dc} - p_{\ell,k} \tag{3.46}$$

where $p_{u,k}^{C}$ and $p_{\ell,k}^{C}$ are the powers passing through the dc link capacitor of the equivalent submodules of the upper and lower arms, respectively. The terms $p_{u,k}^{dc}$ and $p_{\ell,k}^{dc}$ represent the aggregate dc power injected into the dc link of the equivalent submodule of the upper and lower arms, respectively.

The dc power injected into the dc link of the equivalent submodules and the ac power leaving the ac side of the equivalent submodules are required to be equal to maintain the stability of the dc link voltage. Applying this concept to (3.45) and (3.46) and substituting the power leaving the upper and lower arm submodules with (3.42) and (3.43), one finds

$$\left. \begin{array}{l} 0 = p_{u,k}^{dc} - p_{u,k} \\ 0 = p_{\ell,k}^{dc} - p_{\ell,k} \end{array} \right\} \Rightarrow p_{u,k}^{dc} - p_{\ell,k}^{dc} = \underbrace{p_{u,k} - p_{\ell,k}}_{2p_{d,k}} \tag{3.47}$$

As a result, in order to extract the injected dc power from the upper and lower arms, the differential powers has to be controlled at

$$p_{d,k} = \frac{p_{u,k}^{dc} - p_{\ell,k}^{dc}}{2} \tag{3.48}$$

It then follows from the assumed balanced operation that $v_{e,k}$ is a fundamental-frequency sinusoid. Therefore, in order for the right-hand side of (3.44) to have a non-zero value, $i_{d,k}^{ac}$ must also be a fundamental-frequency sinusoid. One constraint, however, is that the ac differential currents of the three legs must sum up to zero. It is reminded that, with respect to Figure 3.5, the grid and differential currents are related to the lower and upper arm currents as

$$i_{s,k} = i_{u,k} + i_{\ell,k} \tag{3.49}$$

$$i_{d,k} = \frac{i_{u,k} - i_{\ell,k}}{2} \tag{3.50}$$

where, based on the foregoing discussions, one has

$$i_{d,k} = i_{d,k}^{dc} + i_{d,k}^{ac} \tag{3.51}$$

To determine the three ac differential currents, one can regard them as the constituents of an unbalanced three-phase set of currents; the imbalance is due to the unequal values of $p_{d,a}$, $p_{d,b}$, and $p_{d,c}$. This, in conjunction with the fact that the three ac differential currents have a zero sum, enables the use of two-dimensional reference frames, e.g., the $\alpha\beta$ frame, for their formulation and control, thus reducing the number of the variables to be controlled. Hence, let us express the ac differential currents in terms of positive- and negative-sequence components as

$$
\begin{aligned}
i_{d,a}^{ac}(t) &= \hat{i}_d^1 \cos\left[\phi(t) + \phi_1\right] + \hat{i}_d^2 \cos\left[\phi(t) + \phi_2\right] \\
i_{d,b}^{ac}(t) &= \hat{i}_d^1 \cos\left[\phi(t) + \phi_1 - \frac{2\pi}{3}\right] + \hat{i}_d^2 \cos\left[\phi(t) + \phi_2 + \frac{2\pi}{3}\right] \\
i_{d,c}^{ac}(t) &= \hat{i}_d^1 \cos\left[\phi(t) + \phi_1 + \frac{2\pi}{3}\right] + \hat{i}_d^2 \cos\left[\phi(t) + \phi_2 - \frac{2\pi}{3}\right]
\end{aligned}
\tag{3.52}
$$

where $\hat{i}_d^1$ and $\hat{i}_d^2$ are the magnitudes of the positive- and negative-sequence components,

respectively, and ϕ_1 and ϕ_2 represent the phase-angles of the positive- and negative-sequence components relative to the internal voltage $v_{e,a}$, respectively. Let us also assume that

$$
\begin{aligned}
v_{e,a}(t) &= \hat{v}_e \cos\left[\phi(t)\right] \\
v_{e,b}(t) &= \hat{v}_e \cos\left[\phi(t) - \frac{2\pi}{3}\right] \\
v_{e,c}(t) &= \hat{v}_e \cos\left[\phi(t) + \frac{2\pi}{3}\right]
\end{aligned}
\tag{3.53}
$$

where $\phi(t)$ is the phase-angle of the space phasor associated with the positive-sequence balanced set $v_{e,abc}$, such that $d\phi/dt = \omega = 2\pi f$, where f is the grid frequency. Then, (3.44) takes the form

$$
\begin{aligned}
p_{d,a} &= \frac{\hat{v}_e \hat{i}_d^1}{2}\cos\phi_1 + \frac{\hat{v}_e \hat{i}_d^2}{2}\cos\phi_2 \\
p_{d,b} &= \frac{\hat{v}_e \hat{i}_d^1}{2}\cos\phi_1 + \frac{\hat{v}_e \hat{i}_d^2}{2}\cos(\phi_2 - \frac{2\pi}{3}) \\
p_{d,c} &= \frac{\hat{v}_e \hat{i}_d^1}{2}\cos\phi_1 + \frac{\hat{v}_e \hat{i}_d^2}{2}\cos(\phi_2 + \frac{2\pi}{3})
\end{aligned}
\tag{3.54}
$$

Despite the known values of $p_{d,k}$, the ac differential currents can still not be determined since the real differential power equations represented in (3.54) do not include terms $\hat{i}_d^1 \sin\phi_1$ and $\hat{i}_d^2 \sin\phi_2$. The reactive differential powers can be expressed as

$$
\begin{aligned}
q_{d,a} &= -\frac{\hat{v}_e \hat{i}_d^1}{2}\sin\phi_1 - \frac{\hat{v}_e \hat{i}_d^2}{2}\sin\phi_2 \\
q_{d,b} &= -\frac{\hat{v}_e \hat{i}_d^1}{2}\sin\phi_1 - \frac{\hat{v}_e \hat{i}_d^2}{2}\sin(\phi_2 - \frac{2\pi}{3}) \\
q_{d,c} &= -\frac{\hat{v}_e \hat{i}_d^1}{2}\sin\phi_1 - \frac{\hat{v}_e \hat{i}_d^2}{2}\sin(\phi_2 + \frac{2\pi}{3})
\end{aligned}
\tag{3.55}
$$

The needed terms are included in the expression of the differential reactive powers. However, if it is needed to control the reactive powers of each phase independently, six independent variables are needed while there exist only three independent variables in the

(3.54) and (3.55). This issue can be resolved by, for example, expressing the sum of the reactive powers that are exchanged with all MMC arms:

$$q_d = -\frac{3}{2}\hat{v}_e \hat{i}_d^1 \, sin\phi_1 \tag{3.56}$$

It then follows from (3.54) through (3.56) that

$$
\begin{bmatrix}
\hat{i}_d^1 cos\phi_1 \\
\hat{i}_d^1 sin\phi_1 \\
\hat{i}_d^2 cos\phi_2 \\
\hat{i}_d^2 sin\phi_2
\end{bmatrix}
=
\frac{2}{3\hat{v}_e}
\begin{bmatrix}
1 & 1 & 1 & 0 \\
0 & 0 & 0 & -1 \\
2 & -1 & -1 & 0 \\
0 & \sqrt{3} & -\sqrt{3} & 0
\end{bmatrix}
\begin{bmatrix}
p_{d,a} \\
p_{d,b} \\
p_{d,c} \\
q_d
\end{bmatrix}
\tag{3.57}
$$

With the measured values for the differential real powers, and an arbitrary value (e.g., zero) for q_d, the commands for the ac differential currents can be determined based on (3.57) as

$$i_{d,\alpha}^{ac*}(t) + j\, i_{d,\beta}^{ac*}(t) = \left[\hat{i}_d^1 \, cos\phi_1 + j\, \hat{i}_d^1 \, sin\phi_1\right] e^{j\phi(t)} + \left[\hat{i}_d^2 \, cos\phi_2 - j\, \hat{i}_d^2 \, sin\phi_2\right] e^{-j\phi(t)} \tag{3.58}$$

which can then be used to generate the three-phase commands $i_{d,a}^{ac*}(t)$, $i_{d,b}^{ac*}(t)$, and $i_{d,c}^{ac*}(t)$. The phase angle of the internal voltage of the MMC, $\phi(t)$, is calculated using the D- and Q-axis components which are generated by the current controller shown in Figure 3.9. Figure 3.7 illustrates the process of generating the ac differential current references using the differential real powers of the legs and sum of the differential reactive powers.

3.5   Submodule DC Voltage Regulation

Consider an MMC with only one submodule per each arm. Then, ignoring the power losses within the submodule, the arm ac-dc power mismatch elimination process described in Section 3.4.2 ensures the stability of the submodule dc voltage in a steady state, since it ensures zero power exchange with the capacitor. Even for this simplistic configuration, however, regulation of the dc voltages calls for an active feedback control, due to the power
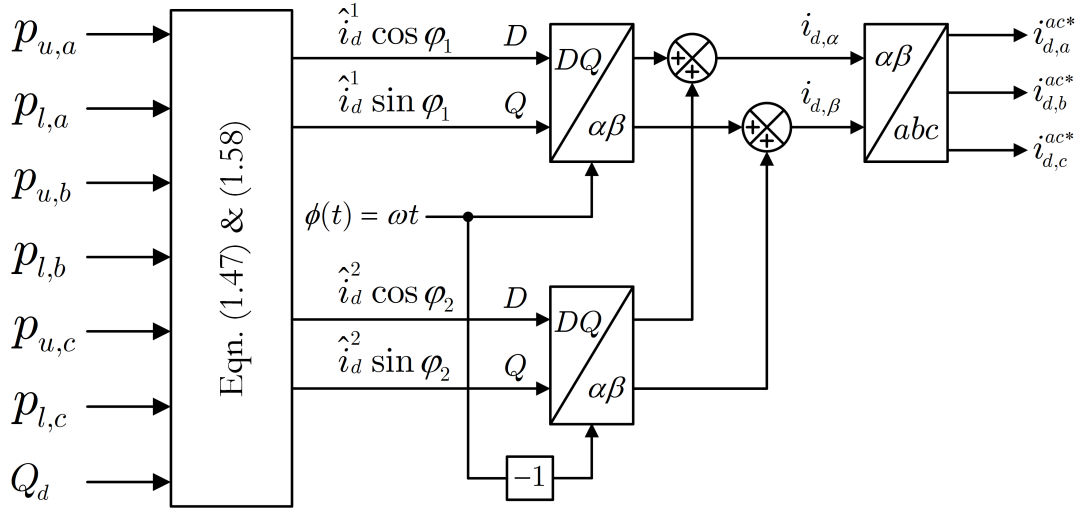
Figure 3.7: Scheme for generating reference ac differential currents.

losses and transient power imbalances. There is an additional difficulty with respect to an MMC with multiple submodules per arm: The arm ac-dc mismatch elimination process may not automatically translate into zero power exchange with all submodule capacitors (it only ensures that the aggregate PV power equals the aggregate real power which leaves the submodule ac-side ports), unless a dc-link voltage balancing algorithm is used to control the dc link voltage of the submodules at their reference. Voltage sorting algorithm presented in Section 2.6.4 is used to regulate the dc link voltage of the submodules. The voltage sorting algorithm sorts the voltages of the dc link of the submodules in each arm. Then, in case of a positive arm current, the required number of submodules with the lowest voltages are switched on. In case of a negative arm current, the required number of submodules with the highest voltages are switched on. This method ensures continuous regulation of the dc link voltage of the submodules of the MMC. The required number of submodules to be switched on is determined using phase-shifted pulse width modulation (PS-PWM) technique, as presented in Section 2.7.3.

3.6 Current Control

As discussed in Sections 3.4.1 and 3.4.2, the power mismatch elimination strategy proposed in this chapter requires controlling the dc and ac differential currents, for the

purposes of leg and arm power mismatch elimination, respectively. In addition, as is also the case with a conventional three-phase grid-connected VSC system, the three-phase current injected into the host grid must be controlled, to in turn enable the control of the real and reactive powers exchanged with the grid, p_s and q_s (see Figure 3.5). The following two subsections present the schemes for controlling the differential and grid currents, respectively.

3.6.1   Differential Current Control Scheme

Regarding node "0", that is the fictitious dc-side midpoint of the MMC, as the potential reference node and applying KVL from nodes p and n towards node s, one finds

$$\frac{v_p - v_n}{2} - L\frac{di_{u,k}}{dt} - Ri_{u,k} - v_{u,k} = v_{s,k} \tag{3.59}$$

$$-\frac{v_p - v_n}{2} - L\frac{di_{\ell,k}}{dt} - Ri_{\ell,k} + v_{\ell,k} = v_{s,k} \tag{3.60}$$

Subtracting (3.60) from (3.59), one finds the relationship between the differential current and the differential voltage, as

$$L\frac{di_{d,k}}{dt} + Ri_{d,k} = v_{d,k} \tag{3.61}$$

where $i_{d,k}$ is given by (3.51), and

$$v_{d,k} = \frac{v_p - v_n}{2} - \frac{v_{u,k} + v_{\ell,k}}{2} \tag{3.62}$$

Equation (3.61) indicates that the differential currents can be controlled by voltage $v_{d,k}$. Thus, as Figure 3.8 shows, for each leg, a corresponding compensator processes the difference between the differential current and its command, $i_{d,k}^*$, and determines $v_{d,k}^*$, that is the desired value for $v_{d,k}$. Figure 3.8 presents a block diagram of the three-
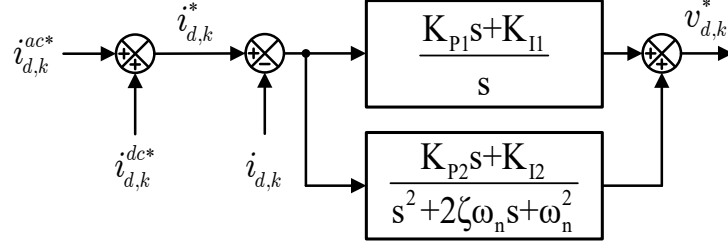
Figure 3.8: Block diagram of the scheme for controlling the differential currents.

channel control scheme since one such controller is needed for each leg of the converter.

3.6.2 Grid Current Control Scheme

Adding (3.59) and (3.60), and eliminating $i_{s,k}$ between the result and (3.49), one obtains

$$\frac{L}{2}\frac{di_{s,k}}{dt} + \frac{R}{2}i_{s,k} = v_{e,k} - v_{s,k} \tag{3.63}$$

where $v_{e,k}$ and $i_{s,k}$ are given by (3.41) and (3.49).

Equation (3.63) constitutes a basis for the control of $i_{s,k}$ by $v_{e,k}$, regarding the grid voltage $v_{s,k}$ as a disturbance signal. The control is most conveniently performed in a rotating reference frame (i.e., a DQ frame) whose direct axis is aligned by a phase-locked loop with the space phasor associated with the grid voltage. The outputs of the grid current control scheme are the commands $v_{e,D}^*$ and $v_{e,Q}^*$, which are transformed to the three-phase commands $v_{e,k}^*$. Then, the arm voltage commands for each leg are produced from $v_{e,k}^*$ and $v_{d,k}^*$, based on (3.41) and (3.62), and delivered to the switching schemes of the submodules. Thus,

$$v_{u,k}^* = \tfrac{1}{2}v_{pn} - v_{d,k}^* - v_{e,k}^* \tag{3.64}$$

$$v_{\ell,k}^* = \tfrac{1}{2}v_{pn} - v_{d,k}^* + v_{e,k}^* \tag{3.65}$$

Figure 3.9 shows the block diagram of the grid current control scheme. The command
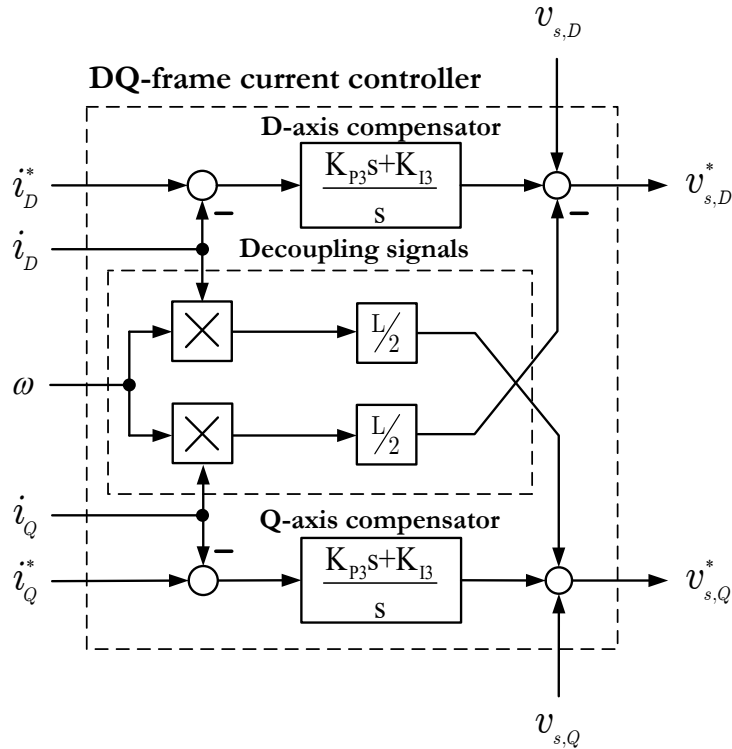
Figure 3.9: Block diagram of the scheme for grid current control.

i_Q^* can be used for reactive power control or, alternatively, it can be produced by a controller for grid ac voltage control. In contrast, i_D^* is calculated from the real power command, p_s^*. In turn, p_s^* is produced by the *virtual dc-link voltage regulation scheme* which is described in the next section.

3.7   Virtual DC-Link Voltage Regulation Scheme

Stable operation of the MMC-based PV system also requires that the right amount of real power is delivered to the host grid, such that the power balance is maintained in both steady-state and transient regimes. This objective is achieved by a virtual dc-link voltage regulation scheme whose function is to produce the command p_s^*. In other words, this scheme is intended to generated a reference real power for the converter that results in power balance between the aggregate generated PV power and the real power delivered to the host grid.

Ignoring the power losses of the DAB converters and half-bridge converters, the dc

voltage dynamics for each submodule of the MMC are governed by

$$\frac{1}{2}C\frac{d}{dt}(v_{sm,jk}^{dc}(t))^2 = p_{sm,jk}^{dc}(t) - p_{sm,jk}^{ac}(t) \tag{3.66}$$

Assuming equal capacitance for all submodule capacitors, (3.66) is lumped into

$$\frac{1}{2}C\frac{d}{dt}v_{dcf}^2(t) =$$
$$\underbrace{\sum_{k=a,b,c}\sum_{j=1}^{2N}p_{sm,jk}^{dc}(t)}_{\simeq p_{PV}} - \underbrace{\sum_{k=a,b,c}\sum_{j=1}^{2N}p_{sm,jk}^{ac}(t)}_{\simeq p_s} \tag{3.67}$$

where

$$v_{dcf}^2(t) = \sum_{k=a,b,c}\sum_{j=1}^{2N}(v_{sm,jk}^{dc}(t))^2 \tag{3.68}$$

Thus, variable $v_{dcf}(t)$ can be regarded as a virtual dc-link voltage for the MMC. Thus, (3.67) describes the dynamics of $v_{dcf}^2(t)$ in terms of the aggregate power generated by the PV panels, p_{PV}, and the real power that the PV system delivers to the grid, p_s. Equation (3.67) then forms a basis for the regulation of $v_{dcf}^2(t)$ at its reference value, v_{dcf}^{2*}, while p_{PV} acts as a disturbance signal. Thus the difference between $v_{dcf}^2(t)$ and v_{dcf}^{2*} is processed by a compensator whose output is p_s^* and delivered to the grid current control scheme of Section 3.6.2. The parameters of the compensator can be determined using the techniques employed for the conventional VSC, and are not discussed here. Regulation of $v_{dcf}^2(t)$ at a constant setpoint will, based on (3.67), result in $p_s \simeq p_{PV}$, which is the ultimate goal of the PV system. The variable v_{dcf}^{2*} is assigned a value of $6N(v_{sm,jk}^{dc*})^2$.

3.8   Simulation Results

To demonstrate the effectiveness of the proposed control, the MMC-based system is simulated in PSCAD/EMTDC software environment, and a selection of the results are

Table 3.1: Parameters of the MMC and grid

Parameter	Value	Parameter	Value
L	$3\,mH$	ζ	0.05
R	$0.1\,\Omega$	K_{P1}	3
L_g	$750\,\mu H$	K_{I1}	100
R_g	$60\,m\Omega$	K_{P2}	100
C	$10\,mF$	K_{I2}	1
f	$60\,Hz$	K_{P3}	1.5
ω_n	$2\pi \times 60$	K_{I3}	50
f_s	$6.3\,kHz$		

presented in this Section. To allow for faster simulations, the DAB converters are represented by controllable sources and the half-bridge converters are represented by their actual switches with on and off states. In its each arm, the simulated PV system has 10 submodules (N = 10), each with a power rating of 100 kW, and with its dc voltage reference set to 0.8 kV. Also, to keep the simulation model tractable, one DAB converter and one aggregated PV generator model are used in each submodule (i.e., n = 1). The aggregate PV model is based on 3 parallel-connected strings of 23 series-connected panels (i.e., 69 panels in total) of the Kyocera KU330-8BCA type; each panel generates 330 W under standard testing condition (STC). In each submodule, the DAB exercises the perturb and observe (P&O) MPPT algorithm. The grid voltage is 4.16 kV (line-to-line, rms). The switching frequency of the arms of the MMC is 6.3 kHz which corresponds to average 630 Hz for each submodule. Table 3.1 lists the other parameters. Proportional coefficients K_{P1} and K_{P1}, and integral coefficients K_{I1} and K_{I1} are designed based on system performance without a systematic approach. However, K_{P3} and K_{I3} are designed according to procedure presented in [51].

(a) Dc power of the arms of leg a

(b) Differential current of leg a

(c) Dc power of the arms of leg b

(d) Differential current of leg b

(e) Dc power of the arms of leg c

(f) Differential current of leg c
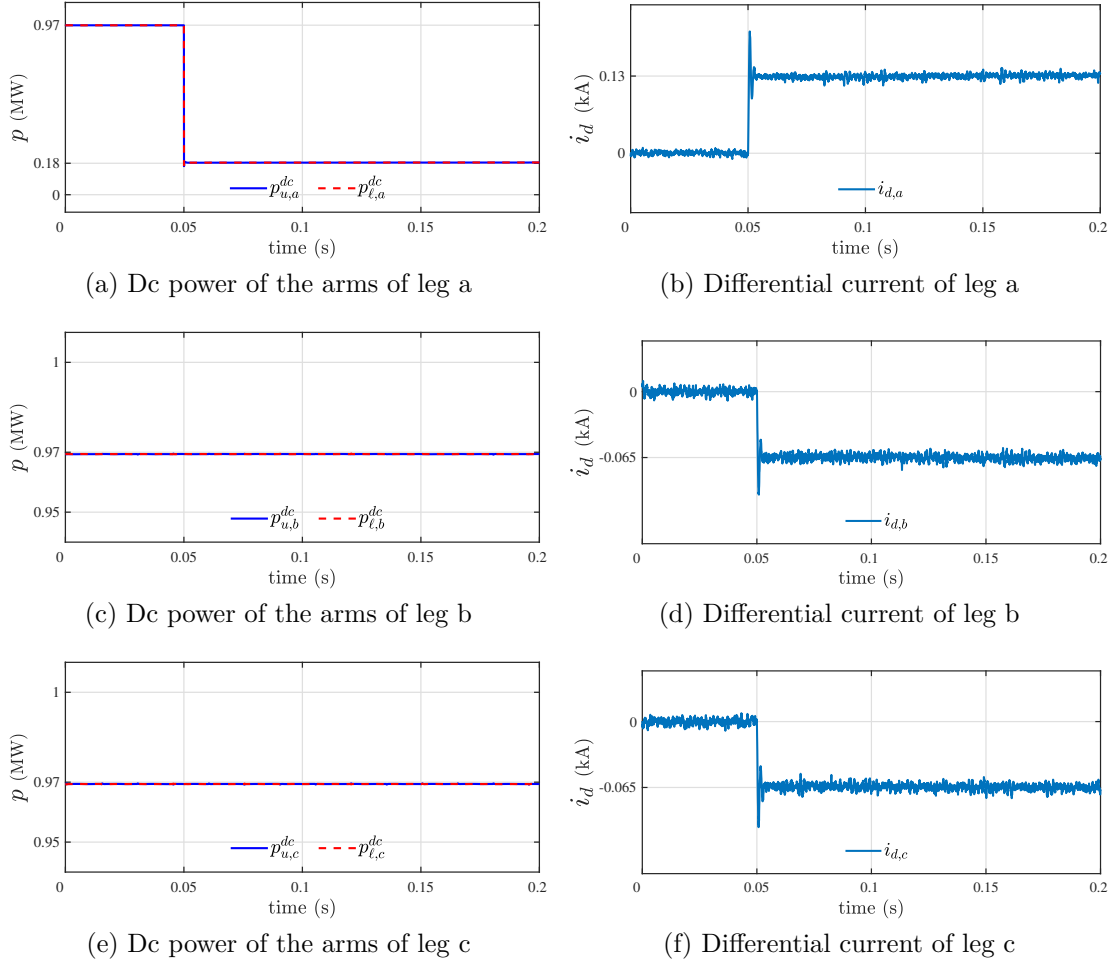
Figure 3.10: Response to leg power mismatch (case 1)

3.8.1 Case 1: Power Mismatch in the Legs

This case demonstrates the performance of the proposed power mismatch elimination strategy in presence of power mismatch between the legs of the MMC. Thus, initially the PV generators are all subjected to STC (solar irradiation $1000\,\mathrm{W/m^2}$ and temperature $25\,^{\circ}\mathrm{C}$). Then, at $\mathrm{t} = 0.05\,\mathrm{s}$, the solar irradiation of the PV generators of leg a is stepped from $1000\,\mathrm{W/m^2}$ to $200\,\mathrm{W/m^2}$. Consequently, subsequent to the disturbance, the power generated by the PV generators of leg a is reduced from $1.94\,\mathrm{MW}$ to $0.37\,\mathrm{MW}$, as Figure 3.10(a), (c), and (e) show. Thus, the control produces a dc differential current to transfer power from the two other legs; Figure 3.10(b), (d), and (f) show the waveforms of the
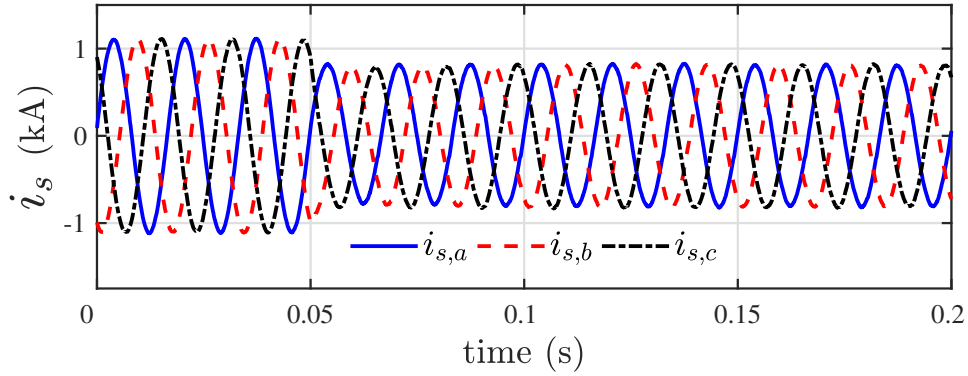
(a) Grid currents
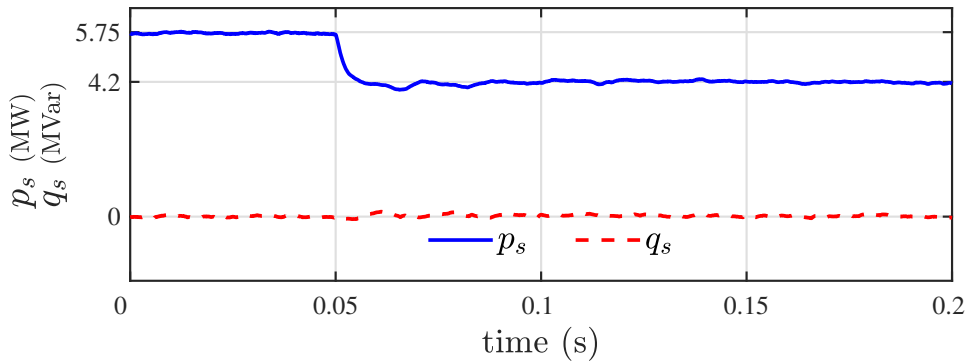
(b) Real and reactive power

Figure 3.11: Grid currents, real, and reactive power of the system in presence of leg power mismatch (case 1)

differential currents. The outcome is that the current injected into the grid retains its balance, as Figure 3.11(a) illustrates. As Figure 3.11(b) shows, due to the solar irradiation drop for the PV generators of leg a, the real power output of the PV system decreases from 5.7 MW to 4.16 MW, whereas the reactive power output remains unchanged at zero.

Figure 3.12 shows the currents of the arms of the converter following the power decline in phase a. The ac component of the currents of three legs of the converter become equal following the leg power mismatch at leg a. Consequently, the current that is injected into the grid remains balanced and symmetrical since it is the sum of the currents of the upper and lower arm current of each leg. The dc components of the leg currents are shown in Figure 3.12 from which it can be deducted that leg a currents have positive dc component while the currents of the other two legs have negative dc components.

(a) Upper arm of phase a

(b) Lower arm of phase a

(c) Upper arm of phase b

(d) Lower arm of phase b

(e) Upper arm of phase c

(f) Lower arm of phase c
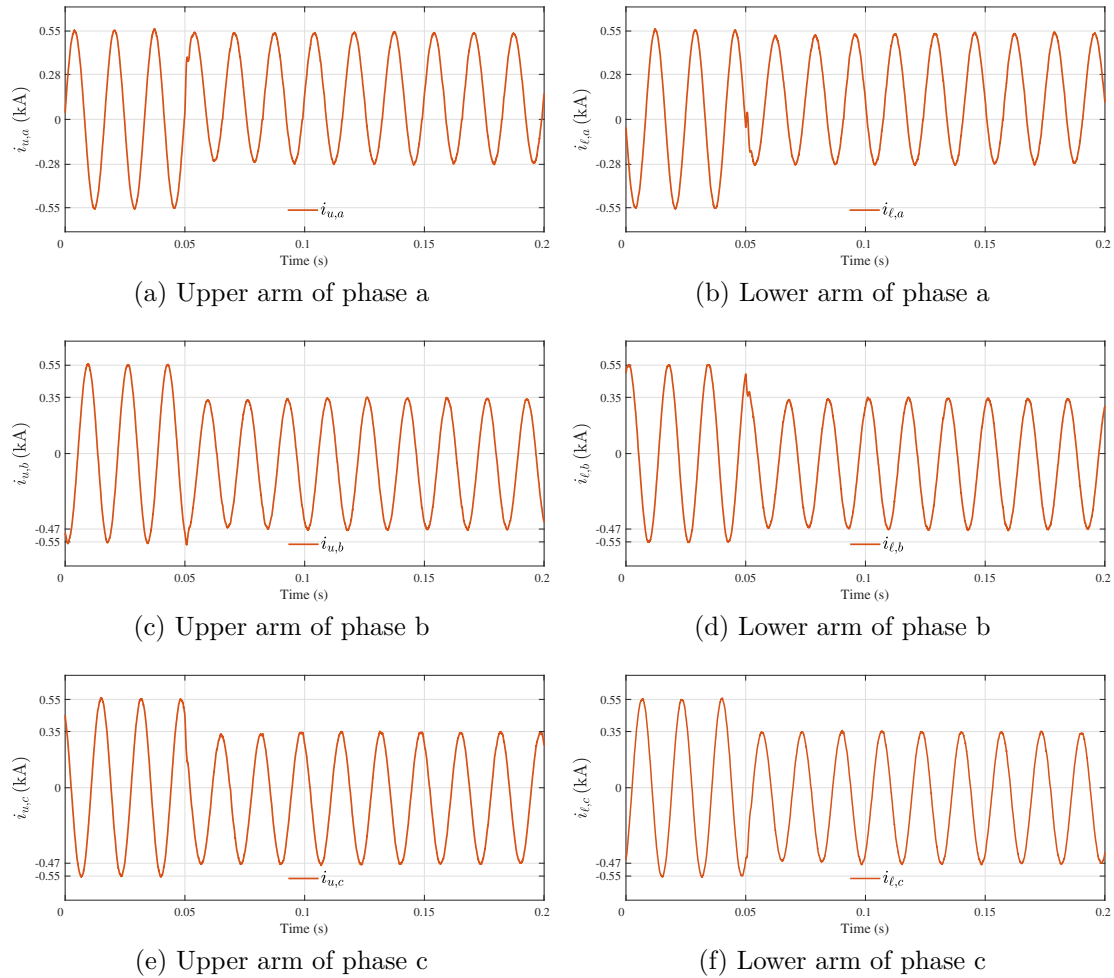
Figure 3.12: Currents of the arms of the converter (case 1)

Dc link voltage of the submodules of the system is the main indicator of the stability of the system following a power mismatch. As a result, the dc link voltages have to be evaluated to ensure they are regulated at their reference voltage by the voltage balancing algorithm. Figure 3.13 shows one sample dc link voltage from each arm of the converter.

As shown in Figure 3.13, the dc link voltage of the submodules experience some disturbance following the power mismatch. However, the voltage sorting algorithm ensures that they are regulated at their reference voltage which is $0.8\,\text{kV}$. The dc link voltage oscillations become smaller following the irradiation reduction because the overall power being generated by the PV generators become smaller than before. Consequently, the magnitude of the arm currents become smaller which results in lower submodule dc link

(a) Upper arm of phase a

(b) Lower arm of phase a

(c) Upper arm of phase b

(d) Lower arm of phase b

(e) Upper arm of phase c

(f) Lower arm of phase c
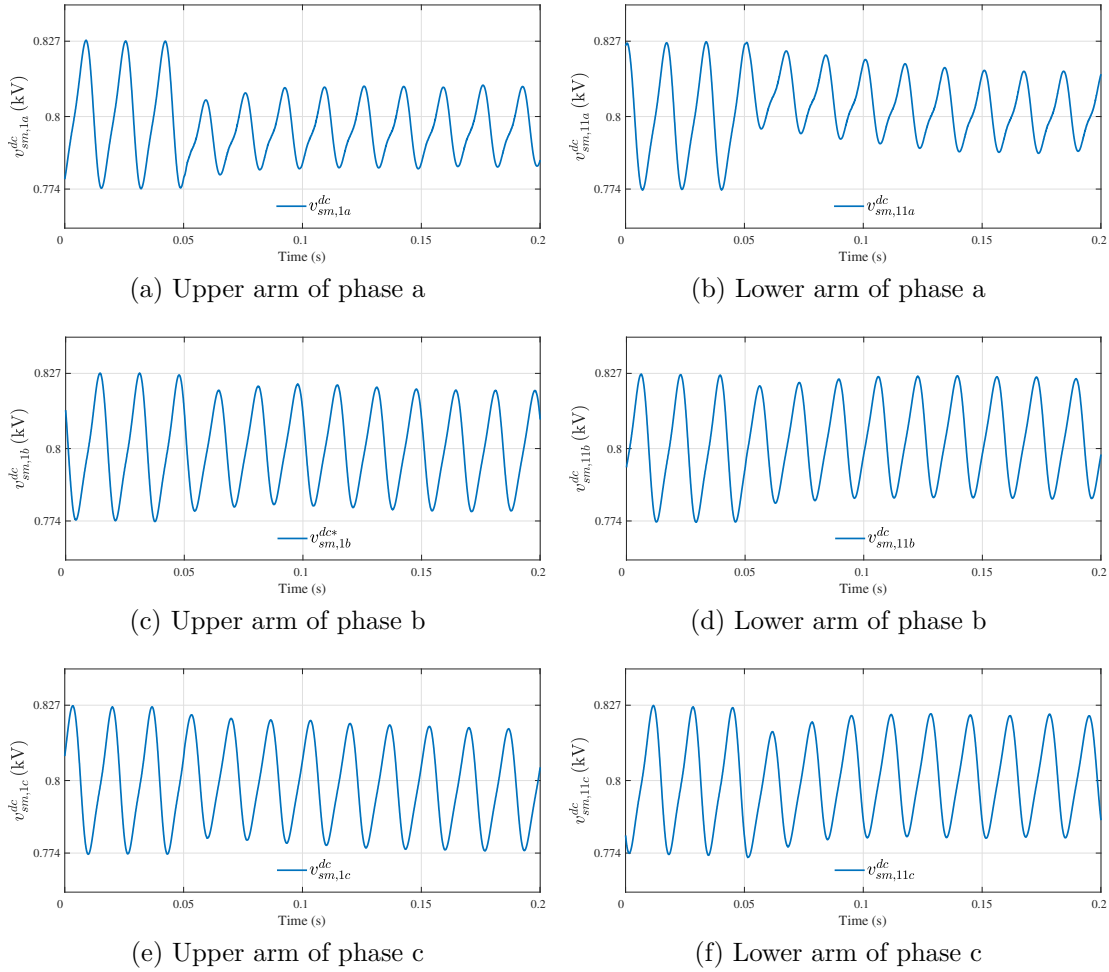
Figure 3.13: Dc link voltage of sample submodules (case 1)

voltage oscillations.

This case study shows the proposed power mismatch elimination strategy is effective in eliminating leg power mismatches. Regardless of the power mismatches, the MMC-based PV system ensures that balanced currents are injected into the grid.

3.8.2   Case 2: Arm Power Mismatch

This case presents the response of the proposed power mismatch elimination strategy to an arm power mismatch. Thus, initially the PV generators are subjected to STC. Then, at $t = 0.05$ s, an arm power mismatch is created for leg a, by decreasing the irradiation of the

(a) Dc power of the arms of leg a

(b) Differential current of leg a

(c) Dc power of the arms of leg b

(d) Differential current of leg b

(e) Dc power of the arms of leg c

(f) Differential current of leg c
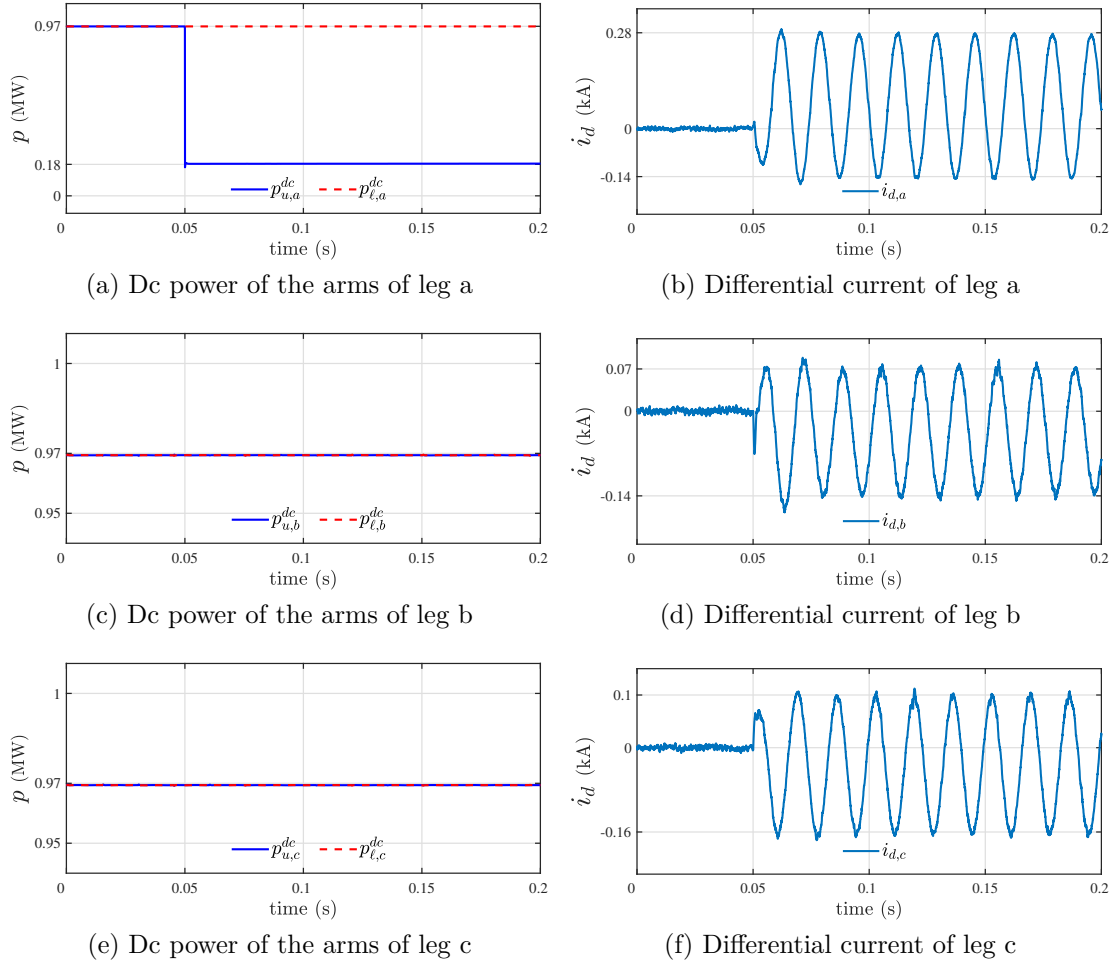
Figure 3.14: Response to arm power mismatch (case 2)

PV generators of the upper arm of the leg, from $1000\,\mathrm{W/m^2}$ to $200\,\mathrm{W/m^2}$. Consequently, the power output of the upper arm PV generators drops from $0.97\,\mathrm{MW}$ to $0.18\,\mathrm{MW}$, whereas the power output of the lower arm PV generators remains unchanged, as Figure 3.14(a) shows. Additionally, as shown in Figures 3.14(c) and (e), the powers generated by the PV generators of the other two legs remain intact. This situation also results in a leg power mismatch. To maintain the balance of the grid currents, therefore, the control responds by producing both dc and ac differential currents in each leg of the MMC, as Figures 3.14(b), (d), and (f) illustrate. Hence, as Figure 3.15(a) shows, the currents injected into the grid remain sinusoidal and balanced, but their magnitudes decline since the overall PV power generation has dropped. Figure 3.15(b) shows the waveforms of

(a) Grid currents

(b) Real and reactive power
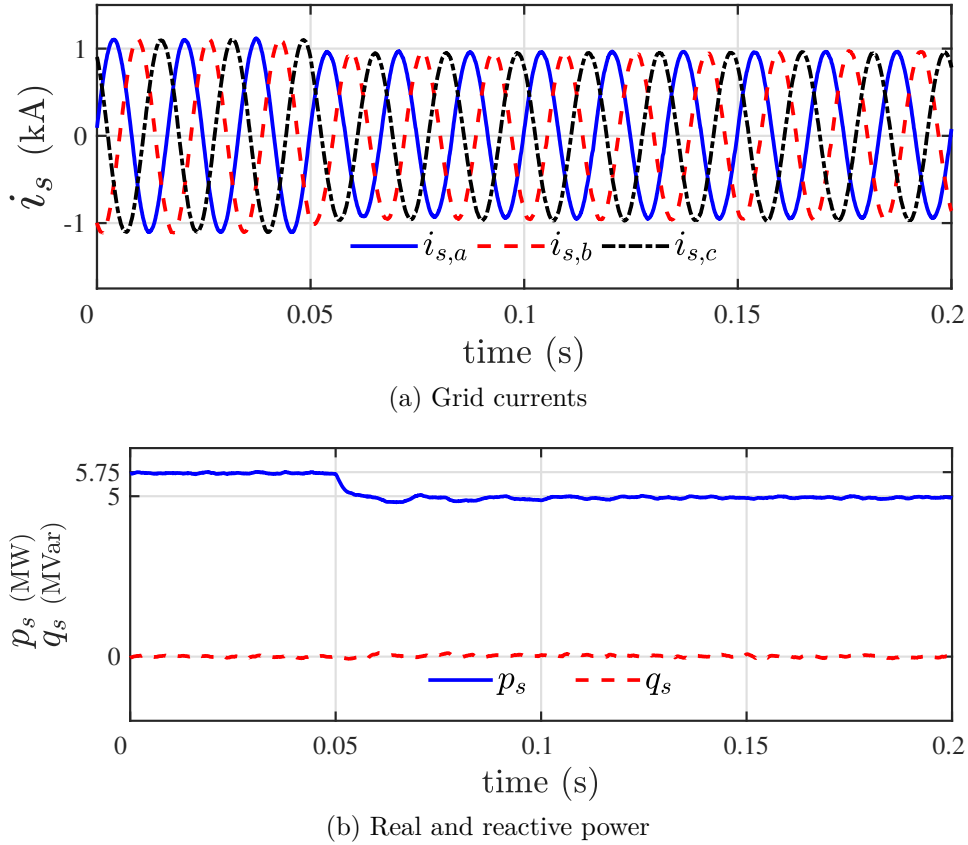
Figure 3.15: Grid currents, real, and reactive power of the system in presence of arm power mismatch (case 2)

the real and reactive powers delivered to the grid. It is observed that, subsequent to the disturbance at $t = 0.05\,\text{s}$, the real power drops to about $5\,\text{MW}$, while the reactive power remains regulated at zero.

The currents of the arms of the converter are manipulated by the proposed power mismatch elimination strategy to extract all the power injected to each leg. The powers delivered to the arms of the converter are different in this case study. As a result, arm currents are required to have an ac component which ensures right amount of power is extracted from each arm of the converter. Figure 3.16 shows the current of each arm of the converter. Following the irradiation decline in the upper arm of leg a, the magnitude of the current of this arm becomes smaller, as shown in Figure 3.16(a), which means less power is extracted from this arm since the power delivered to this arm has declined. Meanwhile, the magnitude of the current of the lower arm of leg a is increased as shown

(a) Upper arm of phase a (b) Lower arm of phase a

(c) Upper arm of phase b (d) Lower arm of phase b

(e) Upper arm of phase c (f) Lower arm of phase c
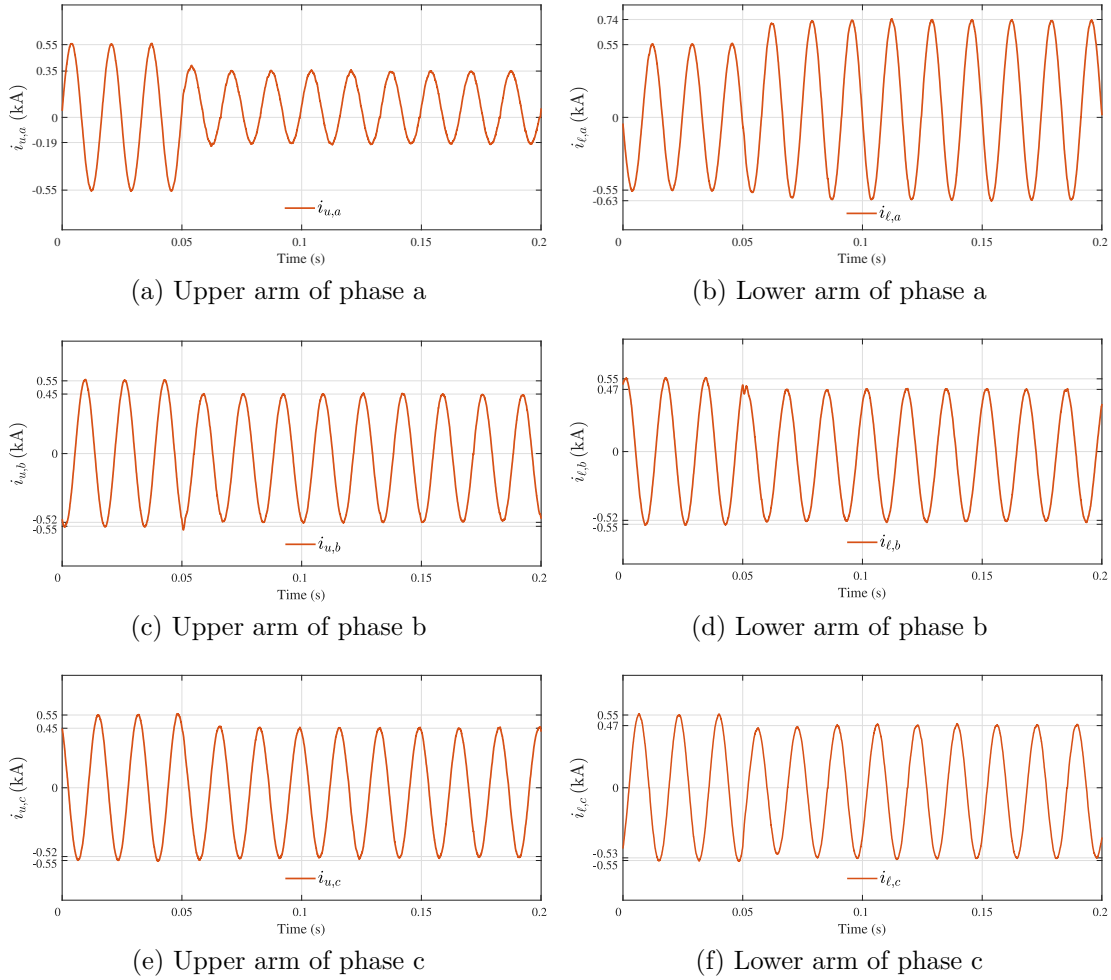
Figure 3.16: Currents of the arms of the converter (case 2)

in 3.16(b). The sum of the currents of the upper an lower arm of leg a is equal to that of the other two legs since the currents injected into the grid are balanced.

To ensure the stability of the dc link voltage of the submodules, one sample dc link voltage of each arm is shown in Figure 3.17. Since the magnitude of the oscillations of the dc link voltage of the submodules depends on the amount of power delivered to their dc link, the oscillations of the dc link voltage of the upper arm of leg a is reduced, as shown in Figure 3.17(a), since the power delivered to the submodules of the upper arm of leg a is reduced. However, the oscillations of the dc link voltage of the submodules of the lower arm of leg a is increased, as shown in Figure 3.17(b), which is due to presence

(a) Upper arm of phase a

(b) Lower arm of phase a

(c) Upper arm of phase b

(d) Lower arm of phase b

(e) Upper arm of phase c

(f) Lower arm of phase c
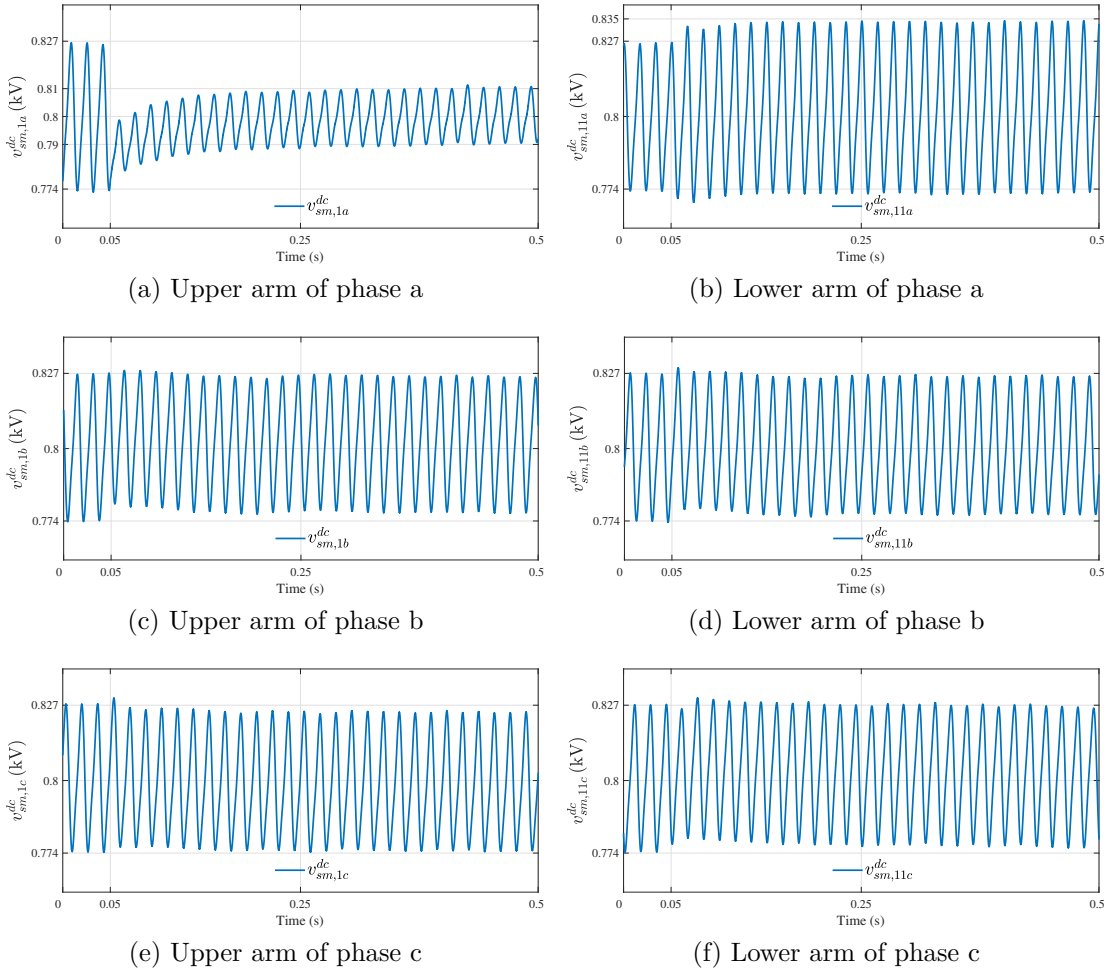
Figure 3.17: Dc link voltage of sample submodules (case 2)

of the ac differential currents in the system.

3.8.3   Case 3: Simultaneous Leg and Arm Power Mismatches

For this case, the PV generators are initially subjected to STC. Then, at $t = 0.05\,s$, the solar irradiation to the PV generators of leg a steps down and causes their power outputs to drop from $0.97\,MW$ to $0.18\,MW$. At $t = 0.15\,s$, the solar irradiation to the PV generators of the upper arm of leg b also decreases, thus causing the power generation of the arm (and, consequently, also that of the leg) to drop by about $0.49\,MW$. At $t = 0.25\,s$, the solar irradiation to the PV generators of the upper arm of leg c also experiences a stepwise decline, which results in $0.79\,MW$ of reduction in the power output of the arm
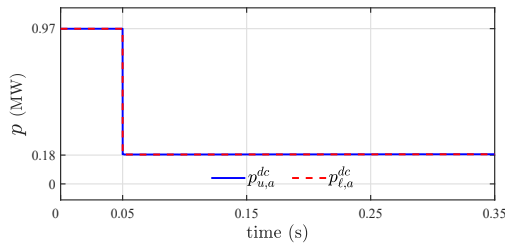
(a) Dc power of the arms of leg a
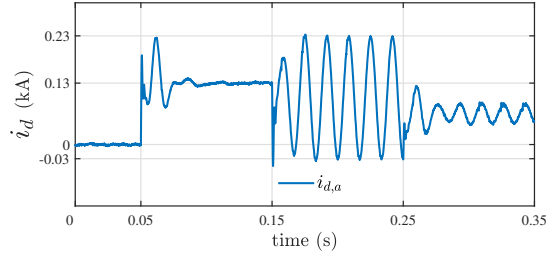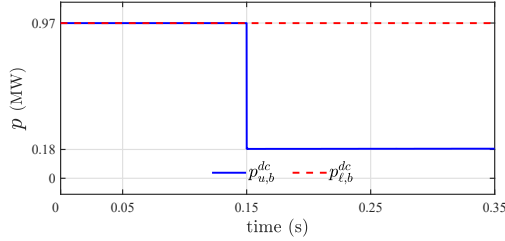
(b) Differential current of leg a

(c) Dc power of the arms of leg b

(d) Differential current of leg b

(e) Dc power of the arms of leg c

(f) Differential current of leg c

Figure 3.18: Response to simultaneous arm and leg power mismatches (case 3)

(and the leg).

Figures 3.18(a), (c), and (e) show the aggregate power generated by the PV generators of the legs of the converter, and the responses of proposed power mismatch elimination strategy are captured in Figures 3.18(b), (d), and (f). Thus, it is observed that the leg power mismatch at $t = 0.05\,\mathrm{s}$ prompts the control to generate dc differential currents. Then, during the period between $t = 0.15\,\mathrm{s}$ and $t = 0.25\,\mathrm{s}$, the arm power mismatch in leg b results in development of ac differential currents, as well as changes in the dc differential currents. The reason is that an arm power mismatch also causes a leg power mismatch. Similarly, the arm power mismatch in leg c at $t = 0.25\,\mathrm{s}$ leads to changes in both the ac and dc differential currents, as Figures 3.18(b), (d), and (f) show.

(a) Grid currents

(b) Real and reactive power
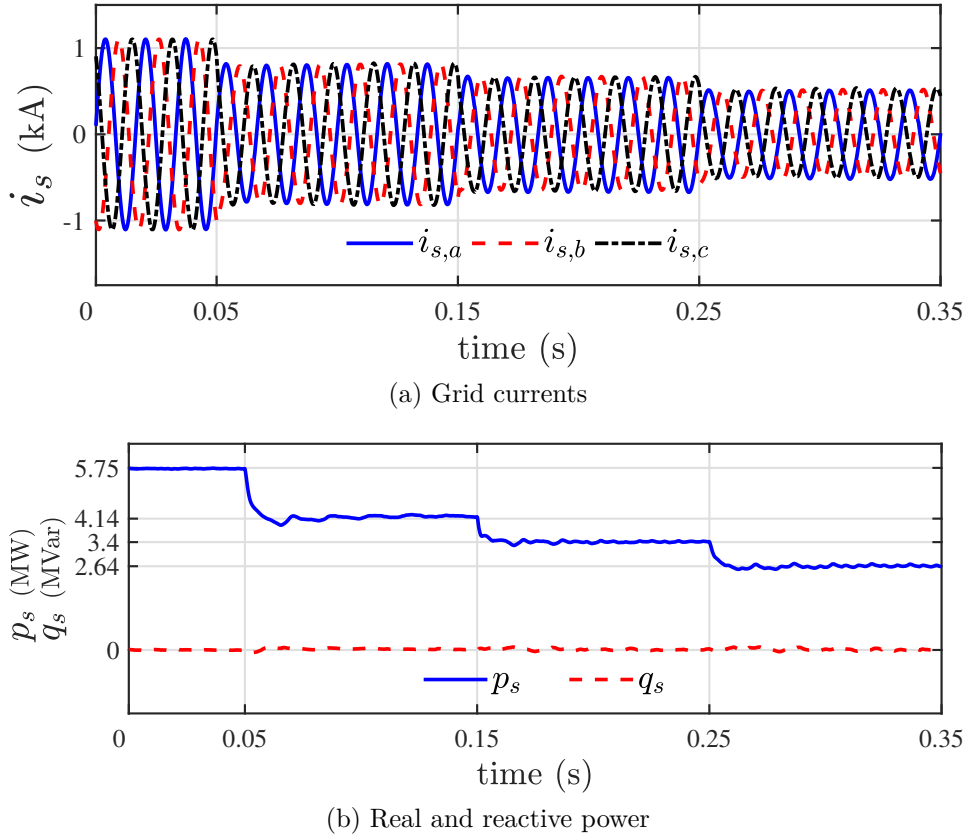
Figure 3.19: Grid currents, real, and reactive power of the system in presence of arm and leg power mismatches (case 3)

In spite of the aforementioned power mismatches, however, the currents injected into the grid remain balanced and sinusoidal, as Figure 3.19(a) demonstrates. Figure 3.19(b) shows that the real power output of the PV system drops after each solar irradiation drop, while the reactive power output remains regulated at zero.

Figure 3.20 shows the arm currents of the MMC-based PV system in presence of simultaneous arm and leg power mismatches. The differential current generated by the proposed power mismatch elimination strategy consists of dc and ac components that are required to eliminate the leg and arm power mismatches, respectively. Following the leg power mismatch at $t = 0.05\,\text{s}$, the currents of the arms decrease to transfer less power to the grid since the aggregate power generated by the PV generators is declined. At $t = 0.15\,\text{s}$, the power generated by the PV generators of the upper arm of leg b is

(a) Upper arm of phase a

(b) Lower arm of phase a

(c) Upper arm of phase b

(d) Lower arm of phase b

(e) Upper arm of phase c

(f) Lower arm of phase c
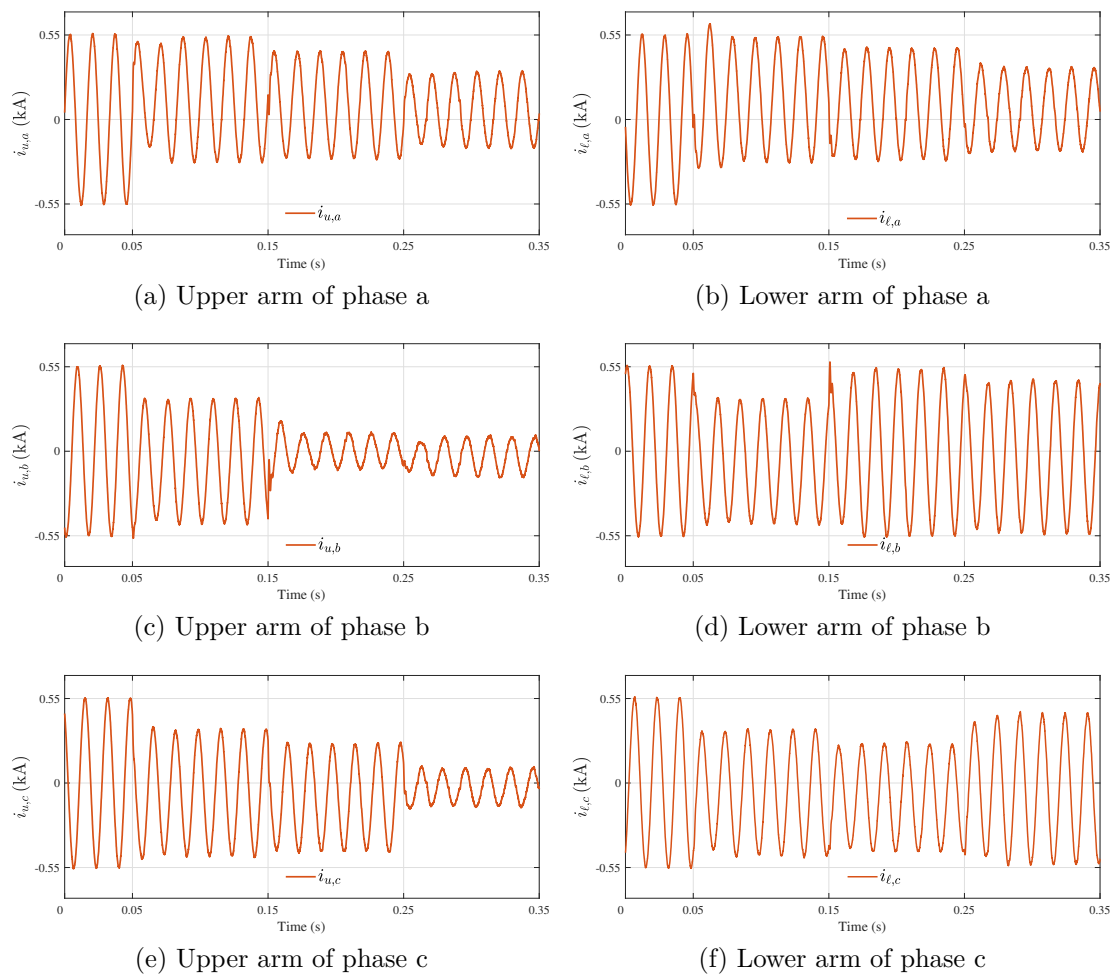
Figure 3.20: Currents of the arms of the converter (case 3)

decreased which leads to reduction of the magnitude of the current of the arm to extract less power from the arm. Less power extraction from the arm leads to stable operation of the dc link of the submodules of the arm. An arm power mismatch happens in leg c at $t = 0.25$ s that reduces the current of the upper arm of leg c, as shown in Figure 3.20(e).

The main indication of the stability of the converter is the dc link voltage of the submodules. As a results, one sample dc link voltage from each arm of the system is shown in Figure 3.21. The magnitude of the oscillations of the dc link voltage of the submodule depends on the amount of the power processed by the submodule. Consequently, the oscillations of the dc link voltage of the submodules with higher power yield is higher

(a) Upper arm of phase a

(b) Lower arm of phase a

(c) Upper arm of phase b

(d) Lower arm of phase b

(e) Upper arm of phase c

(f) Lower arm of phase c
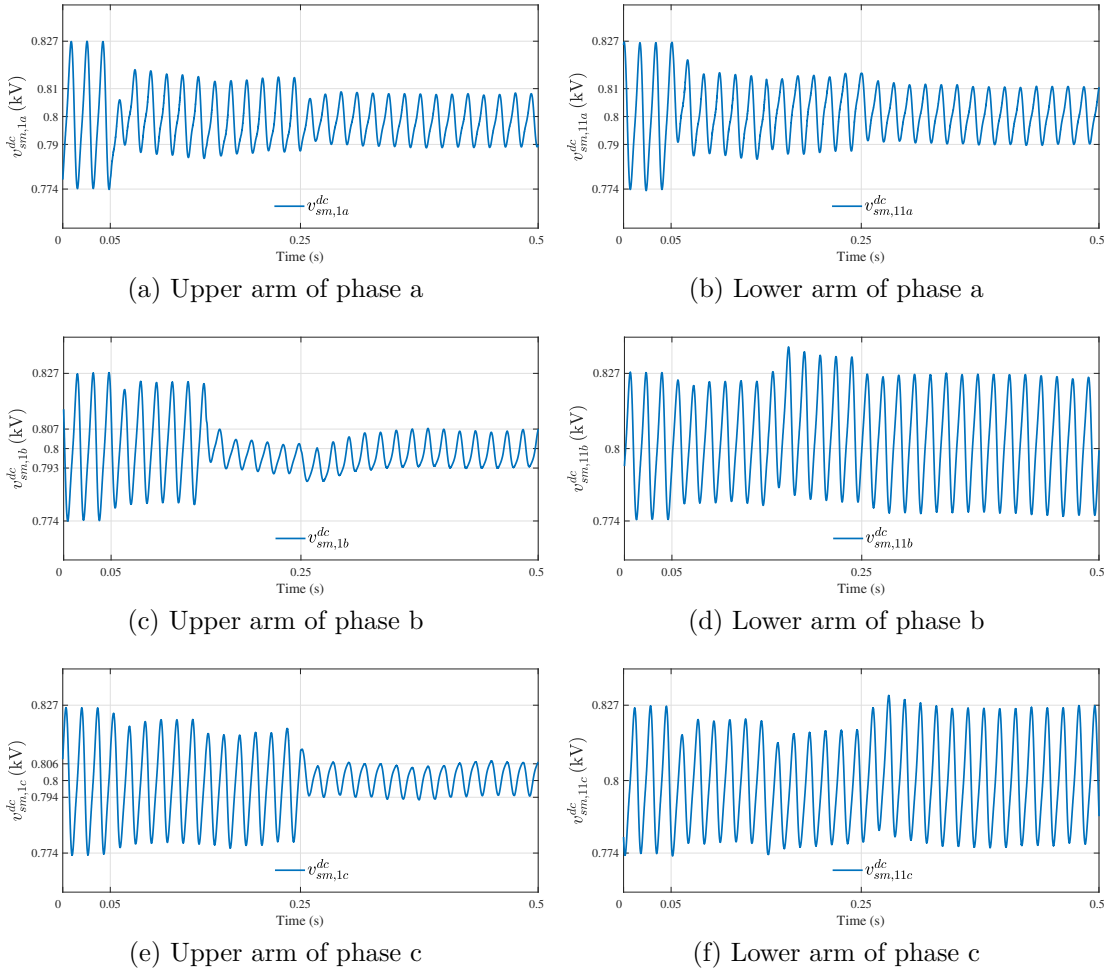
Figure 3.21: Dc link voltage of sample submodules (case 3)

than the submodules with lower power yield. As shown in Figure 3.21, following each irradiation change and power mismatch, the dc link voltage of the submodules experience some transient oscillations. However, the controller of the system ensures that right amount of power is extracted from each leg of the converter that regulates the dc link voltages at their reference.

3.8.4   Case 4: Leg Power Mismatch with Non-zero Reactive Power Injection

This case evaluates the performance of the proposed power mismatch elimination strategy when the converter injects reactive power into the grid. The PV generators are initially
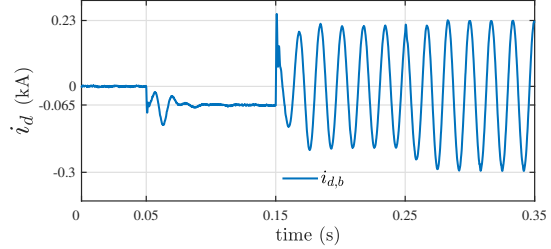
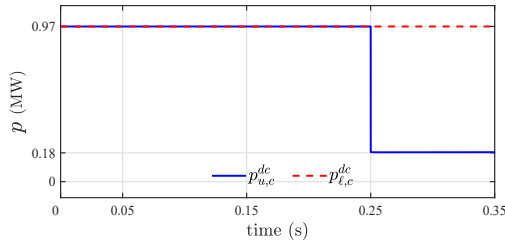(a) Dc power of the arms of leg a

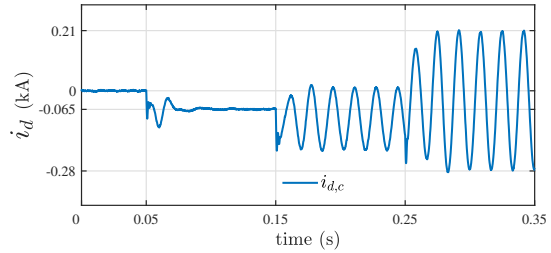(b) Differential current of leg a

(c) Dc power of the arms of leg b

(d) Differential current of leg b

(e) Dc power of the arms of leg c

(f) Differential current of leg c
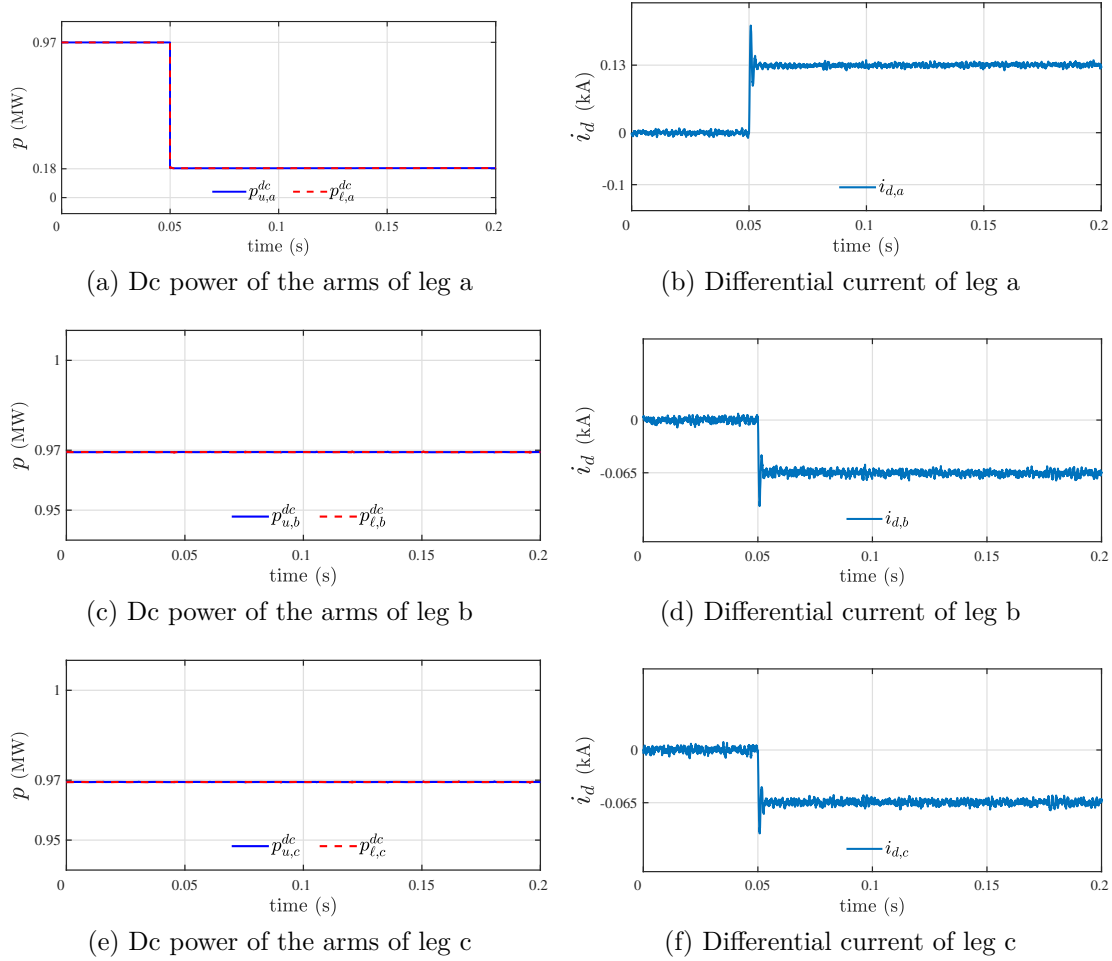
Figure 3.22: Response to leg power mismatch while injecting reactive power into the grid (case 4)

subjected to STC while the converter injects $1\,\text{MVar}$ reactive power into the grid. At $t = 0.05\,\text{s}$ the solar irradiation of the PV generators of leg a declines, causing their power to reduce from $0.97\,\text{MW}$ to $0.18\,\text{MW}$. This condition creates a leg power mismatch in the system while the converter injects reactive power into the grid.

Figures 3.22(a), (c), and (e) show the aggregate power generated by the PV generators of the legs of the MMC. The dc differential currents generated by the proposed power mismatch elimination strategy consequent to the leg power mismatch are shown in Figures 3.22(b), (d), and (f). The current injected into the grid is shown in Figure 3.23(a) which shows that the currents injected into the grid remain balanced in spite of the existing
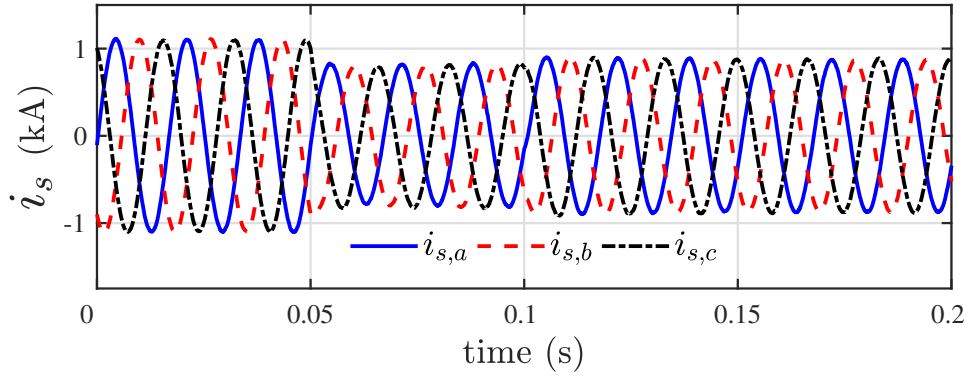
(a) Grid currents
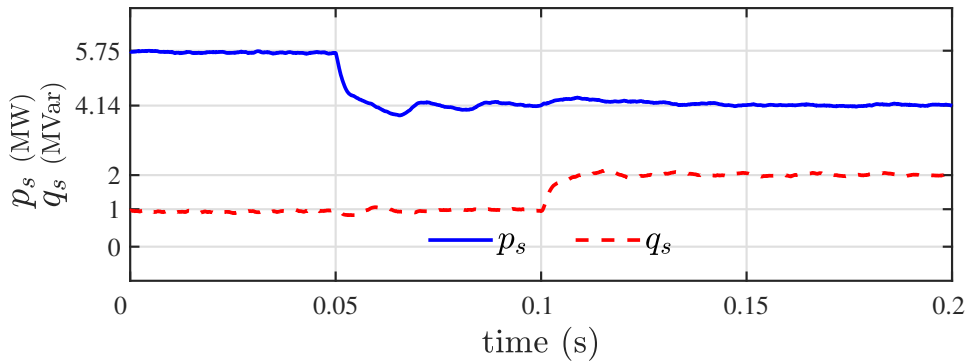
(b) Real and reactive power

Figure 3.23: Grid currents, real, and reactive power of the system while injecting non-zero reactive power into the grid (case 4)

power mismatch and reactive power injection into the grid. Reactive power injection into the host grid does not interfere with the performance of the proposed scheme. As shown in Figure 3.23(b), the real power delivered to the grid declines following the irradiation decline in leg a while the reactive power remains regulated at $1\,\mathrm{MVar}$. At $t = 0.1\,\mathrm{s}$, the reference of the reactive power is changed to $2\,\mathrm{MVar}$. Following this change, the converter regulates the reactive power to its new reference while keeping the current injected into the grid balanced.

Figure 3.24 shows the currents of the arms of the system. Following the power decline at $t = 0.05\,\mathrm{s}$, the magnitude of the current injected into the grid is declined to transfer less power to the grid since the power generated by the PV generators is declined. As a result, the magnitude of the currents of the arms is decreased. The dc component of

(a) Upper arm of phase a

(b) Lower arm of phase a

(c) Upper arm of phase b

(d) Lower arm of phase b

(e) Upper arm of phase c

(f) Lower arm of phase c
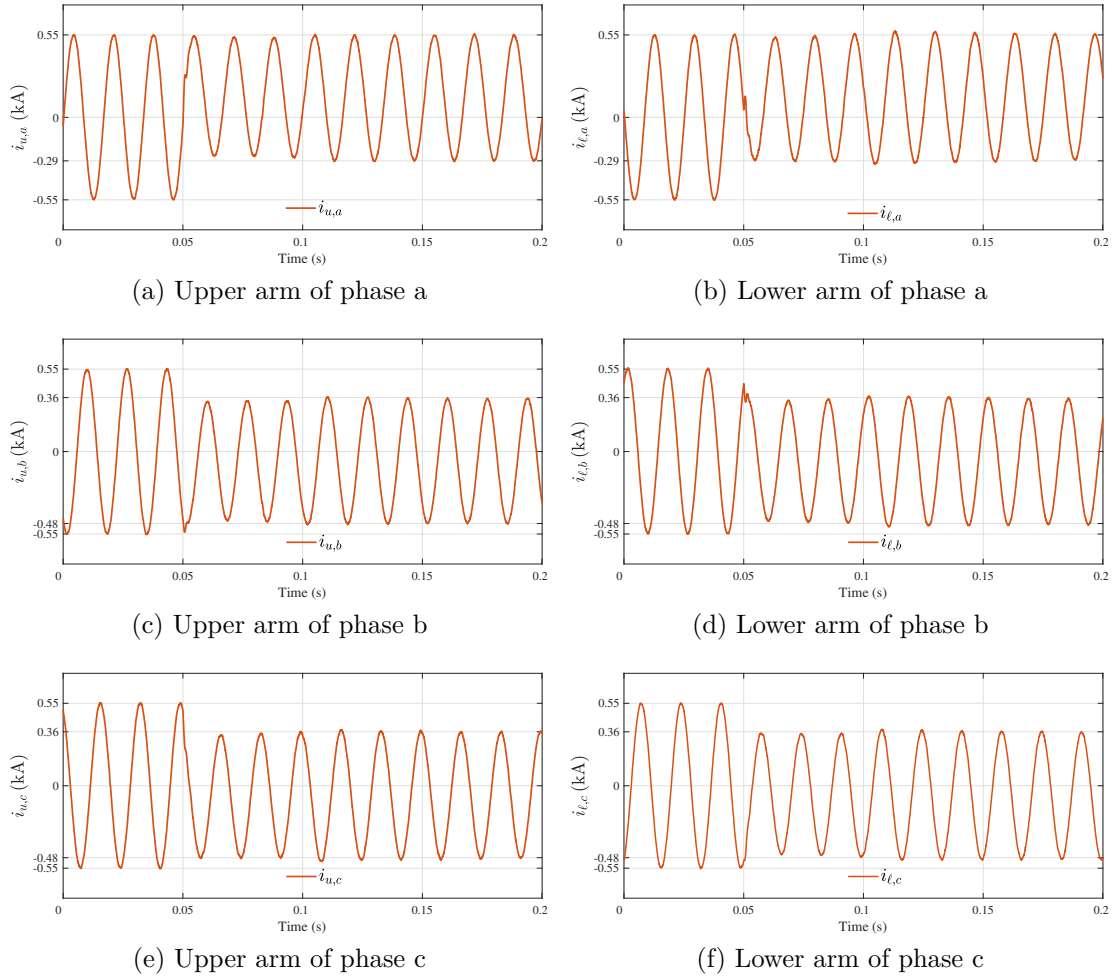
Figure 3.24: Currents of the arms of the converter (case 4)

the differential currents can be perceived from the currents of the arms of the converter. The dc component is the same for the arms of each leg.

Figure 3.25 shows one sample dc link voltage from each arm of the MMC-based PV system. Submodule dc link voltage regulation is not affected by the non-zero reactive power exchange with the grid and successfully regulates the dc link voltages at their reference. As stated earlier, the oscillations of the dc link voltage depend on the amount of power delivered to the submodule by its PV generators. As a result, the oscillations of the dc link voltages of the submodules of leg a are expected to become smaller since the power injected to leg a is decreased which complies with Figures 3.25(a) and (b).

It should be noted that the differential current is created whenever the generated

(a) Upper arm of phase a

(b) Lower arm of phase a

(c) Upper arm of phase b

(d) Lower arm of phase b

(e) Upper arm of phase c

(f) Lower arm of phase c
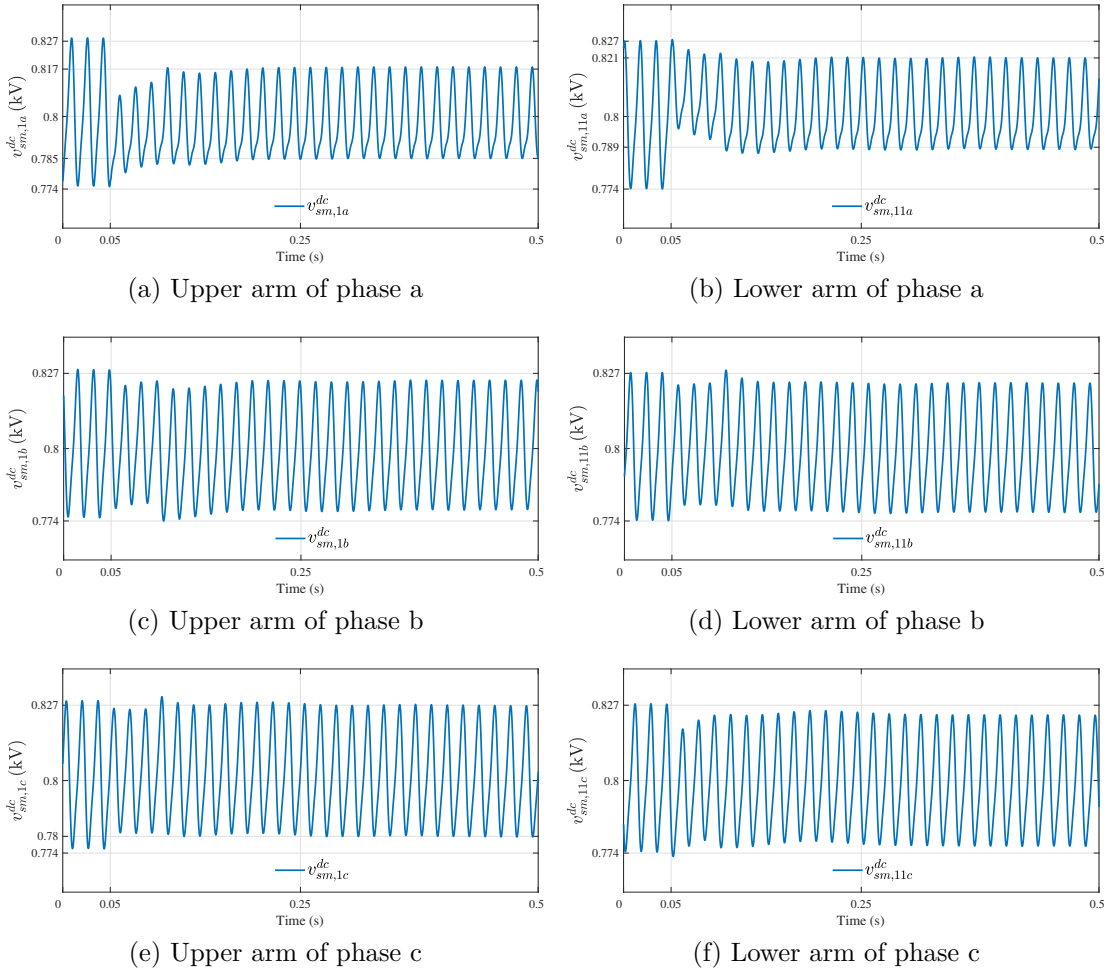
Figure 3.25: Dc link voltage of sample submodules (case 4)

power of the PV generators is less than their nominal values. Consequently, the current rating of the switching devices is not augmented very much. Based on the simulation results, in order to eliminate power mismatch of 50% between the legs and arms of the converter, the current rating of the switches has to be rated only 12% higher than their nominal rating.

3.9   Summary

In this chapter, a power mismatch elimination strategy is proposed for a medium-voltage PV system. The PV system employs a modular multilevel converter (MMC) of which the

submodules are interfaced with PV generators through multiple isolated dc-dc converters, dual active bridge (DAB) converters, enabling independent maximum power point tracking (MPPT) and grounding of the PV generators. The proposed power mismatch elimination strategy produces ac differential currents to equalize the dc and ac powers of the submodules of an arm, to stabilize the submodule dc voltages. It also controls dc differential currents to transfer power from one leg to another, such that one-third of the total PV power flows through each phase of the MMC to the grid. Therefore, balanced currents are injected into the grid, despite unequal PV power generation. Based on the proposed power mismatch elimination strategy, the dc submodule voltages are fixed, thus allowing for both an optimum design of the power-electronic chain and more effective coordination of their switching for cancellation of high-frequency switching harmonics. The chapter presents the mathematical bases and the enabling schemes of the proposed power mismatch elimination strategy. The effectiveness of the proposed power mismatch elimination strategy is demonstrated by time-domain simulations conducted on a representative model featuring actual switches with on and off states for the submodules' dc-ac half-bridge converter. Since the proposed power mismatch elimination only involves the dc-ac half-bridges of the submodules, the modeling of dc-dc converters using their average model does not impact the simulation results in any manner.

Chapter 4

Hybrid MMC-based PV-BES System

Intermittency of the output power of the PV generators is one of the challenges facing this energy resource. The reason for intermittency of their output power is passing clouds that partially or entirely cover the surface of the PV generators. The solution for this problem is to couple PV farms with energy storage systems (ESS) which can store energy and deliver it whenever needed. Battery energy storage (BES) is the most popular solution for the intermittency challenge of PV farms and has been adapted in many installations worldwide. The MMC-based PV system also suffers from intermittency of solar irradiation. The effect of partial shading in conventional PV farms is power fluctuations. However, in the MMC-based PV systems partial shading can lead to power mismatch in the converter in addition to power fluctuations. Consequently, a new structure and its enabling control scheme for a hybrid MMC-based BES-PV system in proposed in this chapter. The proposed configuration and its enabling control scheme smoothen the power fluctuations of the system while eliminating the power mismatches by exchanging power with the arms of the MMC-based PV system.

4.1 Introduction

Photovoltaic solar energy has been growing in a fast pace in the last decade. This growth is associated with concerns about climate change due to the pollution caused by fossil fuel, capital cost reduction of PV panels, and government incentives [76]. As a result, the share of the PV power in the power generation sector is increasing steadily. High penetration of the PV energy resources in the power system poses new challenges which are partially associated with the intermittent nature of the solar irradiation. The challenges caused by the large-scale PV systems are related to power quality degradation, stability, and reliability concerns [77]. The fluctuations of the generated power of the PV power plants would lead to transients that require large variations in the power output of gas turbines to maintain the balance between power generation and load [78]. This effect translates to frequency regulation challenges. PV power fluctuations can also cause undesirable voltage fluctuations in the distribution level causing flicker and excessive operation of automatic load tap changers of transformers [76].

One approach to resolve the challenges related to the intermittency of the PV power is to curtail the power generation of the PV power plants during cloudy days [78]. This approach is undesirable since it causes substantial loss of revenue. The second approach is using the PV inverters to actively regulate the voltage of the grid at point of common coupling (PCC) by exchanging reactive power with the host grid. This action has been explicitly prohibited by IEEE 1547-2008 standard [31]. However, it has been allowed according to IEEE 1547-2018 standard [32]. The third approach is to couple the PV power plants with energy storage systems (ESS). This approach has the potential to mitigate the aforementioned challenges of the intermittent power resources. Some of the energy storage technologies for renewable power generation are pumped hydro [79], super capacitors [80], and batteries [81]. The latter has gained more attention and application due to scalable power rating [80], lower cost [82], high reliability and efficiency [83], and non-polluting [84], and highly recyclable. The batteries have their own challenges such

as relatively short life cycle and some require high maintenance.

The main objective of coupling battery energy storage (BES) systems with PV power plants is to smooth the stochastic power output of the PV plants. In the literature, two strategies have been proposed to operate the BES systems coupled with PV power plants. The first strategy is to operate the PV power plant as a semi-scheduled power generation unit while the second method is to smooth the abrupt changes of the generated PV power. In semi-scheduled mode, a dispatch command which is based on the projected generation is received from the operating company and BES systems is used to remove the discrepancies between the actual and projected power generation [80]. In power smoothing mode, battery energy storage system removes the power oscillations of the PV system and limits the ramp rate of the power delivered to the grid [78]. Consequently, the power injected into the grid becomes smoother with smaller ramp rates.

Modular multilevel converter (MMC)-based PV system is one of the new configurations for integration of utility-scale PV power plants. The MMC-based PV system eliminates bulky grid interface transformers [13], has lower filtering requirements [15], avoids series connection of power switches [27], provides better power quality [16], reduces production costs [26], and improves reliability [28] by virtue of its modularity. The superior performance of the MMC makes it suitable for integration of PV power generators into power system.

Unequal aggregate power generated by the PV generators connected to the arms of the MMC-based PV system is one of the challenges facing the application of MMC for PV integration.

The power mismatch elimination method proposed in Chapter 3 uses differential currents to eliminate the power mismatches in the MMC-based PV system. However, considering that small fluctuations of the solar irradiation is very common, using the strategy proposed in Chapter 3 leads to practically constant presence of differential currents in the structure of the MMC. Consequently, the losses associated with the differential currents increase which can be avoided with integrating BES systems into the structure of the

MMC-based PV system.

A new structure for the MMC-based PV-BES system is proposed in this chapter which embeds one BES in each arm of the system. A new power mismatch elimination strategy using a combination of the embedded BES systems and internal power flow control of the MMC is also proposed in this chapter. The proposed hybrid power mismatch elimination strategy uses the embedded BES systems to eliminate power mismatches which are within the power rating of the BES systems and uses a combination of the BES systems and internal power flow control of the MMC to eliminate larger power mismatches. The new structure and its enabling control scheme minimize or mitigate the need for differential currents to eliminate the adverse effects of the PV power fluctuations. The embedded BES systems exchange power with the arms of the MMC and can eliminate power mismatches without creating differential currents. They are also used for smoothing the output power of the MMC-based PV system.

4.2 Overview of the Energy Storage Systems

A storage system is made up of four main components including the following [85]:

- **Storage medium:** this is the means which stores the energy such as battery.

- **Charging:** this unit permits the flow of energy from the electrical network to the storage medium.

- **Discharging:** it ensures the delivery of the stored energy when demanded.

- **Control:** it governs the entire storage system.

Energy storage systems do not generate power themselves. They have to be charged so they can store energy for later use. Major characteristics of an energy storage system are:

- **Energy:** energy storage technologies vary from those that store only a small amount of energy (daily-used batteries) to systems that store large amount of energy that can supply a city for hours.

- **Rate of power release:** the rate at which the energy storage system can absorb and release power. Some energy storage technologies are relatively slow such as pumped hydro and some are very fast such as super-capacitors.

- **Power density**: power density is the power per unit volume. Both are critical elements in non-stationary energy storage applications such as in electric vehicles and portable backup units.

- **Service lifetime (Cycle life):** all types of energy storage systems wear out over time and therefore have only a finite life, regardless of how well they are maintained. This varies greatly among available technologies, and depends very much on how the energy units are used. Batteries particularly have short lifetimes in applications where they are repeatedly charged and discharged completely.

- **Fault current:** an energy storage device will feed a fault (short circuit in the power system) just as readily as it will feed power to a load power demand. Particularly for technologies that have very high power ratings (e.g. super-capacitors, batteries) the short-circuit capability is a big concern.

- **Response time:** depending on the design of the device and the type of energy storage technology, an energy storage system may be able to vary its output power and voltage rapidly and very precisely.

- **Losses:** a portion of the energy stored in an energy storage system will never be recovered. Losses occur in the electric equipment that converts electric power from the grid into that stored in the storage system, and vice versa, and in the storage medium itself.

Using energy storage systems can be beneficial in power systems and they introduce capabilities which can help the power system in high demand times. The benefits of utilization of energy storage systems are:

- **Peak reduction:** energy storage is often used to store energy during times of low usage and to discharge that energy when demand is high. This function can delay the need for construction of new power generation units or new transmission lines.

- **Making renewable energy resources dispatchable:** both wind and solar energy resources have intermittent nature and their output power depends on the weather. Solar generators do not generate any power at night and very low power in cloudy days. Without energy storage, the power they generate must be consumed at the instant generated. However, the storage systems provide a means to store the energy generated by the PV generators during the day and consume it later when the power demand is higher.

- **Reliability backup:** energy storage can be used to provide power when the grid is unable to supply it due to equipment outages, storms, or other reasons.

- **Spinning reserve:** regional power systems are required to keep significant amounts of generators running, but not producing power. This is so that they can provide power immediately in the event of a major generation loss, which is very expensive. Energy storage can be used to supply the load for a certain amount of time so the backup generators are started and brought up to full power. Battery energy storage is the storage technology used in PV farms nowadays.

- **Regulation and stabilization:** energy storage can be used to inject power into the grid, or absorb power from the grid, to lower the fluctuations and/or regulate the voltage and frequency.

In this chapter, energy storage is firstly used to lower the power fluctuations of the PV system. The second objective of the energy storage system in the MMC-based PV-BES

system is to eliminate the power mismatches between the arms and legs of the system which is unique to the MMC-based PV system topology.

4.3   Overview of the Energy Storage Technologies

In this section the common mediums used to store energy are presented. Energy storage systems convert electrical energy to some form of energy that can be stored and released as needed. The choice of the ESS for an application depends on the application power and energy rating, response time, weight, volume, and operating temperature. The following presents a brief overview of the energy storage technologies.

- **Batteries :** batteries are the most common medium to store electrical energy. Their power rating ranges from very small to very large values since they are stackable and scalable. In batteries, electrical energy is converted and stored in the form of chemical energy.

- **Electrochemical double-layer capacitor (EDLC) :** EDLC works in the same way as a conventional capacitor where there is no ionic transfer resulting in a chemical reaction. In other words, energy is stored in the electrochemical capacitor by simple charge separation.

- **Fuel cell:** Fuel cells are electrochemical conversion devices that consume hydrogen and oxygen to produce electricity and water.

- **Compressed air energy storage (CAES) :** compressed air energy storage (CAES) is a technology that stores energy as compressed air for later use. Energy is extracted using a standard gas turbine, where the air compression stage of the turbine is replaced by the CAES, thus eliminating the use of natural gas fuel for air compression.

- **Flywheel :** flywheels store energy in a rotatory mass. Flywheel systems are characterized by being able to provide very high peak power. In fact, the input/output

peak power is limited only by the power converter. They also have high power and energy density and virtually infinite number of charge and discharge cycles.

- **Superconductive magnetic energy storage (SMES) :** this storage technology consists of storing energy in the magnetic field created by a direct current flowing through a superconducting coil. SMES provides one of the highest densities of any power storage method. Its main advantage is high storage efficiency which is above 90%.

- **Thermoelectric energy storage (TEES) :** this technology is used in solar thermal power plants and consists of a synthetic oil or molten salt that stores energy in the form of heat collected by solar thermal power plants to enable smooth power output during daytime, cloudy periods, and to extend power production for 1 to 10 hours after sunset.

- **Pumped hydro storage (PHS) :** this storage technology stores electrical energy in the form of potential energy in large volume of water by pumping the water to a higher altitude reservoir. In times of need, the water flows from the higher altitude reservoir and energizes a hydro turbine. PHS can be constructed at large capacities over 100 MW range and discharged over periods of time from 100 to 1000 minutes.

4.4 PV-BES Configurations

There are two configurations for coupling a PV system with BES system. The main difference is in the location of the BES system which can be on the dc-side of the converter or the ac-side. The first configuration of the PV-BES system is shown in Figure 4.1(a) in which the storage system is connected to the dc link of the converter while exchanging power with the dc link of the system. This configuration requires a dedicated dc-dc converter for interfacing the BES with the dc link and a common dc-ac converter is used to interface the PV-BES system with the ac system. Figure 4.1(b) shows a PV-BES

system where the storage is connected to the ac-side of the system using a dedicated dc-ac converter. In this configuration, the BES system can be used to smooth the output power of multiple PV systems.

(a) BES connected to dc-side
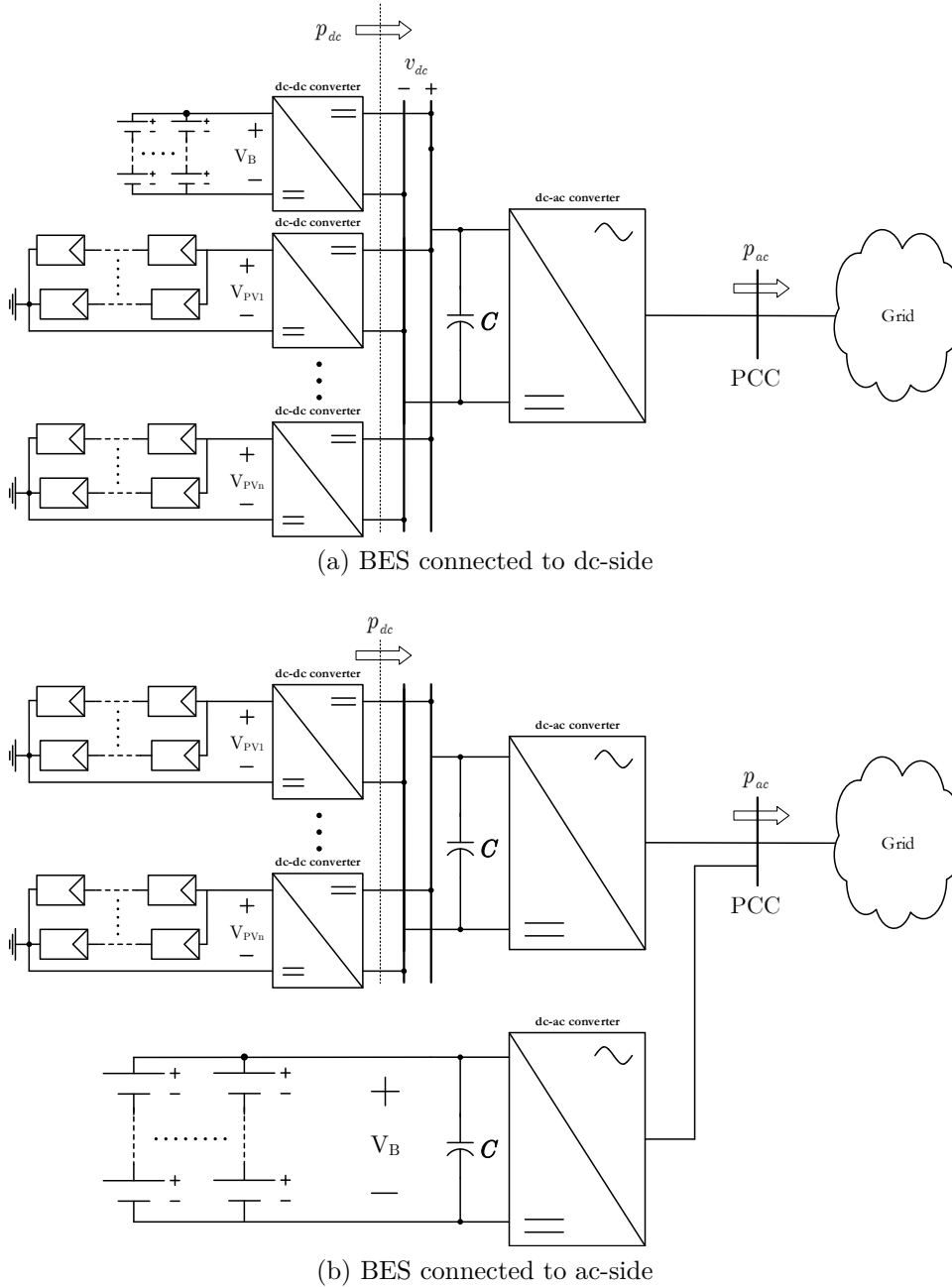

(b) BES connected to ac-side

Figure 4.1: PV-BES system configurations

The MMC-based PV system enables a new configuration for coupling PV generators with BES systems which is unique to the structure of the MMC. In the MMC-based PV

system, BES system can be connected to the common dc link of the converter using a dc-dc converter, it can be connected to the dc link of each and every submodule, or one or several submodules can be dedicated to embed BES systems in the arms of the converter. The latter is proposed in this thesis to incorporate BES system with the MMC-based PV system. The proposed configuration for embedding BES systems into the MMC-based PV system enables power mismatch elimination without the need for differential currents and also can be used to smoothen the output power of the system.

4.5 Structure of the MMC-based PV-BES System

Figure 4.2 shows the structure of the proposed MMC-based PV-BES system. The proposed MMC configuration consists of three legs, corresponding to three phases of the system, and two arms in each leg, namely upper and lower arms. Each arm of the MMC-based PV-BES system embeds one BES submodule along with N PV submodules. As shown in Figure 4.3(a), each PV submodule comprises of a half-bridge dc-ac converter, n sets of series- and parallel-connected PV panels (PV generators) with their associated isolated DAB dc-dc converters. BES submodules, as shown if Figure 4.3(b), replaces the PV generators in PV submodules with battery banks while the rest of the configuration remains unchanged. The DAB dc-dc converters are used to interface the PV generators and the battery banks with the dc side of the half-bridge converters. However, their control objectives are different.

The isolated dc-dc converters are considered to be dual active bridge converter (DAB) with medium frequency isolation transformer. The DAB converters interfacing the PV generators are controlled to extract maximum power from the PV generators using an MPPT algorithm and the DAB converters interfacing the battery banks with the half-bridge converters are controlled to regulate the power of the battery banks. The galvanic isolation provided by the DAB converters enables the grounding of the negative terminals of the PV generators and eliminates the potential-induced degradation (PID)
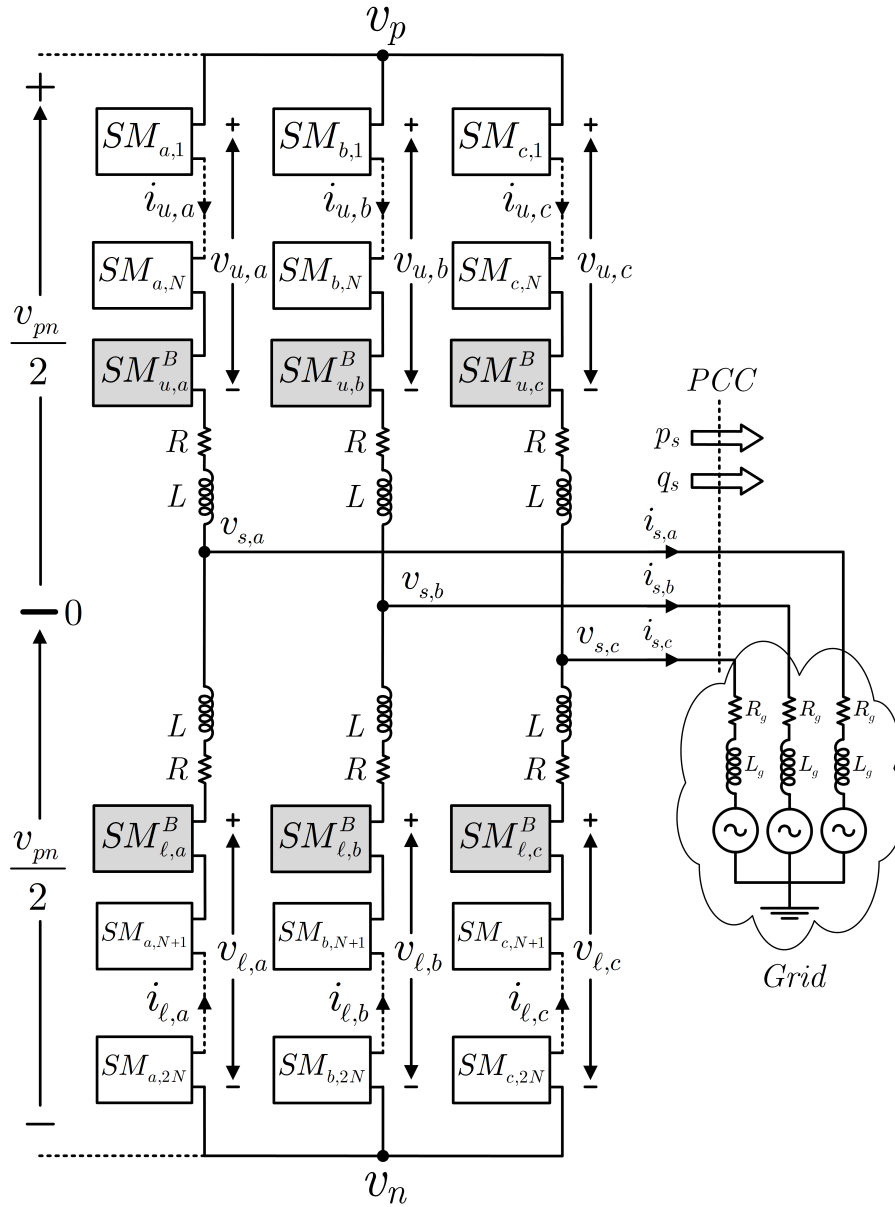
Figure 4.2: Structure of the MMC-based PV-BES system

phenomenon [71].

It should be noted that any dc-dc converter topology featuring galvanic isolation and required power rating could be used instead of the DAB converter. The application of DAB is due to its galvanic isolation and existing practical implementations of up to 100 kW [86–88].
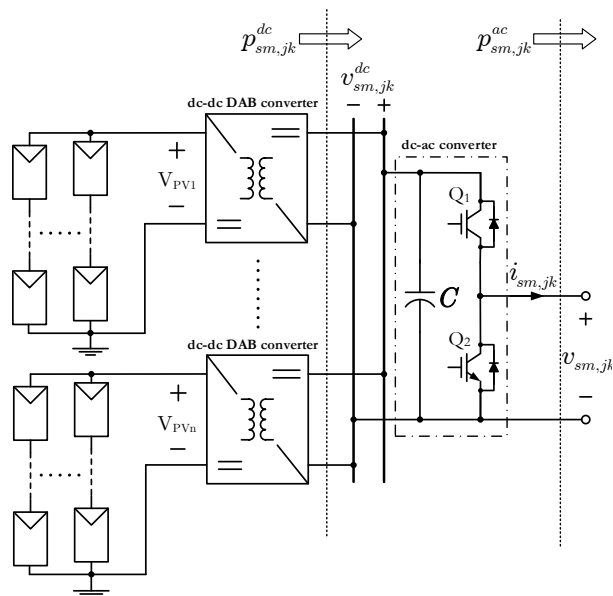
(a) PV submodule
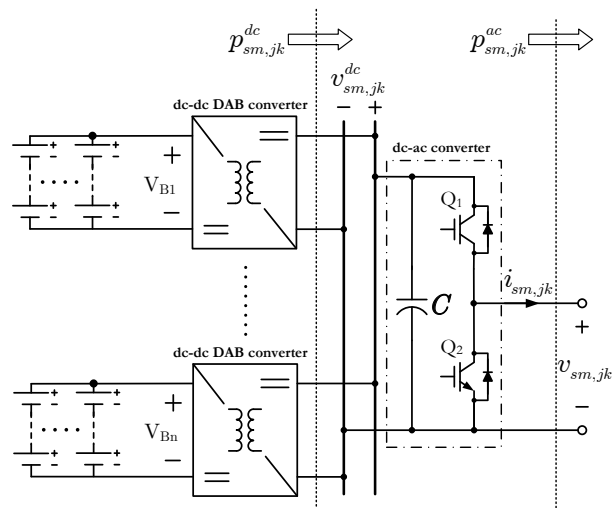
(b) BES submodule

Figure 4.3: Structure of the PV and BES submodules in the MMC-based PV-BES system

4.6 Power Smoothing

One of the main objectives of coupling PV farms with storage systems is to smooth
the abrupt changes of the output power of the PV generators. The fluctuations of the
generated power of the PV farms can cause frequency and voltage regulation problems.
In this chapter, the embedded BES systems are used to smooth the generated power of

the PV generators. Simple moving average (SMA) method is applied to determine the amount of power that the BES systems need to absorb or inject in order to limit the rate of change of the power delivered to the host grid. The aggregate generated power of the PV generators is averaged using SMA method with $1/2\ min$ duration and $1/2\ s$ sampling rate. The difference between the aggregate generated power of the PV generators and the output of the SMA is used as the reference of the BES systems. The reference BES power is divided equally between the BES systems, making them participate equally in limiting the rate of change of the injected power into the host grid.

The simple moving average takes a predefined number of samples measured in equal intervals and calculates their average while adding the latest sample and removing the oldest sample from the buffer. SMA can be represented mathematically as

$$P_{MA}(t) = \frac{1}{m} \sum_{i=1}^{m} P_V(i) \tag{4.1}$$

where m is the number of samples of the aggregate PV power and P_V is a vector of the sampled aggregate PV power containing the m most recent samples. The length of the power vector, m, is considered to be 60 in the simulation section; however, it can have different lengths depending on the sampling rate and the duration of the averaging.

The setpoint for the power of the BES system of each arm due to the power smoothing function is then defined as

$$P_{u,k}^{BS*}(t) = P_{\ell,k}^{BS*}(t) = \frac{P_{MA}(t) - P_{PV}(t)}{6} \qquad k = a, b, c \tag{4.2}$$

where $P_{u,k}^{BS*}(t)$ and $P_{\ell,k}^{BS*}(t)$ are the reference powers for the BES system of upper and lower arms in leg k due to power smoothing function. Since all BES systems are assigned the same power setpoint by the power smoothing function, they will not interfere with the power mismatch elimination function since they do not change the amount of power mismatch between the legs or arms of the system.

4.7 Hybrid Power Mismatch Elimination Strategy

The final goal of the PV-BES system of Figure 4.2 is to extract the maximum power from the PV generators and deliver it to the host grid using balanced three-phase currents. In other words, one third of the aggregate power of the PV generators will be injected into the grid from each phase of the converter.

The proposed MMC configuration and its enabling control strategy ensure that the goal of equal power injection into the host grid is achieved with minimum differential current in the structure of the MMC. Upon occurrence of a power mismatch, a power management strategy uses the embedded BES systems to eliminate the power mismatch. If the power mismatch is within the power rating of the embedded BES systems, the power mismatch will be eliminated without creating differential currents.

The different types of power mismatches that can happen in the structure of the MMC-based PV-BES system can be mathematically shown as:

1. Power mismatch between the legs of the converter described mathematically as

$$p_a^{dc}(t) \neq p_b^{dc}(t) \neq p_c^{dc}(t) \tag{4.3}$$

2. Power mismatch between the arms of leg k

$$p_{u,k}^{dc}(t) \neq p_{\ell,k}^{dc}(t) \tag{4.4}$$

3. Power mismatch between the submodules of one arm

The first and second types of power mismatches are the topic of this chapter. The third item is automatically manged using the voltage sorting algorithm in voltage balancing technique presented in Section 2.6.4.

4.7.1   Elimination of Small Leg and Arm Power Mismatches

One objective of embedding battery energy storage systems in the arms of the MMC-based PV system is to equalize the aggregate power of the legs of the converter and inject equal amount of power into the host grid from each phase. Defining the average leg power as

$$p_{av}(t) = \frac{1}{3} \sum_{k=a,b,c} p_k^{dc}(t) \qquad k = a, b, c \tag{4.5}$$

to ensure that the aggregate power delivered to the legs of the converter are equal, the equalized power of the legs are written as

$$p_{av}(t) = p_k^{dc}(t) + p_{u,k}^{BM*}(t) + p_{\ell,k}^{BM*}(t) \tag{4.6}$$

where $P_{u,k}^{BM*}$ and $P_{\ell,k}^{BM*}$ are the power setpoints for the BES systems of the upper and lower arms of leg k due to power mismatch elimination function, respectively. If the condition shown in (4.6) is met for all three legs, the dc differential currents will not be needed to eliminate the leg power mismatches.

Sum of the powers of the BES systems of the upper and lower arms for leg k is derived from (4.6) as

$$p_{u,k}^{BM*}(t) + p_{\ell,k}^{BM*}(t) = p_{av}(t) - p_k^{dc}(t) \tag{4.7}$$

The second objective is to equalize the aggregate power between the arms of each leg which can be formulated as

$$p_{u,k}^{dc}(t) + p_{u,k}^{BM*}(t) = p_{\ell,k}^{dc}(t) + p_{\ell,k}^{BM*}(t) \tag{4.8}$$

The difference between the powers of the BES of the upper and lower arms for leg k is derived from (4.8) as

$$p_{u,k}^{BM*}(t) - p_{\ell,k}^{BM*}(t) = p_{\ell,k}^{dc}(t) - p_{u,k}^{dc}(t) \tag{4.9}$$

Solving the system of linear equations consisting of (4.7) and (4.9) yields the power setpoint for each BES in the MMC due to power mismatch elimination function as

$$p_{u,k}^{BM*}(t) = \frac{p_{av}(t)}{2} - p_{u,k}^{dc}(t)$$
$$p_{\ell,k}^{BM*}(t) = \frac{p_{av}(t)}{2} - p_{\ell,k}^{dc}(t) \tag{4.10}$$

Having generated the reference powers for the BES of each arm due to power smoothing function using (4.2) and power mismatch elimination function using (4.10), the two power references are added to yield the final power setpoint for each BES system as

$$P_{u,k}^{B*}(t) = P_{u,k}^{BS*}(t) + P_{u,k}^{BM*}(t)$$
$$P_{\ell,k}^{B*}(t) = P_{\ell,k}^{BS*}(t) + P_{\ell,k}^{BM*}(t) \tag{4.11}$$

The power setpoints of the BES systems, calculated using (4.11), correspond to a condition in which the existing power mismatches can be eliminated entirely using power exchange with the BES systems and differential currents will not be needed. However, if the powers calculated in (4.11) are outside the power rating of the BES systems, a differential current will be created, according to the scheme proposed in Chapter 3, to transfer power between the arms and legs of the converter. As a result, the values calculated in (4.11) have to be examined to determine if they are within the power capabilities of the BES systems. Figure 4.4 shows flowchart of the process to examine the reference power of each battery energy storage system. If the power setpoints are withing the power rating of the BES systems, the flowchart will not alter those values. However, if the setpoints are outside the power rating of the BES systems, the flowchart will adjust the BES power setpoints to zero or maximum charging or discharging power.
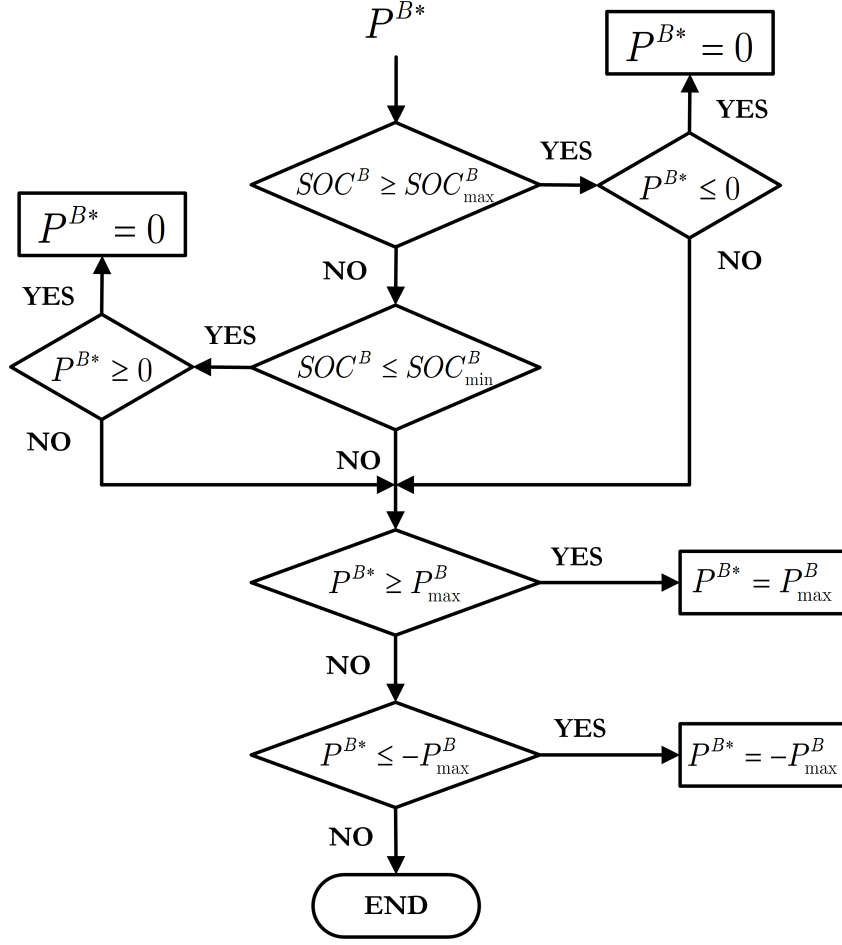
Figure 4.4: Flowchart to examine the reference power of the BES systems

4.7.2   Elimination of Large Leg Power Mismatches

The ultimate goal of the proposed MMC-based PV-BES system is to inject equal powers from each phase of the MMC into grid while keeping the differential currents at minimum. This goal can be represented mathematically as

$$\underbrace{p_{u,k}^{dc} + p_{\ell,k}^{dc}}_{p_k^{dc}} + p_{u,k}^{B} + p_{\ell,k}^{B} + p_k^{ex} = p_{av} \tag{4.12}$$

where $p_k^{ex}(t)$ is the term that needs to be added to the aggregate generated power of the PV generators and BES systems of leg k to equalize the powers injected into the grid by the phases of the system. The term is referred as the *power mismatch* of leg k which

reflects the power mismatch between the aggregate power injected into the legs of the system including the power of PV generators and BES systems.

Equation (4.12) can be rewritten as

$$p_k^{ex}(t) = p_{av}(t) - p_k^{dc}(t) - p_{u,k}^B(t) - p_{\ell,k}^B(t) \tag{4.13}$$

After defining the power mismatch of each leg, $p_k^{ex}(t)$, the setpoint for the dc differential currents of each leg is calculated as

$$i_{d,k}^{dc*}(t) = \frac{p_k^{ex}(t)}{v_{pn}} \qquad k = a, b, c \tag{4.14}$$

Equation (4.14) indicates that the dc differential currents sum up to zero at the positive and negative rails of the MMC. The aggregate power being delivered to the arms of the converter is sum of the arm dc power and the BES power of the arm. If this aggregate power is not equal to the average leg power, the difference is transfered between the legs which ensures that equal currents are delivered to the grid.

4.7.3 Elimination of Large Arm Power Mismatches

The goal of the arm power mismatch elimination strategy is to eliminate the power mismatches between the arms of the legs using embedded battery energy storage systems. The goal is reached by exchanging power between the embedded BES systems and their associated arms to equalize the aggregate power of the arms of each leg. However, if the power setpoint calculated for a BES system is outside its power rating, differential currents are required to eliminate the power mismatches.

Having calculated the reference power of the BES systems of each arm, the flowchart shown in Figure 4.4 is used to examine the power rating limitation of the storage systems and adjust the calculated values of BES power setpoints. Then, the adjusted storage power references are used to define the amount of power that needs to be transferred

between the arms of each leg according to

$$p_{d,k}(t) = \frac{p_{u,k}^{dc}(t) + p_{u,k}^{B}(t) - p_{\ell,k}^{dc}(t) - p_{\ell,k}^{B}(t)}{2} \tag{4.15}$$

where $p_{d,k}(t)$ is the differential power of leg k including the powers of its BES systems which are examined by the power capability flowchart. Having defined the differential power of each leg according to (4.15), the corresponding ac differential currents are calculated using

$$\begin{bmatrix} \hat{i}_d^1 cos\phi_1 \\ \hat{i}_d^1 sin\phi_1 \\ \hat{i}_d^2 cos\phi_2 \\ \hat{i}_d^2 sin\phi_2 \end{bmatrix} = \frac{2}{3\hat{v}_e} \begin{bmatrix} 1 & 1 & 1 & 0 \\ 0 & 0 & 0 & -1 \\ 2 & -1 & -1 & 0 \\ 0 & \sqrt{3} & -\sqrt{3} & 0 \end{bmatrix} \begin{bmatrix} p_{d,a} \\ p_{d,b} \\ p_{d,c} \\ q_d \end{bmatrix} \tag{4.16}$$

With the measured values of the differential real powers, and arbitrary value for aggregate differential reactive power ($q_d = 0$), the required ac differential currents can be calculated in $\alpha\beta$-frame as

$$i_{d,\alpha}^{ac*}(t) + j i_{d,\beta}^{ac*}(t) = \left[\hat{i}_d^1 cos\phi_1 + j\hat{i}_d^1 sin\phi_1 \right] e^{j\phi(t)}$$
$$+ \left[\hat{i}_d^2 cos\phi_2 - j\hat{i}_d^2 sin\phi_2 \right] e^{-j\phi(t)} \tag{4.17}$$

The term $\phi(t)$ is the phase angle of the internal voltage of the MMC which is calculated from the output of the current controller. The $\alpha\beta$-frame values calculated in (4.17) are then used to generate the three-phase ac differential current commands according to Figure 4.5.

The final commands for the differential currents are determined using the dc and ac components of the differential current commands calculated in (4.14) and Figure 4.5 as

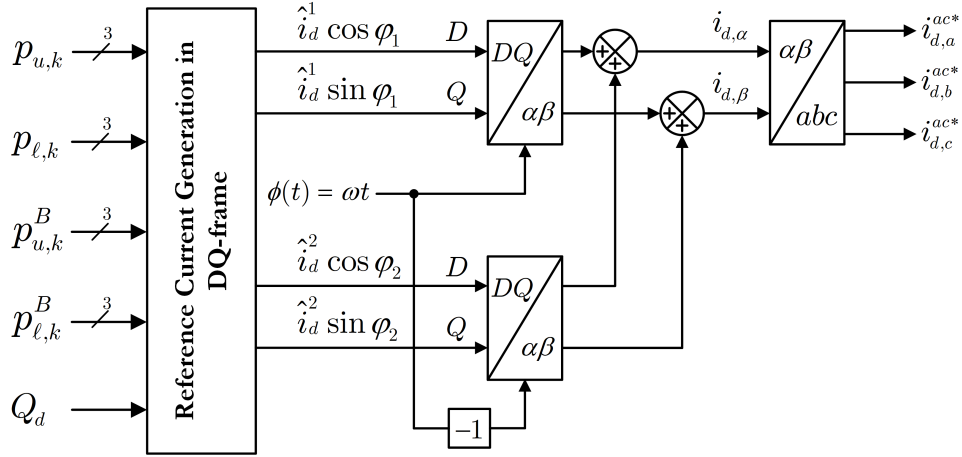$$i_{d,k}^* = i_{d,k}^{*dc} + i_{d,k}^{*ac} \tag{4.18}$$

Figure 4.5: Scheme for generating reference ac differential currents.

Having generated the final commands for the differential currents using (4.18), the differential current controller (DCC) described in Section 2.6.2 is used to generate the differential currents in the legs of the MMC.

4.8 Simulation Results

The MMC-based PV-BES system of Figure 4.2 is simulated in PSCAD/EMTDC software environment. The simulation results demonstrate the effectiveness of the embedded BES systems and its enabling scheme in minimizing/eliminating the need for differential currents to mitigate the power mismatches between the arms and legs of the MMC-based PV system. To allow faster simulations, the DAB converters are represented by controllable current sources and the half-bridge converters are represented by their switched model. The simulated PV-BES system has 9 PV submodules ($N = 9$), and 1 BES submodule in each arm. The power rating of the PV and BES submodules is $100\,\text{kW}$. The dc voltage reference of the submodules is set to $0.8\,\text{kV}$. Also, to keep the simulation model tractable, one DAB converter and one aggregated PV generator model are used in each submodule (i.e., $n = 1$ in the simulation model).

The PV generators consists of 3 parallel-connected strings of 23 series-connected panels of Kyocera KU330-8BCA. Each PV panel generates $330\,\text{W}$ under standard testing

condition (STC). The DAB converters interfacing the PV generators with the dc side of the half-bridge converters exercise the perturb and observe (P&O) MPPT algorithm to maximize the power output of the PV generators. The battery banks consist of 64 batteries of IND27-2V Trojan Battery Company which are configured into strings of 16 batteries to reach the voltage rating of 768 V and 4 such strings are connected in parallel to reach the energy capacity of 97.23 kAh and maximum power rating of 100 kW. Series resistance of the battery bank is considered to be 0.2 ohm. The grid voltage is 4.16 kV (line-to-line, rms). Table 4.1 lists the other parameters of the simulated system.

Table 4.1: Parameters of the MMC-based PV-BES system and the host grid

Parameter	Value	Parameter	Value
L	$3\ mH$	C	$10\ mF$
R	$0.1\ \Omega$	SOC^B_{min}	$\%10$
L_g	$750\ \mu H$	SOC^B_{max}	$\%90$
R_g	$60\ m\Omega$	P^B_{max}	$100\,\text{kW}$

4.8.1 Case 1: Power Smoothing

One of the main applications of the BES systems coupled with PV farms is to smooth the abrupt changes in the generated power of the PV farms. The proposed MMC-based PV-BES system is capable of smoothing the generated power of the PV generators by exchanging power with the arms of the system. Simple moving average (SMA) is used to determine the amount of the power that BES systems need to exchange with each arm in order to reduce the overall power fluctuations of the power injected into the host grid. Simple moving average has been calculated for duration of $1/2$ min with $1/2$ s sampling rate. The difference between the output of the SMA algorithm and the actual aggregate power of the PV generators is used as the power reference for the BES systems.

In this case, the PV generators are subjected to the same irradiation for the duration of the simulation. Consequently, the amount of power delivered to the legs of the system are equal meaning that there is no leg power mismatch in the system. Moreover, the

aggregate power delivered to the arms of the legs are also equal that means there is no arm power mismatch in the system. Due to the absence of any power mismatch in the system, the differential currents are expected to be zero which is confirmed by the simulation results in this section.

All the BES systems are assigned the same power reference since they all contribute in smoothing the output power of the system. The solar irradiation data has been extracted from reference [89].

Initially, the PV generators are all subjected to solar irradiation of $900\,\mathrm{W/m^2}$ and the PV generators of each arm are generating $0.786\,\mathrm{MW}$ power. Then at $\mathrm{t}=5\,\mathrm{s}$, the solar irradiation of all PV generators undergoes intermittent changes due to cloud coverage of the PV generators. Figures 4.6(a) through 4.6(f) show the aggregate dc power delivered to the arms of the system that are equal in this case study. The BES systems are controlled using power smoothing function which assigns equal power reference for all BES systems as shown in Figures 4.6(g) through 4.6(l). Since the powers injected into the arms of the system are equal, the system is completely balanced and there is no power mismatch in the system. As a result, the differential currents are expected to be zero which is confirmed by the simulation results as shown in Figure 4.7(a) through 4.7(c).

Figure 4.7(d) shows the aggregate power of the BES systems which is positive during discharging intervals and negative during charging intervals. The time intervals in which the BES systems absorb power from the arms of the MMC (charging batteries) are shown in green patches and the time intervals in which the BES systems inject power into the arms of the MMC (discharging batteries) are shown in red patches. One of the advantages of the simple moving average is that at the end of the day the batteries will likely have the same state of charge (SOC) they had at the end of the previous day since the average of the changes throughout a day is most likely zero. The aggregate power injected into the grid and the power generated by the PV generators are shown in Figure 4.7(e). As confirmed by Figure 4.7(e), the power injected into the grid is smoother than the aggregate power generated by the PV generators. The reactive power exchanged with
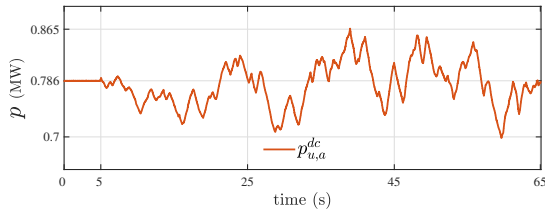
(a) PV power of the upper arm of leg a
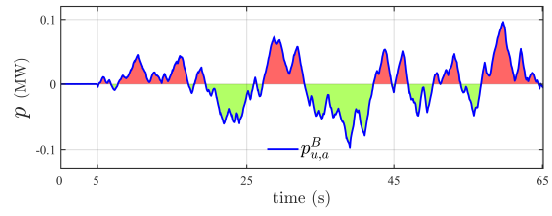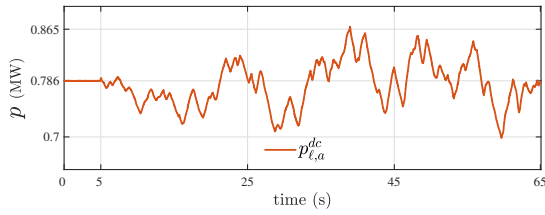
(b) PV power of the lower arm of leg a

(c) PV power of the upper arm of leg b

(d) PV power of the lower arm of leg b
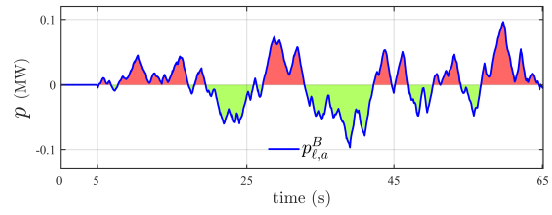
(e) PV power of the upper arm of leg c
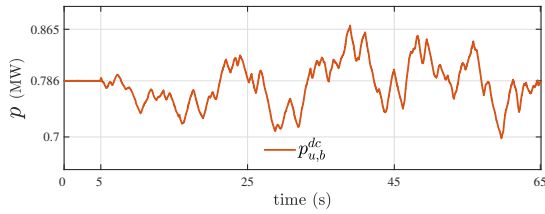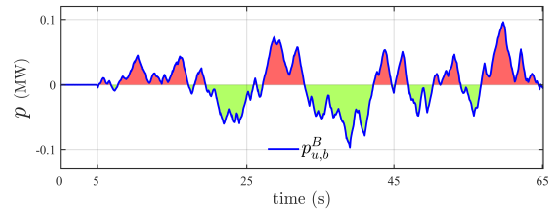
(f) PV power of the lower arm of leg c
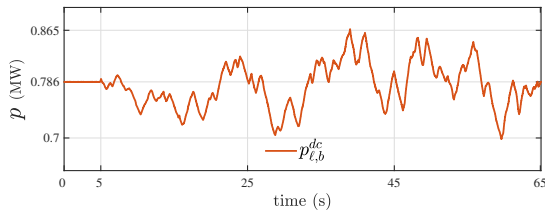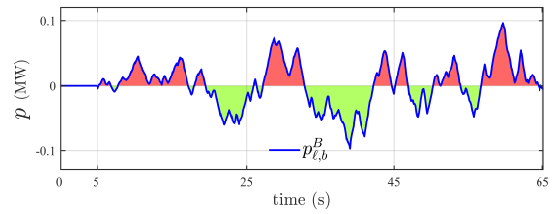
(g) BES power of the upper arm of leg a

(h) BES power of the lower arm of leg a

(i) BES power of the upper arm of leg b

(j) BES power of the lower arm of leg b

(k) BES power of the upper arm of leg c

(l) BES power of the lower arm of leg c

Figure 4.6: PV and BES power for each arm (case 1)

(a) Differential current of leg a

(b) Differential current of leg b

(c) Differential current of leg c

(d) Aggregate power of the BES systems

(e) Aggregate PV power and real power delivered to the grid

(f) Reactive power exchanged with the grid
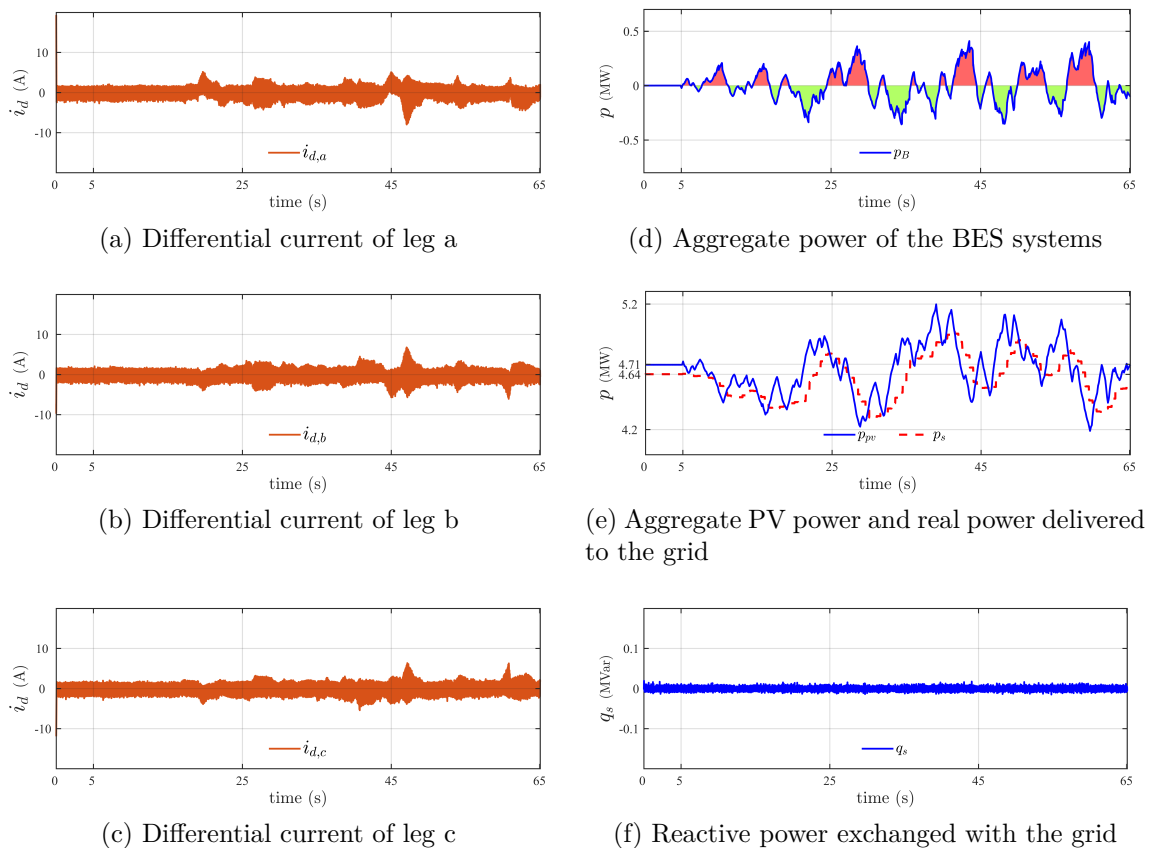
Figure 4.7: Response to power fluctuations (case 1)

the grid is depicted in Figure 4.7(f) which confirms that the reactive power is regulated at zero. This case study demonstrates the effectiveness of exchanging power with the embedded BES systems in limiting the rate of change of the power delivered to the host grid by the MMC-based PV-BES system.

4.8.2 Case 2: Power Mismatches in the Legs and arms

This case demonstrates the performance of the proposed MMC-based PV-BES system and its control strategy in presence of power mismatches between the arms and legs of the converter.

This case does not involve power smoothing function which means that the reference power for the batteries are provided solely by the power mismatch elimination function. Thus, initially the PV generators are all subjected to STC (solar irradiation $1000 \, \text{W/m}^2$

and temperature 25ºC). Then, at $t = 0.05$ s, the solar irradiation of the PV generators of the upper arm of leg a is decreased gradually to $950 \, \text{W/m}^2$ while that of the lower arm of leg a remains unchanged, which results in a decline in the generated power of the PV generators of the upper arm of leg a, as shown in Figures 4.8(a) and 4.8(b). This irradiation change causes $87 \, \text{kW}$ arm power mismatch in leg a and also leg power mismatch since the aggregate power delivered to leg a is less than that of the other two legs. However, since the power mismatch is less than the power rating of the embedded BES systems, the power mismatch is mitigated by exchanging power with the BES systems without creating differential currents. The power exchange of the BES systems of the upper and lower arm of leg a in response to the power mismatch are shown in Figures 4.8(g) and 4.8(h).

As shown in Figure 4.8(c), at $t = 0.1$ s, the power of the PV generators connected to the upper arm of phase b is decreased from $0.873 \, \text{MW}$ to $0.7 \, \text{MW}$. This power mismatch grows beyond the power rating of the BES systems at $t = 0.26$ s where the BES of the upper arm of phase b reaches its power limit, as shown in Figure 4.8(i). The BES system of the lower arm of leg a reaches its maximum charging power at $t = 0.5$ s as shown in Figure 4.8(j). As a result, a differential current is created in the system to transfer power between the arms and legs of the converter as shown in Figures 4.9(a) through 4.9(c). As perceived from Figure 4.9, between $t = 0.05$ s and $t = 0.26$ s, the power mismatches are mitigated using the power exchange with the embedded BES systems without the need for differential currents.

At $t = 0.3$ s, the solar irradiation of the PV generators of the upper arm of leg c is reduced causing their generated power to decrease from $0.873 \, \text{MW}$ to $0.522 \, \text{MW}$. At $t = 0.6$ s the change is reversed to evaluate the performance of the proposed configuration and controller when the power mismatch returns within the power rating of the BES systems. Figures 4.8(e) and 4.8(f) show the power generated by the PV generators of the upper and lower arm of leg c, respectively. As shown in Figure 4.8(k), the power of the BES system of the upper arm of leg c increases upon initiation of the power mismatch
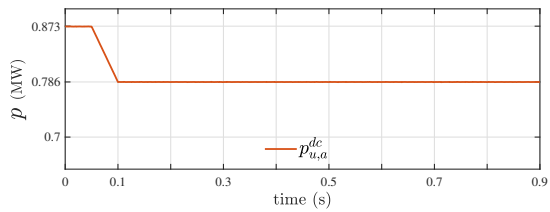
(a) PV power of the upper arm of leg a
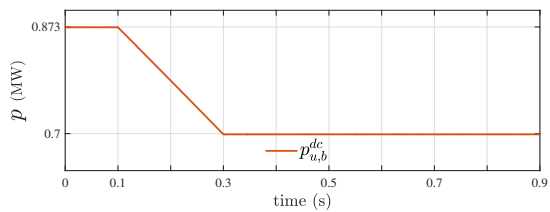
(b) PV power of the lower arm of leg a

(c) PV power of the upper arm of leg b

(d) PV power of the lower arm of leg b

(e) PV power of the upper arm of leg c

(f) PV power of the lower arm of leg c

(g) BES power of the upper arm of leg a
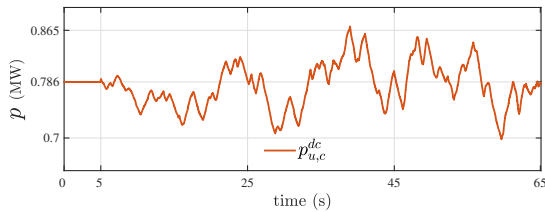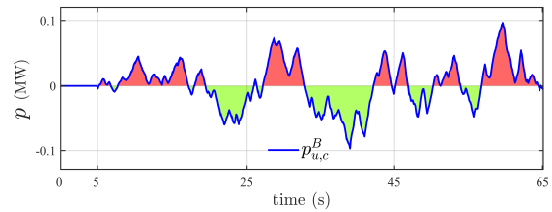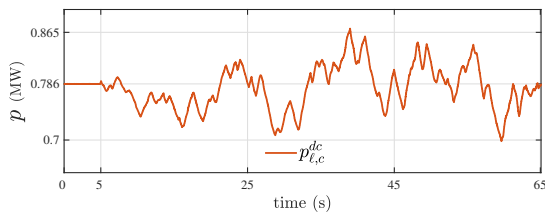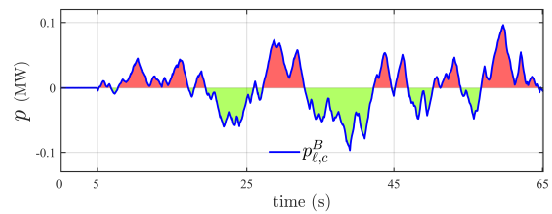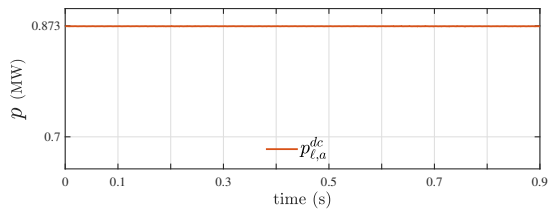
(h) BES power of the lower arm of leg a

(i) BES power of the upper arm of leg b

(j) BES power of the lower arm of leg b

(k) BES power of the upper arm of leg c

(l) BES power of the lower arm of leg c

Figure 4.8: PV and BES power for each arm (case 2)

(a) Differential current of leg a

(b) Differential current of leg b

(c) Differential current of leg c

(d) Aggregate power of the BES systems

(e) Aggregate PV power and real power delivered to the grid

(f) Reactive power exchanged with the grid

Figure 4.9: Response to power mismatches (case 2)

and after reaching its maximum power, a differential current is created to transfer power between arms and legs of the converter as shown in Figure 4.9(a) through 4.9(c). The power of the BES system of the lower arm of leg c reaches its maximum charging power at $t = 0.5$ s as shown in Figure 4.8(l). At $t = 0.7$ s, where the generated power of the PV generators of the upper arm in leg c is increases and the power mismatch falls within the power rating of the BES systems, the differential current becomes smaller while the remaining power mismatch is eliminated by the embedded BES systems.

Figure 4.9(d) shows the aggregate power exchanged with the embedded BES systems to mitigate the power mismatches.The aggregate power generated by the PV generators and the real power delivered to the host grid are shown in Figure 4.9(e). The difference between two powers shown in Figure 4.9(e) is because of the internal power loss of the systems and the power that the BES systems exchange with the arms of the system.

The reactive power exchanged with the grid and measured at PCC is shown in 4.9(f) which shows that the reactive power follows its setpoint and remains at zero with small oscillations during transients.

This case demonstrated the effectiveness of the proposed configuration and its enabling control schemes in minimizing the differential current required to eliminate power mismatches in the MMC-based PV-BES system. Small power mismatches which are within the power rating of the BES systems are eliminated without any differential currents and larger power mismatches are eliminated using the power exchange with the BES systems and power transfer between the legs and arms of the system.

4.8.3 Case 3: Simultaneous Power Smoothing and Power Mismatch Elimination

This case evaluates the performance of the proposed MMC-based PV-BES system and its enabling control scheme in presence of power mismatches and intermittency in the solar irradiation which causes output power fluctuations. In this case, the reference power of the BES systems is the sum of the reference power due to both power mismatch elimination and power smoothing functions. As in the previous two cases, the reference power of the BES systems are examined using the flowchart shown in Figure 4.4 to determine if they are within the power rating of the BES systems.

The PV generators are initially subjected to solar irradiation of $800\,\mathrm{W/m^2}$. Then, at $\mathrm{t}=1\,\mathrm{s}$, the solar irradiation of the PV generators are switched to an intermittent irradiation making their output power fluctuate, as shown in Figures 4.10(a) through 4.10(f). At $\mathrm{t}=4\,\mathrm{s}$, the solar irradiation of the PV generators of the upper arm of leg b is decreased by $100\,\mathrm{W/m^2}$ which corresponds to arm and leg power mismatches while the solar irradiation fluctuates intermittently. The embedded BES systems react to the power mismatches and eliminate them by exchanging power with their corresponding arms, as shown in Figures 4.10(g) through 4.10(l). At $\mathrm{t}=7\,\mathrm{s}$, the solar irradiation of the PV generators of the upper arm of leg c is reduced by $300\,\mathrm{W/m^2}$. The arm and leg
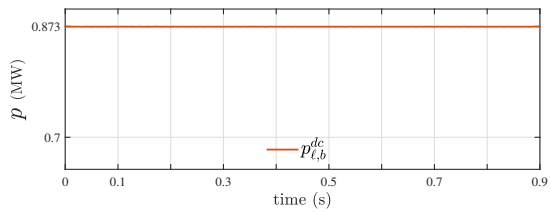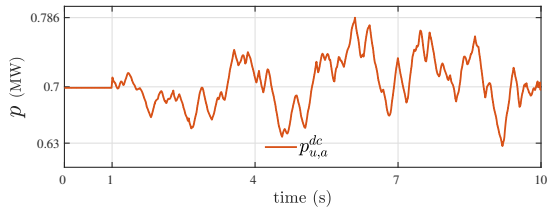
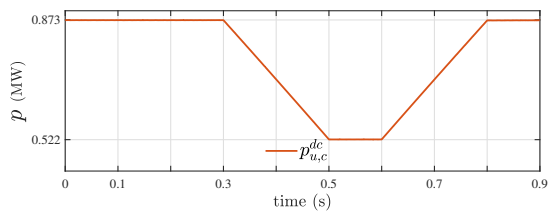(a) PV power of the upper arm of leg a
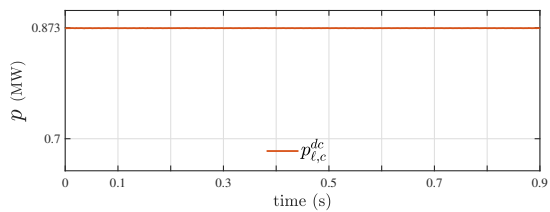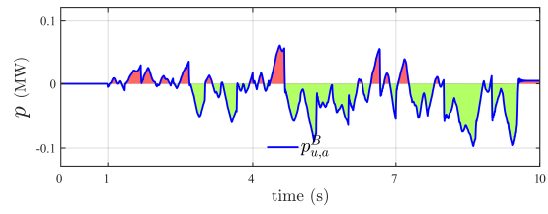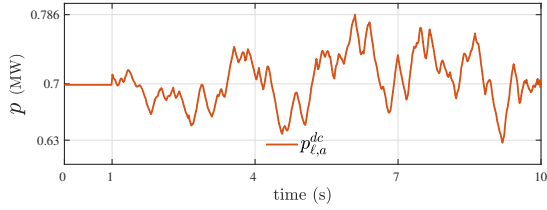
(b) PV power of the lower arm of leg a

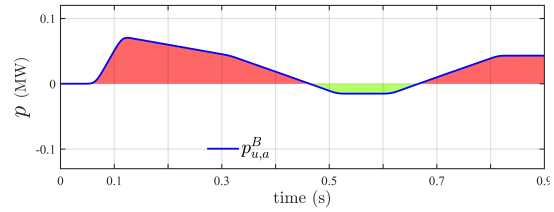(c) PV power of the upper arm of leg b
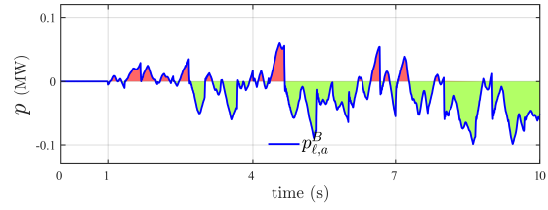
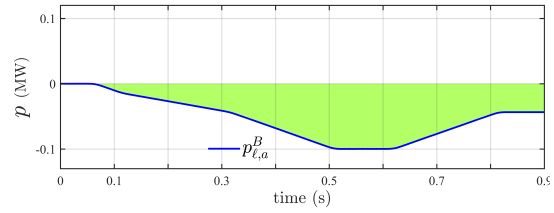(d) PV power of the lower arm of leg b
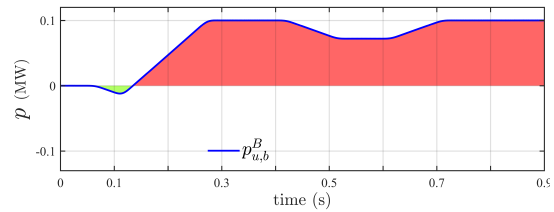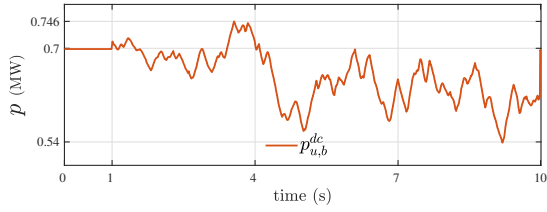
(e) PV power of the upper arm of leg c
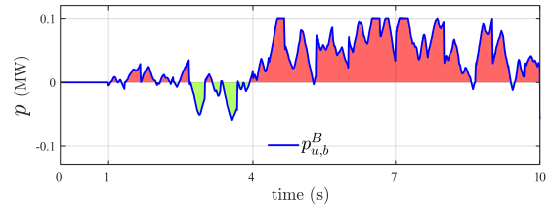
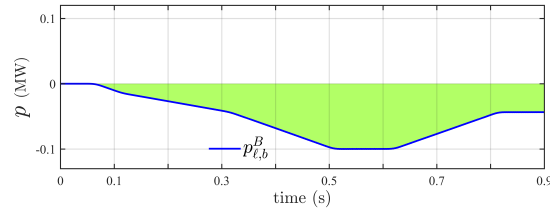(f) PV power of the lower arm of leg c
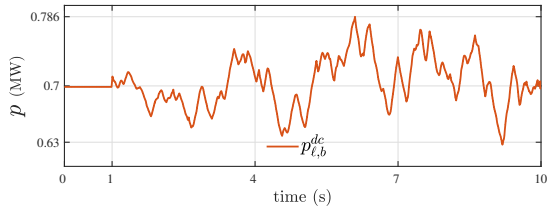
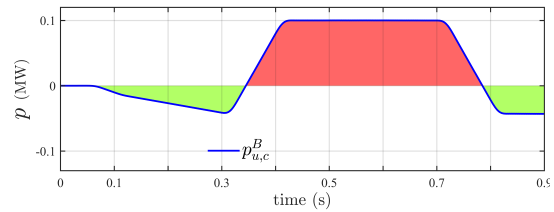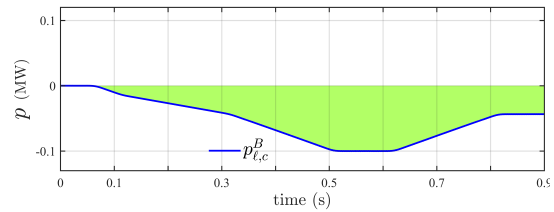(g) BES power of the upper arm of leg a
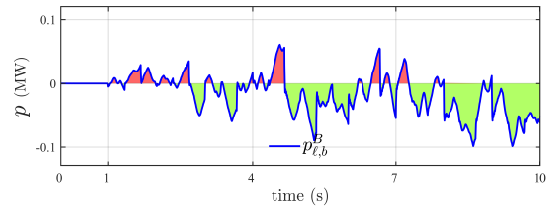
(h) BES power of the lower arm of leg a
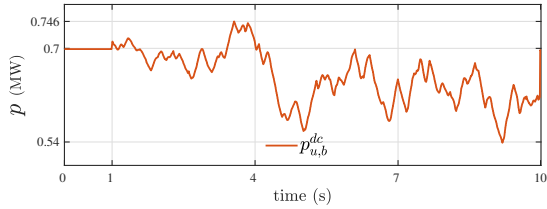
(i) BES power of the upper arm of leg b
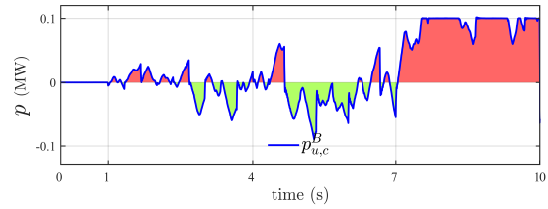
(j) BES power of the lower arm of leg b
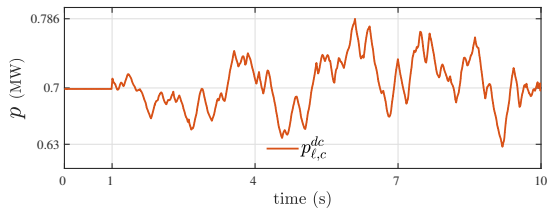
(k) BES power of the upper arm of leg c
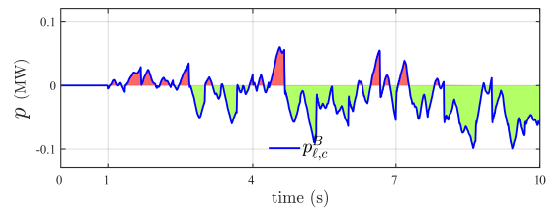
(l) BES power of the lower arm of leg c

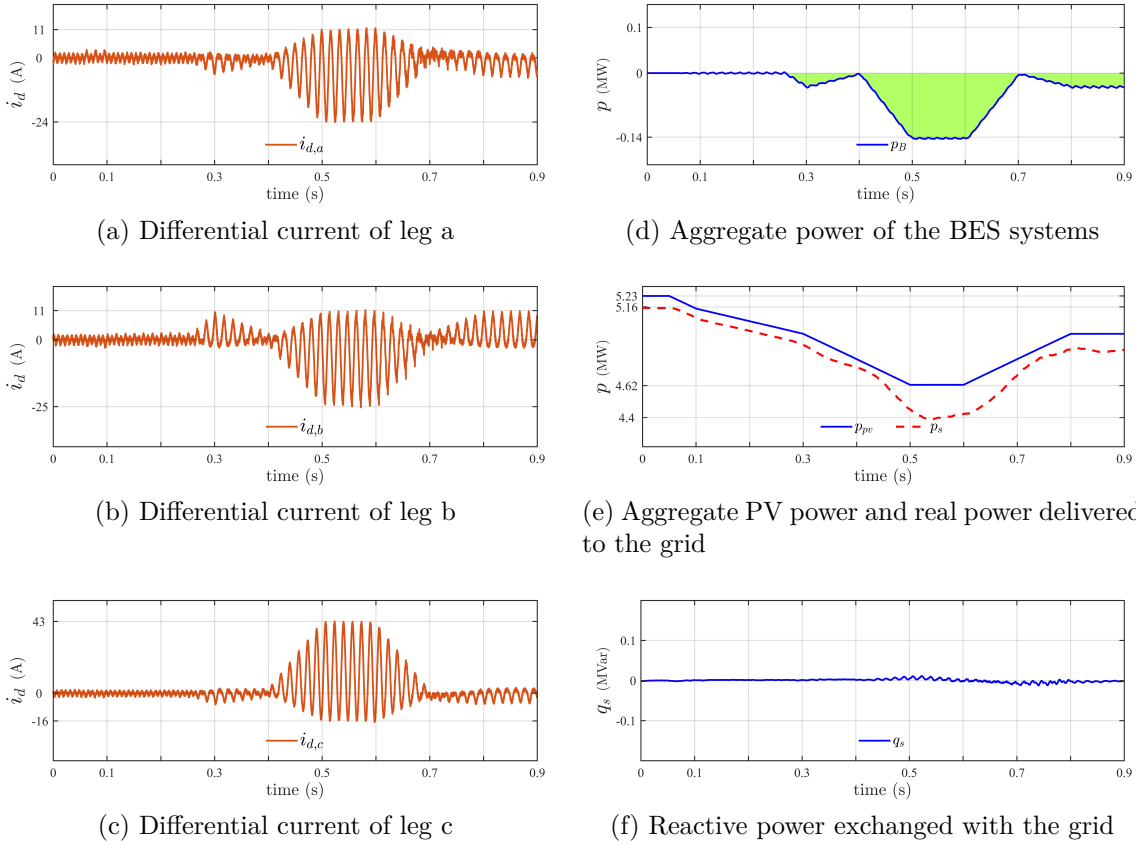Figure 4.10: PV and BES power for each arm (case 3)

(a) Differential current of leg a

(b) Differential current of leg b

(c) Differential current of leg c

(d) Aggregate power of the BES systems

(e) Aggregate PV power and real power delivered to the grid

(f) Reactive power exchanged with the grid
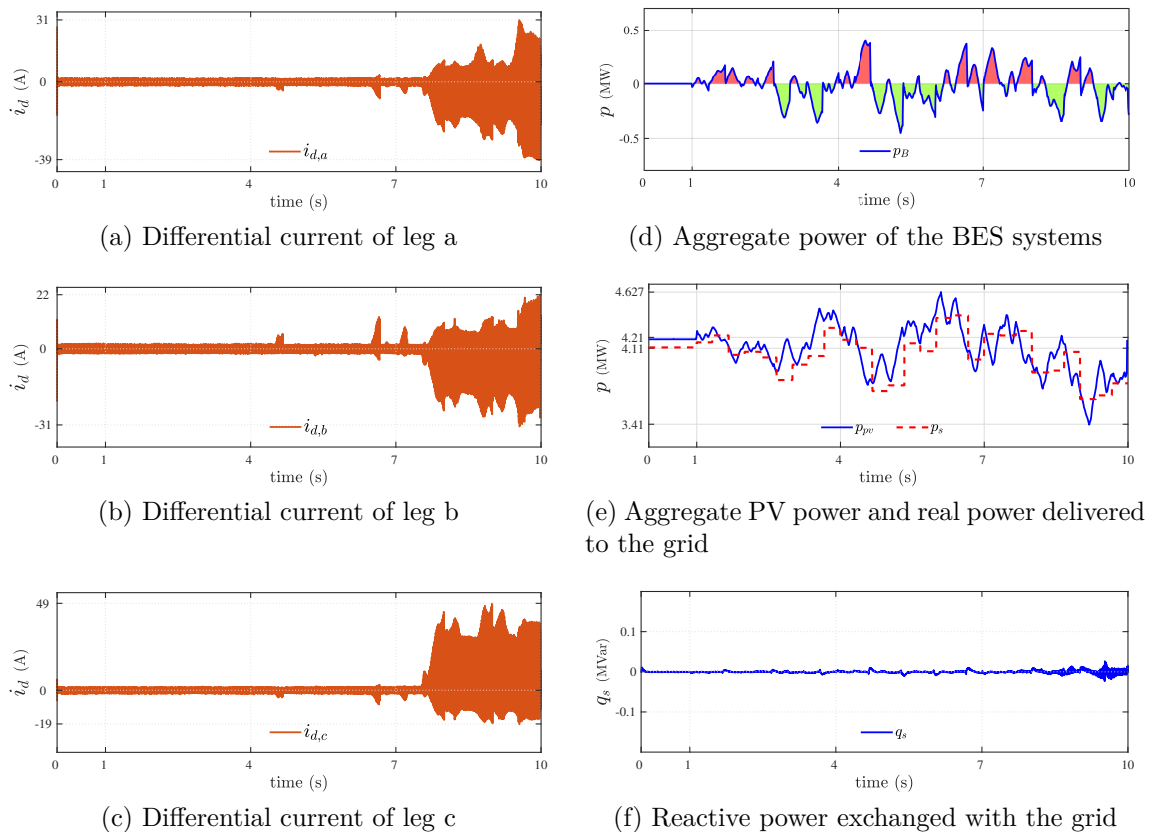
Figure 4.11: Response to simultaneous power mismatches and power fluctuations (case 3)

power mismatches caused by this irradiation decline fall outside the power rating of the BES systems. Consequently, differential currents are created inside the structure of the MMC-based PV-BES system, as shown in Figures 4.11(a) through 4.11(c), which transfer power between the arms and legs of the converter to ensure that balanced currents are injected into the host grid. The differential currents comprise of dc and ac components due to the presence of arm and leg power mismatches.

Figure 4.11(d) shows the aggregate power exchanged with the BES systems. As explained earlier, one of the benefits of using simple moving average algorithm is that at the end of the day, the battery banks will have the same state of charge as they had the previous day since the average of the SMA output is likely zero over the span of a day. Figure 4.11(e) shows the aggregate power generated by the PV generators and the real power exchanged between the MMC-based PV-BES system and the host grid. The power

delivered to the grid is much smoother than the power generated by the PV generators and the differential currents in the structure of the system are minimized both owing to the proposed MMC-based PV-BES configuration and its enabling control scheme. The reactive power follows its reference and remains at zero, as shown in Figure 4.11(f), while the real power changes smoothly according to the output of the SMA algorithm.

4.9 Summary

A new structure and power mismatch elimination strategy for a medium-voltage PV-BES system is proposed in this chapter. The proposed PV-BES system employs a modular multi-level converter (MMC) of which the PV submodules are interfaced with PV generators using multiple dc-dc dual active bridge (DAB) converters enabling independent maximum power point tracking (MPPT) and grounding of the PV generators. The battery energy storage (BES) submodules are embedded into the structure of the MMC system where each arm hosts a BES submodule. The BES submodules are interfaced with the battery banks using a dc-dc DAB converter which controls the amount of power exchange with the batteries. The proposed hybrid power mismatch elimination strategy utilizes the power exchange capability with the embedded BES systems to eliminate small power mismatches without creating differential currents. Moreover, for large power mismatches, the proposed hybrid power mismatch elimination strategy employs the power exchange with embedded BES systems and internal power flow control of the MMC to mitigate the power mismatch with minimum differential current. The proposed power mismatch elimination strategy ensures that one third of the generated PV power is injected into the host grid from each phase of the converter and also keeps the injected currents balanced in despite of unequal PV power generation in each leg of the converter. The embedded storage systems are also used to smooth the output power of the PV system and limit the rate of change of the power injected into the grid. The effectiveness of the proposed power mismatch elimination strategy is demonstrated by time-domain

simulations conducted on a representative model of the system in PSCAD/EMTDC environment.

Chapter 5

Power Mismatch Elimination in Unbalanced Grids

The proposed power mismatch elimination strategy for the MMC-based PV system transfers power between the legs of the converter and ensures that equal amount of power is delivered to the grid from each phase of the converter. The effectiveness of the proposed strategy is confirmed in a balanced grid. However, if the grid voltage is unbalanced, the injection of equal powers from each phase to the grid will result in unbalanced currents since the voltage of the grid is unbalanced. A modified power mismatch elimination strategy is proposed in this chapter which takes into account the unbalanced grid voltages. The amount of power that must be delivered to the grid from each phase of the converter to maintain balanced grid currents is defined according to the voltage magnitude of each phase. Higher power is needed to be delivered to the grid from the phase associated with higher voltage while lower power will be delivered from the phase with lower voltage. Consequently, the currents delivered to the grid remains balanced in spite of the unbalanced grid voltages.

The proposed modified power mismatch elimination strategy is explained throughly and its performance is evaluated in the following sections.

5.1 Structure of the MMC-based PV system

The structure of the MMC-based PV system is the same as that in Chapter 3. However, it has been introduced again for reference purposes. The MMC-based PV system is comprised of three legs that are associated with three phases of the grid. Each leg of the converter includes two arms namely upper and lower arms. The arms of the converter are formed by series connection of N submodules. Each submodule consists of one half-bridge dc-ac converter, n isolated dc-dc converters which are fed by their associated sets of series- and parallel-connected PV generators. The isolated dc-dc converter is assumed to be the dual active bridge (DAB) topology with a medium frequency isolation transformer. Each DAB converter controls the voltage of its associated PV generator to implement maxim power point tracking (MPPT). Due to the galvanic isolation provided by the DAB converters, it is possible to ground the negative pole of the PV generators that enables the alleviation of potential-induced degradation (PID) phenomenon [71]. The dc-dc converter used to interface PV generators with the dc side of the half-bridge converter is required to have galvanic isolation. Consequently, any dc-dc topology which offers galvanic isolation and required power rating could be potentially used. The use of DAB converter is because of its practical implementations of up to 100 kW [86, 87]. Figure 5.1 and 5.2 show the structure of the MMC-based PV system and its submodules for reference purpose.

5.2 Proposed Modified Power Mismatch Elimination Strategy

The final goal of the MMC-based PV system of Figure 5.1 is to exert the maximum power from the PV generators and deliver it to the host grid using balanced and symmetrical currents. However, presence of power mismatches in the structure of the converter interferes with the aforementioned goal. An MMC-based PV system being controlled by the
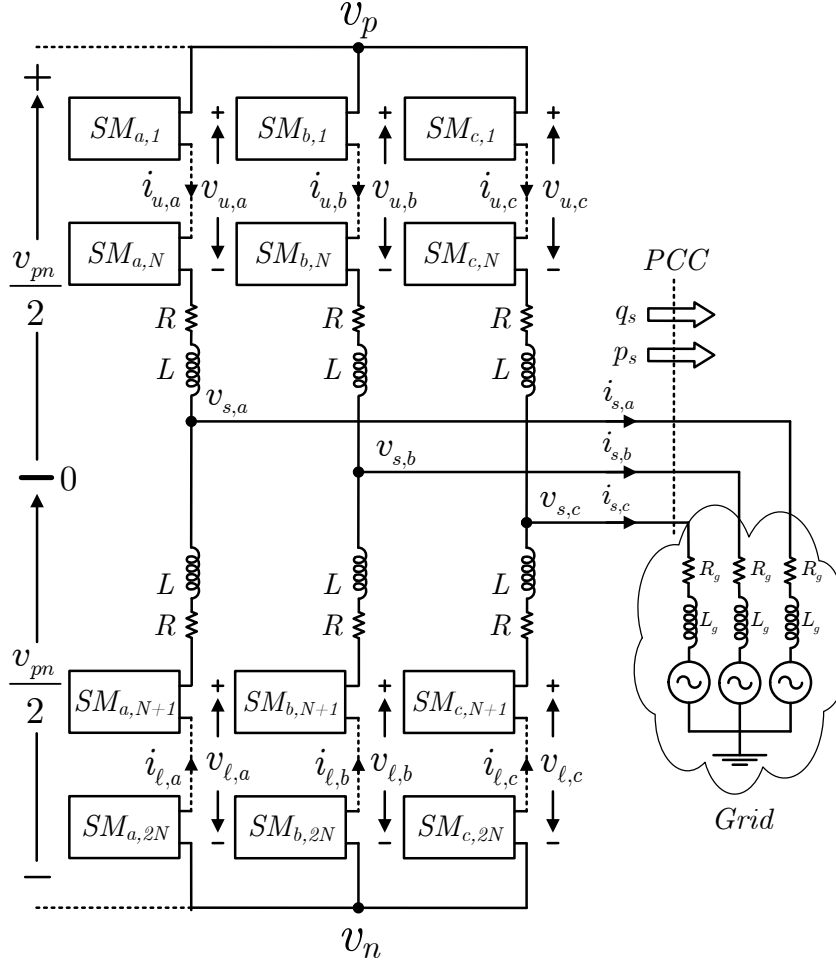
Figure 5.1: MMC-based PV system

conventional current controller fails to inject balanced currents into the grid if a power mismatch exists in the system. There are three possible types of power mismatches in the MMC-based PV system. The first type of power mismatch is *leg power mismatch* which happens between the legs of the converter when the aggregate power delivered to the legs of the converter by their associated PV generators are not equal. The second type of power mismatch is called *arm power mismatch* and happens when the aggregate powers delivered to the upper and lower arm of a phase are not equal. The third type of power mismatch is known as *submodule power mismatch* and happens when the powers delivered to the submodules of one arm are not equal. The leg and arm power mismatches require additional controllers to be alleviated while the submodule power mismatch is mitigated using submodule voltage balancing algorithm.
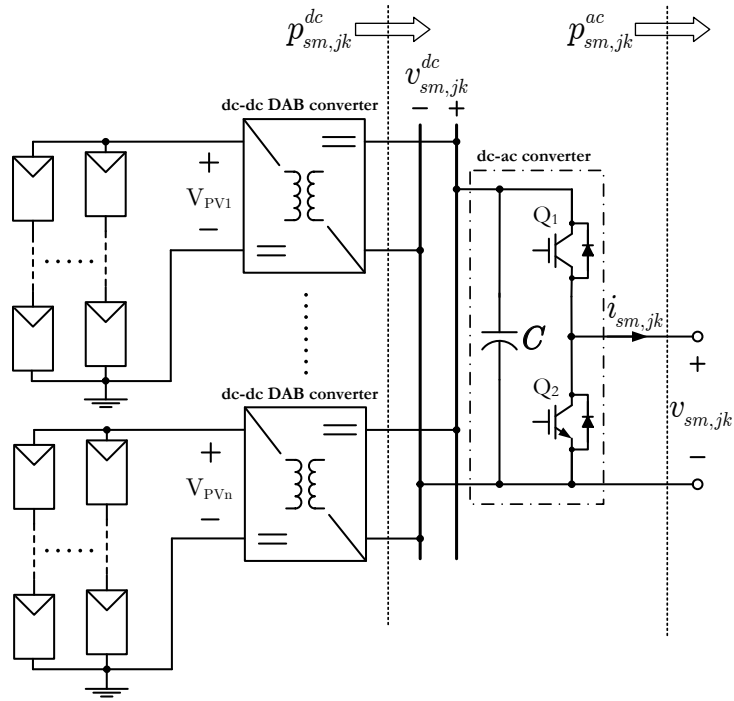
Figure 5.2: Structure of a submodule in the PV system

5.2.1 MMC-based PV system

The impact of unbalanced grid voltage on the current delivered to the grid is nullified using a modification to the power mismatch elimination strategy proposed in Chapter 3. If the grid voltage is balanced, the amount of power injected into the grid through each phase has to be equal to ensure balanced grid currents. However, in an unbalanced grid, the amount of power delivered to the grid through each phase depends on the magnitude of the voltage of that phase. This section elaborates on the modifications applied on the power mismatch elimination strategy for MMC-based PV system.

5.2.1.1 Leg Power Mismatch Elimination

The ultimate goal is to deliver the generated power to the host grid using balanced currents. This criterion can be represented as

$$I_{s,a} = I_{s,b} = I_{s,c} \tag{5.1}$$

where $I_{s,k}$ is the RMS value of the current injected to the host grid by phase k. The average power delivered to the grid through phase k, P_k, is given by

$$P_k = V_{s,k}I_{s,k}cos(\phi_k) \tag{5.2}$$

where $V_{s,k}$ and ϕ_k are the RMS value of the phase voltage and the phase angle of the phase voltage at the PCC, respectively. However, since the asymmetry in the phase angle of the three-phase grid voltage is extremely rare, the imbalance considered in this thesis only includes voltage magnitude imbalance. As a result, (5.2) is reduced to

$$P_k = V_{s,k}I_{s,k}cos(\phi) \tag{5.3}$$

Assuming that the grid voltage is unbalanced, voltage imbalance ratio for each phase is defined as

$$\lambda_k = \frac{V_{s,k}}{V_n} \tag{5.4}$$

where V_n is the nominal RMS voltage of the host grid at PCC. Using (5.1) through (5.4), one can deduct

$$\frac{P_a}{\lambda_a} = \frac{P_b}{\lambda_b} = \frac{P_c}{\lambda_c} \tag{5.5}$$

The sum of the powers delivered to the grid must be equal to the aggregate power delivered to the MMC-based PV system from the PV generators. As a result,

$$P_a + P_b + P_c = P_{PV} \tag{5.6}$$

where P_{PV} is the aggregate power generated by the PV generators. Substitution of (5.5)

into (5.6) yields

$$P_a = \frac{\lambda_a}{\lambda_a + \lambda_b + \lambda_c} P_{PV}$$
$$P_b = \frac{\lambda_b}{\lambda_a + \lambda_b + \lambda_c} P_{PV}$$
$$P_c = \frac{\lambda_c}{\lambda_a + \lambda_b + \lambda_c} P_{PV} \tag{5.7}$$

Equation (5.7) shows that to deliver balanced currents into the grid while the grid voltage is unbalanced, the phase associated with higher voltage must deliver higher power to the grid whereas the phase associated with lower voltage must deliver less power.

The difference between the aggregate power generated by the PV generators of a leg and the power that must be delivered to the grid through its associated phase is called *leg power mismatch* and is mathematically represented as

$$p_k^{ex} = P_k - p_k^{dc} \tag{5.8}$$

where p_k^{dc} is the aggregate power delivered to the dc links of the submodules of leg k. A positive p_k^{ex} means that the aggregate power generated by the PV generators of leg k is smaller than the power that has to be delivered to the grid through its associated phase. Consequently, power equal to p_k^{ex} needs to be transferred from the other two legs to leg k. Similarly, a negative p_k^{ex} means that the aggregate power generated by the PV generators of leg k is larger than the power that has to be delivered to the grid through its associated phase. As a result, power equal to p_k^{ex} needs to be transferred out of leg k. The reference dc differential current, $i_{d,k}^{dc*}$, corresponding to leg power mismatch is given by

$$i_{d,k}^{dc*}(t) = \frac{p_k^{ex}(t)}{v_{pn}} \qquad k = a, b, c \tag{5.9}$$

where v_{pn} is the common dc link voltage of the system, as illustrated in Figure 5.1.

The dc differential currents must not enter the grid. As a conclusion, the sum of the

dc differential currents at nodes p and n which is given by (5.10) must be zero.

$$i_{d,a}^{dc*} + i_{d,b}^{dc*} + i_{d,c}^{dc*} = \frac{p_a^{ex} + p_b^{ex} + p_c^{ex}}{v_{pn}}$$

$$= \frac{(P_a + P_b + P_c) - \overbrace{(p_a^{dc} + p_b^{dc} + p_c^{dc})}^{P_{PV}}}{v_{pn}} \tag{5.10}$$

According to (5.6), the numerator of (5.10) is zero. As a result, the dc differential currents cancel out at nodes p and n, meaning that converter injects balanced currents into the host grid regardless of terminal voltage imbalance.

5.2.1.2   Arm Power Mismatch

If the amount of power delivered to the arms of a leg by their PV generators are not equal, an arm power mismatch exists in the system. Arm power mismatch can potentially cause leg power mismatch as well. Arm power mismatch can be alleviated by exerting unequal powers from the arms. The amount of power leaving the ac terminals of the submodules of each arm has to be equal to the amount of power delivered to the dc sides of the submodules to ensure stable dc link voltages.

In order to maintain dc link voltage stability, an ac differential current has to be generated in the structure of the MMC. The ac differential currents are calculated using differential power of each leg defined as

$$p_{d,k} = \frac{p_{u,k}^{dc} - p_{\ell,k}^{dc}}{2} \simeq \overline{v_{e,k} i_{d,k}^{ac}} \tag{5.11}$$

where $p_{u,k}^{dc}$ and $p_{\ell,k}^{dc}$ are the aggregate powers generated by the PV generators of the upper and lower arm of leg k, respectively. Terms $v_{e,k}$ and $i_{d,k}^{ac}$ are the internal voltage and ac component of the differential current of leg k. Having defined the differential power for each leg, the corresponding reference ac differential currents are calculated using the procedure presented in Section 3.4.2. The relationship between the differential powers

and ac differential currents is given by

$$
\begin{bmatrix} \hat{i}_d^1 cos\phi_1 \\ \hat{i}_d^1 sin\phi_1 \\ \hat{i}_d^2 cos\phi_2 \\ \hat{i}_d^2 sin\phi_2 \end{bmatrix} = \frac{2}{3\hat{v}_e} \begin{bmatrix} 1 & 1 & 1 & 0 \\ 0 & 0 & 0 & -1 \\ 2 & -1 & -1 & 0 \\ 0 & \sqrt{3} & -\sqrt{3} & 0 \end{bmatrix} \begin{bmatrix} p_{d,a} \\ p_{d,b} \\ p_{d,c} \\ q_d \end{bmatrix} \tag{5.12}
$$

Having calculated the ac differential currents corresponding to the differential powers, the $\alpha\beta$-frame components of the ac differential currents are calculated as

$$
\begin{aligned}
i_{d,\alpha}^{ac*}(t) + ji_{d,\beta}^{ac*}(t) &= \left[\hat{i}_d^1 \, cos\phi_1 + j\hat{i}_d^1 \, sin\phi_1 \right] e^{j\phi(t)} \\
&+ \left[\hat{i}_d^2 \, cos\phi_2 - j\hat{i}_d^2 \, sin\phi_2 \right] e^{-j\phi(t)}
\end{aligned} \tag{5.13}
$$

where $\hat{i}_d^1$ and $\hat{i}_d^2$ are the magnitudes of the positive- and negative-sequence ac differential currents, respectively. The terms ϕ_1 and ϕ_2 are the phase angles of the positive- and negative-sequence ac differential currents with respect to the internal voltage of the converter.

The $\alpha\beta$-frame components of the ac differential currents are then transferred to abc-frame using

$$
\begin{bmatrix} i_{d,a}^{ac*} \\ i_{d,b}^{ac*} \\ i_{d,c}^{ac*} \end{bmatrix} = \begin{bmatrix} 1 & 0 \\ -\frac{1}{2} & \frac{\sqrt{3}}{2} \\ -\frac{1}{2} & -\frac{\sqrt{3}}{2} \end{bmatrix} \begin{bmatrix} i_{d,\alpha}^{ac*} \\ i_{d,\beta}^{ac*} \end{bmatrix} \tag{5.14}
$$

Having calculated the dc and ac components of the differential currents using (5.9) and (5.14), final differential current is calculated as

$$
i_{d,k}^* = i_{d,k}^{dc*} + i_{d,k}^{ac*} \tag{5.15}
$$

Then, differential current controller (DCC) is used to generate the reference differential
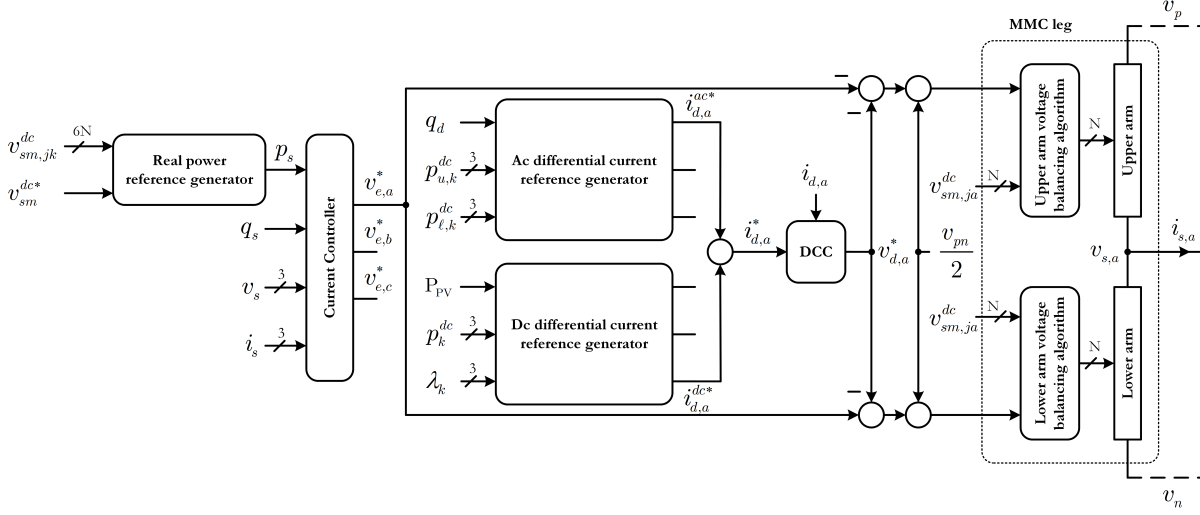
Figure 5.3: Schematic of the controller for the MMC-based PV system

currents inside the structure of the MMC-based PV system. DCC comprises of a PI and a PR compensator tuned at fundamental frequency. Figure 5.3 shows the schematic of the controller elaborating on the reference voltage generation for the upper and lower arms of leg a. The process for generation of the reference voltages for the other two legs is the same as leg a.

5.2.2   MMC-based PV-BES system

There are two distinct approaches to eliminate the effects of unbalanced grid voltage in an MMC-based PV-BES system. The first method is to use the power exchange with the embedded BES systems to deliver unequal powers to the grid from each phase of the converter. However, if the voltage imbalance is persistent, this approach will cause the BES systems to be completely discharged or fully charged which is not desirable in this application. The second approach is to use the power transfer between the legs of the converter without involving the BES systems. The second approach is more desirable and is used in this section for the MMC-based PV-BES system.

The amount of power mismatch for the MMC-based PV-BES system is calculated as

$$p_k^{ex}(t) = P_k(t) - p_k^{dc}(t) - p_{u,k}^{B}(t) - p_{\ell,k}^{B}(t) \tag{5.16}$$

where $P_k(t)$ is calculated using (5.7) that takes into account the voltage imbalance to calculate the power that needs to be delivered to the grid from each phase. The power references for the BES systems, $p^B_{u,k}(t)$ and $p^B_{\ell,k}$, are calculated without considering the grid voltage imbalance as

$$P^{B*}_{j,k}(t) = P^{BS*}_{j,k}(t) + P^{BM*}_{j,k}(t) \qquad (5.17)$$

Having defined the power mismatch for each leg of the converter, DCC is used to generate the differential currents and ensure that balanced currents are delivered to the grid regardless of the unbalanced grid voltage.

5.3 Simulation Results

The effectiveness of the proposed modified power mismatch elimination strategy in presence of grid voltage imbalance is demonstrated using a representative model of the system. Selected simulation results are presented in this section which confirm the effectiveness of the proposed strategy. The simulated MMC-based PV system embeds 10 submodules with power rating of 100 kW, and with dc voltage reference of 0.8 kV in its arms. The grid voltage is 4.16 kV (line-to-line, rms) and is represented using its Thevenin equivalent. Table 3.1 lists the parameters of the MMC-based PV system.

5.3.1 Case 1: Grid Voltage Imbalance

This case demonstrates the performance of the proposed power mismatch elimination strategy in presence of grid voltage imbalance. Throughout the simulation, the PV generators are subjected to standard testing condition (STC). However, the grid voltage is unbalanced at $t = 0.1$ s causing the reaction of the controller.

The ambient condition for the PV generators remains unchanged throughout the simulation. Consequently, the aggregate power delivered to the arms of the converter are

(a) Aggregate dc power of the arms of leg a

(d) Voltage magnitude of phase a

(b) Aggregate dc power of the arms of leg b

(e) Voltage magnitude of phase b

(c) Aggregate dc power of the arms of leg c

(f) Voltage magnitude of phase c
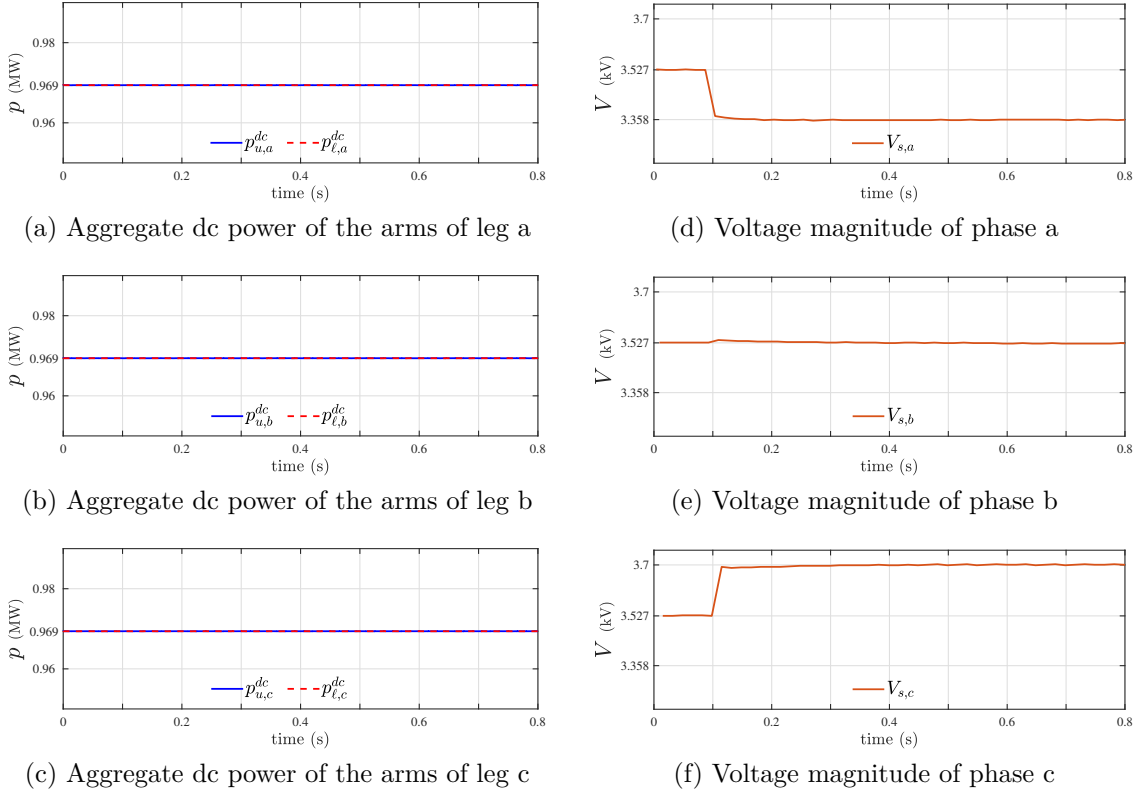
Figure 5.4: Unbalanced grid condition (case 1)

equal as shown in Figures 5.4(a) through 5.4(c). Since the aggregate powers generated by the PV generators of the arms are equal, the system is in balanced condition and power mismatches are zero. At $t = 0.1$ s, the voltage of the grid is unbalanced. The magnitude of the voltage of phase a is decreased to 95% while that of phase c is increased to 105%, whereas, the magnitude of the voltage of phase b remains unchanged. The magnitudes of the phase voltages are shown in Figures 5.4(d) through 5.4(f). The introduced grid voltage imbalance calls for injection of lower power from phase a and higher power from phase c to maintain the balanced operation of the system. Consequently, some power has to be transferred from phase a to phase c. Upon occurrence of the voltage imbalance, the voltage imbalance ratio of each phase is altered leading to power transfer between the legs of the system.

The differential currents generated in the MMC-based PV system due to the grid voltage imbalance are shown in Figures 5.5(a) through 5.5(c). The differential current of

(a) Differential current of leg a

(b) Differential current of leg b

(c) Differential current of leg c

(d) Current magnitude of phase a

(e) Current magnitude of phase b

(f) Current magnitude of phase c
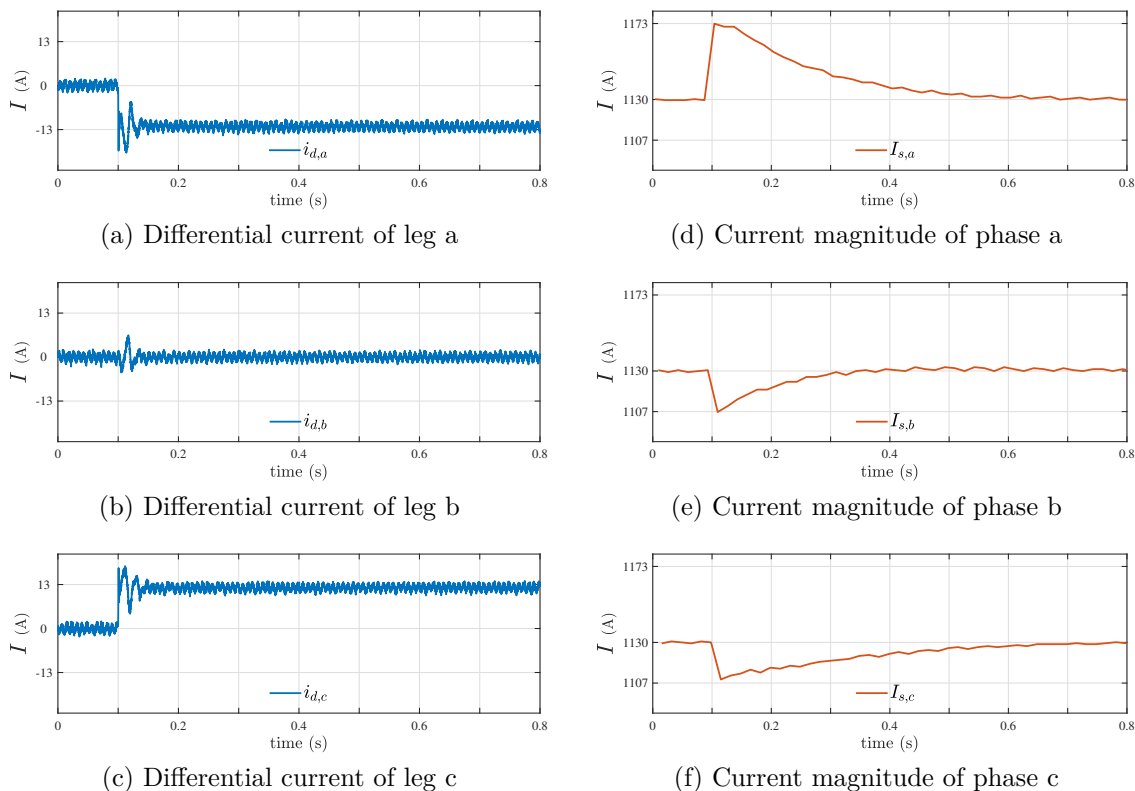
Figure 5.5: Response to unbalanced grid voltage (case 1)

leg a is negative while that on leg c is positive, confirming that power is being transferred from leg a to leg c since the power delivered to the grid through phase c is higher than that of phase a. Following the inception of grid voltage imbalance, the magnitudes of the grid currents become unequal as shown in Figures 5.5(d) through 5.5(f). However, owing to power transfer between leg a and c, the magnitude of the grid currents return to be equal again.

Figure 5.6(a) shows the three-phase grid currents which become unbalanced after the grid voltage imbalance and become balanced again after that the proposed power mismatch elimination strategy transfers power between the legs of the system. The real and reactive power exchanged with the grid is shown in Figure 5.6(b). Both real and reactive powers oscillate following the voltage imbalance and again settle at their respected references.
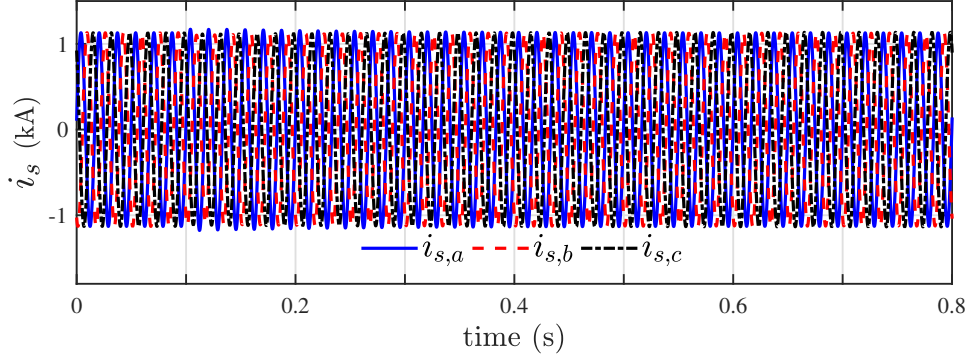
(a) Grid currents
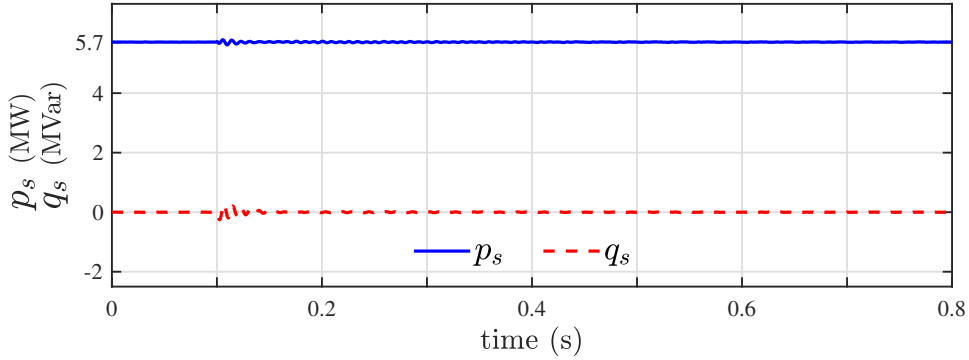
(b) Real and reactive power

Figure 5.6: Grid interactions (case 1)

5.3.2   Case 2: Power Mismatch with Grid Voltage Imbalance

This case evaluates the performance of the proposed modified power mismatch elimination strategy to eliminate leg and arm power mismatches in a grid with unbalanced voltage. Initially, before $t = 0.1$ s, the grid voltage is unbalanced and the controller has generated dc differential currents to transfer power between the legs of the converter, the same as case 1. Then, at $t = 0.1$ s, the solar irradiation of the PV generators of leg a is declined from 1000 W/m² to 500 W/m², decreasing their power output to about half. Consequently, a leg power mismatch develops in the system. The reaction of the modified power mismatch elimination strategy is to transfer power from the other two legs to leg a by creating a dc differential current in the system. At $t = 0.2$ s, the solar irradiation of the PV generators of the upper arm of leg b is decreased from 1000 W/m² to 500 W/m² which corresponds to an arm power mismatch. The proposed modified power mismatch

(a) Aggregate dc power of the arms of leg a

(b) Aggregate dc power of the arms of leg b

(c) Aggregate dc power of the arms of leg c

(d) Voltage magnitude of phase a

(e) Voltage magnitude of phase b

(f) Voltage magnitude of phase c
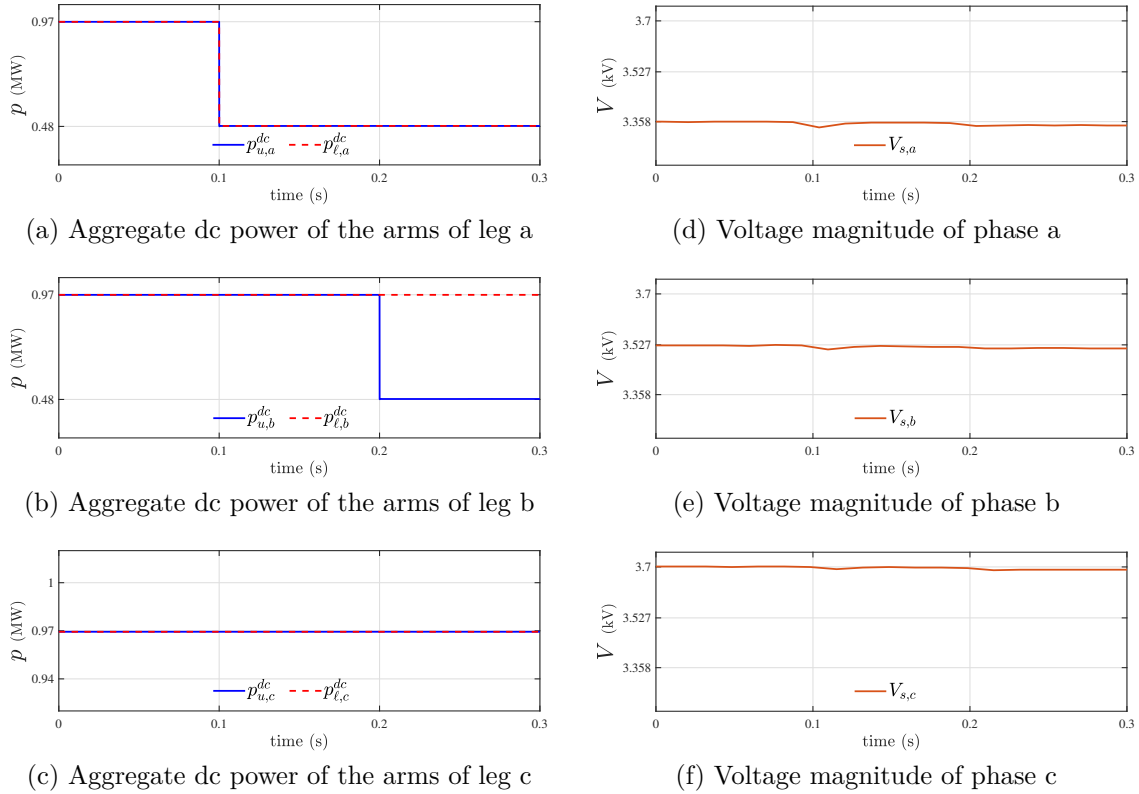
Figure 5.7: Unbalanced grid condition (case 2)

elimination strategy creates an ac differential current which exerts all the power injected into the dc links of the submodules of each arm.

Figures 5.7(a) to 5.7(c) show the dc powers delivered to each arm of the system by their associated PV generators. The voltage of the grid is unbalanced throughout the simulations as shown in Figures 5.7(d) through 5.7(f). The voltage of phase a is 5% lower than nominal voltage while that of phase c is %5 higher than nominal voltage. The voltage of phase b is unchanged and remains equal to the nominal voltage.

The differential currents generated by the proposed power mismatch elimination strategy are shown in Figures 5.8(a) to 5.8(c). Due to the grid voltage imbalance, a small dc differential current is generated by the power mismatch elimination strategy which can be appreciated in Figures 5.8(a) to 5.8(c) before $t = 0.1$ s. Following the leg power mismatch at $t = 0.1$ s, a relatively large dc differential current is generated which transfers power between the legs of the converter. Likewise, following the arm power mismatch at $t = 0.2$ s,

(a) Differential current of leg a

(b) Differential current of leg b

(c) Differential current of leg c

(d) Current magnitude of phase a

(e) Current magnitude of phase b

(f) Current magnitude of phase c
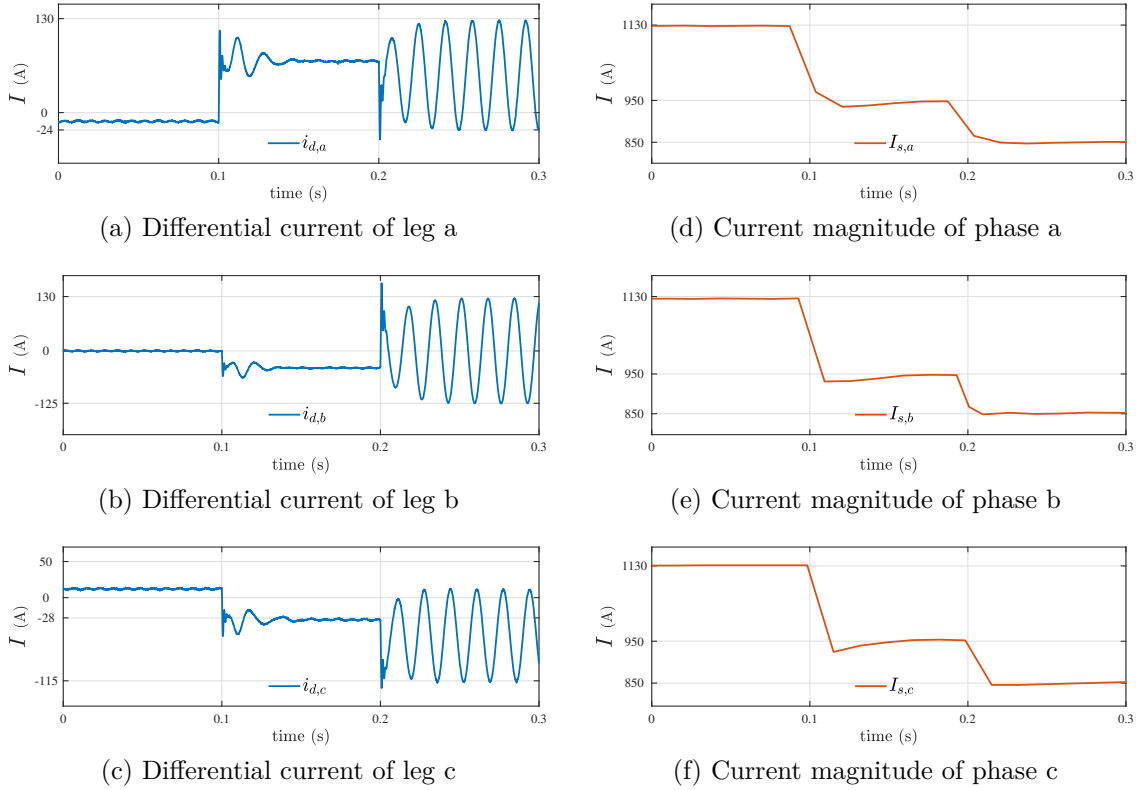
Figure 5.8: Response to unbalanced grid voltage (case 2)

the proposed strategy generates an ac differential current which ensures that right amount of power is extracted from each arm of the converter. Figures 5.8(d) through 5.8(f) show the magnitude of the three-phase currents injected into the grid from each phase of the system. The magnitude of the currents injected into the grid is declined following each solar irradiation decrease while remaining balanced despite the power mismatches and the grid voltage imbalance.

As shown in Figure 5.9(a), the grid currents are balanced in spite of grid voltage imbalance and power mismatches. The magnitude of the grid currents decline after each irradiation decrease to maintain the balance between the generation and the power delivered to the grid. The real and reactive power exchanged with the grid at PCC are shown in Figure 5.9(b). Consequent to each solar irradiation decline, the real power delivered to the grid decreases while the reactive power remains at its reference, i.e. zero.

(a) Grid currents

(b) Real and reactive power
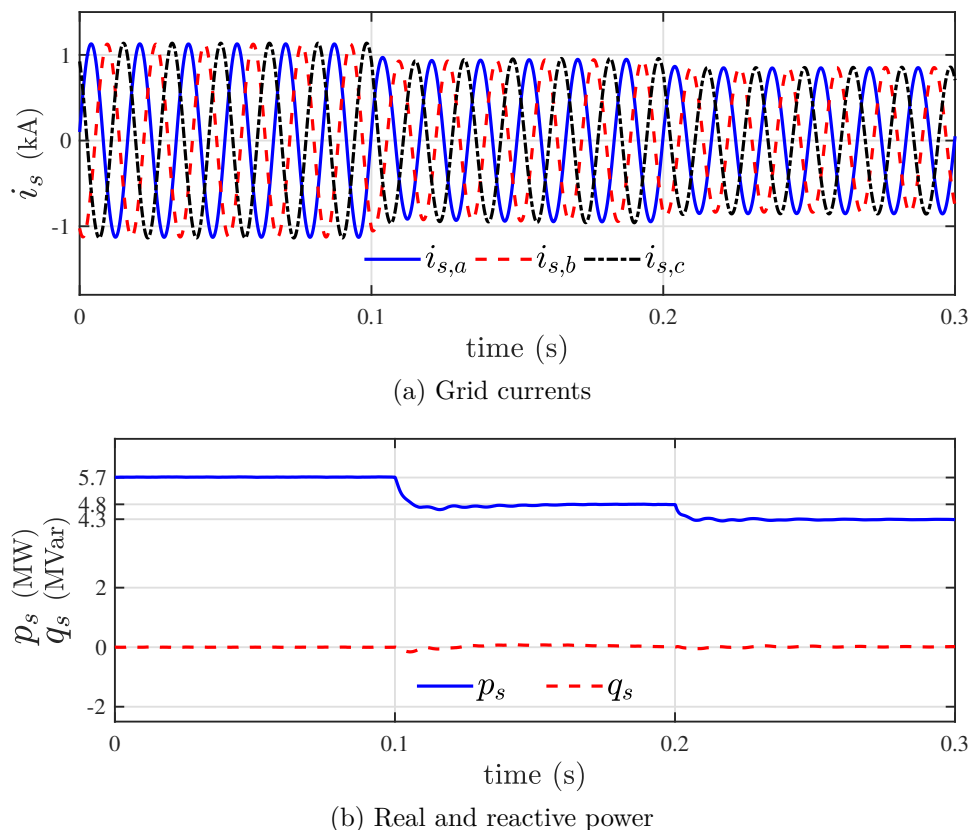
Figure 5.9: Grid interactions (case 2)

5.4 Summary

A modified power mismatch elimination strategy for an MMC-based PV system is proposed in this chapter. The proposed strategy is capable of injecting balanced and symmetrical currents into the grid regardless of grid voltage imbalance and internal power mismatches. In the MMC-based PV system, the PV generators are interfaced with the dc link of the submodules using dual active bridge (DAB) converters. The DAB converters provide galvanic isolation which enables the grounding of the negative pole of the PV strings to alleviate potential-induced degradation (PID). DABs also implement maximum power-point tracking (MPPT) on the PV strings to harvest the maximum power from the PV generators. The amount of the power delivered to the grid through each phase depends on the voltage magnitude of that phase. If the grid voltage is balanced, equal powers will be delivered to the grid through each phase. The power mismatch

elimination strategy uses dc differential currents to transfer power between the legs of the converter. It also uses ac differential currents to exert all the power injected into the arms of the MMC-based PV system. Mathematical bases and enabling schemes of the proposed modified power mismatch elimination strategy are presented in this paper. The effectiveness of the modified power mismatch elimination strategy is demonstrated using a representative model simulation in time-domain simulation environment.

Chapter 6

Conclusion, Contributions, and Future Work

6.1 Summary

The outlook of the growing number of high-power grid-connected PV systems has moti-vated extensive research efforts towards resolving technical challenges of the grid integra-tion of PV farms. The main objective of this thesis is to address some concerns related to transformerless integration of PV farms.

In Chapter 1 of this thesis, the research objectives are presented. Chapter 1 also includes background information on application of MMC for grid integration of PV gen-erators.

Chapter 2 presents the structure of the MMC and modeling of the dynamics of grid current, differential current, and common dc link voltage. The next topic in Chapter 2 is the controller design for grid current, differential current, and common dc link voltage. In the end, modulation techniques for synthesizing the reference voltage of the MMC-based PV system is introduced.

Structure and controller design procedure for the MMC-based PV system is presented in Chapter 3. The proposed power mismatch elimination strategy for the MMC-based

PV system is also presented in this chapter that is able to eliminate leg and power mismatches without any interactions with the host grid.

A new structure for a hybrid MMC-based PV-BES system and its enabling control scheme is presented in Chapter 4. The proposed structure embeds one battery energy storage system in each arm of the converter and the proposed control scheme utilizes the embedded BES systems to eliminate power mismatches and smoothen the output power of the PV system.

In Chapter 5, a modification to the proposed power mismatch elimination strategies is proposed enabling them to maintain balanced grid currents regardless of internal power mismatches and grid voltage imbalance.

6.2   Conclusions

The conclusions drawn from this thesis are aligned with the objectives of the research to enable transformerless grid integration of PV farms using MMC. The research carried out in this thesis is profoundly different from the existing power mismatch elimination method since it does not alter the terminal voltage of the converter in any way, it is capable of removing all types of power mismatches in the system, it can eliminate arm power mismatches, and it can eliminate large power mismatches. All the aforementioned advantages of the proposed techniques are absent in the existing power mismatch elimination techniques. The conclusions are as follows:

- It was discussed that the MMC-based PV system has the potential to be used for grid integration of PV systems. The merits of MMC over other converter topologies are discussed and concluded that the MMC-based PV system offers features which are absent in other topologies.

- The MMC-based PV system can reach medium to high voltages without the need for a central iron-core three-phase transformer operating at 50 Hz or 60 Hz. The modularity offered by the proposed MMC-based PV system, as well as the footprint

and weight characteristics, high manufacturing costs (due to the custom nature of the transformer), and high transportation costs associated with a large iron-core transformer are expected to justify the medium-frequency isolated transformer needed for each submodule of proposed PV system.

- Owing to the isolated DAB converters used in the submodules of the system, the MMC-based PV system can be connected to the host grid without the need for coupling transformer. The required galvanic isolation is provided by the medium-frequency transformer of the DAB converters. The isolation transformer of DAB topology also enables grounding of the negative pole of the PV strings to alleviate potential-induced degradation (PID).

- The proposed real power reference generation scheme removes the nonlinear relationship between the submodules dc link voltages by calculating a virtual voltage which is comprised of the sum of the squares of the submodule dc link voltages and the real power of the system, making it easier to control with a proportional-integral (PI) controller.

- The proposed power mismatch elimination strategy is capable of mitigating leg and arm power mismatches in the MMC-based PV system without altering the terminal voltage of the converter.

- The proposed configuration of the MMC-based PV-BES system enables the utilization of the embedded BES systems to remove power mismatches.

- The proposed enabling scheme for embedding BES systems into arms of the converter enables the power exchange with the BES systems to remove power mismatches and smoothen the output power of the PV system.

- Unbalanced grid voltage requires unequal power injection into the grid from each phase in order to maintain balanced current delivery to the host grid. The proposed modifications to the power mismatch elimination strategy enables them to deliver

balanced currents to the grid regardless of the power mismatches and grid voltage imbalance.

- The proposed power mismatch elimination strategy enables the use of the MMC for PV integration. This method can be very beneficial for companies that already manufacture MMC for HVDC applications. These companies can adapt the proposed techniques to expand the application of their existing MMCs to PV applications.

- The MMC-based PV system removes the need for coupling transformer while adding multiple medium-frequency transformers to the converter. It should be noted that the use of isolating medium-frequency transformers is needed to enable grounding of negative pole of the PV strings and protect the PV generators against high voltages even with existence of a coupling transformer. The power rating of the medium-frequency transformers is much smaller the the coupling transformer and have much smaller footprint. Considering the aforementioned benefits of medium-frequency transformers and the high price of coupling transformer, the use of the multiple low-power medium-frequency transformers instead of a single high-power line-frequency transformer is justified.

6.3 Contributions

The thesis presents the following contributions.

- A new real power reference generation scheme is proposed based on mathematical modeling and lumping the submodules of the system into one equivalent submodule in each arm. The proposed real power reference generation scheme derives a relationship between the real power reference of the system and square of the virtual dc link voltage. This relationship removes the nonlinear relationship between the submodule dc link voltages and the real power reference making real power refer-

ence generation possible with a PI controller. The square of the virtual voltage is equal to the sum of the squares of the dc link voltages of all submodules.

- A new power mismatch elimination strategy for the MMC-based PV system is proposed which can eliminate leg and arm power mismatches with transferring power between legs of the converter. The strategy ensures that one-third of the aggregate power generated by the PV generators is delivered to the grid through each phase of the system leading to balanced current injection into the grid. This contribution can be considered the most important contribution of this work since the next contributions are based on this contribution.

- A new configuration for the MMC-based PV-BES system is proposed which embeds one battery energy storage system in each arm of the converter. The embedded BES systems are then used to provide power mismatch elimination service to the converter.

- A new enabling control strategy for the MMC-based PV system is proposed. The proposed enabling scheme generates the reference powers for the BES systems in an effort to minimize the differential currents. If the power mismatches are within the power rating of the embedded BES systems, the power mismatches will be eliminated by exchanging power with the BES systems without the need for differential currents. However, if the power mismatch is outside the power rating of the BES systems, a combination of power exchange with the BES systems and power transfer between the legs of the converter is used to eliminate power mismatches and deliver balanced currents into the grid.

- The embedded BES systems are used to limit the rate of change of power delivered to the grid. As a result of the power smoothing function of the proposed enabling control scheme for embedded BES systems, the power delivered to the grid is smoother than the aggregate power generated by the PV generators.

- A new modifications on the power mismatch elimination strategy is proposed which takes into account the grid voltage imbalance. Based on the proposed modified power mismatch elimination strategy, the converter phase with higher voltage delivers higher power to the grid and the phase with lower voltage delivers lower power to the grid to ensure that the currents injected into the grid are balanced.

6.4   Future Work

The following topics are suggested for future work:

1. Application of the proposed MMC-based PV-BES system in a hybrid dc and ac microgrid where the converter operates as a generation, storage, and power bridge between the two microgrids. A new addition to the existing controller is required to control the amount of power transfer between two microgrids and generate the references for the BES systems.

2. Using quadruple active bridge (QAB) in the structure of the MMC-based PV system to generate isolated three-phase voltages from a single dc source. This structure potentially removes the inception of power mismatches in the first place by equally dividing the power generated by the PV generators between the legs of the converter.

3. Since the proposed method can deliver desired amount of current from each phase to the grid, this feature can be used to balance the voltage of an unbalanced grid.

Appendix A

PV Model

Parameters of the PV generator used in this thesis are shown in Table A.1. All the parameters are give in standard testing condition (STC).

Table A.1: Parameters of the PV generators

Parameter	Value	Remarks
number of series-connected PV modules per string	23	N_s
number of parallel-connected PV strings	3	N_p
generator short-circuit current (STC)	135 A	I_{sc}
generator open-circuit voltage (STC)	937 V	V_{oc}
generator maximum-power current (STC)	128 A	I_{mp}
generator maximum-power voltage (STC)	762 V	V_{mp}
voltage temperature coefficient	-0.48 A/K	K_V
current temperature coefficient	0.02 A/K	K_I
diode ideality factor	1.3	a
reference solar irradiation	1000 W/m²	G_r
reference p-n junction temperature	25°C	T_r
equivalent series resistor per cell	0.02 Ω	R_s
equivalent parallel resistor per cell	1000 Ω	R_p
PV module maximum power	330 W	P_{mpp}
PV generator maximum power	97.7 kW	P_{pv}

Figure A.1 shows the single-diode equivalent circuit of a real PV cell [90]. The circuit is composed of: the current source I_g, a diode in parallel with the current source , the series resistance R_s, and the parallel resistance R_p. The basic equation describing the nonlinear current-voltage relationship of the PV cell is

$$I(V) = I_i(V)I_p(V) = I_g - I_d(V) - I_p(V)$$
$$= I_g - I_o(e^{\frac{\beta(V+R_sI)}{R_P}}) \tag{A.1}$$

where I and V are the terminal current and voltage of the actual PV cell, I_i and V_i are the terminal current and voltage of the ideal PV cell, I_d is the current through the diode, and I_p is the current through R_p. Current I_o is the diode reverse saturation current and β is the inverse thermal voltage defined as

$$\beta(T) = \frac{q}{kT} \tag{A.2}$$

where k is Boltzmann's constant $(1.3806503 \times 10^{-23}\,J/K)$, q is the electron charge $(1.60217646 \times 10^{-19}\,C)$, and T is the p-n junction temperature.
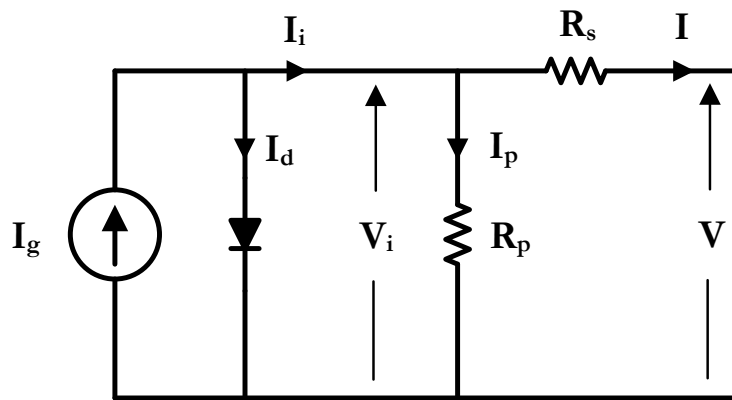
Figure A.1: Single-diode equivalent circuit of PV cell

Figure A.2(a) shows the I-V curve of the PV generator. The short circuit current,
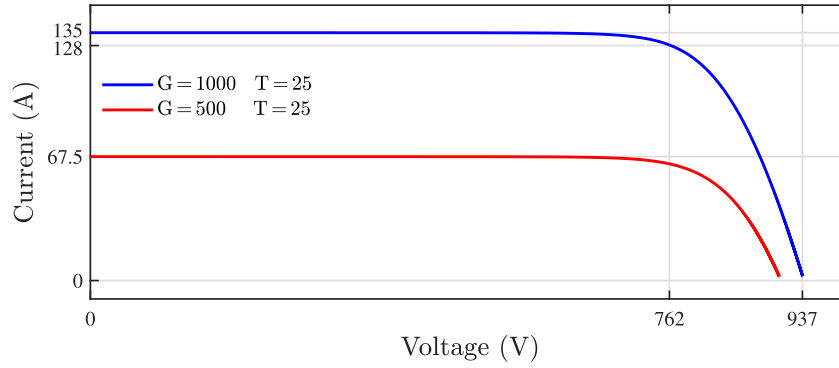
(a) I-V curve
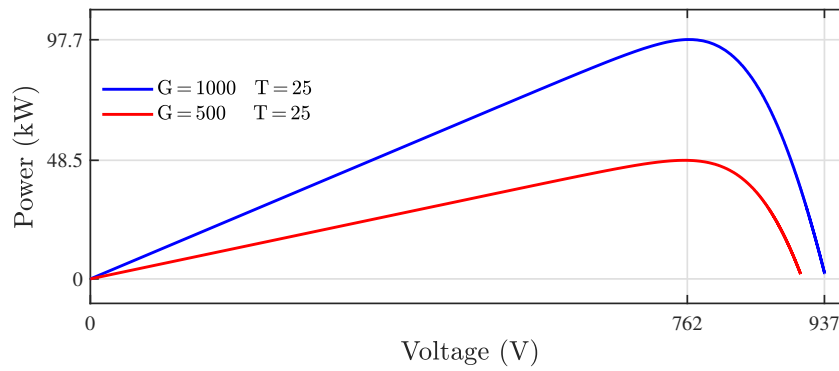
(b) P-V curve

Figure A.2: Characteristic curves of the PV generator

open circuit voltage, and maximum power point current of the PV generators are shown in the A.2(a). The P-V curve of the PV generator is shown in Figure A.2(b) which shows the maximum power and maximum power point voltage of the PV generator.

Appendix B

Battery Model

There are basically three types of battery models reported in the literature, specifically: experimental, electrochemical and electric circuit-based. Experimental and electrochemical models are not well suited to represent cell dynamics for the purpose of state-of-charge (SOC) estimations of battery packs. However, electric circuit-based models can be useful to represent electrical characteristics of batteries. In this thesis, a generic model of battery is used to model the batteries in the BES systems [91]. The battery is modeled using a simple controlled voltage source in series with a constant resistance as shown in Figure B.1. The open circuit voltage is calculated using a non-linear equation based on the actual state of charge (SOC) of the battery.
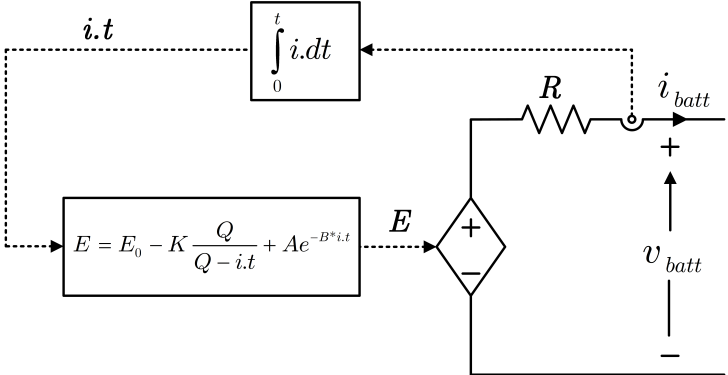
Figure B.1: Battery model

No-load voltage of the battery (E) is calculated using

$$E = E_0 - K\frac{Q}{Q - \int_0^t i.dt} + Ae^{-B\int_0^t i.dt} \tag{B.1}$$

where E_0 is constant voltage of the battery. Other parameters used in (B.1) are

- K: Polarization voltage

- Q: Battery capacity

- i.t: Actual battery charge

- A: Exponential zone amplitude

- B: Exponential zone time constant inverse

- R: Internal resistance

Figure B.2 shows typical discharge curve of a battery modeled using the presented model. The battery banks consist of 64 batteries of IND27-2V Trojan Battery Company which are configured into strings of 16 batteries to reach the voltage rating of 768 V and 4 such strings are connected in parallel to reach the power capacity of 97.23 kAh. Series resistance of the battery bank is considered to be 0.2 ohm.
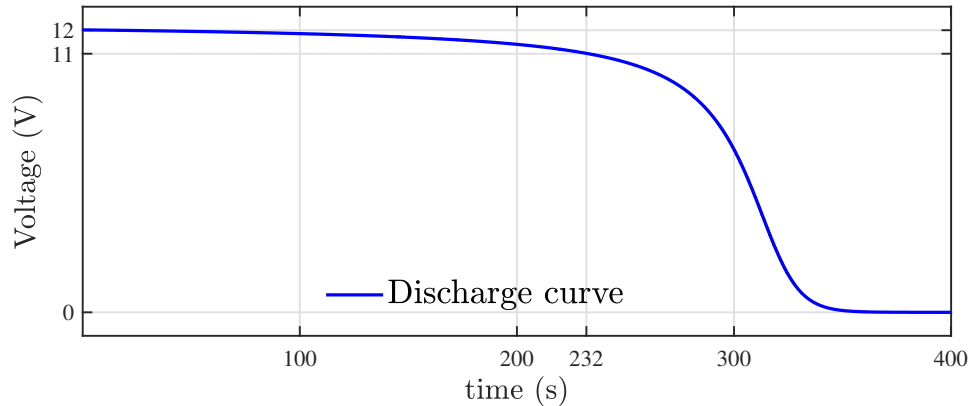
Figure B.2: Battery discharge model

The dc-dc converter used to interface the battery banks with the dc side of the submodule converter controls the power exchanged with the battery bank based on the command received from the power smoothing and power mismatch elimination functions. It also measures the state of charge of the battery banks by continuously integrating the current of the battery banks. The SOC of the battery is used to determine if the storage is able to absorb power or deliver power when requested.

Appendix C

Dual active bridge (DAB) Model

There are different topologies to achieve DC-DC power conversion, however, dual-active-bridge (DAB) converter is considered suitable for a wide range of applications. Microgrids [92,93], hybrid electric vehicles (HEV) [94], fuel cell applications [95], interruptible power supplies (UPS) [95], and energy storage systems [96] are examples of the applications of DAB converter. DAB converter has numerous advantages that make it the converter of choice for the aforementioned applications. Galvanic isolation, zero-voltage switching (ZVS) in a wide loading range, bidirectional power flow, high power, high efficiency, and simple control are prominent advantages of DAB converters.

The galvanic isolation provided by DAB converter through its medium- or high-frequency transformer is much needed in some applications such as PV systems. It enables the grounding of the negative pole of the PV strings and also enables the structure of the MMC-based PV system by preventing the PV submodule from being exposed to high voltages. Figure C.1 shows the topology of the DAB converter used in this thesis. DAB converter is used to interface the PV generators with the dc side of the half-bridge converter of the submodules. The control objective of the DAB used to interface the PV generators is to regulate its input voltage at MPP voltage to extract maximum power from the PV generators.

There are several modulation techniques proposed for DAB converter. The main goal
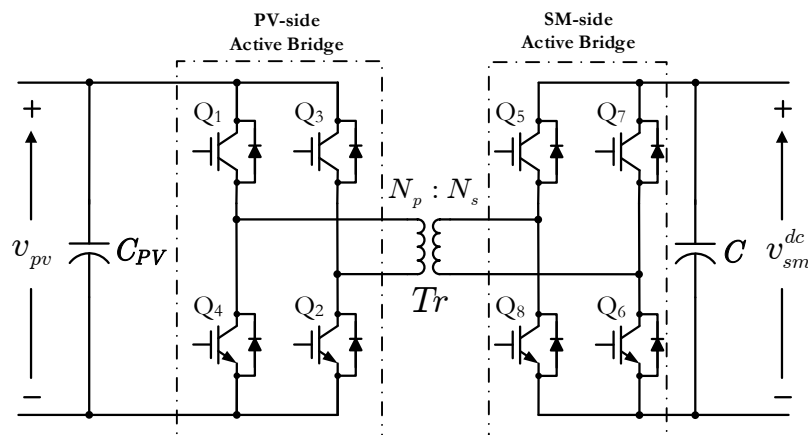
Figure C.1: Dual active bridge (DAB) converter

of modulation techniques is to create a phase shift between the first harmonic of the primary and secondary voltages of the high frequency transformer. Phase shift modulation scheme consists of single phase shift (SPS), dual phase shift (DPS), and triple phase shift (TPS).

SPS is the most popular scheme used in the literature for DAB converter. SPS modulation technique controls a single variable which is the phase angle, ϕ, between the primary and secondary voltages of the transformer. This method controls the amount and direction of real power flow. The simplicity of this modulation method and the possibility of using half bridge circuits to generate the high frequency voltages, $v_p(t)$ and $v_s(t)$, are the main reasons for the wide use of this modulation method. Figure C.2 shows
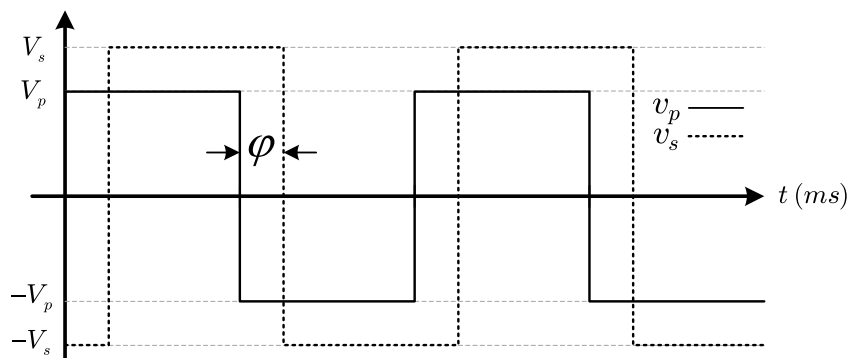
Figure C.2: Single phase shift (SPS)

the waveform of the primary and secondary voltages of the transformer in single phase shift modulation technique.

Limitations of the SPS modulation have persuaded researchers to create a different instance of the phase shift modulation namely dual phase shift (DPS). Beside controlling the phase angle between the primary and secondary voltage of the transformer, this modulation technique generates a three-level voltage at the terminals of the high frequency transformer. The three level voltage is achieved by controlling the duty cycle of the primary and secondary converter. However, the duty cycle of two converters are the same in this scheme [97]. This method enables the control and elimination of circulating reactive current. Figure C.3 shows the primary and secondary voltages in DPS control. Phase angle, ϕ, and duty cycle, D are the two parameters being controlled in this method.
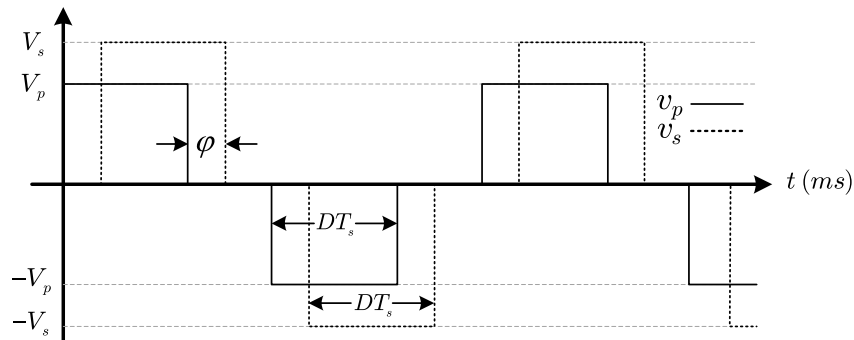
Figure C.3: Dual phase shift (DPS)

Triple phase shift modulation offers three degree of freedom making it more flexible than SPS and DPS. This modulation strategy controls the phase angle between the primary and secondary voltages, the duty cycle of the primary converter, and the duty cycle of the secondary converter independently. Controlling three parameters of the converter, enables this modulation scheme to minimize the current stress of the switches and provides full soft switching operation in the whole load range. The controlled parameters are phase angle ϕ, duty cycle of the primary converter D_1, and duty cycle of the secondary converter D_2 which are depicted in Figure C.4

There are several modeling techniques used to model the behavior of DAB in the
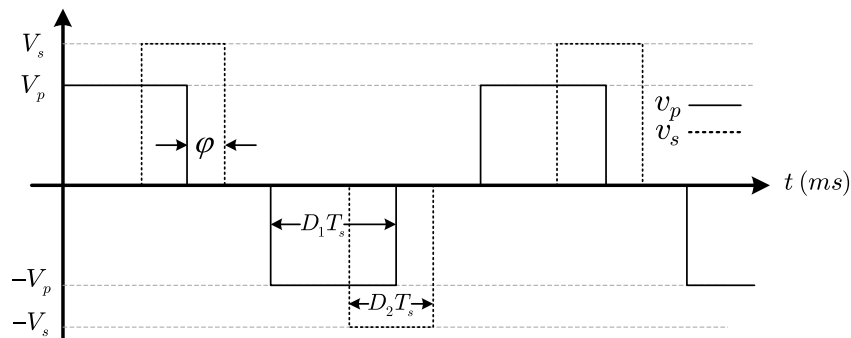
Figure C.4: Triple phase shift (TPS)

literature. The most popular model which gives the behavior of the converter at its input and output terminals is simple average model. This model averages the input and output currents of the converter over a period of switching frequency and uses two controlled current sources to model the DAB converter. The average model of the DAB converter, based on [98], is used for simulation purposes in this thesis. The model is shown in Figure C.5 which replaces the primary and secondary full-bridge converters with controlled currents sources. According to [98], the average input and output currents of
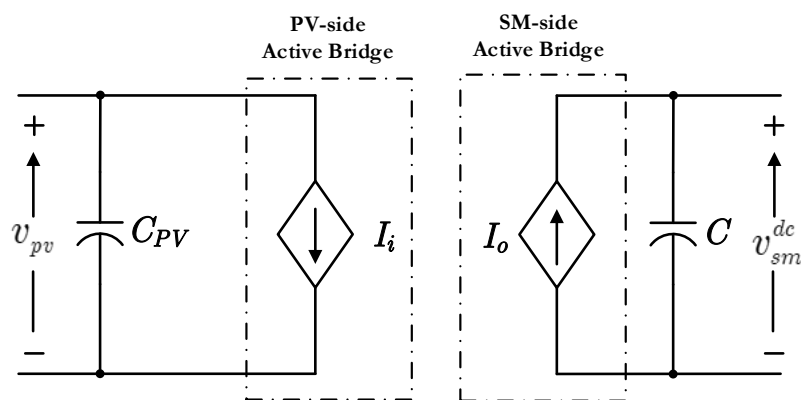
Figure C.5: Average model of the DAB

Table C.1: Parameters of the DAB converter

Parameter	Value	Parameter	Value
L	$60\,\mu H$	f_s	$10\,\text{kHz}$
n	1	v_{pv}	$762\,V$
C	$10\,mF$	v_{sm}^{dc}	800V
C_{pv}	$400\,\mu F$	P_{DAB}	$100\,\text{kW}$

the DAB are

$$I_i = \frac{V_{sm}^{dc}}{2nf_sL}\phi(1 - |\phi|) \tag{C.1}$$

$$I_o = \frac{V_{pv}}{2nf_sL}\phi(1 - |\phi|) \tag{C.2}$$

where n is the turn ratio of the transformer defined as the number of turns of the secondary winding, N_s, divided by that of the primary winding, N_p. The term ϕ represents the phase shift between the square-wave voltage of the primary and secondary bridges. Inductance of the transformer is denoted by L and the switching frequency is represented by f_s. Table C.1 presents the parameters of the DAB used in this thesis.

High-power prototypes of DAB are reported in the literature which have formed the basis for choosing DAB in this thesis. The reported prototypes vary in power rating from very small to $100\,\text{kW}$ implementations. Table C.2 shows a summary of the high-power DAB implementations reported in the literature with their power rating, switch technology, and switching frequency.

Table C.2: Reported high-power DAB prototypes

Reference	[99]	[87]	[86]	[88]
Switch technology	Si-IGBT	Si-IGBT	SiC-MOSFET	SiC-MOSFET
Nominal power	$10\,\text{kW}$	$20\,\text{kW}$	$50\,\text{kW}$	$100\,\text{kW}$
Switching frequency	$20\,\text{kHz}$	$20\,\text{kHz}$	$20\,\text{kHz}$	$20\,\text{kHz}$

Bibliography

[1] Renewable Energy Policy Network for the 21st Century, "Renewables 2015 global status report," 2015.

[2] US Department Of Energy, "The history of solar," 2002.

[3] International Energy Agency (IEA) Power Systems Programme (PVPS), "Annual report 2016," May 2017.

[4] European Photovoltaic Industries Association (EPIA), "Global market outlook for solar power 2017-2021," June 2017.

[5] Renewable Energy Policy Network for the 21st Century, "Renewables 2018 global status report," 2018.

[6] International Energy Agency (IEA) Power Systems Programme (PVPS), "Nationl survey report of pv power applications in canada - 2016," Sept 2017.

[7] S. S. Fazel, D. Krug, T. Taleb, and S. Bernet, "Comparison of power semiconductor utilization, losses and harmonic spectra of state-of-the-art 4.16 kV multi-level voltage source converters," in *Power Electronics and Applications, 2005 European Conference on*, pp. 11 pp.–P.11, Sept 2005.

[8] S. Deore, P. Darji, and A. Kulkarni, "Dynamic phasor modeling of modular multi-level converters," in *Industrial and Information Systems (ICIIS), 2012 7th IEEE International Conference on*, pp. 1–6, Aug 2012.

[9] Q. Song, W. Liu, X. Li, H. Rao, S. Xu, and L. Li, "A steady-state analysis method for a modular multilevel converter," *Power Electronics, IEEE Transactions on*, vol. 28, pp. 3702–3713, Aug 2013.

[10] L. Xiaoqian, S. Qiang, L. Jianguo, and L. Wenhua, "Capacitor voltage balancing control based on CPS-PWM of modular multilevel converter," in *Energy Conversion Congress and Exposition (ECCE), 2011 IEEE*, pp. 4029–4034, Sept 2011.

[11] M. Alsadah and F. Mancilla-David, "Modeling and control of grid-connected photo-voltaic power plants utilizing a simplified model of the modular multilevel converter," in *North American Power Symposium (NAPS), 2014*, pp. 1–6, Sept 2014.

[12] A. Alesina and M. Venturini, "Solid-state power conversion: A fourier analysis approach to generalized transformer synthesis," *Circuits and Systems, IEEE Transactions on*, vol. 28, pp. 319–330, Apr 1981.

[13] M. Glinka and R. Marquardt, "A new AC/AC-multilevel converter family applied to a single-phase converter," in *Power Electronics and Drive Systems, 2003. PEDS 2003. The Fifth International Conference on*, vol. 1, pp. 16–23 Vol.1, Nov 2003.

[14] M. Glinka and R. Marquardt, "A new AC/AC multilevel converter family," *Industrial Electronics, IEEE Transactions on*, vol. 52, pp. 662–669, June 2005.

[15] U. Gnanarathna, A. Gole, and R. Jayasinghe, "Efficient modeling of modular multi-level HVDC converters (MMC) on electromagnetic transient simulation programs," *Power Delivery, IEEE Transactions on*, vol. 26, pp. 316–324, Jan 2011.

[16] F. Deng and Z. Chen, "A control method for voltage balancing in modular multilevel converters," *Power Electronics, IEEE Transactions on*, vol. 29, pp. 66–76, Jan 2014.

[17] R. Darus, J. Pou, G. Konstantinou, S. Ceballos, R. Picas, and V. Agelidis, "A modified voltage balancing algorithm for the modular multilevel converter: Evaluation

for staircase and phase-disposition PWM," *Power Electronics, IEEE Transactions on*, vol. 30, pp. 4119–4127, Aug 2015.

[18] A. Nabae, I. Takahashi, and H. Akagi, "A new neutral-point-clamped PWM inverter," *Industry Applications, IEEE Transactions on*, vol. IA-17, pp. 518–523, Sept 1981.

[19] T. Meynard, H. Foch, P. Thomas, J. Courault, R. Jakob, and M. Nahrstaedt, "Multicell converters: basic concepts and industry applications," *Industrial Electronics, IEEE Transactions on*, vol. 49, pp. 955–964, Oct 2002.

[20] P. Hammond, "A new approach to enhance power quality for medium voltage AC drives," *Industry Applications, IEEE Transactions on*, vol. 33, pp. 202–208, Jan 1997.

[21] A. Lesnicar and R. Marquardt, "An innovative modular multilevel converter topology suitable for a wide power range," in *Power Tech Conference Proceedings, 2003 IEEE Bologna*, vol. 3, pp. 6 pp. Vol.3–, June 2003.

[22] ABB AB Uno Lamm HVDC Centre, "Reference list HVDC light," 2017. Available at `http://new.abb.com/systems/hvdc/hvdc-light`.

[23] Siemens Website, "Reference list HVDC PLUS," 2017. Available at `https://www.energy.siemens.com/ru/en/power-transmission/hvdc/`.

[24] J. Dorn, D. Huang, and D. Retzmann, "Novel voltage-sourced converters for HVDC and FACTS applications," in *Cigre Session, Osaka, Japan*, Nov 2007.

[25] J. Dorn, D. Huang, and D. Retzmann, "A new multilevel voltage-sourced converter topology for HVDC applications," in *Cigre Session, Paris, France*, Aug 2008.

[26] K. Wang, Y. Li, and Z. Zheng, "Voltage balancing control and experiments of a novel modular multilevel converter," in *Energy Conversion Congress and Exposition (ECCE), 2010 IEEE*, pp. 3691–3696, Sept 2010.

[27] S. Debnath, J. Qin, B. Bahrani, M. Saeedifard, and P. Barbosa, "Operation, control, and applications of the modular multilevel converter: A review," *Power Electronics, IEEE Transactions on*, vol. 30, pp. 37–53, Jan 2015.

[28] G. Casadei, R. Teodorescu, C. Vlad, and L. Zarri, "Analysis of dynamic behavior of modular multilevel converters: Modeling and control," in *System Theory, Control and Computing (ICSTCC), 2012 16th International Conference on*, pp. 1–6, Oct 2012.

[29] A. Rasic, U. Krebs, H. Leu, and G. Herold, "Optimization of the modular multilevel converters performance using the second harmonic of the module current," in *Power Electronics and Applications, 2009. EPE 09. 13th European Conference on*, pp. 1–10, Sept 2009.

[30] S. Rivera, B. Wu, R. Lizana, S. Kouro, M. Perez, and J. Rodriguez, "Modular multilevel converter for large-scale multistring photovoltaic energy conversion system," in *Energy Conversion Congress and Exposition (ECCE), 2013 IEEE*, pp. 1941–1946, Sept 2013.

[31] "IEEE application guide for IEEE Std 1547(TM), IEEE standard for interconnecting distributed resources with electric power systems," *IEEE Std 1547.2-2008*, pp. 1–217, April 2009.

[32] "IEEE standard for interconnection and interoperability of distributed energy resources with associated electric power systems interfaces," *IEEE Std 1547-2018 (Revision of IEEE Std 1547-2003)*, pp. 1–138, April 2018.

[33] Q. Tu, Z. Xu, and L. Xu, "Reduced switching-frequency modulation and circulating current suppression for modular multilevel converters," *Power Delivery, IEEE Transactions on*, vol. 26, pp. 2009–2017, July 2011.

[34] Q. Tu and Z. Xu, "Impact of sampling frequency on harmonic distortion for modular multilevel converter," *Power Delivery, IEEE Transactions on*, vol. 26, pp. 298–306, Jan 2011.

[35] Q. Tu, Z. Xu, Y. Chang, and L. Guan, "Suppressing DC voltage ripples of MMC-HVDC under unbalanced grid conditions," *Power Delivery, IEEE Transactions on*, vol. 27, pp. 1332–1338, July 2012.

[36] R. Oliveira and A. Yazdani, "An enhanced steady-state model and capacitor sizing method for modular multilevel converters for HVDC applications," *IEEE Transactions on Power Electronics*, vol. PP, no. 99, pp. 1–1, 2017.

[37] R. Oliveira and A. Yazdani, "A modular multilevel converter with DC fault handling capability and enhanced efficiency for HVDC system applications," *IEEE Transactions on Power Electronics*, vol. 32, pp. 11–22, Jan 2017.

[38] B. Li, S. Zhou, D. Xu, S. J. Finney, and B. W. Williams, "A hybrid modular multilevel converter for medium-voltage variable-speed motor drives," *IEEE Transactions on Power Electronics*, vol. 32, pp. 4619–4630, June 2017.

[39] B. Li, S. Zhou, D. Xu, R. Yang, D. Xu, C. Buccella, and C. Cecati, "An improved circulating current injection method for modular multilevel converters in variable-speed drives," *IEEE Transactions on Industrial Electronics*, vol. 63, pp. 7215–7225, Nov 2016.

[40] J. Kolb, F. Kammerer, M. Gommeringer, and M. Braun, "Cascaded control system of the modular multilevel converter for feeding variable-speed drives," *IEEE Transactions on Power Electronics*, vol. 30, pp. 349–357, Jan 2015.

[41] A. Edpuganti and A. K. Rathore, "Optimal pulse-width modulation for common-mode voltage elimination scheme of medium-voltage modular multilevel converter-fed open-end stator winding induction motor drives," *IEEE Transactions on Industrial Electronics*, vol. 64, pp. 848–856, Jan 2017.

[42] D. Ludois and G. Venkataramanan, "Simplified dynamics and control of modular multilevel converter based on a terminal behavioral model," in *Energy Conversion Congress and Exposition (ECCE), 2012 IEEE*, pp. 3520–3527, Sept 2012.

[43] J. Echeverria, S. Kouro, M. Perez, and H. Abu-Rub, "Multi-modular cascaded DC-DC converter for HVDC grid connection of large-scale photovoltaic power systems," in *Industrial Electronics Society, IECON 2013 - 39th Annual Conference of the IEEE*, pp. 6999–7005, Nov 2013.

[44] Y. Yu, G. Konstantinou, C. D. Townsend, and V. G. Agelidis, "Comparison of zero-sequence injection methods in cascaded H-bridge multilevel converters for large-scale photovoltaic integration," *IET Renewable Power Generation*, vol. 11, no. 5, pp. 603–613, 2017.

[45] Y. Yu, G. Konstantinou, B. Hredzak, and V. G. Agelidis, "On extending the energy balancing limit of multilevel cascaded H-bridge converters for large-scale photovoltaic farms," in *2013 Australasian Universities Power Engineering Conference (AUPEC)*, pp. 1–6, Sept 2013.

[46] C. D. Townsend, T. J. Summers, and R. E. Betz, "Control and modulation scheme for a cascaded H-bridge multi-level converter in large scale photovoltaic systems," in *2012 IEEE Energy Conversion Congress and Exposition (ECCE)*, pp. 3707–3714, Sept 2012.

[47] Y. Yu, G. Konstantinou, B. Hredzak, and V. G. Agelidis, "Optimal zero sequence injection in multilevel cascaded H-bridge converter under unbalanced photovoltaic power generation," in *2014 International Power Electronics Conference (IPEC-Hiroshima 2014 - ECCE ASIA)*, pp. 1458–1465, May 2014.

[48] S. Rivera, S. Kouro, B. Wu, J. Leon, J. Rodriguez, and L. Franquelo, "Cascaded h-bridge multilevel converter multistring topology for large scale photovoltaic sys-

tems," in *Industrial Electronics (ISIE), 2011 IEEE International Symposium on*, pp. 1837–1844, June 2011.

[49] A. Antonopoulos, L. Angquist, and H.-P. Nee, "On dynamics and voltage control of the modular multilevel converter," in *Power Electronics and Applications, 2009. EPE '09. 13th European Conference on*, pp. 1–10, Sept 2009.

[50] Q. Tu, Z. Xu, H. Huang, and J. Zhang, "Parameter design principle of the arm inductor in modular multilevel converter based HVDC," in *Power System Technology (POWERCON), 2010 International Conference on*, pp. 1–6, Oct 2010.

[51] A. Yazdani and R. Iravani, *Voltage-sourced converters in power systems: modeling, control, and applications.* John Wiley & Sons, 2010.

[52] J. W. Moon, C. S. Kim, J. W. Park, D. W. Kang, and J. M. Kim, "Circulating current control in MMC under the unbalanced voltage," *IEEE Transactions on Power Delivery*, vol. 28, pp. 1952–1959, July 2013.

[53] Z. Li, P. Wang, Z. Chu, H. Zhu, Y. Luo, and Y. Li, "An inner current suppressing method for modular multilevel converters," *IEEE Transactions on Power Electronics*, vol. 28, pp. 4873–4879, Nov 2013.

[54] D. Wu and L. Peng, "Analysis and suppressing method for the output voltage harmonics of modular multilevel converter," *IEEE Transactions on Power Electronics*, vol. 31, pp. 4755–4765, July 2016.

[55] B. Li, D. Xu, and D. Xu, "Circulating current harmonics suppression for modular multilevel converters based on repetitive control," *Journal of Power Electronics*, vol. 14, pp. 1100–1108, Nov 2014.

[56] T. Soong and P. W. Lehn, "Internal power flow of a modular multilevel converter with distributed energy resources," *IEEE Journal of Emerging and Selected Topics in Power Electronics*, vol. 2, pp. 1127–1138, Dec 2014.

[57] D. Ludois, J. Reed, and G. Venkataramanan, "Hierarchical control of bridge-of-bridge multilevel power converters," *Industrial Electronics, IEEE Transactions on*, vol. 57, pp. 2679–2690, Aug 2010.

[58] D. Ludois and G. Venkataramanan, "Simplified terminal behavioral model for a modular multilevel converter," *Power Electronics, IEEE Transactions on*, vol. 29, pp. 1622–1631, April 2014.

[59] F. B. Ajaei and R. Iravani, "Enhanced equivalent model of the modular multilevel converter," *IEEE Transactions on Power Delivery*, vol. 30, pp. 666–673, April 2015.

[60] H. Saad, J. Peralta, S. DennetiÃĺre, J. Mahseredjian, J. Jatskevich, J. A. Martinez, A. Davoudi, M. Saeedifard, V. Sood, X. Wang, J. Cano, and A. Mehrizi-Sani, "Dynamic averaged and simplified models for MMC-based HVDC transmission systems," *IEEE Transactions on Power Delivery*, vol. 28, pp. 1723–1730, July 2013.

[61] A. G. M. Strollo, "A new IGBT circuit model for SPICE simulation," in *PESC97. Record 28th Annual IEEE Power Electronics Specialists Conference. Formerly Power Conditioning Specialists Conference 1970-71. Power Processing and Electronic Specialists Conference 1972*, vol. 1, pp. 133–138 vol.1, Jun 1997.

[62] J. Peralta, H. Saad, S. Dennetiere, J. Mahseredjian, and S. Nguefeu, "Detailed and averaged models for a 401-level MMC-HVDC system," *IEEE Transactions on Power Delivery*, vol. 27, pp. 1501–1508, July 2012.

[63] S. Kouro, B. Wu, A. Moya, E. Villanueva, P. Correa, and J. Rodriguez, "Control of a cascaded H-bridge multilevel converter for grid connection of photovoltaic systems," in *Industrial Electronics, 2009. IECON '09. 35th Annual Conference of IEEE*, pp. 3976–3982, Nov 2009.

[64] S. Kouro, M. Malinowski, K. Gopakumar, J. Pou, L. G. Franquelo, B. Wu, J. Rodriguez, M. A. Perez, and J. I. Leon, "Recent advances and industrial applica-

tions of multilevel converters," *IEEE Transactions on Industrial Electronics*, vol. 57, pp. 2553–2580, Aug 2010.

[65] S. B. Kjaer, J. K. Pedersen, and F. Blaabjerg, "A review of single-phase grid-connected inverters for photovoltaic modules," *IEEE Transactions on Industry Applications*, vol. 41, pp. 1292–1306, Sept 2005.

[66] F. Blaabjerg, Z. Chen, and S. B. Kjaer, "Power electronics as efficient interface in dispersed power generation systems," *IEEE Transactions on Power Electronics*, vol. 19, pp. 1184–1194, Sept 2004.

[67] S. Islam, A. Woyte, R. Belmans, P. Heskes, P. Rooij, and R. Hogedoorn, "Cost effective second generation AC-modules: Development and testing aspects," *Energy*, vol. 31, no. 12, pp. 1897 – 1920, 2006.

[68] E. Solas, G. Abad, J. Barrena, S. Aurtenetxea, A. Carcar, and L. Zajac, "Modular multilevel converter with different submodule concepts-part I: Capacitor voltage balancing method," *Industrial Electronics, IEEE Transactions on*, vol. 60, pp. 4525–4535, Oct 2013.

[69] E. Solas, G. Abad, J. Barrena, S. Aurtenetxea, A. Carcar, and L. Zajac, "Modular multilevel converter with different submodule concepts-part II: Experimental validation and comparison for HVDC application," *Industrial Electronics, IEEE Transactions on*, vol. 60, pp. 4536–4545, Oct 2013.

[70] Z. Xu, H. Xiao, and Z. Zhang, "Selection methods of main circuit parameters for modular multilevel converters," *IET Renewable Power Generation*, vol. 10, no. 6, pp. 788–797, 2016.

[71] S. Pingel, O. Frank, M. Winkler, S. Daryan, T. Geipel, H. Hoehne, and J. Berghold, "Potential induced degradation of solar cells and panels," in *2010 35th IEEE Photovoltaic Specialists Conference*, pp. 002817–002822, June 2010.

[72] H. W. van der Broeck, H. C. Skudelny, and G. V. Stanke, "Analysis and realization of a pulse-width modulator based on voltage space vectors," *IEEE Transactions on Industry Applications*, vol. 24, pp. 142–150, Jan 1988.

[73] J. Rodriguez, J.-S. Lai, and F. Z. Peng, "Multilevel inverters: a survey of topologies, controls, and applications," *IEEE Transactions on Industrial Electronics*, vol. 49, pp. 724–738, Aug 2002.

[74] D. G. Holmes and B. P. McGrath, "Opportunities for harmonic cancellation with carrier-based PWM for a two-level and multilevel cascaded inverters," *IEEE Transactions on Industry Applications*, vol. 37, pp. 574–582, Mar 2001.

[75] B. Li, R. Yang, D. Xu, G. Wang, W. Wang, and D. Xu, "Analysis of the phase-shifted carrier modulation for modular multilevel converters," *Power Electronics, IEEE Transactions on*, vol. 30, pp. 297–310, Jan 2015.

[76] G. K. Ari and Y. Baghzouz, "Impact of high PV penetration on voltage regulation in electrical distribution systems," in *2011 International Conference on Clean Electrical Power (ICCEP)*, pp. 744–748, June 2011.

[77] S. Vazquez, S. M. Lukic, E. Galvan, L. G. Franquelo, and J. M. Carrasco, "Energy storage systems for transport and grid applications," *IEEE Transactions on Industrial Electronics*, vol. 57, pp. 3881–3895, Dec 2010.

[78] Y. Moumouni, Y. Baghzouz, and R. F. Boehm, "Power "smoothing" of a commercial-size photovoltaic system by an energy storage system," in *2014 16th International Conference on Harmonics and Quality of Power (ICHQP)*, pp. 640–644, May 2014.

[79] R. Jiang, J. Wang, and Y. Guan, "Robust unit commitment with wind power and pumped storage hydro," *IEEE Transactions on Power Systems*, vol. 27, pp. 800–810, May 2012.

[80] G. Wang, M. Ciobotaru, and V. G. Agelidis, "Power smoothing of large solar PV plant using hybrid energy storage," *IEEE Transactions on Sustainable Energy*, vol. 5, pp. 834–842, July 2014.

[81] H. Beltran, E. Bilbao, E. Belenguer, I. Etxeberria-Otadui, and P. Rodriguez, "Evaluation of storage energy requirements for constant production in PV power plants," *IEEE Transactions on Industrial Electronics*, vol. 60, pp. 1225–1234, March 2013.

[82] P. F. Ribeiro, B. K. Johnson, M. L. Crow, A. Arsoy, and Y. Liu, "Energy storage systems for advanced power applications," *Proceedings of the IEEE*, vol. 89, pp. 1744–1756, Dec 2001.

[83] H. Chen, T. N. Cong, W. Yang, C. Tan, Y. Li, and Y. Ding, "Progress in electrical energy storage system: A critical review," *Progress in Natural Science*, vol. 19, no. 3, pp. 291 – 312, 2009.

[84] S. C. Smith, P. K. Sen, and B. Kroposki, "Advancement of energy storage devices and applications in electrical power system," in *2008 IEEE Power and Energy Society General Meeting - Conversion and Delivery of Electrical Energy in the 21st Century*, pp. 1–8, July 2008.

[85] Quanta Technology, "Electric energy storage systems," 2013.

[86] M. N. Kheraluwala, R. W. Gascoigne, D. M. Divan, and E. D. Baumann, "Performance characterization of a high-power dual active bridge DC-to-DC converter," *IEEE Transactions on Industry Applications*, vol. 28, pp. 1294–1301, Nov 1992.

[87] R. T. Naayagi, A. J. Forsyth, and R. Shuttleworth, "Bidirectional control of a dual active bridge DC-DC converter for aerospace applications," *IET Power Electronics*, vol. 5, pp. 1104–1118, August 2012.

[88] H. Akagi, S. i. Kinouchi, and Y. Miyazaki, "Bidirectional isolated dual-active-bridge (DAB) DC-DC converters using 1.2-kV 400-A SiC-MOSFET dual modules," *CPSS Transactions on Power Electronics and Applications*, vol. 1, pp. 33–40, Dec 2016.

[89] J. Marcos, L. Marroyo, E. Lorenzo, and M. GarcÃŋa, "Smoothing of PV power fluctuations by geographical dispersion," *Progress in Photovoltaics: Research and Applications*, vol. 20, no. 2, pp. 226–237, 2012.

[90] A. Yazdani, A. R. D. Fazio, H. Ghoddami, M. Russo, M. Kazerani, J. Jatskevich, K. Strunz, S. Leva, and J. A. Martinez, "Modeling guidelines and a benchmark for power system simulation studies of three-phase single-stage photovoltaic systems," *IEEE Transactions on Power Delivery*, vol. 26, pp. 1247–1264, April 2011.

[91] O. Tremblay, L. A. Dessaint, and A. I. Dekkiche, "A generic battery model for the dynamic simulation of hybrid electric vehicles," in *2007 IEEE Vehicle Power and Propulsion Conference*, pp. 284–289, Sept 2007.

[92] Q. Ye, R. Mo, and H. Li, "Impedance modeling and verification of a dual active bridge (DAB) DC/DC converter enabled DC microgrid in FREEDM system," in *2016 IEEE 8th International Power Electronics and Motion Control Conference (IPEMC-ECCE Asia)*, pp. 2875–2879, May 2016.

[93] B. Zhao, Q. Yu, and W. Sun, "Extended-phase-shift control of isolated bidirectional DC-DC converter for power distribution in microgrid," *IEEE Transactions on Power Electronics*, vol. 27, pp. 4667–4680, Nov 2012.

[94] F. Krismer and J. W. Kolar, "Accurate small-signal model for the digital control of an automotive bidirectional dual active bridge," *IEEE Transactions on Power Electronics*, vol. 24, pp. 2756–2768, Dec 2009.

[95] H. Tao, J. L. Duarte, and M. A. M. Hendrix, "High-resolution phase shift and digital implementation of a fuel cell powered UPS system," in *2007 European Conference on Power Electronics and Applications*, pp. 1–10, Sept 2007.

[96] G. Ortiz, J. Biela, D. Bortis, and J. W. Kolar, "1 Megawatt, 20 kHz, isolated, bidirectional 12kV to 1.2kV DC-DC converter for renewable energy applications," in *The 2010 International Power Electronics Conference - ECCE ASIA -*, pp. 3212–3219, June 2010.

[97] Z. Zhang and X. Ruan, "A novel double phase-shift control scheme for full-bridge three-level converter," in *Twentieth Annual IEEE Applied Power Electronics Conference and Exposition, 2005. APEC 2005.*, vol. 2, pp. 1240–1245 Vol. 2, March 2005.

[98] A. RodrÃŋguez, A. VÃązquez, D. G. Lamar, M. M. Hernando, and J. SebastiÃąn, "Different purpose design strategies and techniques to improve the performance of a dual active bridge with phase-shift control," *IEEE Transactions on Power Electronics*, vol. 30, pp. 790–804, Feb 2015.

[99] S. Inoue and H. Akagi, "A bidirectional isolated DC-DC converter as a core circuit of the next-generation medium-voltage power conversion system," *IEEE Transactions on Power Electronics*, vol. 22, pp. 535–542, March 2007.

Curriculum Vitae

Name:	Hasan Bayat
Post-Secondary Education and Degrees:	The University of Western Ontario London, ON, Canada 2014 - 2018, PhD in Electrical Engineering Amirkabir University of Technology Tehran, Iran 2008 - 2011, M.Sc. in Electrical Engineering University of Guilan Rasht, Guilan 2004 - 2008, B.Sc. in Electrical Engineering
Honors and Awards:	Western Graduate Research Scholarship 2014-2018
Related Work Experience:	Research and Teaching Assistant The University of Western Ontario 2014 - 2018

Publications:

- H. Bayat and A. Yazdani, "A power mismatch elimination strategy for an MMC-based photovoltaic system," *Energy Conversion, IEEE Transactions on,* vol. 33, pp. 1519-1528, Sept 2018

- H. Bayat, J. Moghani, S. H. Fathi, and H. H. Riazmontazer, "Implementation of a 5 level cascaded h-bridge inverter using PWM strategy with unequal carrier

frequency for optimizing and reducing the switching number," International Review of Electrical Engineering (I.R.E.E), vol. 6, pp. 23-29 , January - February 2011

- H. Bayat, J. S. Moghani, S. H. Fathi, and M. Taheri, "Reduction of switching frequency using reference phase disposition PWM technique in multilevel h-bridge inverters," in 2011 2nd Power Electronics, Drive Systems and Technologies Conference, pp. 27-31, Feb 2011

- M. Taheri, J. Milimonfared, H. Bayat, and S. H. Fathi, "Analysis, design and implementation of a new zerovoltage-switching interleaved asymmetrical half-bridge converter using an integrated transformer," IET Power Electronics, vol. 5, pp. 1912 - 1922, November 2012

- M. Taheri, J. Milimonfared, H. Bayat, H. Riazmontazer, and A. Noroozi, "Analysis and design of a new soft switching interleaved converter using an integrated transformer," in 2011 2nd Power Electronics, Drive Systems and Technologies Conference, pp. 98 - 103, Feb 2011

- H. Riazmontazer, J. Moghani, H. Bayat, and M. Taheri, "An isolated bi-directional dc-dc converter with zero current switching in LV side and zero voltage switching in HV side," International Review of Electrical Engineering (I.R.E.E), vol. 6, pp. 492-499, March - April 2011

- M. Taheri, J. Milimonfared, H. Bayat, H. Riazmontazer, and A. Noroozi, "Analysis and design of a new choke less interleaved ZVS forward-flyback converter," in 2011 2nd Power Electronics, Drive Systems and Technologies Conference, pp. 81-86, Feb 2011

- M. Taheri, J. Milimonfared, A. Namadmalan, H. Bayat, and M. Bakhshizadeh, "Analysis, design and implementation of a new chokeless interleaved ZVS forward-flyback converter," Journal Of Power Electronics (JPE), vol. 11, pp. 499-506, July 2011

- H. Riazmontazer, J. S. Moghani, M. Taheri, and H. Bayat, "Averaged modeling of a new bi-directional dc-dc converter," in 2011 2nd Power Electronics, Drive Systems and Technologies Conference, pp. 574-580, Feb 2011